Full kinematic reconstruction of charged B mesons with the upgraded Inner Tracking System of the ALICE Experiment

Johannes Hendrik Stiller

Dissertation
submitted to the
Combined Faculties of the Natural Sciences and Mathematics
of the Ruperto-Carola-University of Heidelberg, Germany
for the degree of
Doctor of Natural Sciences

Put forward by

Dipl.-Phys. Johannes Hendrik Stiller
born in Cologne, Germany

Oral examination: May 11th, 2016

Full kinematic reconstruction of charged B mesons with the upgraded Inner Tracking System of the ALICE Experiment

Referees: PD Dr. Kai Schweda
Prof. Dr. Ulrich Uwer

Deutsche Zusammenfassung

In dieser Dissertation wurde die zu erwartende Effizienz des verbesserten ALICE-Experiments in der vollen kinematischen Rekonstruktion von B^+ Mesons und seinen Ladungspartnern im Zerfall $\mathrm{B}^+ \rightarrow \overline{\mathrm{D}}^0\pi^+$ ($\overline{\mathrm{D}}^0 \rightarrow \mathrm{K}^+\pi^-$) in 0–10 % zentralen Blei-Blei Kollisionen bei $\sqrt{s_{\mathrm{NN}}} = 5.5\,\mathrm{TeV}$ nach dem Beginn des Run 3 des Large Hadron Collider (LHC) in 2020 bestimmt. Im Rahmen der geplanten Verbesserungen der Detektoren und deren Auslesesysteme wird - um alle Pb–Pb Kollisionen bei ihrer Interaktionsrate von 50 kHz zu untersuchen - insbesondere durch die Installation eines neuen, fein segmentierten inneren Spurdetektors, die volle kinematische Rekonstruktion dieser seltenen Signale in ALICE zum ersten Mal bei mittlerer Rapidität am Large Hadron Collider (LHC) ermöglicht. Dabei werden topologische und kinematische Auswahlkriterien des Beauty-Signals verwendet, um den hohen kombinatorischen sowie korrelierten Untergrund zu unterdrücken. Zusätzlich zu bestehenden vollen Monte-Carlo-(MC)-Simulationen wurde eine schnelle MC-Simulation entwickelt, die Parametrisierungen aller wichtigen Detektoreffekte umfasst und nun generell für alle Studien seltener Zerfälle mit dem verbesserten ALICE-Detektor zur Verfügung steht. So konnten die Abschätzungen des verbleibenden Untergrundes und somit des zu erwartenden Signal-zu-Untergrund-Verhältnisses sowie der statistischen Signifikanz verbessert werden. Innerhalb der Unsicherheiten in bezug auf die zu erwartende Signalhöhe wird eine signifikante Messung (≥ 5) bis zu $p_{\mathrm{T}} \geq 2.0\,\mathrm{GeV}/c$ möglich sein, was etwa 88 % des gesamten Spektrums entspricht. Das vorhergesagte Signal-zu-Untergrund-Verhältnis nimmt im Bereich 0.01 bis 4.0 mit steigendem p_{T} zu. Die notwendige integrierte Luminosität der p+p-Referenzmessung beträgt bei $\sqrt{s} = 5.5\,\mathrm{TeV}$ etwa $100\,\mathrm{pb}^{-1}$. Durch die berechnete Statistik wurde die Präzision der Messungen des nuklearen Modifikationsfaktors R_{AA} sowie des elliptischen Flusses v_2 abgeschätzt. Für $p_{\mathrm{T}} \geq 5.0\,\mathrm{GeV}/c$ wird eine Messung des theoretisch vorhergesagten Wertes bei 0.2–0.5 möglich sein, während für kleinere Impulse die Messung der Erhöhung über $R_{\mathrm{AA}} = 1.0$ hinaus stark von der theoretischen R_{AA}-Vorhersage abhängt. Die statistische Abweichung der theoretischen Vorhersage des elliptischen Flusses von einer Nullhypothese variiert je nach der zu erwartenden Größe und der tatsächlich verfügbaren Statistik für zentrale und mehr periphere Kollisionen im Bereich 1.6–5.3 σ.

English Abstract

In this thesis, the performance of the full kinematic reconstruction of B^+ mesons in the decay channel $\mathrm{B}^+ \rightarrow \overline{\mathrm{D}}^0 \pi^+$ ($\overline{\mathrm{D}}^0 \rightarrow \mathrm{K}^+ \pi^-$) and charge conjugates for the 0–10 % most central Pb–Pb collisions at $\sqrt{s_{\mathrm{NN}}} = 5.5\,\mathrm{TeV}$ is demonstrated for the upgraded ALICE Experiment, which is planned before Run 3 of the Large Hadron Collider (LHC), beginning in 2020. Within the scope of the foreseen detector and readout upgrades to inspect all Pb–Pb collisions at their interaction rate of 50 kHz, in particular through the installation of a new high-granularity pixel inner tracker, for the first time these rare signals will become accessible using full kinematic reconstruction in central Pb–Pb collisions in ALICE at mid-rapidity at the LHC. Topological and kinematic criteria are used to select the beauty signal against the large combinatorial and correlated background. In addition to available full Monte Carlo (MC) simulations, a fast MC simulation, which includes parameterizations of all relevant detector effects, was developed and is now generally available for all rare probe studies with the upgraded ALICE detector. The fast simulation was used to improve the estimate on the residual combinatorial background in order to maximize the expected signal-to-background ratio and statistical significance. Within the uncertainties of the expected signal yield, a significant measurement ($\geq$ 5) will be possible down to $p_{\mathrm{T}} \geq 2.0\,\mathrm{GeV}/c$, corresponding to about 88 % of the yield. The signal-to-background ratio lies between 0.01 and 4.0, increasing with p_{T}. The required reference statistics in p+p collisions at $\sqrt{s} = 5.5\,\mathrm{TeV}$ was estimated to be about $100\,\mathrm{pb}^{-1}$. Considering the calculated expected statistics, the precision of the measurements of the nuclear modification factor R_{AA} and the elliptic flow v_2 were estimated. A measurement of the theoretically predicted R_{AA} of 0.2–0.5 above $p_{\mathrm{T}} \geq 5.0\,\mathrm{GeV}/c$ will be possible, while the sensitivity for lower momenta on the enhancement above $R_{\mathrm{AA}} = 1.0$ is strongly model dependent. The separation power between the theoretically predicted v_2 and a non-flow scenario is within 1.6–5.3 σ for central and more peripheral collisions, depending on the actual magnitude and the available statistical precision.

Acknowledgements

First of all, I want to express my gratitude to my supervisor, *Dr. Kai Schweda*, who accompanied me since my very first semester in physics about nine and a half years ago. I will never forget his talk as our lecture group instructor, in which he explained ALICE and the Quark-Gluon Plasma. It was Kai, who introduced me to the world of particle physics and finally supervised my Diploma thesis in 2011. Without any doubt, I would not have decided to obtain a degree in nuclear physics in ALICE without him, as he always motivated me through his inspiration and physics discussion in his own style.

I want to thank *Prof. Dr. Johanna Stachel*, for the many opportunities I could follow in her group. Frequent travel to CERN, and in particular the work on the ALICE Transition Radiation Detector (TRD), were a fantastic experience I was able to grow upon. Further, I was given the chance to attend international conferences and workshops, where I learnt a lot about this exciting field of physics. I also want to thank the complete ALICE group in Heidelberg for many fruitful discussions on physics and beyond.

There are a few people who are particularly important for the evolution of my work into this thesis. I express my gratitude to *Dr. Andrea Dainese* for his tremendous support and additional guidance throughout the time. Further, I am very thankful to *Dr. Ruben Shahoyan*, *Dr. Marian Ivanov* and *Dr. Jouri Belikov* who never hesitated to explain the (technical) details of the (upgraded) ITS and TPC detectors as well as the tracking algorithm. Further, I want to thank *Dr. Andrea Rossi* and *Dr. Alessandro Grelli* for their help with the algorithms for the full kinematic reconstruction of heavy-flavor mesons. I would like to take the opportunity to thank the complete ITSu working groups under the supervision of *Dr. Luciano Musa* for many shared thoughts, comments and discussion.

I want to thank *Prof. Dr. Ulrich Uwer* for his work as a second referee of this thesis.

I address special thanks to those who helped me improve and advance this document, in particular the contributions by *Dr. Yvonne Pachmayer, Dr. Jochen Klein, Dr. Hans Beck, Sebastian Klewin, Felix Reidt* and *Dr. Sebastian Bachmann*, who supported me with their comments and suggestions.

Further, I want to say thank you to *Dr. Jorge Mercado*, for the fantastic time at CERN. I am very happy to be among those, who were installing and completing the TRD under your supervision.

Finally, I want to express my deepest gratitude to my friends and family in Cologne and Heidelberg, who encouraged me every day in the spirit of the first three paragraphs in the

Kölsches Grundgesetz - *Ground rules in Cologne:*
§1: Et es, wie et es. - *§1: It is what it is.*
§2: Et kütt, wie et kütt. - *§2: What will be, will be.*
§3: Et hätt noch immer joot jejange. - *§3: It always worked out somehow.*

This work has been supported by the Federal Ministry of Education and Research under promotional reference 06HD197D and by the Helmholtz Alliance HA126/EMMI.

Contents

List of Figures

List of Tables

Acronyms

ACORDE	ALICE COsmic Ray DEtector
AD	ALICE diffractive physics Detector
ALEPH	Apparatur for LEP pHysics
ALICE	A Large Ion Collider Experiment
AOD	Analysis Object Data
ATLAS	A Toroidal LHC ApparatuS
BAMPS	Boltzmann Approach to MuliParton Scatterings
BNL	Brookhaven National Laboratory
CERN	Conseil Européen pour la Recherche Nucléaire
CFL	Color-Flavor Locked
CGC	Color Glass Condensates
CMOS	Complementary Metal-Oxide Semiconductor
CMS	Compact Muon Solenoid
CPU	Central Processing Unit
CTP	Central Trigger Processor
CT-PPS	CMS-TOTEM Precision Proton Spectrometer
DAQ	Data AcQuisition system
DCA	Distance of Closest Approach
DELPHI	DEtector with Lepton, Photon and Hadron Identification
DESY	Deutsches Elektronen-SYnchrotron
ECR	Electron Cyclotron Resonance
EMCAL	ElectroMagnetic CALorimeter
EOS	Equation Of State
ESD	Event Summary Data

EYETS	Extended Year End Technical Stop
FET	Fast Estimation Tool
FIT	Fast Interaction Trigger
FMD	Forward Multiplicity Detector
FMCT	Fast Monte Carlo Tool
FONLL	Fixed Order Next to Leading Log
FT2	Fast estimation Tool 2
GEM	Gas Electron Multiplier
GSI	GSI Helmholtzzentrum für Schwerionenforschung GmbH
HBT	Handbury Brown-Twiss
HERA	Hadron Elektron Ring Anlage
HIJING	Heavy-Ion Jet INteraction Generator
HL-LHC	High Luminosity LHC
HLT	High Level Trigger
HMPID	High Momentum Particle IDentification
HPD	Hybrid PhotoDiodes
HV	High Voltage
IBL	Insertable B-Layer
IP	Interaction Point
IROC	Inner ReadOut Chamber
ITS	Inner Tracking System
ITSu	upgraded Inner Tracking System
LEIR	Low Energy Ion Ring
LEP	Large Electron Positron collider
LHC	Large Hadron Collider
LHCb	Large Hadron Collider beauty
LHCf	Large Hadron Collider forward
LIGO	Laser Interferometer Gravitational-wave Observatory

LINAC	LINear ACcelerator
LO	Leading-Order
LP	Large Pitch
LPM	Landau-Pomerantschuk-Migdal
LS	Long Shutdown
MAPS	Monolithic Active Pixel Sensor
MC	Monte Carlo
MCH	Muon tracking CHambers
MCM	Multi-Chip Module
MFT	Muon Forward Tracker
MoEDAL	Monopole and Exotics Detector At the LHC
MRPC	Multigap Resistive Plate Chamber
MTR	Muon TRigger
MWPC	Multi-Wire Proportional Chamber
NBD	Negative-Binomial-Distribution
NLO	Next-to-Leading Order
NMOS	N-type Metal-Oxide-Semiconductor
NNLO	Next-to-Next-to-Leading Order
OCDB	Offline Condition DataBase
OROC	Outer ReadOut Chamber
PHOS	PHOton Spectrometer
PID	Particle IDentification
PMD	Photon Multiplicity Detectors
PMOS	P-type Metal-Oxide-Semiconductor
PS	Proton Synchrotron
PSB	Proton Synchrotron Booster
QCD	Quantum Chromodynamics
QED	Quantum Electrodynamics

QFT	Quantum Field Theory
QGP	Quark-Gluon Plasma
RHIC	Relativistic Heavy-Ion Collider
SciFi	Scintillating Fiber detector
SDD	Silicon Drift Detector
SiPM	Silicon PhotoMultiplier
SP	Small Pitch
SPD	Silicon Pixel Detector
SPS	Super Proton Synchrotron
SSD	Silicon Strip Detector
STAR	Solenoidal Tracker At RHIC
T0	Cherenkov detectors based on photomultiplier tubes
TOF	Time-of-Flight Detector
TOTEM	TOTal Elastic and diffractive cross-section Measurement
TPC	Time Projection Chamber
TRD	Transition Radiation Detector
V0	forward scintillator wheels
VELO	VErtex LOcator
ZDC	Zero Degree Calorimeter

1. Introduction

Indirect evidence for a new state of matter was found in fixed-target experiments at the Super Proton Synchrotron (SPS) at CERN, when lead-nuclei were brought to collision in 1994. The combined measurements in Pb–Pb collisions of hadronic expansion by NA49 [1], J/ψ-suppression by NA50 [2], strangeness enhancement by WA97 [3], and direct photons by WA98 [4], also seen by other experiments at SPS [5], can be considered a door opener into a new era of high-energy heavy-ion physics. Since then, it is recognized that a strongly interacting and color-deconfined state of high energy-density matter, the Quark-Gluon Plasma (QGP), was generated. It is believed that this state resembles the early phases of our universe a few μs after the Big Bang [6], 13.8 billions years ago.

Ultra-relativistic heavy-ion collisions performed at the Relativistic Heavy Ion Collider (RHIC) at BNL or the Large Hadron Collider (LHC) at CERN are well suited to reproduce this extreme environment under controlled laboratory conditions, where the particle debris of the plasma is analyzed in large experiments operated by thousands of scientists all over the world. An event display of particle tracks from such a central Pb–Pb collision at $\sqrt{s_{\mathrm{NN}}} = 5.02\,\mathrm{TeV}$ recorded by A Large Ion Collider Experiment (ALICE) during the dedicated LHC heavy-ion run in 2015 is shown in figure 1.1. Due to color confinement in the underlying description of the strong interaction, the transient existence of the QGP can currently only be studied through the memory of the particles on their re-interactions with the hot matter, which imprints collective phenomena on the escaping hadrons from the fireball volume. Here, comparisons to reference measurements taken in p+p and p–Pb collisions are a particularly useful tool to study QGP-induced effects. Eventually, these comparisons lead to the observation of suppression patterns of highly energetic particles in the nuclear modification factor, which tell us that energy loss of partons propagating through the medium occurs [7]. Further, at RHIC and LHC the medium was also quantified as an almost perfect liquid with very small shear viscosity to entropy density ratio $\eta/s \approx 0.2$, which can be studied through momentum anisotropies of the produced hadrons and corresponding theoretical modeling [8].

Among these measurements of the QGP, heavy-flavored mesons and baryons containing charm or beauty quarks are of particular interest as they are calibrated probes of the medium: Heavy quarks are generated in hard initial scatterings of the colliding nuclei at a time scale of $0.02\,\mathrm{fm}/c$ (for beauty), before the QGP formation [9]. Due to their long lifetimes ($\mathcal{O}(\mu\mathrm{m}/c)$ [10]) they can experience the full evolution of the medium, which has a lifetime of about $10\,\mathrm{fm}/c$ [9]. Further, it is expected that the heavy-quark yield remains stable due to their large mass, as it is unlikely that more heavy-quarks are produced through thermal in-medium generation [11].

With a center-of-mass energy of up to $\sqrt{s_{\mathrm{NN}}} = 5.5\,\mathrm{TeV}$ in Pb–Pb collisions, the LHC provides a unique opportunity to study charmed and beauty mesons and baryons, for example via the full kinematic reconstruction of their decay daughters. With this approach, evidence for energy loss of heavy-flavored mesons at a similar magnitude than light-flavor partons

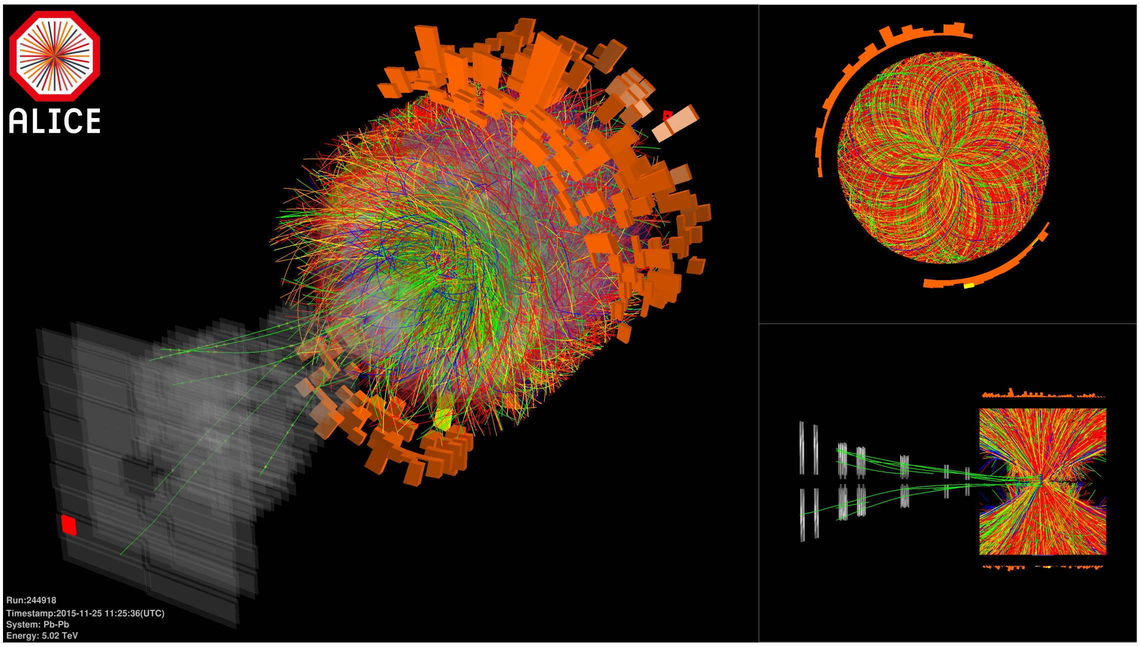

Figure 1.1.: Event display of charged particle tracks from a central Pb–Pb collision at $\sqrt{s_{\mathrm{NN}}} = 5.02\,\mathrm{TeV}$ recorded by ALICE during the dedicated LHC run in 2015. In addition, the magnitude of the energy loss of electrically charged and neutral particles in the electromagnetic calorimeters is displayed as towers. This figure has been taken from [12].

was found [13], and first hints that charmed mesons participate in the collective elliptic motion of the QGP were detected [14].

At LHC, ALICE, with its outstanding particle identification, vertexing and tracking capabilities, has contributed a wealth of information for charmed signals and performed first investigations of the beauty sector via the decay into electrons [15] and J/ψ mesons [16]. Due to the large branching ratios ($\approx 10\,\%$) of charmed and beauty mesons into semi-leptonic decay channels, these decays are particularly well-suited for analyses. However, on the one hand trigger thresholds on the transverse momentum prevent measurements down to lowest p_{T}, while on the other hand kinematic information is largely lost as not all decay daughters can be reconstructed. Up to the current date, only the CMS Collaboration was capable to completely reconstruct beauty mesons via the full kinematic reconstruction of $\mathrm{B}^+ \rightarrow \mathrm{J}/\psi(1\mathrm{S})\mathrm{K}^+$ ($\mathrm{J}/\psi(1\mathrm{S}) \rightarrow \mu^+\mu^-$) in p–Pb [17] and Pb–Pb collisions [18] at mid-rapidity. However, at mid-rapidity the muon trigger and selection capabilities as well as the detector acceptance restrict the observation to a lower limit of about $p_{\mathrm{T}} = 10\,\mathrm{GeV}/c$, which prevents detailed measurements of the elliptic flow and the nuclear modification factor.

With the foreseen upgrade of the ALICE Experiment, which will be installed during the second Long Shutdown (LS2) of the LHC, it is planned to turn current measurements into high-precision analyses of heavy-flavored hadrons and to extend the measurements to the full kinematic reconstruction of beauty hadrons in heavy-ion collisions [19]. These beauty signals are limited by their production cross-sections as well as branching ratios into hadronic channels, and become only available in this approach through the prospective detector and readout upgrades [19]. These upgrades will allow ALICE to inspect all Pb–Pb collisions provided by the LHC at a rate of 50 kHz ($\mathcal{L} = 6 \cdot 10^{27}\,\mathrm{cm}^{-2}\mathrm{s}^{-1}$), such that a total integrated luminosity of $\mathrm{L}_{\mathrm{int}} = 10\,\mathrm{nb}^{-1}$ will be accumulated beyond 2020 without any additional trigger requirements. The upgraded Inner Tracking System (ITSu) is particularly important for the analyses of heavy-flavored mesons and baryons, as it is crucial to identify the displaced secondary vertices of the decay. With the improved spatial and momentum resolution, the new detector will allow to efficiently select the signal on top of a large combinatorial background. After the exploration of the charm sector in Pb–Pb collisions at mid-rapidity, the upgraded ALICE Experiment will have access to fully reconstructed beauty hadrons over a wide p_{T}-range [20]. Due to their large mass $m_{\mathrm{b}} = 4.66 \pm 0.03\,\mathrm{GeV}/c^2$ [10], beauty quarks are a new probe to characterize the QGP as they are extremely sensitive to the Equation Of State (EOS) of the deconfined medium [11]. In particular the new measurements of the elliptic flow and the nuclear modification factor will provide new insight on the relativistic hydrodynamic evolution of the medium and will allow to investigate whether the expected hierarchy in the quark energy loss ($\Delta E_{\mathrm{g}} > \Delta E_{\mathrm{u,d,s}} > \Delta E_{\mathrm{c}} > \Delta E_{\mathrm{b}}$) [21] is present. Thus, with a particular focus on the new silicon pixel detector, the expected performance of the upgraded ALICE Experiment is studied within this thesis in dedicated full and fast Monte Carlo (MC) simulations of the weak beauty decay $\mathrm{B}^+ \rightarrow \overline{\mathrm{D}}^0\pi^+$ ($\overline{\mathrm{D}}^0 \rightarrow \mathrm{K}^+\pi^-$) and their charge conjugates, with branching ratios of $\mathrm{BR}(\mathrm{B}^+ \rightarrow \overline{\mathrm{D}}^0\pi^+) = (4.81 \pm 0.15) \cdot 10^{-3}$ and $\mathrm{BR}(\overline{\mathrm{D}}^0 \rightarrow \mathrm{K}^+\pi^-) = (3.88 \pm 0.05) \cdot 10^{-2}$ [10], respectively.

High-statistics MC simulations are mandatory in order to precisely quantify the expected reconstruction efficiency and the statistical significance as well as signal-to-background ratio of the signal decay, such that good knowledge of the underlying particle background is gained. However, for the rare signals like the presented $\mathrm{B}^+ \rightarrow \overline{\mathrm{D}}^0\pi^+$ ($\overline{\mathrm{D}}^0 \rightarrow \mathrm{K}^+\pi^-$), conventional full MC methods are at the limit of generating sufficient statistics, constrained by finite available computing resources. For this purpose, a new parameterized fast MC method (FT2) was developed and applied, which is about three to four orders of magnitude faster than full MC simulations while reproducing the ALICE performance to a high precision. This tool serves as a general baseline for future developments and is now available for the study of rare probes with the upgraded ALICE Experiment.

This thesis is structured as follows: The physics of the QGP produced in heavy-ion collisions, with a focus on the production of beauty particles, is summarized in section 2, which concludes with an outline of the current status of open heavy-flavor measurements. An overview of the LHC and the ALICE Experiment, in particular of the planned ITS upgrade project, is presented in section 3. As it is a crucial ingredient for the background analysis of the presented analysis of B^+ mesons, the newly developed simulation tool is explained in detail in section 4. This includes a general introduction into Monte Carlo and data handling in ALICE, with a review of the underlying Kalman filter track reconstruction. The selection strategy and performance of the full kinematic reconstruction of $\mathrm{B}^+ \rightarrow \overline{\mathrm{D}}^0\pi^+$ ($\overline{\mathrm{D}}^0 \rightarrow \mathrm{K}^+\pi^-$) in Pb–Pb collisions is presented in section 5, which is followed by a calculation of the required p+p reference statistics in section 6. The expected sensitivity of the measurement on key observables is evaluated in section 7 while a summary and outlook are given in section 8.

2. Quantum Chromodynamics in heavy-ion collisions

In this section an outline of the physics background of relativistic heavy-ion collisions is presented. After a short introduction of the Standard Model of particle physics and some of the underlying mechanisms of the formulation in Quantum Chromodynamics (QCD), fundamental properties of the QGP are highlighted. A special focus is given on the production of heavy-flavor quarks in nucleon-nucleon and heavy-ion collisions. This section is concluded with a short overview of the current status of charm and beauty observables.

2.1. The Standard Model of particle physics

The Standard Model of particle physics as we know it today, is a great triumph of particle physics as it is capable of explaining most experimental measurements while providing true predictions for new particles. It was built upon many years of successful interplay between the theoretical explanations and predictions as well as experimental observations. For example, the predecessor of the Standard Model was developed by Glashow, Weinberg and Salam in the 1960s [22, 23, 24] and predicted a neutrally charged partner of the $\mathrm{W}^{\pm}$ bosons. After the proof of renormalizability of the underlying Quantum Field Theory (QFT) by 't Hooft and Veltman in 1971 [25, 26] the first clear evidence of neutral-current interactions were then observed in 1973 [27]. Such observations eventually improved into precision measurements of the Z^0 mass pole obtained in $\mathrm{e}^+\mathrm{e}^-$-collisions at LEP, which, in turn, determined the number of light neutrino families [28].

The building blocks of the Standard Model are schematically presented in figure 2.1. It is constructed from fundamental spin-$\frac{1}{2}$ particles, the fermions, split into six quarks (q) and six leptons (l), which are further grouped by their mass into three generations. Leptons consists of the electrically charged electrons (e), muons (μ) and tauons (τ), with their corresponding electrically neutral partners, the neutrinos (ν_e, ν_μ, ν_τ). Light quarks are labeled as *down, up* (u, d), and *strange* (s), whereas the heavy quarks are called *charm, beauty* (c, b), and *top* (t). For each of these particles, there exists an anti-particle, which carries the opposite quantum numbers. As outlined in the following sections, quarks are typically bound in baryons (qqq) and mesons ($\mathrm{q\overline{q}}$), which eventually decay rapidly into their light partners, the protons and neutrons [29].

The underlying theoretical framework is a gauge QFT, obeying the internal symmetries of the unitary group $\mathrm{SU(3)_C \times SU(2)_L \times U(1)_Y}$ [30]. Here, C, L and Y stand for color, left-handedness and the weak hypercharge, which are characteristic for the coupling of the mediating spin-1 bosons. The corresponding interactions are indicated by shaded areas in figure 2.1.

The interactions between members of the $\mathrm{SU(2)_L \times U(1)_Y}$ group correspond to the massive $\mathrm{W}^{\pm}$ and Z^0 bosons, discovered in 1983 [31, 32, 33, 34], and the photon. While the photon

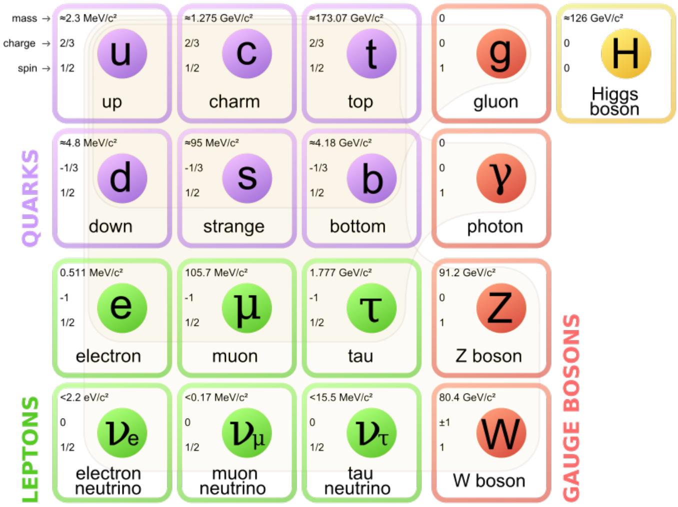

Figure 2.1.: Fundamental particles and their interaction bosons in the Standard Model of particle physics. The masses for quarks correspond to the bare quark masses, where the recent values are available in: [10]. In this figure, the underlying fundamental forces are linked to their interaction particles through shaded areas. The charges are given in units of the electron charge. This figure has been taken from [35].

is the interaction boson of the electromagnetic force, coupling to the electric charge of the fermions and described by Quantum Electrodynamics (QED), the massive bosons mediate the charged and neutral current weak interactions. The mass of the bosons is a consequence of the spontaneous electroweak symmetry breaking [23]. Their coupling to the scalar Higgs field generates the masses of the three massive electroweak gauge bosons [29]. The corresponding boson was recently discovered by the ATLAS and CMS Collaborations at the LHC [36, 37] at a mass of $125.09 \pm 0.24\,\mathrm{GeV}/c^2$ [10].
The interactions between the ground states of the $\mathrm{SU}(3)_\mathrm{C}$ group corresponds to the strong interaction characterized by QCD. This theory describes the strong interaction, which couples to the color charge of the quarks, mediated via eight colored gluons. As it is most important for heavy-ion collisions, some relevant properties of QCD will be highlighted in the subsequent section 2.1.1. Note, that the quark masses in figure 2.1 correspond to the bare quark masses, which are set by the renormalization scale μ_R, contrary to the much larger constituent quark masses, which are the effective masses of quarks bound into hadrons.
The strong force is two orders of magnitude stronger than the electromagnetic interaction and a factor 10^{12} stronger than the weak interaction. The gravitational force, supposedly mediated by a hypothetical elementary particle, the graviton, is completely negligible on the scales of subatomic processes. Even though the graviton itself has not (yet) been discovered, the recent first observation of gravitational waves by the LIGO and Virgo[i] interferometers [38] can be used to improve the upper limit on the mass of the graviton to $m_g \leq 1.2 \cdot 10^{-22}\,\mathrm{eV}/c^2$ at 90 % confidence [39].

---

[i] named after the Virgo Cluster in the corresponding constellation

2.1.1. Properties of Quantum Chromodynamics

Quantum Chromodynamics is the formal theory which describes the strong interaction between colored quarks and gluons. Contrary to QED, which is a U(1) local gauge symmetry, QCD is invariant under SU(3) local phase transformations. The eight generators of this symmetry group are represented in 3×3 matrices and the particle wave function must include three additional degrees of freedom, the so called color charges *red, blue* and *green*. Only (anti-)quarks and gluons carry (anti-)color, where the states are ordered by two additive quantum numbers, the third component color isospin I_3^c and the color hyper charge Y^c. The force-mediating gluons, which correspond to the eight non-diagonal generator matrices, consist of a combination of color and anti-color. The color charge is conserved in the strong interaction and the gluon color octet can be written as

$$\left(r\overline{g},\ g\overline{r},\ r\overline{b},\ b\overline{r},\ g\overline{b},\ b\overline{g},\ \frac{1}{\sqrt{2}}\left(r\overline{r} - g\overline{g}\right) \text{ and } \frac{1}{\sqrt{6}}\left(r\overline{r} + g\overline{g} - 2b\overline{b}\right) \right) \text{ [29].} \tag{2.1}$$

An important feature in QCD is the spontaneous chiral symmetry breaking, which is responsible for most of the visible mass in the universe. The relation between the constituent mass (total quark mass) and the fraction of mass obtained via the Higgs field is presented in figure 2.2. The large displacement of the light quark masses to the right of the diagonal represents the large fraction of mass assigned via the spontaneous chiral symmetry breaking in the QCD vacuum. This means that quarks bound into hadrons acquire masses larger by $\mathcal{O}(10^2\,\mathrm{MeV}/c^2)$ compared to their bare masses. For heavy quarks, this fraction becomes almost negligible.

An important difference to QED is, that in QCD the mediating gluons are self-interacting, which give rise to triple and quartic gluon self-interaction vertices. The existence of these interaction vertices might be connected to *color confinement*, which is not yet understood.

2.1.1.1. Color confinement and running coupling

Even though there is no analytic proof of the concept, color confinement is an experimentally established phenomenon of QCD [29, 40]. As a consequence of color confinement, no single free quarks, carrying fractional charge, can be observed, as they are always bound into color singlet states with zero net-color charge. Conceptually, this limits the type of possible bound hadronic states to (anti-)mesons ($\mathrm{q\overline{q}}$), (anti-)baryons (qqq), and any combination of these, e.g. pentaquarks ($\mathrm{qqqq\overline{q}}$), as recently confirmed by the LHCb Collaboration [41]. Color confinement is phenomenologically described by a linear term in the non-relativistic QCD potential between two quarks at a relative distance $\vec{r}$:

$$V_{\mathrm{q\overline{q}}}(\vec{r}) \;=\; -\mathrm{C}\frac{\alpha_{\mathrm{S}}}{\mathrm{r}} + \kappa \mathrm{r}, \tag{2.2}$$

where α_{S} is the strong coupling constant, $\mathrm{r}=|\vec{r}|$ and $\kappa \approx 1\,\mathrm{GeV/fm}$, determined experimentally (e.g. [42, 43, 44]). The color factor $\mathrm{C} = \frac{4}{3}$ is derived from the interaction between quarks and gluons [29]. In case the two quarks are pulled apart, the gluon self-interaction constrains the field into a color-tube between the quarks. The required energy to separate the quarks grows so large that the additional generation of $\mathrm{q\overline{q}}$-pairs is energetically more favorable.

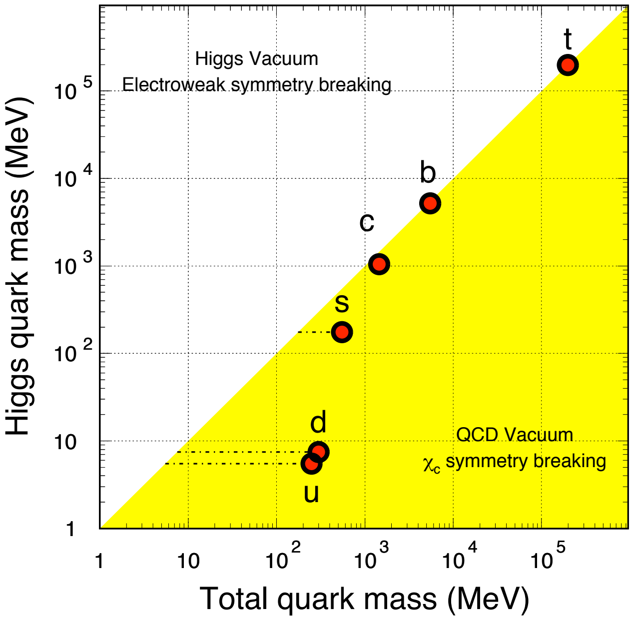

Figure 2.2.: Correlation of Higgs quark mass and the total (=constituent) quark mass generated by chiral symmetry breaking in the QCD vacuum. Chiral symmetry restoration is expected in the Quark-Gluon Plasma phase, as presented in section 2.2. This figure has been taken from [11].

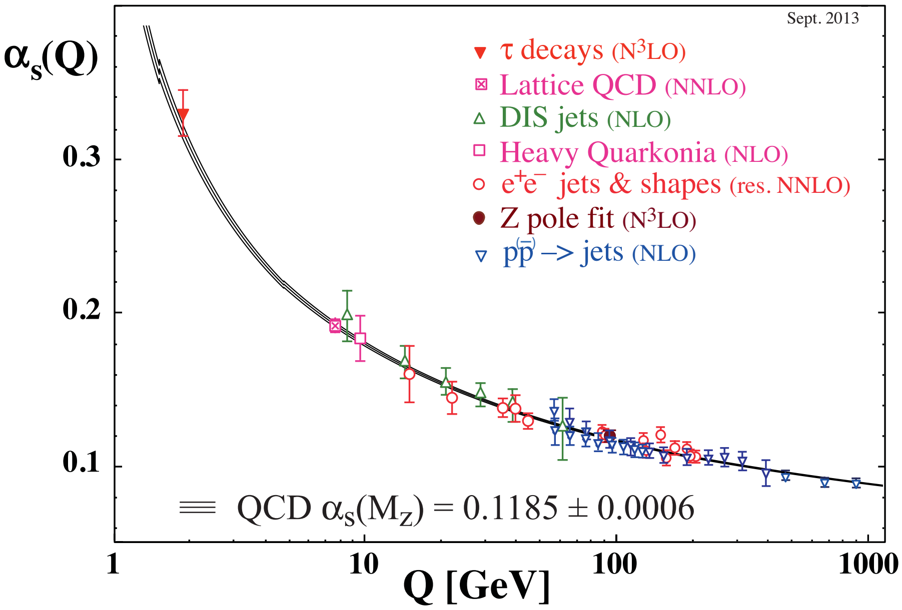

Figure 2.3.: Strong coupling constant measured at different momentum transfer using different methods, superimposed on QCD calculations. Small edges in the calculations indicate the onset of different quark flavors. The best prediction is obtained with higher-order fits to the Z^0 pole width in e^+e^- collisions [28]. This figure has been taken from [10].

When the quarks are brought closer to each other, which corresponds to an increasing momentum transfer Q between them, they interact not as strong with each other. This phenomenon is called *asymptotic freedom*, which is a consequence of the decrease of the QCD coupling α_S with increasing momentum transfer, as depicted in figure 2.3. As in QED, this behavior is a consequence of the required renormalization of the theory, without which the higher-order Feynman diagrams of the interaction would result in divergent integrals over the four momentum of the particles. However, in QED *vacuum polarization* is the dominating effect, which corresponds to a shielding effect of the charges and thus a decreasing coupling strength for decreasing Q (larger distance between the charges). Even though this effect is also present for gluons in QCD, the self-interaction of the gluons leads to a dominating anti-shielding contribution [40]. Theoretically, the evolution of $\alpha_\mathrm{S}(\mathrm{Q}^2)$ then corresponds to:

$$\alpha_S(\mathrm{Q}^2) = \frac{1}{B \cdot \ln\left(\mathrm{Q}^2/\Lambda^2_\mathrm{QCD}\right)}, \text{ where } B = \frac{11N_c - 2N_f}{12\pi}. \tag{2.3}$$

Here, $N_c = 3$ is the number of colors, and $N_f \leq 6$ the number of included quark flavors. $\Lambda_\mathrm{QCD} \approx 200\,\mathrm{MeV}$ is the experimentally determined renormalization scale. This behavior implies that QCD can be used perturbatively for large enough scales.

Note, that figure 2.3 displays various measurements of $\alpha_\mathrm{S}(\mathrm{Q}^2)$, where the highest precision is obtained from the analysis of the QCD corrections to the measured Z^0 pole width in $\mathrm{e}^+\mathrm{e}^-$ collisions [28]. At the LHC, measurements are made at higher energies through multi-jet analysis [43, 44].

2.2. Phase diagram of Quantum Chromodynamics

The thermodynamics of QCD can be expressed via the external thermodynamic parameters of temperature T and the baryo-chemical potential μ_B. The understanding of these properties is essential for the theoretical descriptions of phenomena such as neutron stars or the QGP state of the universe shortly after the Big Bang.

The state of quarks and gluons can be visualized in a phase diagram of QCD, describing the behavior for changes of the thermodynamic parameters. A schematic view of this phase diagram is displayed in figure 2.5, where ordinary nuclear matter is located at $\mathrm{T} = 0\,\mathrm{MeV}$ and $\mu_B = 922\,\mathrm{MeV}/c^2$ [45]. At low temperatures and low momentum transfer Q, α_S is large and QCD is non-perturbative. In this regime the chiral symmetry is spontaneously broken in its ground state and for low temperatures nuclear matter behaves as a hadron gas. However, for temperatures $\mathrm{T} \gg \Lambda_\mathrm{QCD}$ the coupling becomes asymptotically free. Due to the color screening, which corresponds to the linear term in equation 2.2, quarks and gluons can be considered quasi-free, which results in chiral-symmetry restoration. Considering the observed finite quark masses, and thus in the absence of exact chiral symmetry, there must be a smooth crossover region for $\mu_B = 0$, which was also confirmed by lattice QCD calculations [46, 47]. Within the region of the critical temperature, the typical kinetic energy of a non-relativistic particle is of similar size as the temperature, and QCD cannot be used perturbatively, as the running coupling is not small. Thus, the only way to obtain sophisticated results are lattice QCD calculations [48]. Here, calculations to find the partition sum Z based on the QCD-Lagrangian are arranged on a four dimensional

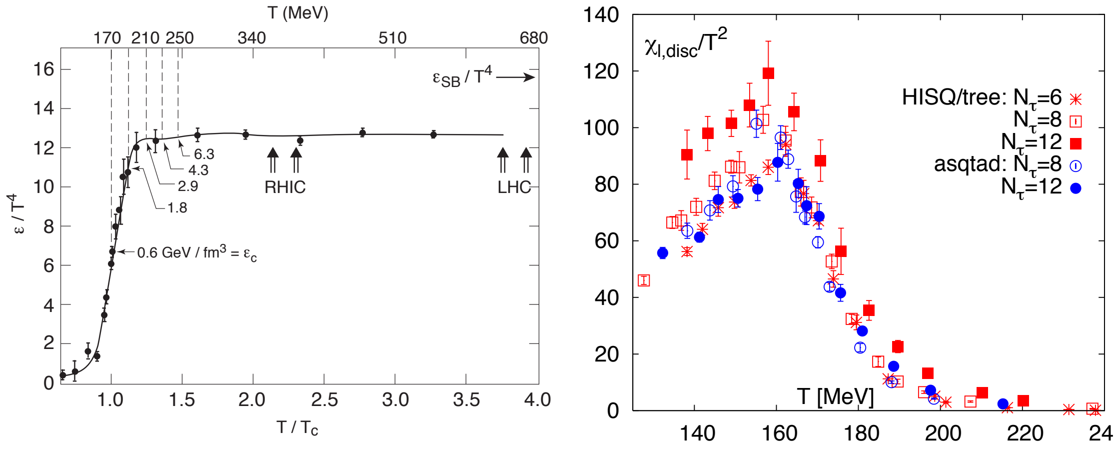

(a) **(b)**

Figure 2.4.: (a) displays the energy density obtained from lattice QCD calculation, with a rapid rise due to the sudden liberation of quarks and gluons from hadrons at T_c. At the high-temperature limit, the energy density approaches the indicated Stefan Boltzmann limit. The peak of the chiral susceptibility at the critical temperature is visible in (b). These figures have been taken from [45] and [49], respectively.

space-time lattice, which is used to control the ultraviolet divergence, while maintaining local gauge invariance on all field variables and actions on the lattice [50]. From this partition sum, thermodynamic properties can be calculated, for example

$$\epsilon = \frac{T^2}{V}\left(\frac{\partial \ln(Z)}{\partial V}\right)_V \text{ [51]}, \tag{2.4}$$

$$\text{and } \chi = \frac{T}{V}\frac{\partial^2 \ln(Z)}{\partial m_q^2} \text{ [49]}, \tag{2.5}$$

where ϵ is the energy density, χ the chiral susceptibility, V the system volume, T the temperature, and m_q the quark mass. Lattice QCD calculations can provide the Equation Of State (EOS) of QCD, however due to the sign problem [52], thermodynamic variables are only available for (almost) vanishing baryo-chemical potentials. The energy density ϵ/T^4 is depicted in figure 2.4a for 2+1 quark flavors (up and down + strange). The rapid rise of the energy density reflects the sudden change of the number of degrees of freedom, which corresponds to liberation of the quarks and gluons from hadrons, dominating the thermal medium at high temperatures. For increasing temperatures, the energy density asymptotically approaches the free gas limit of gluons and the given number of quark flavors n_f, which is the Stefan Boltzmann limit at energy density ϵ_{SB} and pressure p_{SB}. It is set by the assumption of an ideal hadron gas, where only elastic interaction occurs.

$$\frac{\epsilon_{SB}}{T^4} = \frac{3p_{SB}}{T^4} = \left(16 + \frac{21}{2}n_f\right)\frac{\pi^2}{30} \text{ [50]}. \tag{2.6}$$

The chiral susceptibility, shown in equation 2.5, is a derivative of the chiral order parameters with respect to the quark mass. As displayed in figure 2.4b, it peaks at the same critical temperature, which indicates that the restoration of chiral symmetry coincides with deconfinement.

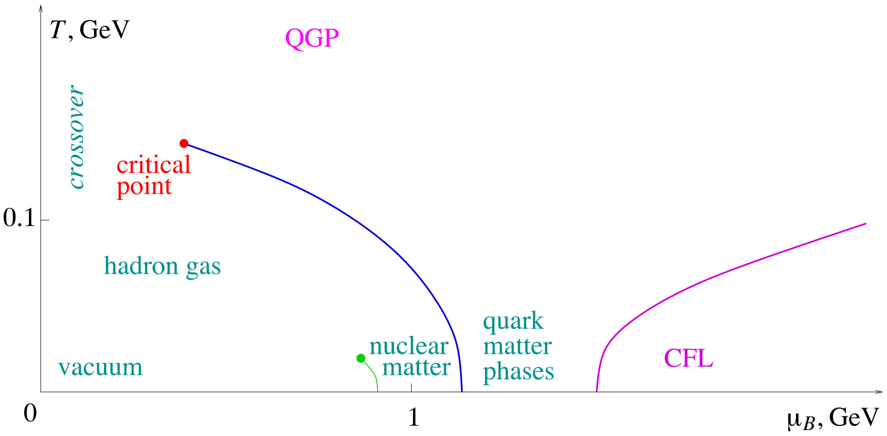

Figure 2.5.: Schematic phase diagram of QCD. At vanishing baryo-chemical potential and high temperatures, a crossover from a hadron gas into the Quark-Gluon Plasma state is calculated. As a first order phase transition is present for finite baryo-chemical potential, there must be a critical point when approaching the crossover region. At high μ_B models predict a state as expected within the core of a neutron star. This figure has been taken from [48].

For large baryo-chemical potentials and low temperature, a transition into a color-superconducting state is anticipated, as it is expected inside the core of neutron stars. For three quark flavors, a possible occurrence of a Color-Flavor Locked (CFL) state is expected in some models [53]. Experimentally this region is difficult to access.
As a consequence of the first order phase transition for finite baryo-chemical potential and temperature on the one hand, and the crossover region at $\mu_B = 0$ and $T_c = 150$–$170\,\mathrm{MeV}$ ($\approx \Lambda_{\mathrm{QCD}}$) on the other hand, the transition between ordinary hadronic matter and the QGP state must have a critical point in between, which remains to be fully determined theoretically and experimentally [48].
Relativistic heavy-ion collisions are the ideal candidates to study these phase transitions and the generated QGP in a controlled laboratory environment. Given the high energy, and thus temperature, the baryo-chemical potential is almost zero in these collisions at LHC and RHIC, which means that the top-left region of the phase diagram is covered. On a small scale, these highly-energetic collisions allow to trace back the evolution of our universe, when it cooled off into the QGP state about 1 ps–10 μs [6] after the Big Bang and eventually into the bound hadronic state, as it is observed today.

2.3. Quark-Gluon Plasma in heavy-ion collisions

As outlined above, heavy-ion collisions such as Pb–Pb collisions at the LHC, are a prominent tool to study the phase diagram of QCD, as they are powerful enough to create the QGP medium at low baryo-chemical potential and high temperatures. After a brief introduction into some geometric variables, more detailed explanations on the parameters and evolution of the generated matter state will be given in the following section.

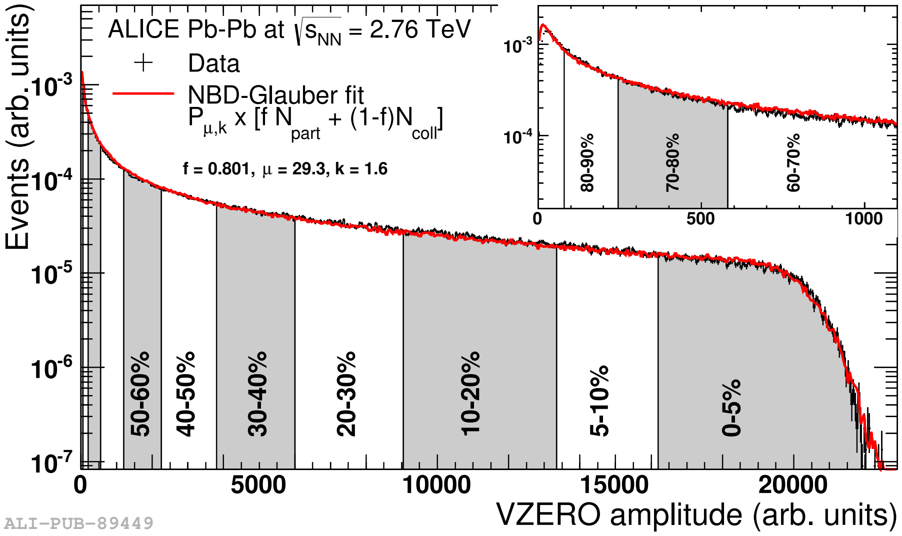

Figure 2.6.: Centrality measurement of spectator nucleons by the V0 detector in ALICE. The data was fit with a NBD-Glauber MC, from which the geometric parameters of the collision are determined. Here, $P_{\mu,k}$ corresponds to a Negative-Binomial-Distribution, which reflects the probability of measuring a given amount of hits per ancestor using the mean multiplicity μ and the width k. This figure has been taken from [54].

2.3.1. Geometric variables

The geometry of a heavy-ion collision is described by the centrality percentile, which is dependent on the impact parameter b between the two colliding nuclei with macroscopic radii R_1 and R_2. The geometric description becomes meaningful, as the de Broglie wavelength of the nucleons is small compared to the size of the nuclei. For $b = 0$, a collision is called *head-on* or *central*, while *minimum-bias* collisions correspond to impact parameters $b \in (0, R_1 + R_2]$. However, these (initial) geometric quantities are not experimentally accessible, but can be related to the observed particle multiplicity and the number of spectator nucleons. This is based on the assumptions that the measured released energy and particle multiplicity is proportional to the number of nucleons, which participated in the collisions. In heavy-ion collisions typically Glauber-type Monte Carlo simulations [55] are employed to relate the different quantities. These models depend on a non-diffractive inelastic nucleon-nucleon cross-section $\sigma_{\text{inel}}^{\text{NN}}$ (e.g. $\sigma_{\text{inel}}^{\text{p+p}} = 62.8^{+2.4}_{-4.0}\,(\text{model}) \pm 1.2\,(\text{lumi})\,\text{mb}$ for p+p collisions at $\sqrt{s} = 2.76\,\text{TeV}$ [56]) and a Woods-Saxon nuclear density profile

$$\rho\,(r) = \frac{\rho_0}{1 + \exp\left(\frac{r - r_0}{c}\right)}, \tag{2.7}$$

where r is the radial distance to the center of the nucleus with a radius $r_0^{\text{Pb}} \approx 6.62\,\text{fm}$ [57] and a skin depth $c^{\text{Pb}} \approx 0.546\,\text{fm}$ [57] obtained in elastic electron-nucleus scattering experiments, while $\rho_0 \approx 0.17\,\text{fm}^{-1}$ [55] is the nuclear density constant in the center of heavy nuclei. The number of binary collisions N_{coll} and participating nucleons N_{part}, as well as $\sigma_{\text{inel}}^{\text{NN}}$, can then be determined from a fit to the observed signal, for example in the V0 detectors of ALICE (see section 3.2).

As it is displayed in figure 2.6 the centrality percentiles are grouped in bins, e.g. 0–5 % (most central), according to their fractional yield of the overall integrated cross-section. In the presented approach a Negative-Binomial-Distribution (NBD)-Glauber fit is applied to the data. This Glauber MC corresponds to a two-component model, which defines N_{part} and N_{coll} for a given impact parameter b [54]. The particle multiplicity per nucleon-nucleon collision is parameterized by the NBD and decomposed into soft and hard interactions. In this approach, the average particle multiplicity generated by soft interaction is proportional to N_{part}, while the probability for hard interactions is proportional to N_{coll}. Independent of the actual process or emitting sources of particles, the total number of “ancestors“ of the two processes can be parameterized as $N_{\text{ancestors}} = f \cdot N_{\text{part}} + (1 - f) \cdot N_{\text{coll}}$, where f is a fit parameter. The average number of binary collisions N_{coll} relates to the total inelastic nucleon-nucleon cross-section via the nuclear overlap function T_{AA} such that

$$\langle N_{\text{coll}}(b)\rangle = \langle T_{AA}(b)\rangle \cdot \sigma_{\text{inel}}^{\text{NN}}. \tag{2.8}$$

2.3.2. Space-time evolution of the Quark-Gluon Plasma

It is a great challenge to link the dynamic aspects of heavy-ion collisions, which evolve within a few fm/c, to the static formulation of the QGP. Hydrodynamic evolution of heavy-ion collisions establishes this link as it can describe the space-time evolution of thermodynamic variables. The evolution is described by the Bjorken reaction picture, which was developed for increased incident energies of the incoming nuclei from the Landau picture [58]. In the Bjorken model two highly relativistic nuclei punch through each other during a collision, as they appear transparent to each other at large center-of-mass energies. However, they leave a trace of highly excited matter between them. In the pre-equilibrium phase $\tau < \tau_0$ the energy quanta de-excite into real quarks and gluons, the QGP, which reaches thermal equilibrium at τ_0. The space-time evolution is schematically displayed in figure 2.7. At LHC energies, the generated medium is characterized by an almost zero net-baryon density and a mean free path l of the constituent particles much shorter than the system size L. The equation of state can be obtained from lattice QCD calculations, while initial conditions must be taken from other models, such as the Color Glass Condensate (CGC). These CGC models are capable of describing the properties of the high-density gluon fields within heavy ions (e.g. [59]). Assuming a perfect liquid without viscosity, the system expands according to ideal relativistic hydrodynamics, as depicted in figure 2.7. The expectation values of the medium are parameterized solely as a function of the local energy density ϵ and pressure P. The energy-momentum tensor $T^{\mu\nu}$ and baryon number current must be conserved, thus

$$\begin{aligned} \partial_\mu T^{\mu\nu}(x) &= 0,\ \text{using } T^{\mu\nu}(x) = \begin{pmatrix} \epsilon(x) & 0 & 0 & 0 \\ 0 & P(x) & 0 & 0 \\ 0 & 0 & P(x) & 0 \\ 0 & 0 & 0 & P(x) \end{pmatrix} && (2.9) \\ \partial_\mu j_{\text{B}}^{\mu}(x) &= n_{\text{B}}(x)\, u^{\mu}(x) = 0, && (2.10) \end{aligned}$$

using the four-velocity $u^{\mu}(x)$ as well as the baryon number density $n_{\text{B}}(x)$, defined in the local rest frame of the fluid [58]. Further, the entropy current

$$s^{\mu}(x) = s(x)\, u^{\mu}(x) \tag{2.11}$$

has to be conserved as well. The fluid motion is adiabatic and reversible as implied by the absence of viscosity and thermal conductivity. The assumption of a perfect liquid with a low viscosity seems legitimate, as suggested by comparisons of data and theoretical models at RHIC [60]. In case of non-vanishing values of the viscosity, the currents above need to be modified with additional terms to include the derivatives of the flow velocity and thermodynamical variables. During the hydrodynamic period, the thermalized QGP expands and cools down to the point of a phase transition, which occurs when the mean free path of the constituent particles is not small any more relative to the system size. This process happens in two stages: After the phase transition at the critical temperature T_c, the chemical freeze-out occurs at T_{ch}, at which the abundancies of each particles species are frozen, while the equilibration in the phase-space is maintained. The generated hadrons may still interact and can be described by the Boltzmann equation for a hadron gas, until this stage freezes out at T_{fo}, after which the kinetic equilibrium is not maintained.

The space-time evolution of collisions can be studied by interferometric measurements of identical particles. In this approach, known as Handbury Brown-Twiss (HBT) analysis, the Bose-Einstein enhancement of identical bosons emitted at short distance in phase space with respect to each other is exploited. In ALICE, two-pion correlations were determined in central Pb–Pb collisions at $\sqrt{s_{\text{NN}}} = 2.76\,\text{TeV}$ and a decoupling time at mid-rapidity larger than $10\,\text{fm}/c$ was found, which is $40\,\%$ larger than previous RHIC measurements [61]. However, in earlier measurements it was found that the source radii as obtained from Bose-Einstein correlations of neutral and charged kaons are consistently smaller as for pions [62], implying that kaons freeze out earlier than pions.

Additional constraints on the initial conditions and the subsequent relativistic hydrodynamic evolution, can be obtained from model fits on observables well-accessible to the experiments, as for example for the magnitude of the shear viscosity presented in figure 2.9. The two most prominent candidates, the (collective) flow of the system as well as the energy loss of constituent quarks measured via the nuclear modification factor R_{AA} of the corresponding hadrons, are outlined in the following sections. In addition, two models, which are used later in this thesis, are summarized in order to highlight the understanding of the underlying mechanisms in the QGP.

2.3.3. Flow

In heavy-ion collisions, correlations between detected (identified) particles are a useful tool to understand the properties and dynamics of the collision system, as the generated QGP imposes a collective behavior. From the conservation laws in equations 2.9 and 2.10, a relativistic generalization of the Euler equation can be derived [58], which links the total derivative of the fluid motion $\vec{v}$ to the pressure gradient ∇P in the considered fluid cell

$$\frac{\partial \vec{v}}{\partial t} + (\vec{v} \cdot \nabla)\,\vec{v} = -\frac{1 - \vec{v}^2}{\epsilon + P}\left[\nabla P + \vec{v}\frac{\partial P}{\partial t}\right]. \tag{2.12}$$

As a consequence, any observed collective motion of the QGP constituents is induced by the pressure gradient of the medium, which originates from the geometric overlap region and the initial spatial density profiles of the nuclei. This collectivity is studied for example via the event plane method, which quantifies the invariant particle yield via a Fourier

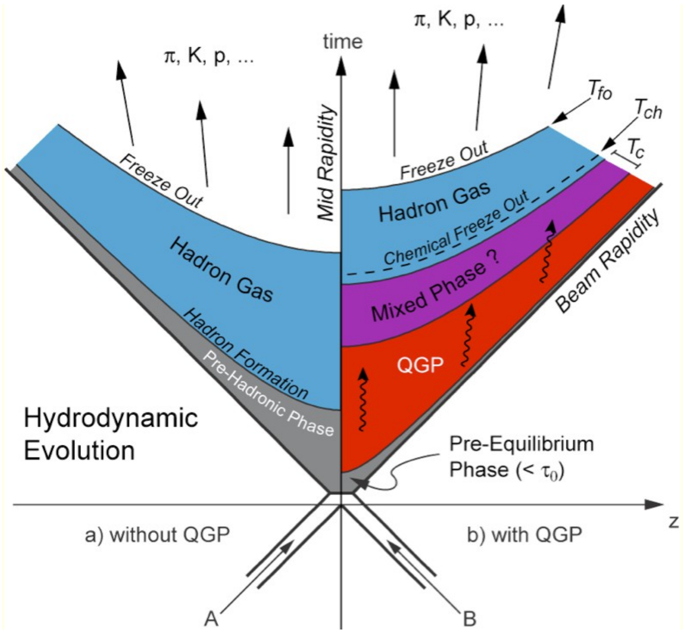

Figure 2.7.: Sketch of the hydrodynamic evolution of a nuclear collision with and without QGP phase in Minkowski coordinates. Both situations are displayed within the physical light cone. On the left, a hadron gas forms after the de-excitation of the initial phase, which freezes out into single hadrons at a later stage. If a QGP phase exists, the liberated quarks and gluons experience the kinetic freeze-out at T_{c}, after which they form hadrons at the chemical freeze out T_{ch} (depicted on the right side). This figure has been taken from [63].

decomposition, as the pressure gradient cannot be measured directly by itself:

$$
\begin{aligned}
E\frac{\mathrm{d}^3N}{\mathrm{d}^3p} &= \frac{\mathrm{d}^3N}{p_{\mathrm{T}}\mathrm{d}p_{\mathrm{T}}\mathrm{d}y\mathrm{d}\phi}\left(p_{\mathrm{T}},y,\phi\right) = \frac{1}{2\pi}\frac{\mathrm{d}^2N}{p_{\mathrm{T}}\mathrm{d}p_{\mathrm{T}}\mathrm{d}y}\left[1+\sum_{n=1}^{\infty}2v_n\left(p_{\mathrm{T}},y\right)\cos\left[n\left(\phi-\Psi_n\right)\right]\right] \\
&= \frac{1}{2\pi}\frac{\mathrm{d}^2N}{p_{\mathrm{T}}\mathrm{d}p_{\mathrm{T}}\mathrm{d}y}\left[1+2v_1\left(p_{\mathrm{T}},y\right)\cos\left[\phi-\Psi_1\right]+2v_2\left(p_{\mathrm{T}},y\right)\cos\left[2\left(\phi-\Psi_2\right)\right]+...\right],
\end{aligned}
$$

Here, the azimuthal distribution of the particles is obtained relative to the symmetry plane angles Ψ_n, which are indicated in figure 2.8. These are determined on an event-by-event basis using the azimuthal distribution of the invariant particle yield itself. In this approach, the remaining (sine) terms vanish due to the reflection symmetry, introduced with the symmetry plane angles [64].

As visible in figure 2.8, the angles Ψ_n are specific to the order of the harmonic v_n under investigation. The first harmonic v_1 is called directed or radial flow, and results from the general pressure gradient between the hot center and the surface of the fireball. The second order harmonic v_2 is called elliptic flow, and originates from the asymmetry of the nuclear overlap region for collisions with finite impact parameters. Here, the overlap region has a lenticular shape, which means that the pressure gradient is larger along the direction perpendicular to the indicated event plane ψ_2. This effect is reflected in the azimuthal distribution of the particles. Note, that in the presented figure, the event plane does not correspond to the reaction plane, which is spanned by the vector product of the impact parameter of the nuclei and their direction of flight. In the illustration this would correspond

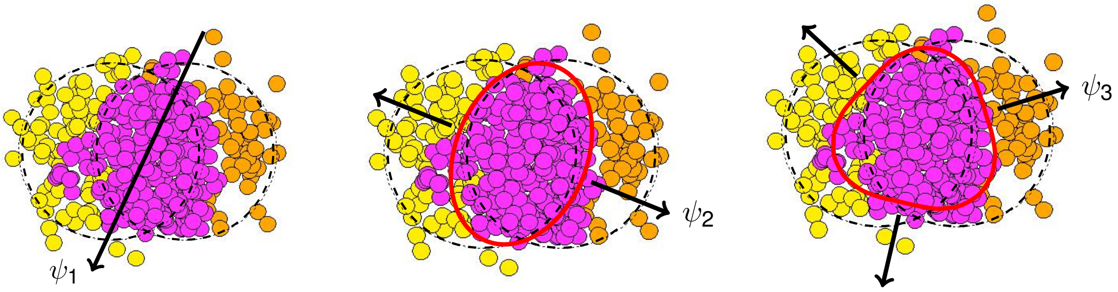

Figure 2.8.: Illustration of the simultaneous orientation of directed (Ψ_1), elliptic (Ψ_2) and triangular (Ψ_3) flow in a single event from Glauber Monte Carlo simulations. Whereas directed and elliptic flow originate from the macroscopic nuclear overlap, triangular (and higher order) flow comes from the geometric distributions of the participating nucleons within the nuclei. This figure has been taken from [65].

to a horizontal plane. The deviation is caused entirely by fluctuations of the initial nucleon density profiles in the nuclei, which gives rise to the odd harmonics, quantified through the triangular v_3 flow (and higher orders). The overall magnitude of the harmonics decreases with increasing increasing order.

The harmonics themselves are obtained through the calculation of the average values over all particles with angle ϕ_i for a given rapidity and transverse momentum at fixed centrality in all events:

$$v_n\left(p_{\mathrm{T}}, y\right) = \left\langle\cos\left[n\left(\phi_i - \Psi_n\right)\right]\right\rangle \text{ [64].} \tag{2.13}$$

However, the final v_n is only available after division by the event plane resolution for each harmonic, which corrects for the limits of the finite multiplicity in the estimation of the angles. The drawback of this approach is, that it strongly depends on the quality of the event place resolution, which must be further corrected for acceptance effects of the detector. This approach is for example used here: [66].

The harmonics may also be measured directly via a fit of the two-particle azimuthal distribution, where all pairs of particles in a given kinematic region are correlated and no event plane needs to be determined [67]. However, this approach is sensitive to non-flow effects, such as hadronic jets, strange hadron decay and to some extent momentum conservation. Such effects may be significantly reduced by using multi-particle correlations, which however requires more statistics. In either case, acceptance correlations have to be removed using a mixed-event background [64].

In flow analyses of heavy-flavor hadrons, where the signal is strongly statistically limited, the determination of the harmonics must be simplified by inspecting only two complementary angular $\Delta\phi$-bins, $N_{\text{in-plane}}$ and $N_{\text{out-of-plane}}$ [66]:

$$N_{\text{in-plane}} = \frac{N_0}{2\pi}\cdot 2n\cdot\int_0^{\pi/2n}\left[1+2v_n\cos\left(n\Delta\phi\right)\right]\,d\Delta\phi = \frac{N_0}{2\pi}+\frac{2N_0v_n}{\pi} \tag{2.14}$$

$$N_{\text{out-of-plane}} = \frac{N_0}{2\pi}\cdot 2n\cdot\int_{\pi/2n}^{\pi/n}\left[1+2v_n\cos\left(n\Delta\phi\right)\right]\,d\Delta\phi = \frac{N_0}{2\pi}-\frac{2N_0v_n}{\pi} \tag{2.15}$$

$$\rightarrow v_n = \frac{\pi}{4}\frac{N_{\text{in-plane}}-N_{\text{out-of-plane}}}{N_{\text{in-plane}}+N_{\text{out-of-plane}}}. \tag{2.16}$$

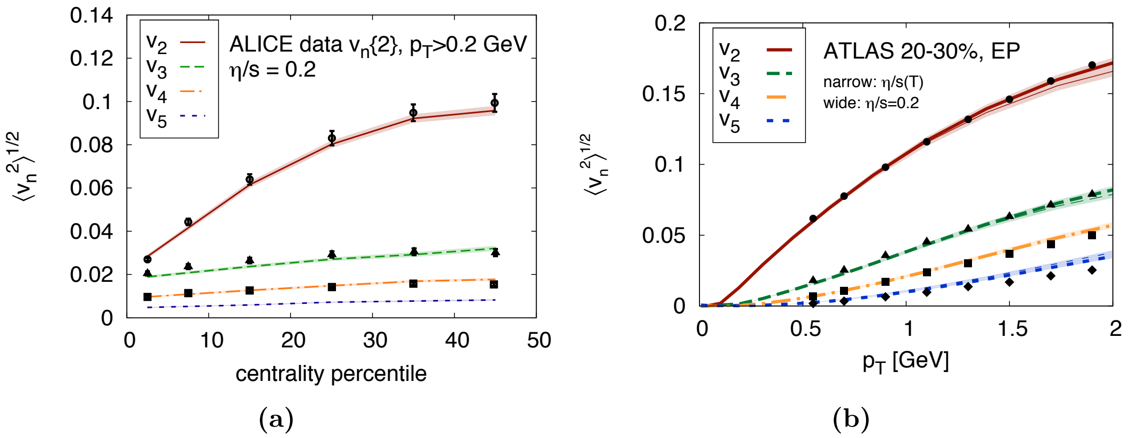

Figure 2.9.: (a) displays the anisotropic flow as a function of centrality measured by ALICE in Pb–Pb collisions. As the overlap of the nuclei decreases, the elliptic flow increases. Higher harmonics remain almost constant, as the fluctuation of the nucleon distributions functions is independent of the initial macroscopic overlap. In this analysis, two-particle correlations are used in the data analysis and compared to the hydrodynamical model MUSIC with $\eta/s = 0.2$. The corresponding p_{T} dependence using the event-plane method is measured by ATLAS and displayed in (b). Again, the data is explained best with a finite value of $\eta/s = 0.2$, while the general trend is also reproduced with a temperature-dependent $\eta/s(T)$. These figures have been taken from [8].

In Pb–Pb collisions at $\sqrt{s_{\mathrm{NN}}} = 2.76\,\mathrm{TeV}$ at the LHC, harmonics up to the fifth order were observed [68]. A comparison of experimental data from the ALICE and ATLAS experiments at the LHC to the viscous hydrodynamic model MUSIC [69] is presented in figures 2.9a and 2.9b respectively. Here, the first five harmonics are displayed as a function of centrality, as well as transverse momentum, using two-particle correlations.

As v_2 originates from the overlap region of the two nuclei, it shows a strong dependence on centrality: For most central collisions, the anisotropy and thus the elliptic flow are small. With increasing asymmetry v_2 increases up to about 0.1, and eventually decreases again for more peripheral collisions. Odd harmonics show almost no dependence on centrality, as they originate entirely from spatial fluctuations of the nucleon distributions within the nuclei. All harmonics show a strong increase with transverse momentum. However, finite values at larger transverse momentum $p_{\mathrm{T}} \gtrsim 5\,\mathrm{GeV}/c$ are not generated by flow, but originate from the path-length dependence of the particles traversing the asymmetric fireball in- and out-of-plane, as they experience different energy loss [64].

The time scale of converting the pressure to a momentum distribution in the hydrodynamic evolution reflects the interaction strength of the medium, which is linked to the EOS and the shear viscosity to entropy density ratio η/s. In the presented model, finite viscosity was assumed and the shear viscosity to entropy density ratio was either set to a constant value of 0.2 or based on the temperature of the medium. The good agreement between data and theory implies that the medium indeed rapidly thermalizes. The small value of $\eta/s = 0.2$ used in this calculation indicates, that the QGP behaves almost like a perfect fluid. The agreement with other relativistic hydrodynamic models underline these observations (e.g. [70, 71]).

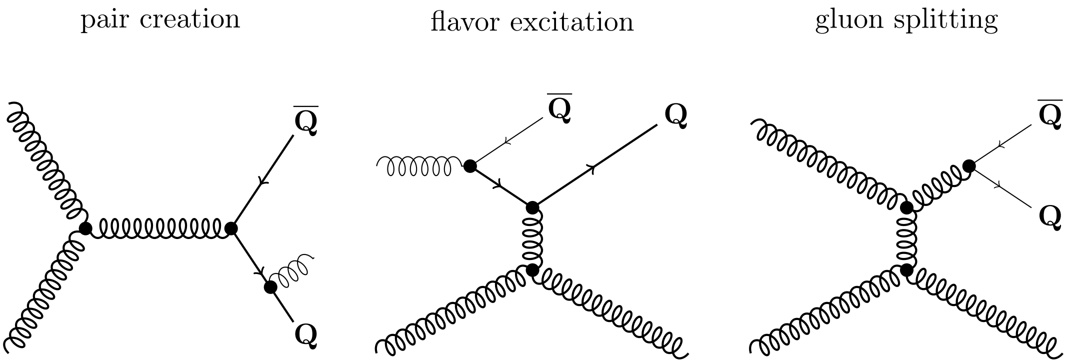

Figure 2.10.: Examples for the dominant production processes of hard probes at next-to leading order in high-energy nuclear collisions. Hard processes are indicated by the thick lines, which corresponds to the interactions with the largest momentum transfer. In *pair creation* two heavy quarks are generated in the final state, whereas in *flavor excitation* a heavy quark generated by gluon splitting in a proton is put on mass shell by scattering off of a parton of the other beam. In *gluon splitting* a heavy-quark pair is produced in the final state without participating in the hard process. The corrections above next-to leading order are small, as the quark masses are large [9].

2.3.4. Hard probes at the Large Hadron Collider

Qualitatively, in minimum bias Pb–Pb collisions at the LHC about 98 % of the initial partons are exclusively generated in hard scattering processes (Q $\gg \Lambda_{\mathrm{QCD}} \approx 200\,\mathrm{MeV}$) [72], which means they are either produced with large momentum or mass. As it is particularly relevant for this thesis, the production of b quarks will be explained to demonstrate why these probes are especially interesting in heavy-ion collisions.

2.3.4.1. Beauty production in nucleon-nucleon collisions

At leading order, beauty (or bottom) quarks are produced by primary partonic scatterings via *pair creation* ($gg \to b\bar{b}$, $q\bar{q} \to b\bar{b}$), *flavor excitation* ($qb \to qb$, $gb \to gb$) and *gluon splitting* ($g \to b\bar{b}$) at the early stage of the collision [9]. Some of the more complicated next-to-leading order processes are depicted in figure 2.10. Given their large mass and the high virtuality $Q = 2m_b = 9.32\,\mathrm{GeV}$, the heavy-quark production cross-section can be calculated using perturbative QCD, as terms which are higher than next-to-leading order are small and can be neglected [9]. The beauty quark production as a function of rapidity in p+p collisions using Fixed Order Next to Leading Log (FONLL) [73, 74, 75] calculations is presented in figure 2.11. In p+p collisions, the total hadronic cross-section is then calculated by convoluting the partonic cross-section, taken from the perturbative QCD calculations, with the parton distributions functions of the initial protons (using factorization) $f^{\mathrm{p}}_{q,\bar{q},g}$, measured in $e^{-}p^{+}$ deep-inelastic scattering, for example at H1 and ZEUS at the DESY facility:

$$\sigma^{b\bar{b}}_{\mathrm{pp}} = \sum_{i,j=q,\bar{q},g} \int_{4m_b^2/s}^{1} \frac{\mathrm{d}\tau}{\tau} \delta\left(x_i x_j - \tau\right) f^{\mathrm{p}}_i\left(x_i, \mu_F\right) f^{\mathrm{p}}_j\left(x_j, \mu_F\right) \hat{\sigma}_{ij}\left(\tau s, m_b^2, \mu_R, \mu_F\right), \quad (2.17)$$

with the sum over all parton masses and μ_F and μ_R being the factorization and renormalization scales, as well as $\tau = \hat{s}/s$ [9]. In perturbative QCD, the factorization and renormalization scales are necessary to solve the long- (infrared) and short- (ultraviolet) range singularities, respectively. The variable $\hat{s} = x_i x_j s$ describes the partonic center-of-mass energy for two partons with momentum fractions x_i and x_j. As an example, the CTEQ6M parton distribution function at a momentum transfer Q, well above the beauty production threshold, is depicted in figure 2.12. In the Breit-frame x represents the fraction of overall momentum, which a parton carries. At these high values of Q, the shape of the respective quark and gluon distributions change strongly going towards lower x. As a consequence of the flavor independent evolution, the sea quark distributions become more flavor symmetric, as at low x there are more sea quarks and the gluon distribution is dominating. The probed x-region can be determined from the center-of-mass energy (per nucleon pair) $\sqrt{s_{\mathrm{NN}}}$, the invariant mass of the beauty quark pair $m_{b\bar{b}}$, and the corresponding rapidity $y_{b\bar{b}}$. Considering leading-order production through gluon-gluon fusion, and neglecting the intrinsic transverse momentum of the parton, the invariant mass of the quark pair is determined as [9]:

$$Q^2 = (2m_b)^2 = x_1 x_2 s_{\mathrm{NN}}, \tag{2.18}$$

where x_1 and x_2 are the momentum fractions of the two gluons. These can be simplified for a symmetric colliding system to

$$x_1 = \frac{m_{b\bar{b}}}{\sqrt{s_{\mathrm{NN}}}} \exp\left(+y_{b\bar{b}}\right) \text{ and } x_2 = \frac{m_{b\bar{b}}}{\sqrt{s_{\mathrm{NN}}}} \exp\left(-y_{b\bar{b}}\right). \tag{2.19}$$

Thus, for a rapidity range of $|\mathrm{y}| < 0.9$, the regions of $2.71 \cdot 10^{-4} \leq x_{1,2} \leq 1.64 \cdot 10^{-3}$ and $6.89 \cdot 10^{-4} \leq x_{1,2} \leq 4.16 \cdot 10^{-3}$ are probed with p+p collisions at $\sqrt{s_{\mathrm{NN}}} = 14\,\mathrm{TeV}$ and $5.5\,\mathrm{TeV}$, where the gluon distributions are dominating by more than one order of magnitude. As will be explained later in section 3.2, this rapidity range is accessible in the central barrel of the ALICE Experiment. The total production cross-section of b quarks in p+p collisions at $\sqrt{s} = 13\,\mathrm{TeV}$ is presented in figure 2.11, where FONLL calculations were performed to determine the rapidity dependence for different momentum thresholds [75]. The cross-section shows a plateau at mid-rapidity, while a decrease to about 50 % of the maximum value is only observed for $|\mathrm{y}| > 2.0$. The largest uncertainty arises from variations of the factorization and renormalization scales μ_{F} and μ_{R}, and decreases for an increasing p_{T} threshold. Generally, parton distribution functions contribute the smallest fractions to the full uncertainty, while the impact from variations of the quark masses is again strongly dependent on the lower kinematic boundary. Note, that within the uncertainties of the FONLL calculations the results are equally probable.

2.3.4.2. From quarks to mesons

Up to this point, only quark production in p+p collisions has been considered. The fragmentation of quarks into hadrons cannot be calculated perturbatively any more, as it is a soft process and the strong coupling constant does not remain small. However, these fragmentations functions can be theoretically modeled: The parameterization obtained by Peterson [76] and Kartvelishvili [77] are most commonly used (the latter model for example in figures 2.11). The parameterization by Peterson has been included in simulations by the DELPHI Collaboration at the Large Electron Positron collider (LEP), which were compared

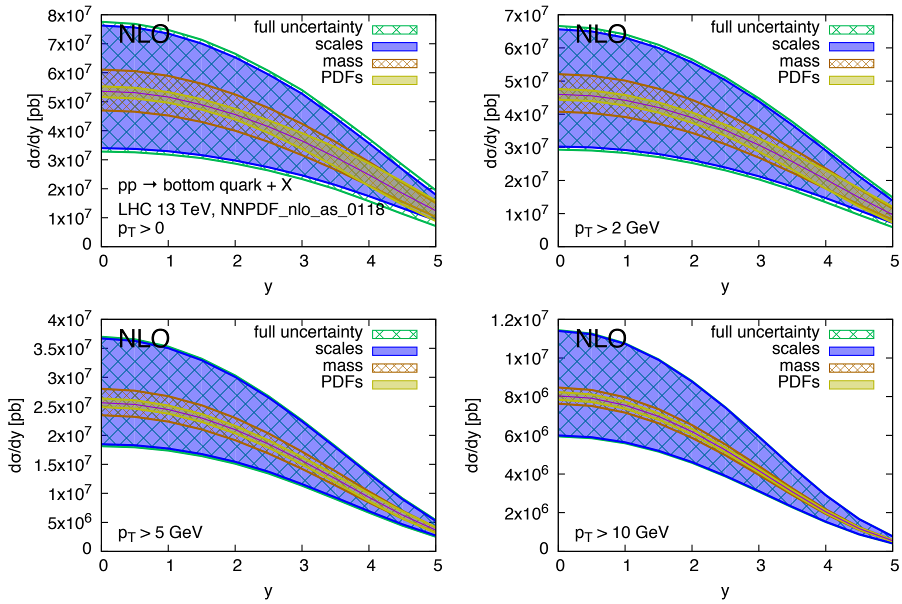

Figure 2.11.: FONLL calculations of the b quark production cross-section in p+p collisions at $\sqrt{s}$ = 13 TeV as a function of rapidity and different quark-p_{T} thresholds. Uncertainties from variations of the factorization and renormalization scales μ_{F} and μ_{R} are dominating the full uncertainty. This figure has been taken from [75].

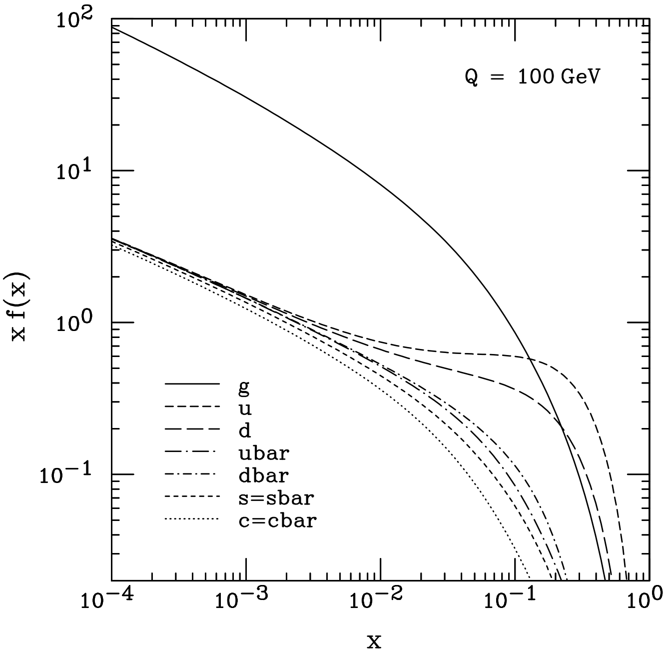

Figure 2.12.: CTEQ6M parton distribution function for valence and sea quarks as well as gluons in protons at Q = 100 GeV, relevant for beauty production. At the LHC the small-x region ($x < \mathcal{O}\left(10^{-3}\right)$) can be probed for example through the production of $b\bar{b}$ and $c\bar{c}$ pairs, where the parton distribution function are fully dominated by the gluon distribution [9]. This figure has been taken from [78].

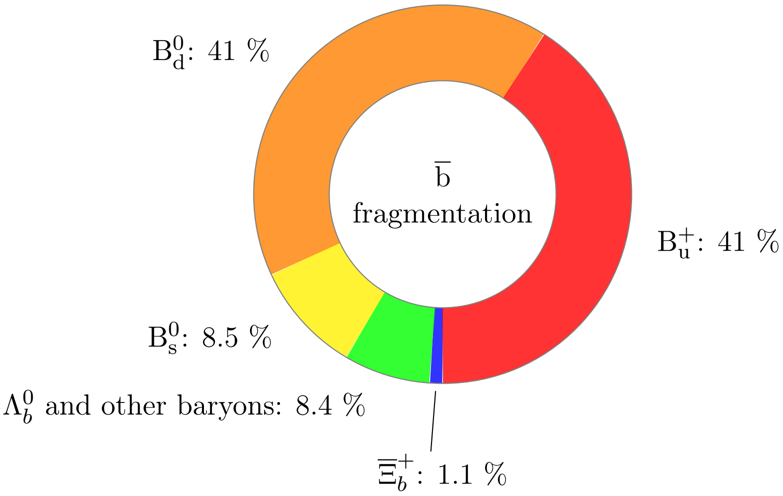

Figure 2.13.: Measured b-quark fragmentation into charged and neutral b-hadrons by the DELPHI detector at LEP [79].

to data in order to measure the branching fractions of b quarks into charged and neutral b hadrons. For this purpose, the Collaboration investigated Z^0 decays into b quarks, which are the largest source of b quarks in $\mathrm{e^+e^-}$ collisions. The results are presented in figure 2.13.

As a consequence of isospin symmetry realized at the LHC, the fraction of neutral and charged mesons must be the same $f_{\mathrm{B^+_u}} = f_{\mathrm{B^0_d}}$. From the experimental point of view, electrically charged and neutral B mesons are the preferable particles to inspect b quarks, as their relative production yield is largest. However, as they also cannot be directly measured, their reconstructable yield is further reduced through the branching fractions of their (hadronic) decays into experimentally accessible particles, as will be discussed in section 5.

2.3.4.3. Beauty physics in nucleus-nucleus collisions

Heavy quarks are particularly useful probes for the inspection of the QGP, as pairs of $b\bar{b}$ are produced early in the collision. The time scale can be estimated from the Compton wavelength of the exchanged virtual gluon in the left Feynman diagram [9] in figure 2.10:

$$\tau_b \approx \frac{\lambda_g^{\mathrm{Compton}}}{c} = \frac{\hbar}{2m_b c^3} = 0.02\,\mathrm{fm}/c. \tag{2.20}$$

This space-time scale is much smaller than the expected formation time of the QGP (about one fm/c at the LHC), thus the heavy quark production is unaffected by final state effects of the medium. However, initial state effects as k_t-*broadening* and *nuclear shadowing* are expected to influence their production. The former is an effect of the intrinsic transverse momentum k_t, assigned to the two colliding partons in perturbative QCD calculation. Whereas this factor is usually sampled from a Gauß-distribution with $\langle k_\mathrm{t}^2 \rangle = 1.0\,\mathrm{GeV}^2$ [80], in Pb–Pb collisions it has to be increased to $\langle k_\mathrm{t}^2 \rangle = 1.7\,\mathrm{GeV}^2$ to match the data [9, 80]. It is understood to be an effect of partonic multiple scattering between the ions. The latter

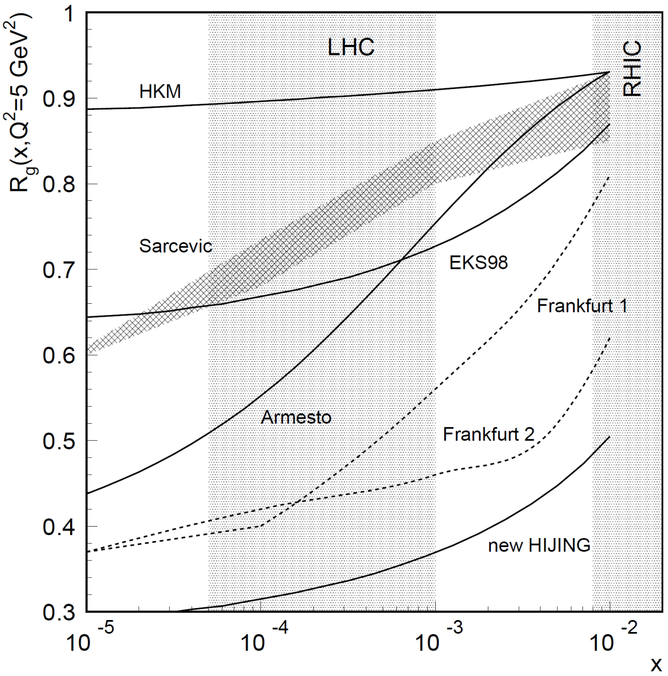

Figure 2.14.: The ratio between the parton distribution functions in lead ions and protons is displayed in this figure for $Q^2 = 5\,\mathrm{GeV}^2$. Initial state effects lead to a change of the distribution, as indicated by various models. The probed x-regions at LHC and RHIC are indicated by shaded areas. This figure has been taken from [9].

effect, *nuclear shadowing*, is a consequence of the low momentum fractions x related to the production of hard probes. When the two nuclei approach each other, each nucleus sees a superposition of about $\mathrm{n} = \mathrm{A}\cdot 1/x$ partons of the other nucleus. This corresponds to about $\mathcal{O}(10^5)$ partons from the opposite nucleon in Pb–Pb collisions ($\mathrm{A} = 82$) at the LHC. At these large densities, two partons with a low momentum fraction merge together to a single parton with summed Bjorken-x, thus depleting the small-x region. As a consequence nuclear shadowing decreases the number of available partons and reduces the overall heavy-quark cross-section [9]. Experimentally, this effect is studied through deep-inelastic scattering of electrons on nuclei in the region $5 \cdot 10^{-3} < x < 1$ [81], and extrapolated to lower values accessed by the LHC. The ratio between the gluon distribution functions in a Pb-nucleus compared to those of a proton, is presented for different models in figure 2.14.

Given their early production, heavy quarks experience the complete evolution of the QGP. As presented in figure 2.2, they also remain heavy during the phase of chiral symmetry restoration, as their mass is generated almost entirely from the their coupling to the Higgs field. Due to this large mass, thermal production in the medium is heavily suppressed, which means the overall production yield remains unchanged [9]. A currently open topic is whether eventually heavy quarks participate in the collective motion and may even kinetically equilibrate, as indicated by measurements of charmed mesons [14].

The interaction with the QGP can be measured, when the transverse momentum spectrum is compared between nucleus-nucleus collisions (e.g. Pb–Pb) and a scaled superposition of nucleon-nucleon collisions (e.g. p+p) at similar energies, where the average number of

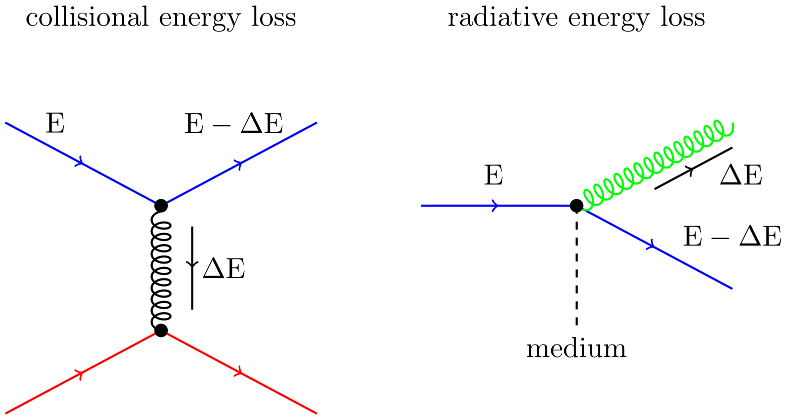

Figure 2.15.: Feynman graphs for collisional and radiative energy loss of quarks in the QGP medium. These figures have been inspired from [51].

binary collisions $\langle N_{\text{coll}} \rangle$ is used for scaling. The ratio is called the *nuclear modification factor* R_{AA}, and is mathematically defined as

$$R_{\text{AA}} = \frac{1}{\langle N_{\text{coll}} \rangle} \frac{\mathrm{d}N_{\text{AA}}/\mathrm{d}p_{\text{T}}}{\mathrm{d}N_{\text{NN}}/\mathrm{d}p_{\text{T}}}. \tag{2.21}$$

If no nuclear or QGP-induced effects are present, this ratio is unity per definition. In the initial assumptions on quark energy loss in the hot and dense medium by Bjorken [82], it was expected that collisional energy (elastic scattering) would be the dominant process. However, it was observed that this only accounts up to $\mathcal{O}\left(10^{-1}\,\text{GeV/fm}\right)$ [83], and that radiative energy loss from multiple (inelastic) scattering ("gluon-Bremsstrahlung") is significantly larger, quenching the hard partons by an overall energy loss of $\Delta E_{\text{total}} = \Delta E_{\text{rad}} + \Delta E_{\text{coll}}$. The corresponding Feynman diagrams are displayed in figure 2.15. For the radiative energy loss additional corrections have to be considered.

On the one hand, in case of a thick medium, the Landau-Migdal-Pomeranchuck (LPM) effect [84] becomes relevant: The time it takes for a quark to radiate a gluon is finite, and another interaction between the considered quark or gluon and the medium partons can occur in between. Thus, several scatterings are coherently summed into one effective scattering center, which changes the gluon emission spectrum [85].On the other hand, the so called *dead-cone effect* needs to be taken into account. The double differential gluon emission spectrum was calculated as a function of the emission angle θ with respect to the flight direction of the quark [86], and a dependence on the quark mass M and energy E was found:

$$\omega \frac{\mathrm{d}I}{\mathrm{d}\omega \mathrm{d}k_{\text{T}}} = \frac{\frac{4\alpha_{\text{S}}}{3\pi k_{\text{T}}^2}}{\left(1 + \frac{(M/E)^2}{\theta^2}\right)^2}. \tag{2.22}$$

Here, I is the intensity and ω the energy of the emitted gluon. As visible from the denominator on the right side of equation 2.22, for small angles the spectrum is increasingly suppressed for heavy-flavor quarks.

The exact implementation of the quark interaction with the medium is model dependent.

However, these effects are well established and need to be considered in order to obtain a complete picture, which is capable to simultaneously describe the two key observables for heavy-flavor hadrons: (elliptic) flow and the nuclear modification factor. In the following, two models which exhibit good overall agreement with the experimental data are briefly summarized. Both will be utilized at a later stage in this thesis (chapter 5).

- Boltzmann Approach to MultiParton Scatterings (BAMPS) [87, 88]: BAMPS addresses the question of thermalization of gluons and quarks performing a full 3+1 dimensional Monte Carlo cascade simulation based on the solution of the Boltzmann equations for partons. Initial conditions are generated by independent minijets, distributed by scaled proton-proton collisions using the Glauber model. Subsequently, quarks and gluons are considered as on-shell classical Boltzmann particles, solving the Boltzmann equation

  $$\left(\frac{\partial}{\partial t} + \frac{\vec{p}_i}{E_i}\frac{\partial}{\partial \vec{r}}\right) f_i\left(\vec{r}, \vec{p}_i, t\right) = \mathcal{C}_i^{2\rightarrow 2} + \mathcal{C}_i^{2\rightarrow 3} + ..., \tag{2.23}$$

  where all processes in the light parton sector are implemented. Proceeding collision processes are determined in a stochastic manner by sampling possible transitions in a given volume and time interval. Inelastic and elastic gluon (g) interactions are included via $gg \rightarrow gg$, $ggg \rightarrow gg$ and $gg \rightarrow ggg$, where the last process is most important for thermalization, elliptic flow and jet-quenching of gluons. The cross-sections are calculated using leading-order perturbative QCD, where the LPM effect is modeled as an effective cutoff function in the radiative matrix elements [89]. The subsequent evolution of the gluon matter then shows almost ideal hydrodynamic behavior.
  Heavy quark distributions are generated using next-to-leading order (NLO) calculations MC@NLO [90, 91]. Currently, only elastic collisions of heavy quarks (Q) are implemented ($gg \leftrightarrow Q\overline{Q}$, $q\overline{q} \leftrightarrow Q\overline{Q}$, $gQ \rightarrow g\overline{Q}$ and $qQ \rightarrow q\overline{Q}$), however radiative corrections are absorbed by an additional factor K, which is scaling the elastic cross-section to be compatible with data. The partons are fragmented into mesons using the Peterson parameterization, and the subsequent decay is performed with PYTHIA 8.1 [92]. In this way, BAMPS is capable of simultaneously predicting elliptic flow as well as the nuclear modification factor for heavy quarks for experimentally accessible particles and decays.

- TAMU [93, 94, 95]: The building block of this model is the heavy-flavor transport through the QGP using non-perturbative interactions for heavy quarks, embedded into a hydrodynamic bulk evolution. Subsequently, hadronization occurs and the interactions in the hadronic phases of the nuclear collisions are further considered. The initial conditions are taken from a Glauber model without initial flow or fluctuations. FONLL calculations are used to obtain the initial heavy quark spectra, including different fragmentation functions for charm and beauty. In this non-perturbative diffusion framework, the space-time evolution of the heavy-quark phase-space distribution in hadronic matter (QGP) is computed using the Fokker-Planck equation, which follows from the Boltzmann equation through a second-order expansion in the momentum transfer, implemented via Langevin dynamic equations:

$$\mathrm{d}\vec{x} = \frac{\vec{p}}{E}\mathrm{d}t, \tag{2.24}$$

$$\mathrm{d}\vec{p} = -\Gamma(p)\,\vec{p}\mathrm{d}t + \sqrt{2D(\vec{p}+\mathrm{d}\vec{p})\,\mathrm{d}t}\rho, \tag{2.25}$$

where $\vec{x}$ and $\vec{p}$ are the position and momentum vector of the heavy quark with energy $E(p) = \left(m_Q^2 + \vec{p}^2\right)^{1/2}$. The drag and (diagonal) diffusion coefficient are described by $\Gamma(p)$ and $D(p)$, while ρ is the standard Gauß-noise variable. Inside the hadronic matter, the thermal relaxation rates for heavy quarks are taken from the thermodynamic T-matrix approach [96, 97, 98], using the input potential (EOS) from thermal lattice QCD calculations. The heavy-flavor quarks then diffuse in an evolving medium tuned by the ideal AZHYDRO code [99]. The resonance recombination model [100] is used to hadronize the quarks at a (pseudo-)critical temperature of $T_{\mathrm{pc}} = 170\,\mathrm{MeV}$, matched to a hadron resonance gas EOS with chemical freeze out at $T_{\mathrm{ch}} = 160\,\mathrm{MeV}$. The diffusion of the heavy-flavored mesons is continued in hadronic matter, such that estimates on the nuclear modification factor and elliptic flow are predicted.

Examples of the model predictions are presented in figures 2.16a and 2.16b respectively. On the left side of figure 2.16, the elliptic flow estimate from BAMPS is compared to the results from fully reconstructed D^0 mesons in ALICE, inspecting Pb–Pb collisions at $\sqrt{s_{\mathrm{NN}}} = 2.76\,\mathrm{TeV}$ at 30–50 % centrality. Within the large uncertainties of the data, the theoretical model describes the measurement well. On the right side, the nuclear modification factor measured for non-prompt J/ψ (from B) at CMS is compared to the expectations by TAMU. However, here the J/ψ momentum was not rescaled to reflect the parent B meson p_{T}. The theoretical model reproduces the trend of the measured data to a large extend, even though a systematic offset to larger values is visible.

2.3.5. Current status of heavy-flavor measurements in AA and nucleon-nucleon collisions

The highest precision in the analyses of collective flow and nuclear modification factor of heavy-flavor mesons is obtained through the full kinematic reconstruction of all decay daughters. Additional information on heavy-flavor production can be investigated through observations of semi-leptonic heavy-flavor hadron decays [15].
In the following a compilation of recent results is presented. A more complete discussion can be found in [101], while a summary of charmed mesons in ALICE is presented in [102]. In figure 2.17a, the energy dependence of the total charm production cross-section is presented, measured by various experiments at different facilities. For a valid comparison, a Glauber model was used to scale down the measured cross-section in deuteron-nucleus and proton-nucleus collisions by the respective number of binary nucleon-nucleon collisions. The ALICE Collaboration measured the charm cross-section within $|\mathrm{y}| < 0.5$ via fully reconstructed D mesons and charge conjugates in the channel $\mathrm{D}^0 \rightarrow \mathrm{K}^-\pi^+$, $\mathrm{D}^+ \rightarrow \mathrm{K}^-\pi^+\pi^+$ as well as $\mathrm{D}^{*+} \rightarrow \mathrm{D}^0\pi^+$ [103, 104], and extrapolated the results of the experimentally covered phase space into the full phase space using the central parameters of

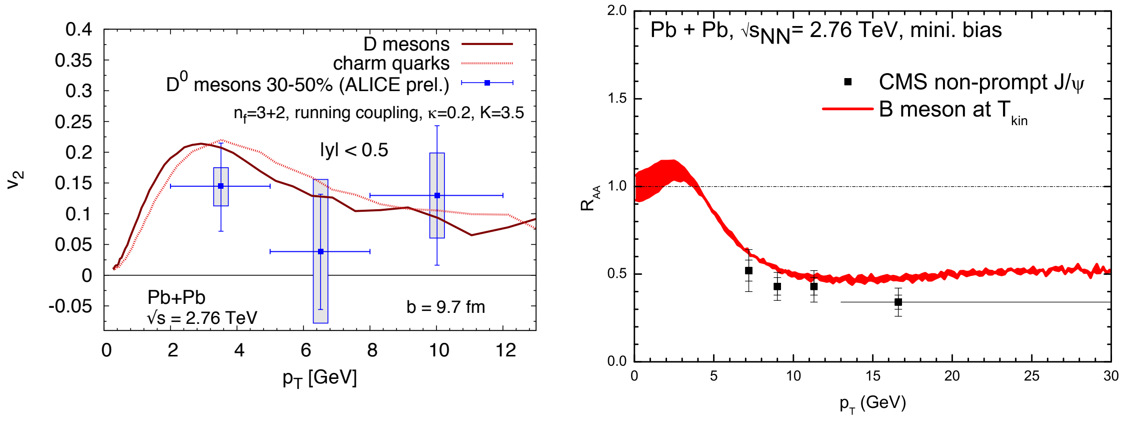

(a) (b)

Figure 2.16.: (a) displays a comparison between the calculated charm quark and meson elliptic flow by BAMPS with the data from fully reconstructed D^0 mesons by ALICE. Within the uncertainties, a hint of collective motion is visible in the data. In (b), a comparison between the beauty meson R_{AA}calculated by TAMU and the measurement of non-prompt J/ψ by CMS is shown. A significant suppression induced by the QGP is observed. Note, that the data points are not rescaled to the B meson p_{T}. These figures have been taken from [91] and [98], respectively.

FONLL calculations [105]. At center-of-mass energies just above 20 GeV, fixed target experiments contribute the measurements with the highest precision by inspecting light-hadron beams with nuclei (e.g. [106]). At LHC energies, the LHCb Collaboration contributes the most precise measurement in forward direction [107] in fair agreement with the results by ALICE and ATLAS at mid-rapidity. Even though the central FONLL prediction (MNR framework [108]) systematically underestimates the measured data, general good agreement with perturbative QCD calculations over a wide energy range is achieved within uncertainties.

A similar trend is observed for the beauty production cross-section, presented in figure 2.17b. Here, beauty hadrons within $|y| < 0.8$ and $1 < p_{\mathrm{T}} < 10\,\mathrm{GeV}/c$ were reconstructed via electrons from semi-leptonic decays, identified by their impact parameter to the primary vertex. Similar to the measurement of the total charm production cross-section, the results were extrapolated to full phase space using FONLL. It would be desirable to constrain the perturbative model predictions to high precision, however the current experimental uncertainties are too large to do so. Larger data samples and extended experimental p_{T}-coverage to lower momentum are necessary for a significant improvement, as for example the ALICE measurement of the $b\bar{b}$ cross-section $\sigma_{\mathrm{b\bar{b}}} = 130 \pm 15.1\,(\mathrm{stat})\,^{+42.1}_{-49.8}\,(\mathrm{sys})\,^{+3.4}_{-3.1}\,(\mathrm{extr}) \pm 2.5\,(\mathrm{norm}) \pm 4.4\,(\mathrm{BR})\,\mu\mathrm{b}$ is limited mainly by systematic uncertainties. Here, the uncertainty of the charmed hadron decay background generates the largest contribution to the uncertainty [109], which could be reduced for example by additional constraints through more differential analyses.

Current state-of-the-art measurements of the charm elliptic flow and the nuclear modification factor are presented in figures 2.18a and 2.18b respectively. The charm v_2 measurement of the ALICE Collaboration is superimposed on the results for (light) charged particles and gives a clear indication that low-p_{T} charm quarks participate in the collective motion of the

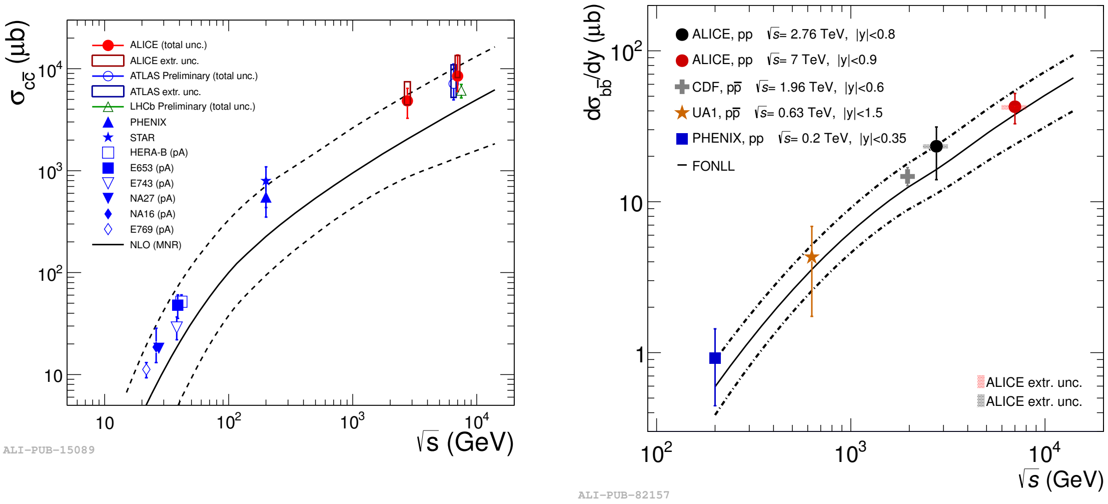

(a) **(b)**

Figure 2.17.: Production cross-section for pairs of charmed (a) and beauty (b) quarks at various center-of-mass energies. FONLL calculations generally agree with the data, but systematically underestimate the cross-sections. These figures have been taken from [103] and [109], respectively.

medium. In this comparison, charmed mesons were reconstructed in the three mentioned decay channels and averaged into a single result.

The same results were used in a comparison of the nuclear modification factors measured by ALICE at the LHC and STAR at RHIC. Due to the interactions of the heavy quarks with the partons of the hot medium, both measurements show a significant suppression in central Pb–Pb or Au–Au collisions. However, within uncertainties some differences are observed for the measurements at different collisions energy, e.g. at $p_\mathrm{T} \approx 1.5\,\mathrm{GeV}/c$ the STAR Collaboration observes an enhanced R_AA, while ALICE measures a suppression $R_\mathrm{AA} \approx 0.7$. These deviations originate from a general difference in the shape of the corresponding p+p references, different modifications of the underlying nuclear PDFs and from variations in the observed radial flow.

However, despite large statistical and systematic uncertainties, some differences are observed comparing the previously mentioned results by ALICE to measurements of prompt D^0 mesons by CMS [110], as ALICE predicts a stronger suppression for charmed mesons with $p_\mathrm{T} > 16\,\mathrm{GeV}/c$. The deviations may be induced by the different p+p references.

Comparisons between the observed R_AA for charmed and beauty mesons, shown in figure 2.19a, are particularly interesting, as they allow to investigate whether the expected hierarchy in the quark energy loss ($\Delta E_\mathrm{g} > \Delta E_\mathrm{u,d,s} > \Delta E_\mathrm{c} > \Delta E_\mathrm{b}$ which may result in $R^{\pi}_\mathrm{AA} < R^{\mathrm{D}}_\mathrm{AA} < R^{\mathrm{B}}_\mathrm{AA}$) [21] is observed. In this comparison, the kinematics of the non-prompt J/ψ ($\mathrm{B}^+ \rightarrow \mathrm{J}/\psi(1\mathrm{S}) + \mathrm{X}$) measured in CMS were matched to the kinematic bins of the reconstructed charmed mesons. Although the uncertainties are large, a direct indication of the mass hierarchy is visible, with a strong dependence on the collision centrality. This result is further supported by the D^0 measurement of CMS [110]. The observation is in line with mass-dependent energy loss calculated from perturbative QCD models, where an example is given in the figure. Here, the difference between the two depicted predictions

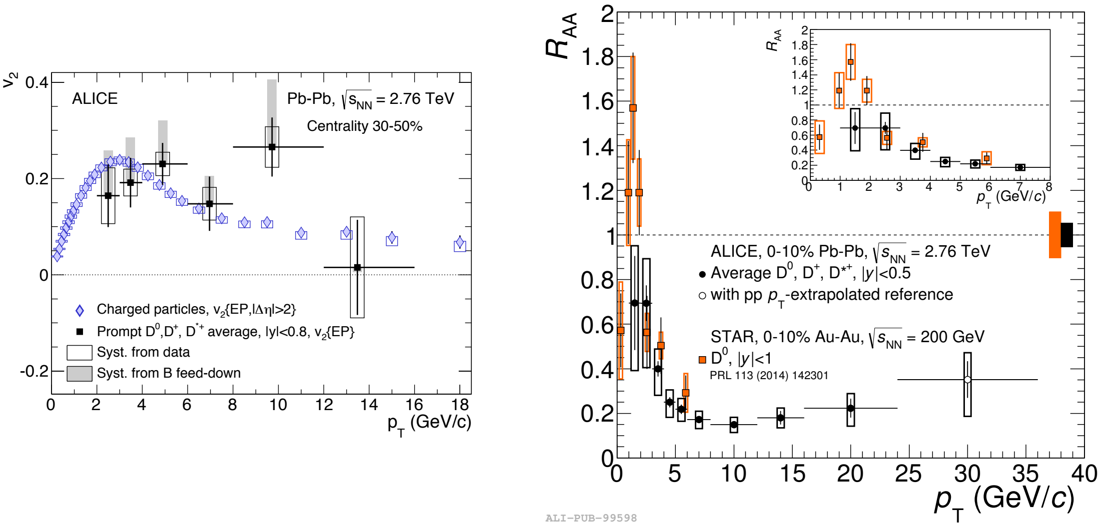

(a) **(b)**

Figure 2.18.: In (a), the measured elliptic flow of charmed mesons is superimposed on the observation for charged particles. For both measurements, the event-plane method was used. Within the large statistical (bars) and systematic (boxes and shaded areas) uncertainties, a hint of elliptic flow of a similar magnitude than for light charged hadrons is observed. (b) shows the corresponding R_{AA} measurement by ALICE, compared to the observations by STAR at RHIC. At low momentum, there are differences between the measurements, which can be explained by different modifications of the nuclear PDFs as well as variations in the observed radial flow. These figures have been taken from [14] and [13], respectively.

is induced by the mass difference of c and b quarks in the calculation. As Shown in figure 2.19b, CMS has already extended its Pb–Pb measurements into the beauty sector, by fully reconstructing B mesons in the channel $\mathrm{B}^+ \to \mathrm{J}/\psi(1\mathrm{S})\mathrm{K}^+$ $(\mathrm{J}/\psi(1\mathrm{S}) \to \mu^+\mu^-)$, limited to $p_{\mathrm{T}} > 10\,\mathrm{GeV}/c$ [18]. As no particle identification for the kaon daughter of the beauty meson is available in CMS, correlated background sources from $\mathrm{B}^+ \to \mathrm{J}/\psi(1\mathrm{S}) + \mathrm{X}$ have to be simulated and subtracted from the invariant mass spectrum.

Given the low branching ratios of hadronic beauty decays, such observables are yet unmeasured at mid-rapidity by other collaborations, as they are typically inaccessible with the current available statistics. In the forward region the LHCb Collaboration will likely contribute complementary Pb–Pb measurements in the heavy-flavor sector, soon.

It is the topic of this thesis to evaluate the performance of the measurement of charged B mesons in the channel $\mathrm{B}^+ \to \overline{\mathrm{D}}^0\pi^+$ $(\overline{\mathrm{D}}^0 \to \mathrm{K}^+\pi^-)$, foreseen by ALICE in future runs of the LHC. The strategy of the full kinematic reconstruction is described in section 5. As presented in section 3.3.2, the upgrade strategy of the ALICE Collaboration additionally foresees to advance current charm measurement into high precision observations.

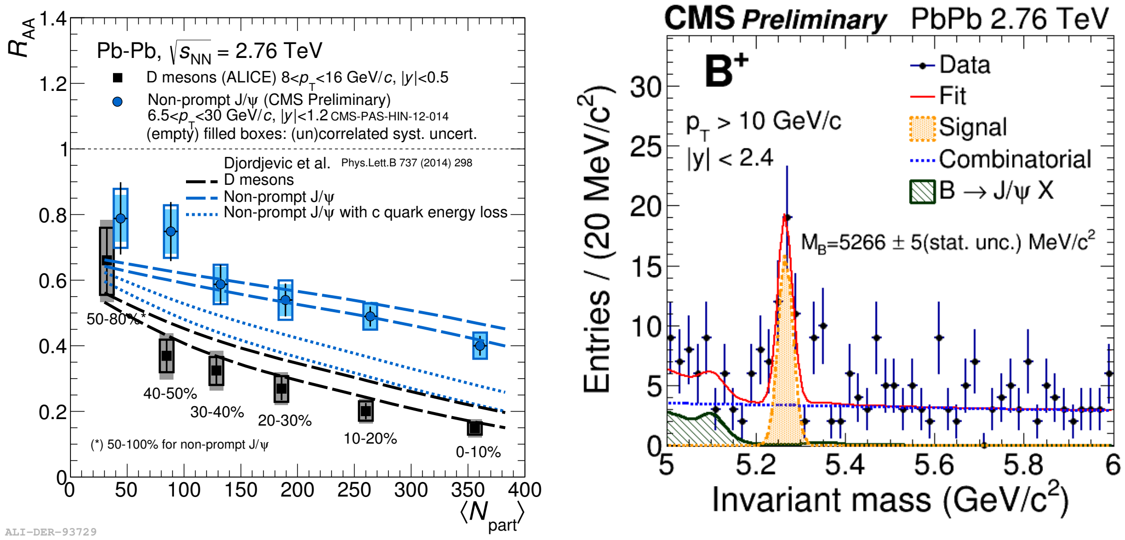

(a) **(b)**

Figure 2.19.: In (a), the R_{AA} of D mesons and non-prompt J/ψ R_{AA} are presented together with a mass dependent QCD calculation. Within the uncertainties, a hierarchy in energy loss is visible, supported by model calculations. (b) shows the reconstruction performance of CMS for charged B mesons in $\mathrm{B}^+ \to \mathrm{J}/\psi(1\mathrm{S})\mathrm{K}^+$ ($\mathrm{J}/\psi(1\mathrm{S}) \to \mu^+\mu^-$) in Pb–Pb collisions at $\sqrt{s_{\mathrm{NN}}} = 2.76\,\mathrm{TeV}$. These figures have been taken from [111] and [18], respectively.

3. Experimental access

Detailed measurements in particle and nuclear physics are well suited to be performed in a controlled laboratory environment, which allows a full reconstruction of the examined probe. The analysis of rare probes at the LHC, such as heavy-flavor mesons, requires effective filtering of the signal candidates on top of the high-intensity particle background. The European Organization for Nuclear Research (CERN), near Geneva, provides the ideal infrastructure of particle accelerators, including the Large Hadron Collider (LHC). It is capable of colliding Pb-ions at energies up to $\sqrt{s_{\mathrm{NN}}} = 5.5\,\mathrm{TeV}$, which are of special interest to the dedicated heavy-ion experiment at the second interaction point of the collider, the ALICE Experiment. Whereas ALICE will be explained in detail in section 3.2, the other experiments, which are installed at and around three other interaction regions of the LHC, are briefly outlined in section 3.1.2.

3.1. The Large Hadron Collider

Located in up to 110 meters depth, the LHC [112, 113] was built into the existing 26.7 km long tunnel of the former Large Electron-Positron collider (LEP) [114], which was shut down in 2000. Albeit the first electron-positron collisions just taking place inside LEP in 1989, the LHC was discussed as a successor already in 1984 [115], when synchrotron radiation was already understood as a fundamental limit of electron colliders. Given the available infrastructure, the aim to study small interaction cross-sections at the highest possible energies lead to the design of superconducting dipole magnets housing two beam pipes. The magnetic field of 8.33 T is just powerful enough to control two counter-rotating beams of 7 TeV, where the maximum energy is limited by the charge-to-mass ratio of the protons. The LHC was designed to provide p+p collisions at a center-of-mass energy of $\sqrt{s} = 14\,\mathrm{TeV}$ at an instantaneous peak luminosity of $\mathcal{L} = 10^{34}\,\mathrm{cm}^{-2}\mathrm{s}^{-1}$ and a peak bunch crossing rate of 40 MHz. In addition, dedicated periods of Pb–Pb beams colliding at up to $\sqrt{s_{\mathrm{NN}}} = 5.52\,\mathrm{TeV}$ are performed at a luminosity of $\mathcal{L} = 10^{27}\,\mathrm{cm}^{-2}\mathrm{s}^{-1}$. The possibility to collide p–Pb, or even fixed target collisions (p–Ne, p–He, p–Ar and Pb–Ar) at the LHCb experiment [116], were only considered afterwards. Illustrated in figure 3.1, the LHC requires pre-acceleration of the hadron beams to an energy of 450 GeV, before it can ramp up the beams to their final energy. Here, protons and Pb-ions undergo different stages before they are injected in bunches into the final collider [117]:

- p+p: Extracted from hydrogen gas, the protons are accelerated in a linear accelerator, LINAC 2, whereafter the hadrons are transferred into the Proton Synchrotron Booster (PSB). Subsequently, they are injected into the Proton Synchrotron (PS) and Super Proton Synchrotron (SPS), where the beam reaches its energy of 450 GeV and is injected into the LHC for the final acceleration through radio frequency cavities.

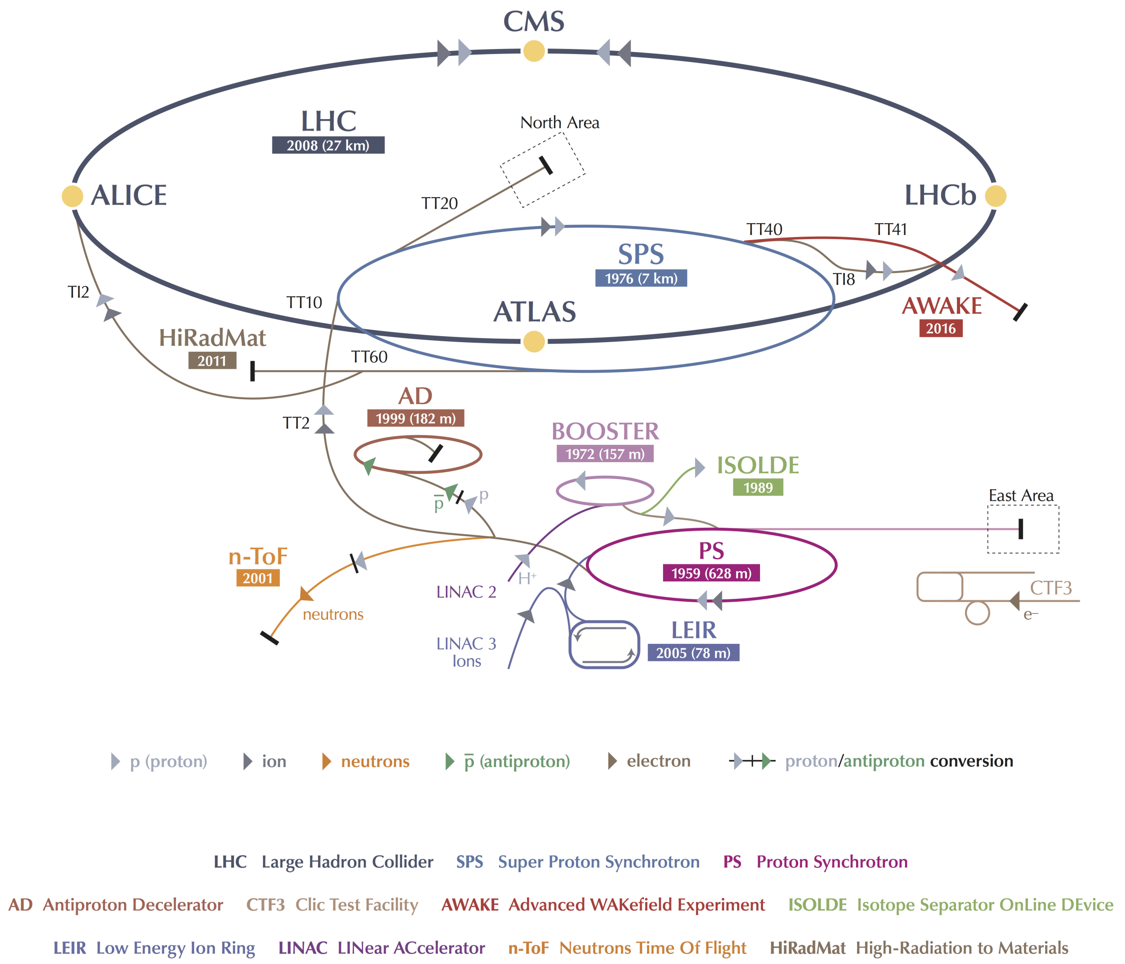

Figure 3.1.: CERN accelerator complex. As indicated in the figure, the accelerators were added consecutively throughout the years. For the final acceleration in the LHC, the different stages are used to pre-accelerate the particles. This figure has been taken from [118].

- Pb–Pb: Pb-atoms are evaporated from a piece of pure lead and ionized in an Electron Cyclotron Resonance (ECR) source. Stripped to the state Pb^{27+} they are accelerated in the LINAC 3. At an energy of 4.2 MeV/nucleon the ions are further stripped to Pb^{54+} and filtered into the Low Energy Ion Ring (LEIR), where they are accumulated. After their injection into the PS, where they reach 5.9 GeV/nucleon, the Pb-ions are fully stripped to Pb^{82+} and transferred into the SPS. Here, they are accelerated to 177 GeV/nucleon and injected into the LHC, inside which they are brought into collision at full energy.

3.1.1. Long term schedule

The current long term schedule of the LHC, in which five technical Long Shutdowns are foreseen, extends to 2037 [119, 120]. In Run 1, the LHC delivered an integrated luminosity in p+p collisions at $\sqrt{s} = 7$ and 8 TeV of about $30\,\mathrm{fb}^{-1}$, with a peak luminosity of up to $7.7 \cdot 10^{33}\,\mathrm{cm}^{-2}\mathrm{s}^{-1}$ [119]. In addition, two Pb–Pb runs were performed at $\sqrt{s_{\mathrm{NN}}} = 2.76$ TeV, with peak luminosities of $\mathcal{L} = 3.0 \cdot 10^{25}$ and $4.7 \cdot 10^{26}\,\mathrm{cm}^{-2}\mathrm{s}^{-1}$ in 2010 and 2011 respectively [121]. The latter corresponds to about twice the design luminosity at this energy. After further p+p data taking, a dedicated p–Pb run at $\sqrt{s_{\mathrm{NN}}} = 5.02$ TeV ($\mathcal{L} = 1.2 \cdot 10^{29}\,\mathrm{cm}^{-2}\mathrm{s}^{-1}$) was performed in 2012. During the first Long Shutdown (LS1), the LHC itself was prepared for the final design energy of up to 14 TeV, with a planned instantaneous (design) luminosity of $10^{34}\mathrm{cm}^{-2}\mathrm{s}^{-1}$ and an expected bunch spacing of 25 ns. This included major repair works on the interconnection between the superconducting magnets, which were necessary to recover from a major failure of the collider in 2008. After the restart of the LHC and the beginning of Run 2, it is now foreseen to deliver more than $50\,\mathrm{fb}^{-1}$ of p+p collisions to the experiments until the next Long Shutdown (LS2) [119]. Note, that the presented schedule is tentative and already changed: Currently LS2 is expected to take place during 2019 and 2020, which means that the schedule presented in figure 3.2 is shifted by two years after 2017 [122].

In LS2 the new LINAC4 will be integrated into the injector complex and the LHC injector chain will be further improved (Phase 1 Upgrade), such that it can deliver two times larger nominal luminosity in p+p collisions. It is expected that about $300\,\mathrm{fb}^{-1}$ will be accumulated before the third Long Shutdown (LS3) [119]. The evolution of the (expected) peak and integrated luminosity until LS3 are displayed in figure 3.2. An additional longer shutdown, the Extended Year End Technical Stop (EYETS), is foreseen between the years 2016 and 2017, which was requested by the CMS Collaboration for installation of a new pixel detector (see section 3.1.4 for CMS detector upgrade). For a maximization of the potentially available integrated luminosity in Pb–Pb collisions, the upgrade of the SPS injection kicker to a rise time of 100 ns is a crucial ingredient [123]. Reducing the β^* to 0.4 m and further aiming for a 50 ns bunch spacing, peak luminosities in excess of $\mathcal{L} = 7.2 \cdot 10^{27}\,\mathrm{cm}^{-2}\mathrm{s}^{-1}$ are in reach [19]. This peak luminosity is limited by the electromagnetic fields around the colliding nuclei, which can generate additional interactions and eventually modify the mass or the net-charge ($^{208}\mathrm{Pb}^{82+} +^{208} \mathrm{Pb}^{82+} \rightarrow^{208} \mathrm{Pb}^{82+} +^{208} \mathrm{Pb}^{81+} + \mathrm{e}^{+}$). A secondary beam is emitted from the interaction point, which, when it hits the beam pipe, has enough power to potentially quench a superconducting magnet [123]. Thus, additional collimators are needed for interception in the dispersion region in front of the collision point, where this secondary beam is sufficiently separated from the actual Pb-beams. These collimators are

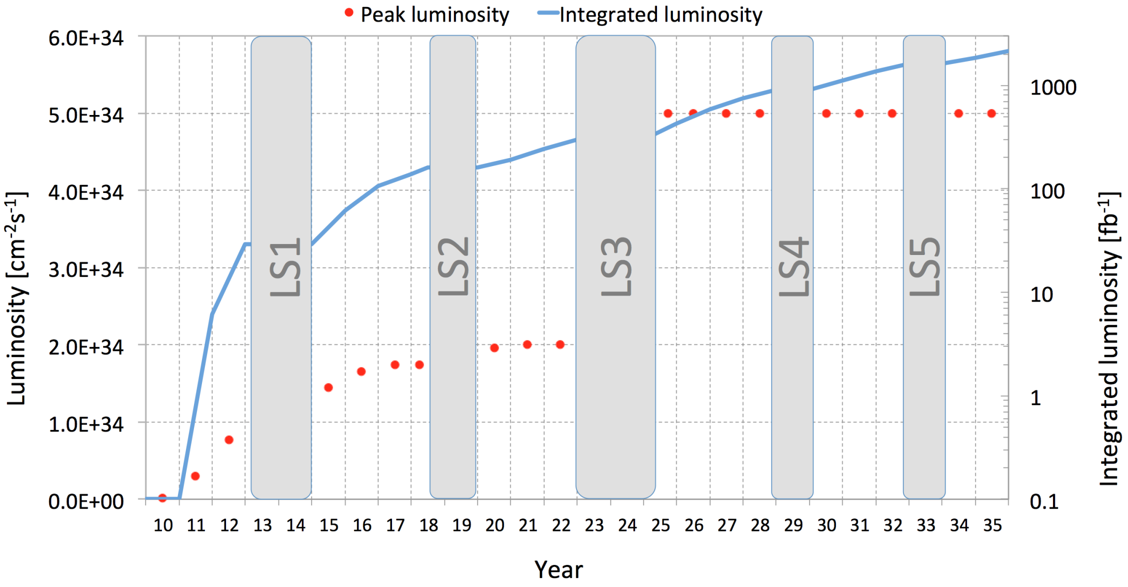

Figure 3.2.: LHC luminosity evolution between 2010 and 2035, after the fifth Long Shutdown. The peak luminosity is presented with red dots, whereas the blue line shows the integrated luminosity. This figure has been taken from [120]. Note, that this schedule is tentative, and changes (shift by two years of LS2 and afterwards) apply already [122].

planned for installation during the LS2, too. Based on these considerations, an ultimate luminosity goal of $\mathrm{L}_{\mathrm{int}} = 10\,\mathrm{nb}^{-1}$ is aimed for in Run 3 and beyond [124], collected in dedicated, annual heavy-ion runs, as outlined in section 3.3. For the peak luminosity in Pb–Pb collisions, using $\sigma^{\mathrm{hadronic}}_{\mathrm{Pb-Pb}} = 8\,\mathrm{b}$, the hadronic interaction rate is expected to be as high as 50 kHz. Additional p–Pb runs are foreseen.

During LS3, the High Luminosity LHC (HL-LHC) [125] will be installed, which will allow for more populated and denser bunches at the collision regions of ATLAS and CMS. A peak luminosity of $(5\text{–}7) \cdot 10^{34}\,\mathrm{cm}^{-2}\mathrm{s}^{-1}$ can be reached, delivering an integrated luminosity of almost $4\,000\,\mathrm{fb}^{-1}$ in Phase-II of the LHC until 2037 [120].

3.1.2. LHC experiments

The four major LHC experiments are indicated at their respective Interaction Point (IP) in figure 3.1. Two general purpose experiments, A Toroidal LHC Apparatus (ATLAS) and the Compact Muon Solenoid (CMS), are installed at IP1 and IP5, respectively. The LHC beauty (LHCb) detector is located at IP8, whereas A Large Ion Collider Experiment (ALICE) measures at IP2. ATLAS is accompanied by the detectors of the LHC forward (LHCf) experiment, while the TOTal Elastic and diffractive cross-section Measurement (TOTEM) detectors are installed around CMS. The Monopole and Exotics Detector At the LHC (MoEDAL) is deployed around the interaction point at LHCb. In the following, these seven LHC experiments are briefly outlined:

The largest of the LHC experiments was specifically designed for the Higgs boson search [126]. After the discovery, the collaboration now investigates the properties of the boson and compares it to the Standard Model expectations. In addition, physics beyond the Standard Model are evaluated, such as supersymmetry, extra dimensions and dark matter. Inside the experiment, the inner tracking detectors and the transition radiation tracker are housed in a central solenoid, surrounded by the liquid Argon electromagnetic and hadronic calorimeters. An additional magnetic field is supplied by a large, superconducting barrel toroid, in which a standalone muon detection system is installed.

The second general purpose experiment, CMS, investigates similar physics objectives as ATLAS and is supplied with the same beam conditions [127], such that both collaborations can record equally large data sets. However, in CMS different detector technologies are used: Silicon tracking detectors as well as a lead-tungstate calorimeter are located within a 3.8 T strong solenoidal field. The iron return yoke serves as muon filter and houses the muon chambers of the experiment.

In addition to its large program on Standard Model physics, the asymmetric LHCb detector is searching for new physics in direct and indirect CP violations of rare probes in the forward region, where heavy-flavor quarks are very strongly boosted [128]. The single arm spectrometer consists of a dipole, which is arranged behind a silicon VErtex LOcator (VELO) and a ring-imaging Cherenkov detector, necessary for precise determination of secondary vertices as well as particle identification. Additional tracking stations, Ring-Imaging Cherenkov counters (RICH), calorimeters and muon chambers are located behind the dipole magnet.

The ALICE detector is the dedicated heavy-ion experiment at the LHC [129]. It consists of many different subsystems, which are located in a central barrel and a muon arm and are optimized for tracking and particle identification. With a focus on the planned detector and readout upgrade, it will be explained in greater detail in sections 3.2 and 3.3.

TOTEM measures particle scatterings at small angles and determines the total p+p cross-section for elastic and diffractive scattering [130]. It is technically incorporated into CMS and located about 200 m away on each side around the same interaction region. The two telescopes each consist of a cathode strip chamber and a gas electron multiplier, and are accompanied each by a Roman Pot, which houses silicon trackers.

Comparable to TOTEM at CMS, LHCf [131] is installed around the ATLAS detector. The two electromagnetic calorimeters measure neutral-particle production cross-sections in the forward region via neutral pions and hadrons in order to gain insight into physics similar to the development of atmospheric showers, which are produced by highly-energetic cosmic ray particles.

MoEDAL [132] consists of an array of plastic nuclear track detectors and is installed around the LHCb VELO. The collaboration searches directly for Magnetic Monopoles and other highly ionizing, stable massive particles.

3.1.3. Experiment upgrades during Long Shutdown 1

The first Long Shutdown of the LHC gave the opportunity to review the performance of the existing detectors. Further, it allowed for long access time to all experiments and thus for significant work on the individual detectors [133], which is outlined in the following.

- The ATLAS Collaboration underwent an extensive upgrade and consolidation campaign: The silicon pixel detector was extracted and individual non-working modules were repaired. In addition the readout speed of the first two pixel layers was doubled. A fourth layer of pixel detectors, the Insertable B-Layer (IBL) [134, 135], was installed as a major upgrade, which will improve the vertexing and b-tagging capabilities of the detector. This was possible through the insertion of a new Be-beam pipe with a smaller diameter by 11 mm (outer diameter: 29 mm).

- New chambers were installed as an extension of the current muon detection system in the CMS experiment [136]. 72 cathode strip chambers were added, and 133 resistive plate chambers were fitted to the endcaps of the detectors. The highest priority was given to the new operation mode of the silicon tracker at cold temperatures of -20°C, which allows to mitigate the expected damage of the high particle flux. As for ATLAS, the beam pipe was replaced. Further, CMS and TOTEM have a joint physics program until LS2. With the installation of the CMS-TOTEM Precision Proton Spectrometer (CT-PPS), the precision proton tracking in the forward region is improved [137].

- LHCb used the time for significant consolidation of the infrastructural services, such as the gas system [138]. The beam pipe was removed for the preparation of a third section, and a new, much lighter support structure of the pipe. In addition, this allowed consolidation works on the large LHCb dipole magnet. Further, the iron shielding downstream of the experiment was substantially enlarged in order to protect the muon systems from particles entering through the LHC tunnel.

3.1.4. Experiment upgrades during Long Shutdown 2

In order to cope with the expected high particle rates at the LHC, significant detector upgrades are foreseen for all of the four large LHC experiments. Whereas the upgrade of the ALICE detector will be explained in greater detail in section 3.3, the plans for ATLAS, CMS and LHCb are outlined in the following. Note, that the most important upgrades for ATLAS and CMS will be installed during LS3, which is not covered in this thesis.

- ATLAS aims to perform current measurements with high precision, and plans to continue characterizing the newly discovered Higgs boson. As the LHC approaches peak luminosities of $(2\text{–}3) \cdot 10^{34}\,\mathrm{cm}^{-2}\mathrm{s}^{-1}$, 55 to 80 (pile-up) interactions per bunch crossing are expected in the ATLAS interaction region [139]. In order to maintain the diverse physics program, the collaboration mainly focuses on the improvement of present Level-1 trigger capabilities, such that it is kept at an acceptable rate, while current p_{T}-thresholds for single isolated electrons and muons are maintained. This includes the installation of a new trigger and tracking detector in the inner layers of the forward spectrometer (for leptons) [140] and new trigger read-out boards for the electromagnetic and forward calorimeters [141], eventually leading to a better rejection of fake electron triggers. In addition, a new forward detector will be installed [142] and the data acquisition system will be extended to include the new detectors as well as to maintain the detector performance, as the LHC reaches more-than-design luminosity [143]. These upgrades are fully compatible with the Phase-II upgrades, planned during LS3 [144], which are needed for operation in the era of the HL-LHC.

- Having similar physics objectives as ATLAS, the high rates at the LHC also demand upgrades of the CMS detector: The collaboration plans to replace the current pixel tracker with a new, low-mass detector of four central layers, and three forward/backward disks to cover a pseudo-rapidity range of $|\eta|<2.5$ [145]. However, because of the relatively easy access, CMS is preparing to replace the present detector, if necessary, already at the year-end technical stop of 2016/17. In LS2, the hadron calorimeter will receive a new readout system and electronics, using silicon photomultiplier (SiPM) technology instead of the current hybrid photodiodes (HPDs) [146]. As a consequence of the extended LHC performance, also CMS needs to improve its muon system in forward direction ($1.6<|\eta|<2.2$) [147], accompanied by a complete trigger upgrade, in order to maintain its performance throughout Phase-I and Phase-II of the LHC [148]. As for ATLAS, additional, significant detector upgrades are planned during LS3, such as a full replacement of the inner tracker [119].

- LHCb aims for precision measurements of indirect effects of new physics in CP violation and rare decays. As the current LHCb detector is limited by the detector performance in high-occupancy events as well as particle rates and radiation load, it can only measure about $1\,\mathrm{fb}^{-1}$ per year. Thus, most importantly, it is foreseen to improve the readout rate of all detectors to 40 MHz and to replace all subsystems, which cannot cope with the expected high particle rates at the LHC [149, 150]. In line with this strategy, new silicon pixel sensors will be installed together with a completely new infrastructure [151]. Further, a full upgrade of the particle identification detectors is foreseen: improved RICH optics will be equipped with new photon detectors and the readout of the calorimeter is going to be replaced, while an upgrade of the muon system will be installed [152]. The tracking will be improved by a new scintillating fiber detector (SciFi), read out by silicon photomultipliers (SiPMs) [153]. These detector improvements are accompanied by the corresponding upgrade of the trigger [154].

3.2. The ALICE Experiment at the Large Hadron Collider

A Large Ion Collider Experiment [129] follows a physics program, focused to the inspection of QCD matter produced in collisions of highly energetic lead nuclei [155, 156]. These observations are complemented by measurements of p+p and p–Pb collisions at similar center-of-mass energies. The detector capabilities were optimized for excellent tracking and particle identification (PID) in a high-particle density environment of up to 8 000 charged

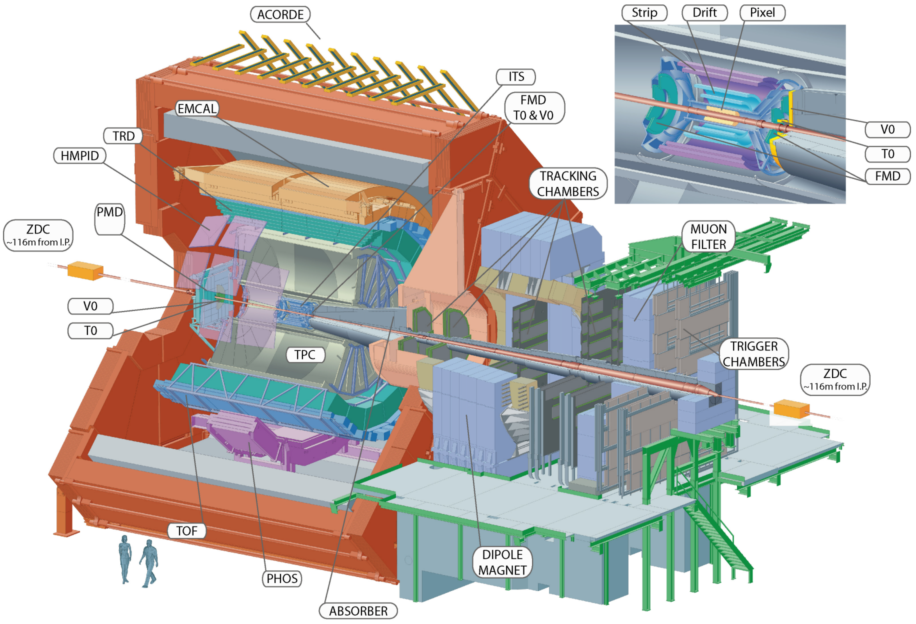

Figure 3.3.: Schematic view of the ALICE Experiment at the LHC. The central barrel detectors are installed inside the red dipole magnet, whereas a muon spectrometer extends into forward direction. The new ALICE diffractive detector, described in section 3.2.5, is installed just outside of the solenoid. In the direction of the Muon spectrometer, this corresponds to the position just behind the trigger chambers. This figure has been taken from [156].

particles per unit of pseudo-rapidity. ALICE is capable of tracking particles down to a low transverse momentum threshold of about $150\,\mathrm{MeV}/c$ and maintains good PID up to $20\,\mathrm{GeV}/c$, which both are necessary for the measurements of global event characteristics, such as collective flow, R_{AA}, and collision centrality, as well as total particle yields. The study of high-p_{T} phenomena, i.e. particle jets, further requires good momentum resolution at up to $100\,\mathrm{GeV}/c$.

The central barrel detectors are housed inside a large solenoid magnet of strength $\mathrm{B} = 0.5\,\mathrm{T}$ and investigate particle production around mid-rapidity. Going from the collision point in outward direction, the major tracking detectors are the Inner Tracking System (ITS) [157], the Time Projection Chamber (TPC) [158] and the Transition Radiation Detector (TRD) [159], which cover the full azimuth and also have particle identification capabilities. Additional detectors dedicated to particle identification at different kinematic ranges are the High Momentum Particle Identification (HMPID) detector [160], the ElectroMagnetic CALorimeter (EMCAL) [161] and the Time-Of-Flight Detector (TOF) [162, 163]. While the EMCAL measures jets and photons in a wide pseudo-rapidity range of $|\eta| < 0.7$, the Photon and Forward Multiplicity Detectors (PMD [164, 165] and FMD [166]) investigate electromagnetic radiation at forward and backward direction of the interaction region. In addition, the PHOton Spectrometer (PHOS) [167] uses lead tungstate crystals for precision photon measurements in a small geometrical region of $|\eta| < 0.12$ and 100° in azimuth. On top of the dipole magnet, ALICE COsmic Ray DEtector (ACORDE) [168] is installed for cosmic ray measurements. Further, some smaller subsystems are installed for event characterization and triggering purposes: The T0 detectors [166], which consists of two

Cherenkov counters (T0A and T0C) are located on both sides of the interaction point ($-3.28 < |\eta| < -2.97$ and $4.61 < |\eta| < 4.92$) and measure the time and longitudinal position of the interaction. In addition, two sets of plastic scintillators, the V0A and V0C detectors [166], specified on the determination of the centrality and the corresponding event plane angle in Pb–Pb collisions, are placed at $-3.7 < \eta < -1.7$ and $2.8 < \eta < 5.1$ respectively. Outside of the central barrel, the Zero Degree Calorimeter (ZDC) [169], which consists of two sets of two tungsten-quartz neutron and proton calorimeters each, is positioned symmetrically about 137 m upstream and downstream of the interaction region. It contributes another centrality measurement via the detection of spectator neutrons.

A muon spectrometer [170, 171], which consists of an absorber, muon filters, five tracking (MCH) and two triggering stations (MTR), is arranged around an additional dipole magnet of 3 Tm. It is designed to measure quarkonium and light vector meson production in a region of $-4.0 < \mathrm{y} < -2.5$, as well as high-p_{T} muons from the decay of heavy-flavor hadrons.

The ALICE detector geometry follows a global, right-handed cartesian coordinate system with the origin located at the ideal interaction point within the beam pipe. The global Z-axis points away from the Muon spectrometer in anti-clockwise direction of the LHC, whereas the global Y and X coordinate point into vertical and horizontal direction respectively. From the origin on the x-axis, the azimuthal angle ϕ increases into anti-clockwise direction, whereas the global polar angle θ increases in clock-wise direction. A more detailed schematic view is presented later in figure 4.5.

The subsystems, which are necessary for the measurement of heavy-flavor mesons at mid-rapidity, such as the presented study on $\mathrm{B}^+ \rightarrow \overline{\mathrm{D}}^0\pi^+(\overline{\mathrm{D}}^0 \rightarrow \mathrm{K}^+\pi^-)$, are described in greater detail in the following.

3.2.1. Inner Tracking System

Within the Inner Tracking System (ITS) [157] of the ALICE Experiment, three different technologies of silicon semiconductor detectors are used. Shown in the inlet of figure 3.3, the system consists of six cylindrical layers placed symmetrically around the beam pipe with a combined pseudo-rapidity coverage of $|\eta| < 0.9$. At radii between 39 to 430 mm, two layers of each technology are used: The silicon pixel detector is closest to the interaction point, with its minimal distance limited by the radius of the beam pipe. It is followed by a silicon drift detector and a silicon strip detector. To achieve the required impact parameter resolution in an environment of extremely high particle densities (≈100 particles per cm^2 for Pb–Pb collisions at $\sqrt{s_{\mathrm{NN}}} = 5.5\,\mathrm{TeV}$), silicon pixel detectors are the only choice for the two innermost layers due to their high granularity. The large outer radius of the outer silicon strip detectors is required by the aim to optimize the track-matching efficiency between the ITS and the TPC. Further, the drastically reduced particle flux allowed to employ different silicon technologies, which have smaller granularity, but include particle identification capabilities.

As the ITS is the first sensitive detector closest to the interaction region, it plays a crucial role in the tracking of charged particles and thus practically contributes to almost all measurements in the ALICE central barrel. It was specifically designed to:

- Identify the primary vertex with a resolution better than 100 μm.

- Reconstruct secondary vertices of heavy-flavor meson decays, such as $\overline{\mathrm{D}}^0 \rightarrow \mathrm{K}^+\pi^-$ and $\mathrm{B}^+ \rightarrow \overline{\mathrm{D}}^0\pi^+$.

- Identify and track particles with $p_\mathrm{T} \leq 200\,\mathrm{MeV}/c$, which either do not reach the TPC (low p_T) or propagate a long path in the dead regions of the detector (high p_T).

- For tracks jointly reconstructed with the TPC, extend the lever arm of the momentum measurement, and thus the momentum resolution, towards largest possible values.

- Have a minimal impact on the particle trajectory, with a material thickness as low as $x/X_0 = 1.1\,\%$ per layer, which minimizes the multiple scattering contribution to the position uncertainty of a track.

3.2.1.1. Silicon Pixel Detector

The Silicon Pixel Detector (SPD) consists of about $9.8 \cdot 10^6$ hybrid silicon pixels, which are connected to 1 200 chips and mounted on 60 support staves. The working principle of such a hybrid pixel is illustrated in figure 3.4. Individual pixels of the size $(50 \cdot 425)\ \mu\mathrm{m}^2$ $(r\phi \cdot z)$ and a thickness of $200\,\mu$m are grouped in a matrix of $(256 \cdot 160)$ cells, and bump bonded to five $150\,\mu$m-thick front-end chips. The bond establishes a conducting connection between the electronics chip and the sensing pixel. Inside the sensing chip, a p^+-implant collects the released holes from the fully depleted sensor, when a charged particle passes the active area. The electrons are absorbed via ohmic n-side contacts in the back side bias. The (average) total amount of deposited charge depends on the specific energy loss of the incoming, (minimum) ionizing particle. For example, a $0.5\,\mathrm{GeV}/c$ pion generates about 60 electrons per μm path length in a thin silicon layer. Inside the depletion zone, the holes drift towards the sensing diode and induce the signal. The choice of p^+-n sensor design is driven by the moderate total expected radiation levels, which correspond to a cumulated dose of 130 krad and $3.2 \cdot 10^{11}\,\mathrm{cm}^{-2}$ neutron fluence. Compared to ATLAS and CMS ($\mathcal{O}(10^{15})$) these are relatively low [172].

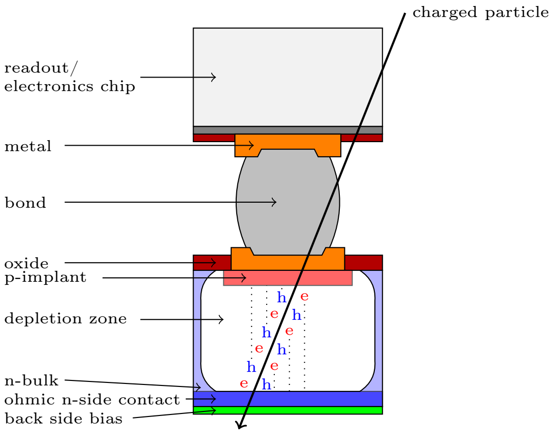

Figure 3.4.: Schematic view of a silicon hybrid pixel chip, as used for the ALICE SPD. Each pixel is bump-bonded to a readout/electronics chip, where the signal is further processed.

The front-end chips are wire-bonded to the pixel bus, which transports the information to the Multi-Chip Module (MCM) at the end of a half stave, where the signal is read out. Assuming 100 % dead time, the maximum readout time of the SPD is 296 μs at a rate of 3.3 kHz. It is thus capable to contribute hit-multiplicity and hit-topology based triggers to the Level 0 (L0) contribution in the Central Trigger Processor (CTP, section 3.2.4). The SPD itself covers the full azimuth and a polar angle of $|\eta| < 2.0$, with a spatial resolution of $\sigma_{xy} = 12\,\mu$m ($\sigma_z = 100\,\mu$m) in transverse (longitudinal) direction. The material budget traversed by a track perpendicular to the detector surface sums up to $x/X_0 = 2.8\,\%$ (including a thermal shield/support behind the outer layer). The heat load of about 23 W per stave is cooled by an evaporative system of C_4F_{10}.

3.2.1.2. Silicon Drift Detector

Located at a radial distance of 15.0 and 23.9 cm, two layers of silicon drift technology provide the first two dE/dx samples, which are needed for the ITS particle identification. The 300 μm-thick silicon is split by a central electrode strip into two, fully depleted drift regions. Both surfaces are covered by 291 cathode strips each, with a pitch of 120 μm. A homogenous drift field is generated parallel to the chip surface, as the drift cathodes (p^+-implants) are split by voltage dividers in direction away from the central electrode, towards the collection anode. At a bias voltage of -2.4 to -1.65 kV [129], the maximal drift velocity ranges from 5.6 to 8.1 μm/ns with a maximum drift time of 4.3 to 6.3 μs. The Silicon Drift Detector (SDD) provides an average resolution of better than 34 μm along the electron drift direction, which corresponds to the global ALICE rϕ-coordinate. The longitudinal position (along the global ALICE Z-coordinate) is measured via the charge collection of the corresponding anode, as shown in figure 3.5 where a resolution of 25 μm is achieved. The amount of deposited charge by a particle from the interaction region is further used for particle identification. The SDD constitutes a sensitive area of (70.17 · 72.25) mm^2, covers the full azimuth and a polar angle of $|\eta| < 0.9$. In total 256 modules are mounted on 36 ladders. The material budget of the SDD amounts to $x/X_0 = 2.64\,\%$ (including a thermal shield/support in front of the inner layer). The detector has a busy time of 1023 μs at a readout rate of 985 Hz. At this distance to the collision region, the expected particle flux may reach up to 7 per cm^2 [129]. Two independent under-pressure water circuits are used to cool the detector and provide a temperature stability of 0.1 K.

3.2.1.3. Silicon Strip Detector

The ITS is completed by two outer layers of double-sided silicon strip technology, which are crucial for the matching of tracks between ITS and TPC. Located at radii of 37.8 and 42.8 cm, the detection layers of the Silicon Strip Detector (SSD) have a sensitive area of 2.2 and 2.8 m^2 for the inner and outer layers. A total of 1 698 modules are mounted on 34 and 38 ladders, which surround the interaction in a turbine-like shaped cylinder. A single module is 300 μm thick, with an active area of (73 · 40) mm^2 [129]. As indicated in figure 3.6, on each side of the pn-junction, 768 read-out strips of 40 mm lengths at a pitch of 95 μm are surrounded by a bias ring and a guard ring to protect the sensor from instability effects bear the border. As the probability that a single strip detects more than one particle is non-negligible, the strips are mounted with a small angle of 7.5 mrad and 27.5 mrad on

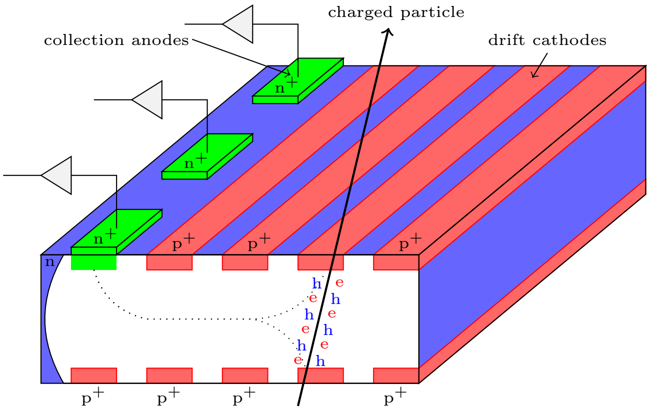

Figure 3.5.: Illustration of the working principle of the ALICE SDD. Charges are generated by a particle, passing through the detector. The space point is measured via collection of the deposited charge at the cathodes and the corresponding drift time of the electrons.

the p- and n-side, such that a total stereoscopic angle of $\alpha = 35\,\mathrm{mrad}$ is achieved. This angle is optimized to resolve ambiguities in combination with the readout of the correlated charges on p- and n-side. In addition, the two layers are mounted opposite to each other with either the n-side or p-side facing the interaction region, such that the strips are placed in four different orientations. With this configuration the fake (or ghost) track probability is significantly reduced, and a spatial resolution of $\sigma_{r\phi} = 20\,\mu\mathrm{m}$ and $\sigma_z = 20\,\mu\mathrm{m}$ is obtained [129]. The modules are equipped with a leak-tight water cooling system. Even though the system is optimized for a low total material budget of $x/X_0 = 2.22\,\%$ (including a thermal shield/support in front of the inner layer), it is capable of providing particle identification of low-p_{T} particles via their $\mathrm{d}E/\mathrm{d}x$ information.

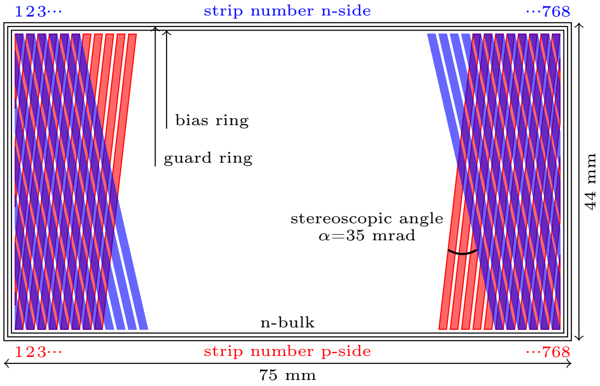

Figure 3.6.: Schematic view of the ALICE SSD sensor layout, looking from the n-side. The n-implants (blue) are visible on the top side, superimposed on the p-implants (red), which are on the bottom side of the sensor. For an optimal rejection of fake (ghost) tracks, the strips are tilted in opposite direction with respect to the other side of the sensor.

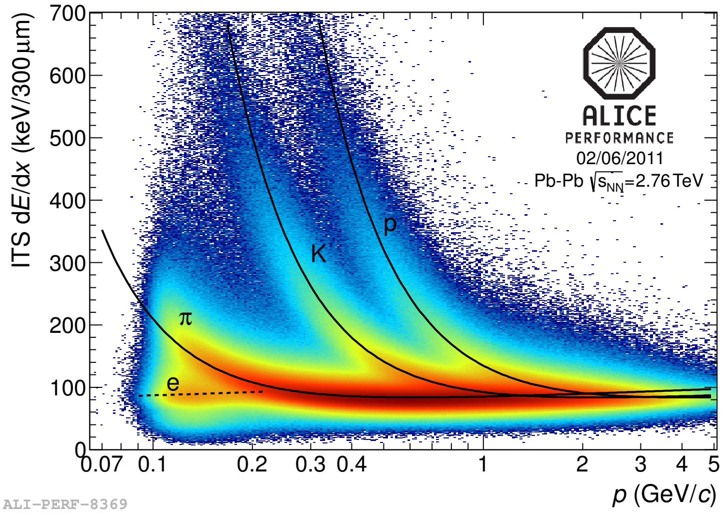

Figure 3.7.: ITS PID performance in Pb–Pb collisions at $\sqrt{s_{\mathrm{NN}}} = 2.76$ TeV. The parameterized Bethe-Bloch expectations are indicated by solid lines. A similar figure can be found here [173].

3.2.1.4. Particle identification

The particle identification capabilities of the combined ITS detector elements (SDD+SSD) is shown in figure 3.7 for ITS standalone tracks [156]. For each particle species, the Bethe-Bloch parameterization is indicated by a solid line. Using the $\mathrm{d}E/\mathrm{d}x$ calculated via a truncated mean, the final resolution is about 10 % with respect to the expected energy loss. Typically, for pions a 2σ-selection on the lower bound is applied to reject contamination by electrons at low momentum [173]. For low momentum, the kinematic range is limited by the ITS standalone tracking efficiency. With increasing momentum, a π/K separation power of 2σ is managed up to $\mathrm{p} \approx 0.5\,\mathrm{GeV}/c$. For higher momentum the contamination from other particles species is increasing and does not allow a clean pion identification.

3.2.2. Time Projection Chamber

The largest and most important tracking device in the ALICE central barrel is the TPC [158], which has a radial coverage from 83 to 250 cm and a total longitudinal extent of 500 cm. It is capable of tracking charged primary particles above $p_{\mathrm{T}} \gtrsim 0.15\,\mathrm{GeV}/c$ and covers a pseudorapidity range of $|\eta| < 0.9$. In addition, particle identification is obtained via the measurement of the specific energy loss characteristic for each particle species. The TPC vessel, shown in a simplified technical drawing in figure 3.8a, was operated until 2011 with a gas mixture of Ne-CO$_2$-N$_2$ and between 2012-2015 with Ne-CO$_2$ as drift and counting gas. Since 2015, a mixture of Ar-CO$_2$ is used, which has a larger primary ionization and thus an improved momentum resolution despite the increased diffusion and high-particle fluxes [174]. Embedded into the solenoidal magnetic field of $\mathrm{B} = 0.5\,\mathrm{T}$, the magnetic field lines are parallel to the drift field of the detector, which is split into two parts by a central electrode. At an electric field strength of 400 V/cm, charge clusters, generated by particles traversing the active volume, drift towards the endcaps of the TPC, where multi-wire proportional chambers (MWPCs) are amplifying and recording the signal. The

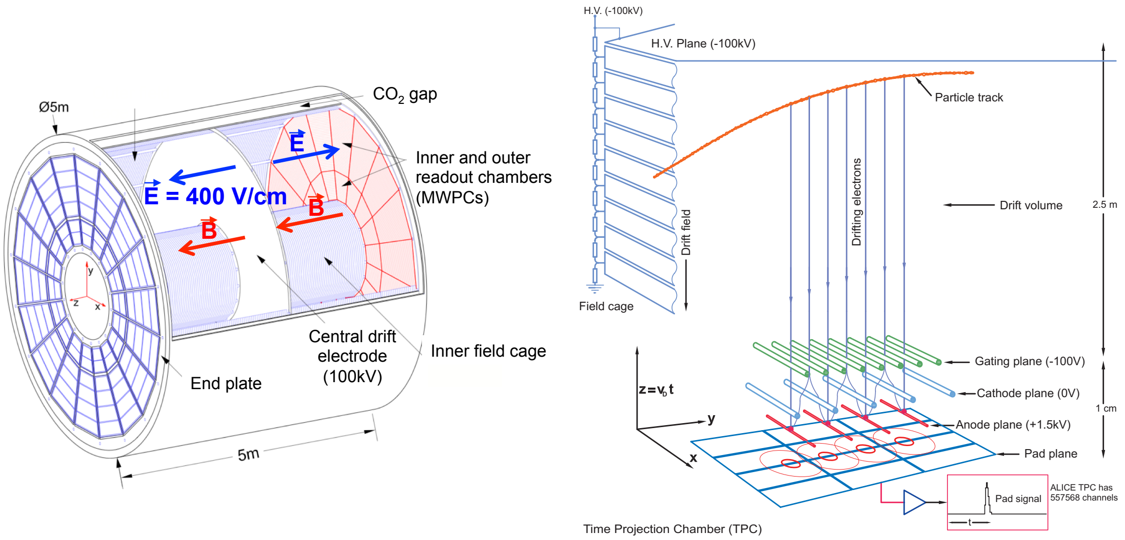

(a) **(b)**

Figure 3.8.: (a) displays a simplified technical drawing of the ALICE TPC, indicating the magnetic and electric field direction. In (b), the detailed working principle of the ALICE TPC is sketched. These figures have been taken from [175] and [176] respectively.

readout plane is segmented into 159 pad rows in radial direction for spatial information in rϕ-direction. The first 63 rows are part of the inner readout chamber (IROC) and have a pad size of $(4 \cdot 7.55)\,\text{mm}^2$ $(\phi \cdot r)$ [129]. The outer readout chamber (OROC) has a pad size of $(6 \cdot 10)$ and $(6 \cdot 15)\,\text{mm}^2$ for the remaining 64+32 pads, increasing for larger radii. The z-coordinate is obtained from a measurement of the drift time with respect to an external starting time signal, given for example by the T0 or V0 detectors [156]. In the design gas mixture of Ne-CO$_2$-N$_2$, the drift velocity is $2.7\,\text{cm}/\mu\text{s}$, with which the drift time over the full length of 250 cm is limited to $92\,\mu\text{s}$. The position resolution is $\sigma_{r\phi} = 1\,100$ $(800)\,\mu\text{m}$ for the IROC (OROC), and $\sigma_z = 1\,250$ to $1\,100\,\mu\text{m}$ in longitudinal direction [129]. Note, that the support structure of the MWPC intersects the individual readout chambers in $r\phi$-direction. In order to limit the ion back flow of the amplified signal in the MWPC, gating grid wires are installed in front of the readout chambers. As visible in the top left of figure 3.8b, the electric field cage consists of individual conducting foil bands, which provide the homogeneous electric field, as they are connected to an equidistant high-voltage potential. Upon a Level 1 trigger, the gating grid is opened for the duration of one maximal drift-time interval. For tracks near small rapidities, an overall low material budget of $x/X_0 = 3.5\,\%$ is achieved.

The inverse-p_T resolution in p–Pb collisions for TPC standalone tracks as well as ITS+TPC combined tracks is shown in figure 3.9a. For tracks at high momentum, the resolution improves by up to a factor of six for ITS+TPC tracks compared to the standalone TPC case. Using an additional vertex constraint, TPC standalone tracks almost perform as well as ITS+TPC combined tracking, as the additional constraint is included in the Kalman filter track reconstruction. In case the full ITS information is used an subsequent improvement is observed, as not just the spatial coordinates but also additional information

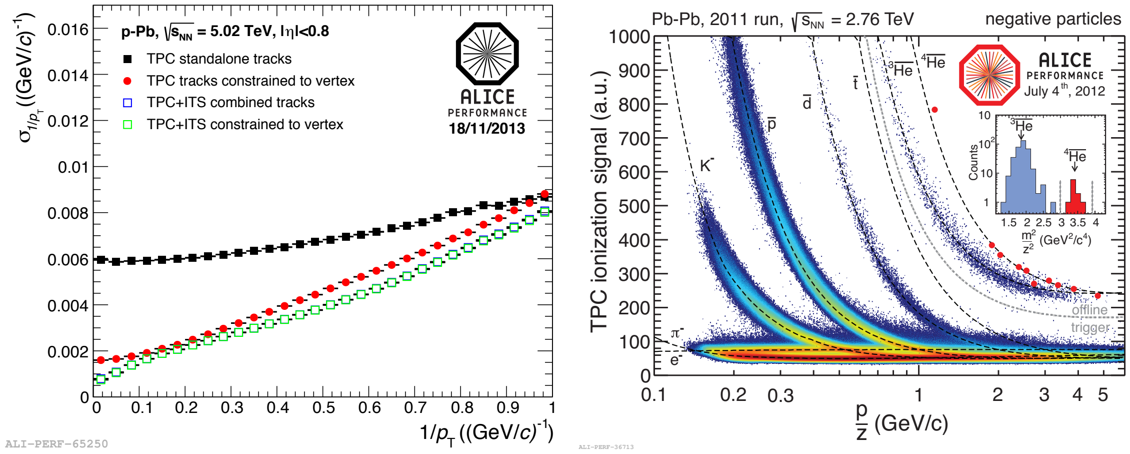

(a) (b)

Figure 3.9.: In (a), the standalone and combined inverse-p_T resolution for ITS+TPC tracks in p–Pb collisions. The specific energy loss of negatively charged particles in Pb–Pb collisions is shown for particles as a function of rigidity after additional offline selection in (b). These figures have been taken from [156] and [177] respectively.

from the direction of the propagation is used. For central Pb–Pb collisions the performance deteriorates only by up to 15 % [156].

3.2.2.1. Particle identification

Charged particles traversing the TPC ionize the gas along their trajectory. The up to 159 measured charge clusters are not only used for the track reconstruction, but the deposited charge further allows for particle identification over a wide momentum range [173]. As the released charges are proportional to the energy lost per unit length dE/dx, a fit with the ALEPH TPC Bethe-Bloch parameterization for each particle type is used to give a hypothesis on the true particle mass and species [156]. The performance of the particle identification in Pb–Pb collisions is depicted in figure 3.9b as a function of rigidity, where the dashed lines indicate the fitted Bethe-Bloch parameterization. Here, only negatively charged particles are displayed after additional offline trigger selection. With a dE/dx resolution of 6 %, light flavor species are clearly identified over a wide range of momentum, and even anti-alpha candidates are found. Note, that the TPC particle identification capabilities are complementary in terms of momentum coverage to the other central barrel detectors. For low momentum up to 200 MeV/c, the ITS PID can be effectively used to separate pions and electrons. For momentum above 1 GeV/c, where electrons cannot be distinguished track-by-track through their specific energy loss alone, the Transition Radiation Detector (TRD) provides complementary electron identification. In addition, as will be shown in section 3.2.3.1, pions and kaons can be identified in the TOF detector up to 2.5 GeV/c, where the bands of the Bethe-Bloch parameterization already overlap in the TPC and the specific energy loss measurement of the TPC alone is not sufficient to differentiate between pions, kaons and protons on track-by-track basis.

3.2.3. Time-Of-Flight detector

Installed just outside of the TRD at a radius of 370 cm, the 18 sectors of the Time-Of-Flight (TOF) detector [162] cover a pseudo-rapidity range of $|\eta| \leq 0.9$ and the full azimuthal angle. The TOF detector was built to extend the momentum range of the particle identification using the particle time-of-flight information from the primary collision vertex. The TOF detector itself is based on 10-gap double-stack Multigap Resistive-Plate Chamber (MRPC) technology, operated at atmospheric pressure. The detector is operated with a gas mixture of $C_2H_2F_4$ (90 %), i-C_4H_{10} (5 %) and SF_6 (5 %). An example of such a MRPC design is shown for a 3-gap double-stack prototype design in figure 3.10a. When a particle traverses the gas-filled gaps, the produced ionization will trigger a charge avalanche, which is induced by the high voltage between cathode and anode. An avalanche is created within each gap and a signal, in form of the analogue sum of the individual gap signals is recorded on the segmented readout plane. Inside the 1 593 installed MRPCs, 152 928 pads of size $(2.5 \cdot 3.5)\ \mathrm{cm}^2$ cover an area of $141\,\mathrm{m}^2$. The major advantage of the MRPC design is, that the time jitter is caused only by fluctuations in the avalanche development, and not by the drift time. For particle multiplicities in the 70 % most central Pb–Pb collisions, a time resolution of 80 ps for pions at 1 GeV/c is achieved with a maximum trigger rate of 2 800 Hz. In total, the detector contributes $x/X_0 = 29.5\,\%$ to the overall material budget.

3.2.3.1. Particle identification

The actual particle identification is based on the time-of-flight information t of a given particle, compared to the expectation for different species. For triggering the start time at the primary vertex is provided for example by the T0 detector [156]. Based on the reconstructed track length l, the relativistic velocity β can be calculated via $\beta = l/(c\tau)$, which is also related to the track momentum [178]:

$$\beta = \frac{p}{E} = \frac{p}{\sqrt{m^2 + p^2}} \Leftrightarrow p = \frac{\beta m}{\sqrt{1 - \beta^2}} \tag{3.1}$$

The corresponding measurement is shown in figure 3.10b for Pb–Pb collisions. The bands of electrons, pions, kaons, protons and deuterons are clearly visible over a wide momentum range. Reliable particle identification up to 2.5 GeV/c is possible for pions and kaons, whereas protons can even be identified up to 5 GeV/c.

3.2.4. Trigger detectors and event selection

The trigger signals of the relevant subsystems as well as information on the LHC bunch filling scheme are collected in the Central Trigger Processor (CTP) [179, 180] of ALICE, which then generates the trigger decision [156]. The fastest trigger decision, the so called Level 0 trigger (L0), is performed in about 0.9 μs after a collision, based on information from V0, T0, EMCAL, PHOS, and MTR. The triggered events are propagated after 6.5 μs to the Level 1 trigger (L1), which, together with the L0 decision, triggers the buffering of the event data in the detector front-end electronics [156]. After about 100 μs, which corresponds to the drift time of the TPC, the buffered data is forwarded to the High Level Trigger (HLT), which plays a crucial role in data compression for future measurements, and to the Data AcQuisition system (DAQ). The most important triggers in Pb–Pb collisions

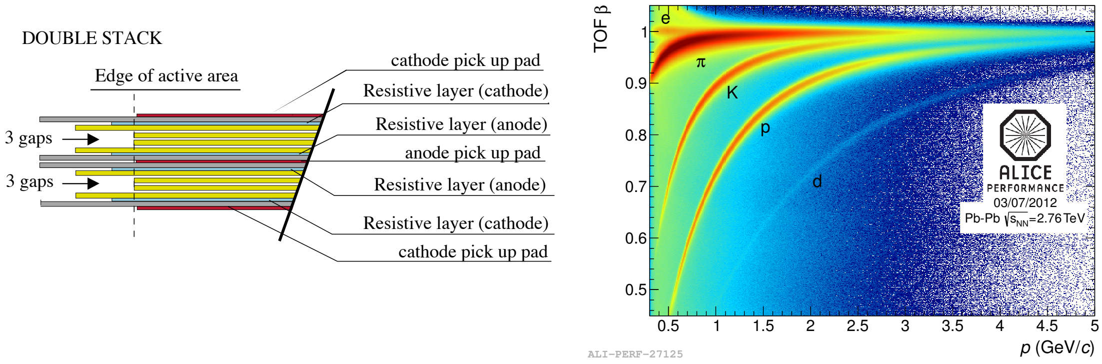

(a) (b)

Figure 3.10.: (a) displays a schematic view of a 3-gap double-stack MRPC prototype of the ALICE TOF detector. The particle identification capabilities via the flight-time measurement of the TOF detector in Pb–Pb collisions at $\sqrt{s_{\mathrm{NN}}} = 2.76\,\mathrm{TeV}$ is shown in (b). The bands of the individual species are clearly visible and allow for good identification of the different particle types. These figures have been taken from [162] and [156].

are typically minimum bias and centrality triggers, based for example on the hit-multiplicity in the SPD, or signal amplitude in the V0 or ZDC detectors.

3.2.5. Upgrade and completion of the detector during Long Shutdown 1

During the first Long Shutdown of the LHC, the ALICE detector was completed as well as extended by two subsystems. Five remaining super modules of the TRD were installed and the low voltage infrastructure was reworked. In addition, the optical readout links were doubled in their speed to 4 GB/s [181]. The electromagnetic calorimeter system (EMCAL) was extended with a new dijet calorimeter (DCal) [182], now covering a combined azimuthal angle of 174°. The new calorimeter is located in longitudinal direction before and after the photon spectrometer (PHOS).

In addition, two double layers of scintillator of the new ALICE diffractive physics Detector (AD) [183] were commissioned 16 m upstream and 19 m downstream of the interaction region. The overall sensitivity on diffractive physics and photon induced processes is enhanced with this new set of detectors [184].

As mentioned before, the TPC was filled with a new gas mixture, while the muon spectrometer underwent hardware consolidations. The work was concluded with an optimization of the DAQ and HLT systems resulting in an increased running efficiency in Run 2 [133, 174].

3.3. Upgrade of the ALICE Experiment during Long Shutdown 2

As described in section 3.1.1, the upgrade and extension of the LHC will allow higher luminosity in Pb–Pb collisions, which is of special interest for the ALICE Collaboration [19, 185]. Whereas the currently approved running scenario is limited to a data set of $\mathrm{L_{int}} = 1\,\mathrm{nb}^{-1}$ (10^{10} interactions), ALICE aims for an improved running scenario based on the presented LHC parameters. Under the assumption of stable LHC beam duration of Pb–Pb beams during one month per year, an integrated luminosity of $\mathrm{L_{int}} = 2.85\,\mathrm{nb}^{-1}$ per year can be recorded. After the second Long Shutdown of the LHC, ALICE is expecting a peak luminosity of $6 \cdot 10^{27}\mathrm{cm}^{-2}\mathrm{s}^{-1}$ and an average luminosity of $2.4 \cdot 10^{27}\mathrm{cm}^{-2}\mathrm{s}^{-1}$, which would allow to record $\mathrm{L_{int}} = 10\,\mathrm{nb}^{-1}$ of Pb–Pb collisions between 2020 and 2026, and additional reference data taken in dedicated p+p and p–Pb runs in 2021 and 2025 respectively. The plan includes a period of Pb–Pb data taking of $\mathrm{L_{int}} = 2.85\,\mathrm{nb}^{-1}$ with a reduced magnetic field, to extend the measurements towards lower transverse momentum.

3.3.1. Scientific scope of the upgrade

The available high statistics will open new possibilities for the characterization of the Quark-Gluon Plasma state [186, 20]. On the one hand, current measurements, for example of heavy-flavor mesons and charmonium states, could be performed as high-precision measurements, as the increase in statistics is expected to reduce also the systematic uncertainty in some measurements [186]. On the other hand, rare physics channels will be accessible for the first time and, in combination with the foreseen detector upgrade (section 3.3.2), allow for new measurements and insights into the deconfined QCD phase. In the following, a few examples are summarized:

- Heavy-flavor production via charmed and beauty mesons and baryons: The measurement of physics observables such as v_2, R_{AA} and baryon-to-meson ratios will be significantly improved in the charm sector. Especially measurements of the charmed meson production, i.e. $\overline{\mathrm{D}}^0 \rightarrow \mathrm{K}^+\pi^-$, will turn into high precision measurements with negligible statistical (and improved systematic) uncertainty down to $p_{\mathrm{T}} = 0\,\mathrm{GeV}/c$. Charm and strangeness production via $D_s^+ \rightarrow \phi\pi^+ \rightarrow \mathrm{K}^+\mathrm{K}^-\pi^+$ will be extended towards lower p_{T}. Further, charmed baryon production via $\Lambda_c^+ \rightarrow p^+\mathrm{K}^-\pi^+$ will be measured for the first time in Pb–Pb collisions at the LHC. Eventually improved beauty production measurements will become accessible, for example via the analysis of non-prompt D^0. In addition, full kinematic reconstruction of beauty mesons down to low p_{T} via $\mathrm{B}^+ \rightarrow \mathrm{J}/\psi(1\mathrm{S})\mathrm{K}^+$ ($\mathrm{J}/\psi(1\mathrm{S}) \rightarrow e^+e^-$) and $\mathrm{B}^+ \rightarrow \overline{\mathrm{D}}^0\pi^+$ ($\overline{\mathrm{D}}^0 \rightarrow \mathrm{K}^+\pi^-$), as presented in this thesis, will be possible for the first time. The foreseen measurements are complementary to existing analyses by CMS (i.e. to those shown in figure 2.19), extending the overall measured p_{T}-range towards lower values. These are further accompanied by the measurement of beauty baryons via $\Lambda_b^0 \rightarrow \Lambda_c^+\pi^-$ ($\Lambda_c^+ \rightarrow p^+\mathrm{K}^-\pi^+$).
- Quarkonium production in the central and forward rapidity region: At mid-rapidity, a measurement with good significance up to $p_{\mathrm{T}} \approx 5$–$6\,\mathrm{GeV}/c$ will be possible with $\mathrm{L_{int}} = 10\,\mathrm{nb}^{-1}$, which may allow direct access to elliptic flow of J/ψ from B hadrons as well. In the forward region, the measurements of prompt and non-prompt J/ψ and ψ' down to zero-p_{T} are accessible with strongly reduced uncertainty [185]. Further, it will be possible to search for charmed and beauty separately via measurements of single daughter muons.

- Thermal electromagnetic radiation via low-mass dileptons: The experimentally challenging measurement of electron-positron pairs in Pb–Pb collisions will be extended to a range of $p_{\mathrm{T}} \approx 0.1$–$0.2\,\mathrm{GeV}/c$. Here, the data taking will significantly profit from a dedicated Pb–Pb run with reduced magnetic field strength of $\mathrm{B} = 0.2\,\mathrm{T}$, which is necessary for low-p_{T} particles to reach the TOF detector for additional PID information.

- Extended jet measurements: Identified jet fragmentation functions and their in-medium modification will be measured over a wide p_{T} range, starting from low p_{T} and thus complementary to the other LHC experiments. In addition, heavy-flavor production in jets will be accessible as a consequence of the improved vertexing capabilities (section 3.3.2). Further correlation studies are planned, such as photon-jet correlations.

- Heavy nuclear states: The high statistics provided to the experiments will significantly improve the statistics of the current measurements, such as $\overline{^{4}\mathrm{He}}$ anti-nuclei (figure 3.9b). It may also be possible to detect light multi-hyper-nuclei, for example ${}^{5}_{\Lambda\Lambda}\mathrm{H}$, and extend the search for other exotic objects.

For the outlined physics landscape, it is necessary that ALICE records the statistics at the rate of Pb–Pb collisions at 50 kHz, where the requirement of an online event filtering must be dropped [186]. For example, because of the low signal-to-background ratio and high abundance of background candidates, a trigger on the $\overline{\mathrm{D}}^{0} \rightarrow \mathrm{K}^{+}\pi^{-}$ and $\Lambda_{c}^{+} \rightarrow p^{+}\mathrm{K}^{-}\pi^{+}$ channels alone would correspond to a rate of about 27 kHz. This is already close to the actual collision rate, but would also require a low momentum threshold of $p_{\mathrm{T}} > 2.0\,\mathrm{GeV}/c$ for the Λ_{c}^{+}, which may prevent a measurement at low p_{T} [186].

3.3.2. Upgrade strategy

In order to perform these measurements, significant detector upgrades are required. It is planned to significantly increase the readout speed in p+p collisions and to read out every Pb–Pb collision delivered by the LHC. Further, the upgrade strategy foresees to improve the vertexing and tracking capabilities as well as preserve the excellent particle identification. The vertexing and tracking is improved by moving the first detection layer closer to the interaction region, and by reducing the material budget of the inner detectors (ITS) significantly. In addition, a new readout technology of the ALICE TPC [187] is required, which is capable of continuous readout while maintaining the current PID performance. The detector upgrade thus includes:

- Installation of a new, high-resolution Inner Tracking System (ITSu) [186, 20]. The upgraded detector is explained in section 3.3.3.

- Upgrade of the readout system of the TPC to Gas-Electron Multipliers (GEM-TPC) [187]. The development of the GEM-TPC readout is outlined in section 3.3.5.

- Installation of a new Muon Forward Tracker (MFT) [185]. Based on the same Monolithic Active Pixel Sensors (MAPS) as the ITSu detector, the MFT consists of five discs, arranged between the interaction region and the absorber, covering

$-3.7 < \eta < -2.5$, which corresponds to almost the full acceptance of the muon arm. Each layer is optimized for a low material budget of $x/X_0 = 0.4\,\%$. The complete detector will inspect the interactions at a rate of 200 kHz in p+p, and 50 kHz in Pb–Pb.

- Upgrade of the (forward) trigger systems for high-rate operation with a new Fast Interaction Trigger (FIT) detector [188]. At the expected collisions rates after LS2, the forward detectors which currently provide minimum bias trigger, multiplicity trigger and beam-gas event rejection (T0, V0 and FMD), will need to be upgraded. It is planned to replace these detectors with FIT, which will consist of an improved technology, either based on the current T0 or current V0 detectors, or on both. In any case, FIT has to provide trigger efficiencies similar to the current V0 detector as well as perform vertex location comparable to the present T0 system, with a time resolution better than 50 ps.

- Upgrade of the online and offline systems (O^2) [189] as well as readout electronics of most subsystems [19]. In the ALICE upgrade strategy it is foreseen that all detector data is transferred to the computing system, while data reduction is performed on the fly and in parallel to the data collection. This requires online detector calibration and data reconstruction such, that for example instead of TPC raw data, reconstructed TPC clusters are used. Eventually, full replacement of the CTP, DAQ and HLT systems by the new common O^2 framework is planned.

3.3.3. Upgrade of the Inner Tracking System

Despite the optimization for vertexing and tracking capabilities and the low material budget, the current ITS detector is not suited to achieve the performance necessary for the physics aims after LS2. On the one hand, the current impact parameter resolution is not good enough to detect displaced vertices of $\Lambda_c^+ \rightarrow p^+\mathrm{K}^-\pi^+$, which has a mean proper decay length $c\tau = 60\,\mu\mathrm{m}$. On the other hand, the present detector is fundamentally limited by the maximum readout rate of 1 kHz of the SDD. As no dedicated trigger selections are foreseen, the ITS detector could thus only inspect a small fraction of the foreseen collision rate at the LHC.

The new ITSu is aiming to fulfill the improved vertex and tracking requirements using new MAPS, which allow a high granularity and spatial resolution at reduced material budget. The new design consists entirely of MAPS, which increases the pixel density by a factor 25. The benefits and specific design of the MAPS of the ALICE ITSu will be outlined in section 3.3.3.1. In line with the strategy outlined in section 3.3.2, the upgraded detector comes with an improved impact parameter resolution: As the beam pipe itself will have a reduced radius (29 mm→19 mm, 0.8 mm thick), the first detection layer can be moved to a minimum radius as low as 22.4 mm. As displayed in figure 3.11, the detector will be extended by an additional sensitive layer. The detection layers will be radially grouped into the inner (first three layers) and outer barrel (remaining four layers), with the individual layer positions optimized to improve the tracking efficiency as well as the p_T resolution. In addition, the layer positions were specifically chosen to improve the pointing resolution towards the primary vertex and to provide redundancy against failure of individual detector modules, using Monte Carlo simulations. The new stave design also

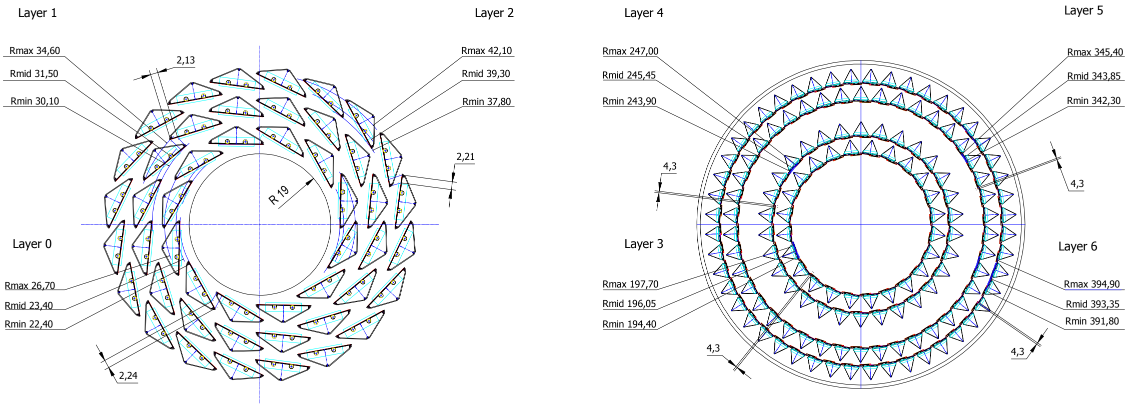

Figure 3.11.: Cross-section of the new ITSu detector. The foreseen detectors will be split into an inner barrel (left, three innermost layers) and outer barrel (right, four outermost layers). This figure has been taken from [20].

has a longer longitudinal extension, such that the track acceptance in the ITSu increases to $|\eta| < 1.22$.

Currently, different versions of the final pixel design with different readout architectures, are evaluated. The final design will meet the requirements to readout every single interaction in Pb–Pb collisions. Including a safety margin of a factor two with respect to the ALICE upgrade requirements, the new readout will be capable of a rate of 100 kHz to inspect Pb–Pb collisions, and 400 kHz for p+p measurements. Within the MAPS technology optimized to the needs of the ALICE Experiments, a binary readout without information on the charge signal amplitude is integrated directly on the readout chip. The ITSu detector will thus not have PID capabilities, because the marginal improvement of the foreseen measurements with possible ITSu PID was studied, and did not justify further consideration [20]. The new readout is optimized for a fast charge collection time and readout speed, while it maintains a low power consumption. The latter is driven by the low material budget requirements, which impose strong constraints on the available detector cooling material. The current design foresees water cooling of all seven ITSu layers, where the cooling pipes induce the highest, but local material budget $x/X_0 = 1.25\,\%$. For the inner barrel, an average material budget of $x/X_0 = 0.3\,\%$ is achieved, whereas the outer barrel has a slightly larger value of $x/X_0 = 1.0\,\%$, mainly due to the increased contribution to the material budget from the flexible printed circuit boards [20].

In addition, the ITSu is designed to be rapidly accessible during LHC shutdowns, independently of the removal of other subsystems such as the TPC. The current ITS detector can only be removed after complete extraction of the TPC. The geometric parameters of the upgraded ITS detector are summarized in table 3.1.

3.3.3.1. Monolithic Active Pixel Sensors

Recent developments in silicon pixel design allow the implementation of new silicon technology in particle physics experiments. The radiation tolerance of the doped silicon material was gradually improved, and the gate oxide thickness reduced. In addition the production of thin high-resistivity epitaxial layers became possible in the CMOS process.

	Inner Barrel			Outer Barrel			
	Inner Layers			Middle Layers		Outer Layers	
	Layer 0	Layer 1	Layer 2	Layer 3	Layer 4	Layer 5	Layer 6
Radial position (min.) (mm)	22.4	30.1	37.8	194.4	243.9	342.3	391.8
Radial position (max.) (mm)	26.7	34.6	42.1	197.7	247.0	345.4	394.9
Length (sensitive area) (mm)	271	271	271	843	843	1475	1475
Pseudo-rapidity coverage	±2.5	±2.3	±2.0	±1.5	±1.4	±1.4	±1.3
Active area (cm^2)	421	562	702	10 483	13 104	32 105	36 691
Pixel chip size (mm^2)	$15 \cdot 30$						
# of pixel chips	108	144	180	2 688	3 360	8 232	9 408
# of staves	12	16	20	24	30	42	48
Staves overlap in rϕ (mm)	2.23	2.22	2.30	194.4	243.9	342.3	391.8
Gap between chips in z (μm)	100						
Chip dead area in rϕ (mm)	2						
Pixel size ($\mu\mathrm{m}^2$)	$\mathcal{O}(30 \cdot 30)$						

Table 3.1.: Summary of the geometrical parameters of the upgraded ITS detector as it is presented in the TDR [20]. The pixel size was updated with recent developments [190, 191].The pseudo-rapidity coverage of the individual layers is computed with respect to the interaction point at $z = 0$ cm.

This allows a production of pixel structures, which include the front-end chip directly on the sensing pixel, opposite to the hybrid technology, where the two chips are interconnected by a bond (see figure 3.4).

Typically, standard pixel implementations of a sensing diode use an n-well. Any additional PMOS transistor, which would be necessary for more advanced hit discrimination and low power consumption, would be embedded into another n-well, acting as a competing diode and reducing the signal. With only NMOS transistors available within the matrix, the in-pixel circuitry is limited to simple amplifiers and hit discrimination circuits. The deep p-well circumvents the problem of the competing diodes, as demonstrated for a single transistor in figure 3.12, thus more sophisticated front-end circuits are possible. The availability of the deep p-well allows the implementation of complex logic in the pixel matrix, such that the insensitive area covered by digital circuitry at the periphery of the pixel matrix can be minimized. Improved routing of the metal layers also supports this approach. Further, the

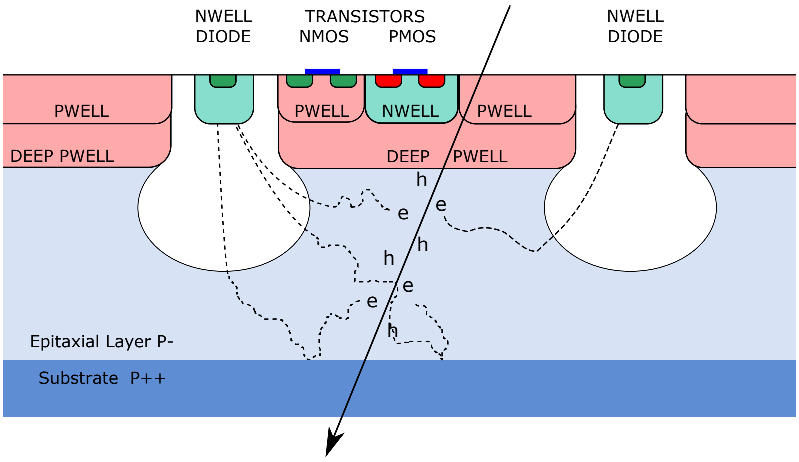

Figure 3.12.: Schematic view of a MAPS in the TowerJazz 180 nm CMOS Imaging Process on a high-resistivity epitaxial layer. The deep-p well allows the use of PMOS transistors within the pixel matrix enabling more complex in-pixel circuitry. This figure has been taken from [192].

combination of a high-resistivity epitaxial layer and a reverse substrate bias results in a larger depletion and thus faster charge collection, as well as in less trapping by material defects, induced by non-ionizing energy loss. The pixel itself is a reverse-biased diode. The electron-hole pairs induced by a charged particle diffuse in the epitaxial layer and eventually the electrons drift in the depletion zone to the sensing n-well diode [192]. However, the absolute amount of charge collected by the seed pixel also depends on the size and shape of the depletion volume. For increased thickness of the epitaxial layer the overall charge increases, but due to the limited size of the depletion zone, generated charges can spread over a larger area and may be shared among more pixels. The size of the depletion zone thus needs further optimization through a combination of doping concentration and reverse bias voltage, such that the absolute charge in the seed pixel is maximized. Another benefit of the increased depletion zone is the faster charge collection. The typical pixel size used in the development of the MAPS for the ALICE ITSu corresponds to $\mathcal{O}((28 \cdot 28)\,\mu\text{m}^2)$ and a thickness of the epitaxial layer of up to $40\,\mu$m.

3.3.4. Detector performance

Dedicated full Monte Carlo simulations of the current design options of the ITSu detector [20] have been carried out with an extended GEANT [193] simulation (see section 4.2). The pixel chip response was added, which is dependent on a few fundamental characteristics, independent of the actual pixel chip and front-end design. Taken from test beam data, the following parameters were set:

- The average pixel noise distribution is described by a Gauß-function (sometimes with an additional tail) distribution (depending on the chip design), with an average pixel noise of 17.53 electrons and a sigma of 2.93 electrons.

- The noisy pixel rate was evaluated after a threshold-over-noise cut at five.

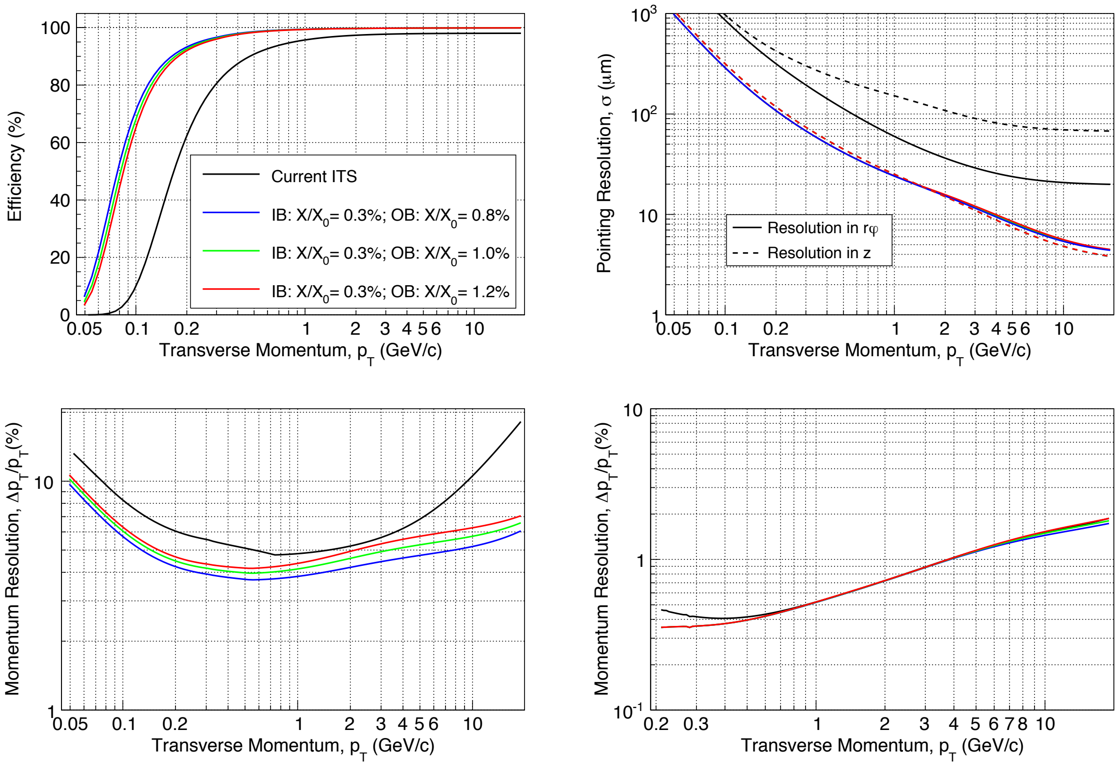

Figure 3.13.: Performance of the ITSu detector for charged pions, with different material thickness configurations in the outer barrel. The standalone track reconstruction efficiency and the pointing resolution are displayed in the upper two figures, whereas the momentum resolution for standalone ITS (left) and combined ITS+TPC tracking (right) tracking is displayed in the lower two figures. These figures have been taken from [20].

- The charge spread function was evaluated for each chip in the test beam and directly fed as input to the simulation.

In the following a square pixel of size $(20 \cdot 20)\ \mu\text{m}^2$ is used, not taking into account radiation damage and considering operation temperature of 30 °C. Further, simplified tracking tools were used to evaluate the performance of the new detector. These tools, the *Fast Estimation Tool* and the *Fast Monte Carlo Tool* will be explained in greater detail in section 4.3.1.

The performance of the new ITSu detectors, with different material-budget options of the final detector, is presented for charged pions in figure 3.13. The expected standalone tracking efficiency, shown on the top left, will be extended to lower momentum. Compared to the current ITS, the significant improvement is a consequence of the addition of one detection layer, as well as of the increased number of channels (all silicon pixel). The improvement of the pointing resolution, displayed on the top right, mainly comes from the significantly lower material budget of the new detector, as well as from the location of the first sensing region, closer to the interaction region. At 400 MeV/c the resolution improves by a factor 3 (5) in $r\phi$- (z-) direction to about 50 μm. The expected momentum resolution is shown for standalone ITSu (left) and combined ITS+TPC tracking (right) in

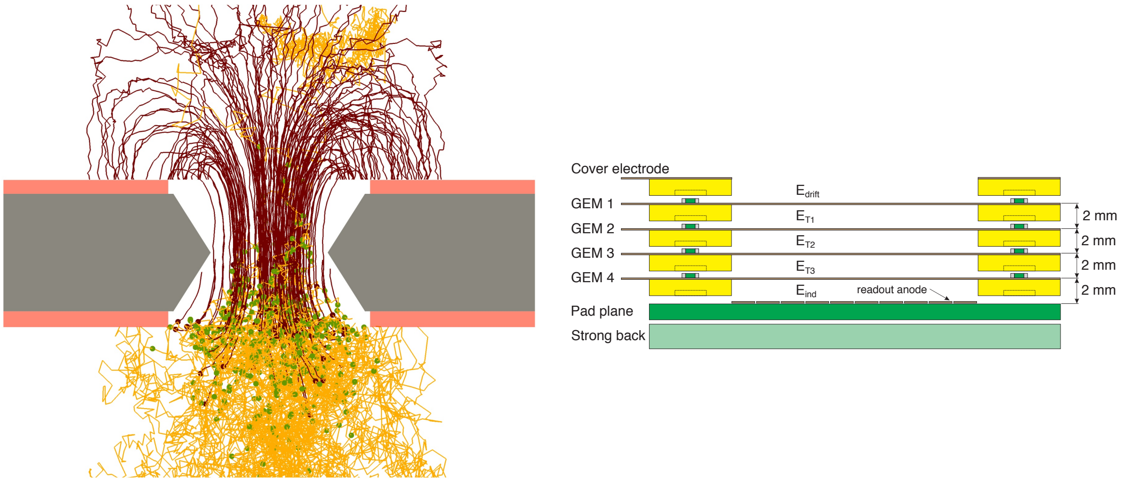

(a) **(b)**

Figure 3.14.: (a) displays the simulation of charge dynamics for two electrons entering a GEM hole. The location of ionization multiplication is indicated by green dots, whereas the drift paths of electrons (light orange) and ions (dark red) are presented as solid lines. A cross-sectional view of a quadruple GEM stack is presented in (b). The four GEMs may consists of different foil configurations, for example using Small Pitch (SP) and Large Pitch (LP) GEM foils in the order SP-LP-LP-SP. The electric fields are denoted E_{drift} for the drift region, E_{Ti} for the transfer fields between the foils and E_{ind} for the induction field between GEM 4 and the read out pad plane. These figures have been taken from [187].

the lower two panels. The improved resolution is crucial to extend the measurements of, for example, heavy-flavor mesons down to ultra-low momentum. For standalone ITSu tracking, a momentum resolution of about 4 % is achieved at 400 MeV/c. Note, that there is no significant dependence on the presented material budget options for the outer barrel (last four sensing layers). In these simulations, a detector resolution of (4 μm, 4 μm) is assumed.

3.3.5. Upgrade of the Time Projection Chamber

As the ALICE upgrade strategy foresees to inspect all Pb–Pb interactions at a rate of 50 kHz, the ALICE TPC must be upgraded as well in order to maintain the detector's particle identification capabilities and momentum resolution. With the aim of a continuous readout, the current gating grid operation of the TPC is no longer possible, which motivates the complete replacement of the MWPC readout with Gas Electron Multiplier technology (GEMs), as they intrinsically suppress the ion back flow (IBF) into the drift volume. A simulation of electrons entering a GEM hole is displayed in figure 3.14a, where the gas multiplication occurs in the lower half of the hole. Most of the generated ions drift to the GEM surface, where they are absorbed. The space-charge distortions of the electric field, induced by the back-drifting ions, are tolerable to an upper limit of 1 % at a gas gain of 2 000, where they stay below 10–20 cm and can be calibrated to sufficient precision of a few hundred μm. These distortions appear static in time intervals of about 5 ms, which correspond to the rate at which they must be corrected. In addition, the limited bandwidth of the data acquisition systems requires a significant reduction of the online data by a factor of about 20. The current readout chamber design, displayed in figure 3.14b,

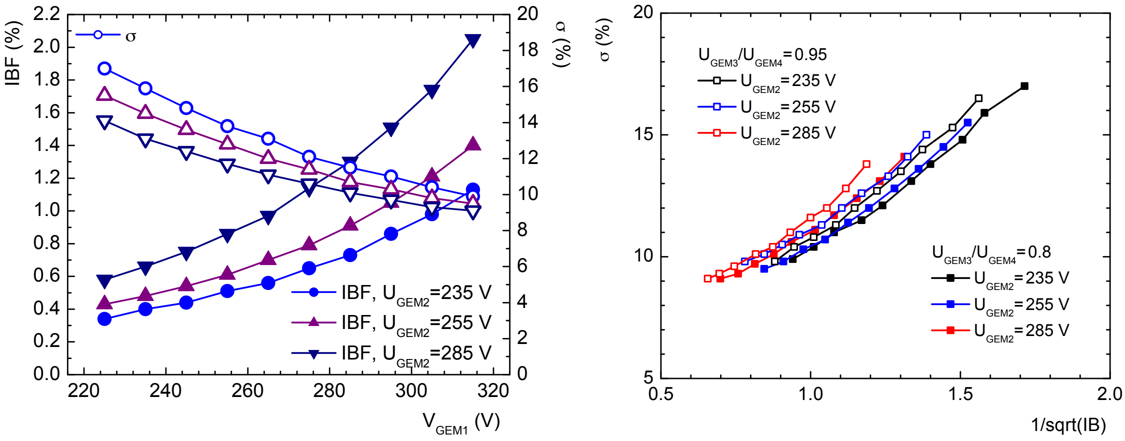

Figure 3.15.: On the left, the energy resolution and ion back flow performance of a quadruple GEM stack is shown for various voltage settings. The correlation between energy resolution and IBF (denoted as IB in the figure) is presented on the right. These figures have been taken from [187].

foresees a GEM stack of four foils, where the inner two foils consist of GEM foils with a pitch of 280 μm (Large Pitch (LP)), opposite to the two remaining foils, which have a pitch of 70 μm (Small Pitch (SP)). The benefit of the LP foils lies within their smaller optical transparency, which means that they block ions more effectively. Typical high voltage settings, which corresponds to a gas amplification of 200 and an efficiency of $\epsilon < 20$ back-drifting ions per electron, are 3 150 V, 2 080 V, 1 430 V and 1 140 V, going from the top to the bottom plane. However, the final design and configuration is still under development. The performance of a quadruple GEM stack with this configuration is shown in figure 3.15, as a function of different potential difference between the two sides of a foil $(\Delta U_{\mathrm{GEM1}} = U_{\mathrm{GEM1top}} - U_{\mathrm{GEM1bot}}, \Delta U_{\mathrm{GEM2}} = U_{\mathrm{GEM2top}} - U_{\mathrm{GEM3bot}}, ...)$. Even though the ultimate goals of 1 % IBF and optimal energy resolution of about 6 % are not yet reached, the slope of the dependencies and correlations, as well as the flexibility in the choice of operation parameters, indicate that the design parameters are well within reach.

4. Monte Carlo and data generation, simulation and reconstruction in ALICE

Full Monte Carlo (MC) simulations are a class of computational algorithms, which rely on repeated, random sampling of numerical results. As such, they are an ideal tool to study common processes in high-energy physics. A famous recent example of their application is the discovery of the Higgs boson at the LHC by ATLAS and CMS [36, 37], where MC simulation were not only used to generate physics events based on the known Standard Model processes, but also to determine the detection sensitivity to the different physics processes. The results were then compared to combinations of measured data in expected decay channels of the boson and revealed a significant excess in the invariant mass spectrum through the newly discovered particle.

Also in ALICE, detailed full MC simulations of hadron-hadron collisions and the subsequent transport through a realistic description of the geometry of the apparatus are used for example to determine the acceptance of the detector and the reconstruction efficiency on physics processes such as open heavy-flavor decays, jets, heavy nuclei, photons, and many others. Further, they are used to obtain realistic estimates of the performance of planned detector concepts and are thus a crucial ingredient for the development and optimization of new devices, such as the upgraded ITS [186, 20].

Within ALICE, the ROOT-based AliRoot framework is used, which incorporates the raw data readout, interfaces to Monte Carlo event generators and the full calibration as well as physics analysis algorithms [194, 195, 196]. As visible in figure 4.1, the conceptual flow within ALICE from physics generation to an analyzable format is structured into three major stages: *Event Generation*, *Simulation* and *Reconstruction* [197, 198]. In this section, all three stages will be explained in detail, with a focus on the general track reconstruction. Further, within this thesis a new fast simulation tool (FT2) was developed based on existing approaches and with input from other members of the collaboration [199, 200, 201, 202]. Additional information on full MC reconstruction and actual data recording in ALICE is collected here: [156].

4.1. Monte Carlo generation of physics processes in heavy-ion collisions

In order to evaluate the performance of, for example, the full kinematic reconstruction of heavy-flavor meson decays such as $\mathrm{B}^+ \to \overline{\mathrm{D}}^0\pi^+$ ($\overline{\mathrm{D}}^0 \to \mathrm{K}^+\pi^-$), large-statistics samples of dedicated MC simulations are necessary, which are required to analyze the detector response to the expected physics signal on top of the particle background generated in

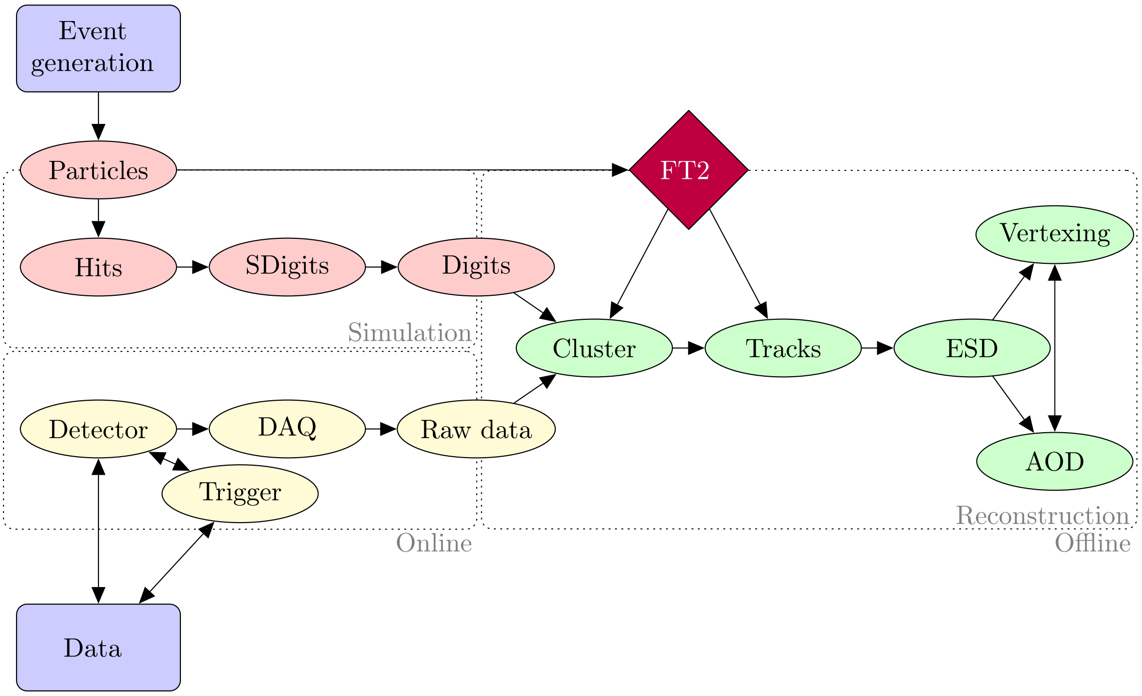

Figure 4.1.: Flow chart of the simulation and data reconstruction scheme in ALICE. In addition, the conceptual approach of a newly developed fast simulation tool (FT2) is presented.

the hadron-hadron collisions. The *Heavy-Ion Jet INteraction Generator* (HIJING) [203] is specifically designed for the simulation of nucleus-nucleus collisions. Here, perturbative-QCD inspired models for multiple jet productions are combined with low p_{T} multistring phenomenology to simulate background processes. Even though these are not part of the predicted strongly interacting medium, these interactions may already lead to a variety of correlations and features unrelated to the QGP, such as kinematic or multi-particle correlations in the azimuthal distribution. Such effects must be considered in order to extract QGP observables, such as the nuclear modification factor R_{AA} and the elliptic flow v_2, in a realistic approach.

For correct event multiplicity estimates, typically Glauber model calculations are employed [55] (section 2.3.1). For the analysis of specific rare probes, such as the B^+ decay, the signal is injected at an artificially high rate on top of the actual HIJING background event, such that the simulation of the signal can be analyzed with an acceptably low statistical uncertainty and without introducing a significant bias of the event multiplicity. For such purposes, typically the particle generator PYTHIA [204], which is normally used to generate p+p collisions, is employed to simulate realistic particle momentum spectra and angular distributions. The drawback of this method is, that a specific scaling factor has to be evaluated, which normalizes the injected particle yields back to the expected realistic cross-section. Even more simple approaches are justified and may be used for efficiency and performance estimation, for example as used in section 5.2.2, where the generation of particles with a flat p_{T} distribution leads to a homogenous amount of generated statistics, even at high-p_{T}. In addition to these approaches, specific decay channels or other physics processes can be enforced, to further enhance the probability of the occurrence of the studied signal in the simulation.

The result of the generation step is stored in a kinematic tree[i], which carries the complete production history. Besides the kinematic information of all generated particles, this tree contains the information on the relationship between particles (mother ↔ daughter) and their specific production vertex up to the quark and gluon level. It is subsequently used by a *transport package*, which propagates the particles through the detector and estimates the interaction with the material of the device structures.

Notice, that despite the fact that the generation of HIJING background processes of Pb–Pb collisions usually takes a few seconds per event, the subsequent simulation and transport through the experimental setup is extremely demanding on computing resources in terms of processing time and storage. Typically, a single (central) Pb–Pb collision generates around 10^5 particles, which are then propagated and reconstructed in the ALICE detector geometry. In addition, secondary (weak) decays of (strange) particles, material interaction and particle production by radiative processes are computed by the transport package, which increases the processing time per event to several thousands of seconds. For Pb–Pb collisions of 0–10 % centrality, typically a few 10^3 reconstructed tracks per event remain in the acceptance of the central barrel detectors, passing the track quality cuts (see section 5.1.2.1). These track quality cuts consist of different selection criteria such as the number of charge clusters generated in the (upgraded) ITS, and are applied in the analysis in order to maintain a good precision on the parameters of the reconstructed track as well as to have a well defined set of tracks.

4.2. Full detector simulation and central barrel track reconstruction

Once the particles are generated and the kinematic tree is available, the transport package is used to propagate the particles through the detectors and eventually takes into account the interaction with the material, as well as particle decays. Here, a complete and realistic description of the full geometry of the devices is mandatory in order to evaluate their acceptance and performance, as well as their general impact on the measurement. Within the virtual Monte Carlo [206] framework used by ALICE, GEANT3 [193], Geant 4 [207] and the FLUKA [208] MC transport packages are available to simulate the passage of particles through matter, where GEANT3 is the default option.

As outlined in figure 4.1, when the generated particles are transported through the detectors, so-called *hits* are created, which reflect the energy deposition at a given space point in the active detector volume. The original particle label information is kept for reference and allows for precise book-keeping of interaction processes for each particle. For each track passing the sensitive volume of a detector the corresponding detector response is used to convert the *hits* into *(summable) digits*. For *summable digits*, no noise-suppression thresholds are applied, such that they remain additive and can be used for event merging [197]. Simulated *digits* contain similar information as *raw data*, as they are generated based on realistic detector thresholds on top of noise simulations and are eventually reconstructed into tracks. The

---

[i] Here, a tree is a ROOT class [205], which is designed to hold any kind of ROOT data. It is optimized for reduced disk space and enhanced access speed.

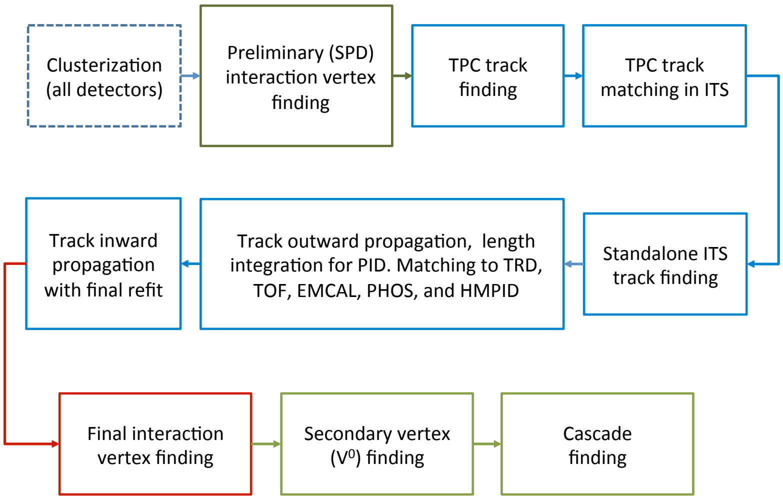

Figure 4.2.: Schematic view of the track finding and reconstruction algorithm in the ALICE Experiment. The concept follows an inward-outward-inward scheme. This figure has been taken from [156].

same reconstruction code can be used for *digits* and *raw data*, which provides a one-to-one test framework for the reconstruction code. Typically, in full MC, *digits* are reconstructed into *clusters*, while in real data *raw data* is mostly reconstructed directly into *clusters*, which hold the information on signal amplitude and time as well as their position and associated uncertainties. These clusters serve as input to the track filtering technique based on a Kalman filter [209]. The working principle of the Kalman filter technique as well as the application and arising track uncertainties in ALICE are explained in greater detail in section 4.2.1, as they are also a crucial ingredient in the FT2 development. The space points of a cluster are defined at the crossing point of a matched track and the center of the corresponding sensitive plane [156]. Due to the high charged-particle densities per unit of (pseudo-)rapidity in central Pb–Pb collisions, e.g. $\mathrm{d}N_{\mathrm{charged}}/\mathrm{d}\eta = 1\,601 \pm 60$ measured in $|\eta| < 0.5$ for 0–5 % centrality at $\sqrt{s_{\mathrm{NN}}} = 2.76\,\mathrm{TeV}$ [210], clusters from different tracks can overlap and eventually merge. Additionally, space-charge distortions and imperfections in the electric and magnetic fields in the central barrel ($\vec{\mathrm{E}} \times \vec{\mathrm{B}}$) significantly displace space points by up to 1.3 cm in radial and transverse direction along the drift length in the TPC (section 4.3.8.4), which leads to inefficiencies near the sector edges of the detector.

In the first step of the reconstruction stage, as indicated in figure 4.2, an estimate of the primary interaction vertex is determined based on the information of the two inner SPD layers and track finding is started [156]. Here, an inward-outward-inward scheme is followed, which is one of the most challenging and fundamental tasks in the experiment. Note, that kink topology finding is used during all three stages. A kink is a distinct, small-angle deflection and may be visible for example in the trajectory of a charged kaon, which decays into a muon and a neutrino [156].

In the first iteration, tracking is performed from the TPC to the ITS and the information is used to updated preliminary primary vertex position. Beginning at the large outer radius of the TPC, the first track seeds are built based on the information of two reconstructed TPC clusters and the interaction vertex. These seeds are further propagated inwards along the nearest clusters, which respect a proximity cut [156]. It is possible that a cluster may be used for multiple different seeds and thus a single track could be reconstructed several times. This feature is suppressed by an algorithm, which compares two tracks with a large fraction of common clusters. Based on different quality criteria, such as the number of clusters for a corresponding track momentum, the worse candidate is rejected [156].

Out of the 159 possible clusters per track in the TPC, it is required that the seed contains at least 20 TPC clusters, indicating that it must have passed though at least about one third of the length of the inner readout chamber. In addition, a miss-rate of less than 50 % compared to the expected number of clusters, which is based on the track position within the detector. The track candidates are propagated towards the inner TPC radius, and based on the specific energy loss in the TPC, the mass of the most probable particle identity is assigned (as described in section 3.2.2). From this point on, this mass assignment is used for the estimate on ionization energy loss and multiple scattering during the propagation of the seed. The pion mass is assigned as default assumption, because the ambiguity of the electron identification does not allow a clean identification. Details will be discussed in section 4.3.8.

Propagated to the outermost layer of the ITS, the TPC tracks serve as seeds for the ITS track finding. Within the ITS, the seeds are propagated inwards layer-by-layer using clusters within a proximity cut in the sensitive areas. After each step, the information on the track position and the uncertainty are updated and saved as a new seed. In case a given seed is missing in a detection layer, for example as a consequence of a noise threshold in the device, an additional penalty factor is assigned to the χ^2 of the seed. Once generated for all TPC tracks, the complete set of prolongated candidates in the ITS is sorted according to the values of χ^2_{red}. Shared clusters are evaluated and tried to be resolved by finding alternative candidates of the conflicting track hypotheses. If this is unsuccessful, the track with the worst quality is labeled as containing a (potentially) fake cluster. The consequences will be evaluated in section 4.3. The highest quality track candidate from each set of hypothesis is added to the reconstructed event and after the complete reconstruction in the ITS the tracks are propagated to the distance of closest approach with respect to the preliminary primary vertex. From this point, all tracks are propagated outward along the previously determined clusters. At the outer radius of the TPC the propagated tracks are attempted to be paired to TRD track segments (*tracklets*) in each of the six stacked TRD layers and afterwards matched to the clusters of the TOF subsystem. The integrated track length and time-of-flight are computed step-by-step for different species assumptions (e, μ, π, K, p) in the particle identification with TOF. The tracks are further matched with the signals of other subsystems in the ALICE central barrel, e.g. EMCal, PHOS and HMPID.

In the last stage, the tracks are refitted inwards with the Kalman filter beginning at the outer TPC radius and using the previously determined clusters, and the track parameters (position, direction, inverse curvature) and the corresponding covariance matrix are determined, as outlined in the following section 4.2.1. Based on this information the final primary vertex is evaluated and further algorithms, e.g. the secondary vertex reconstruction, are invoked. All track information is stored in the *event summary data* (ESD), which also includes

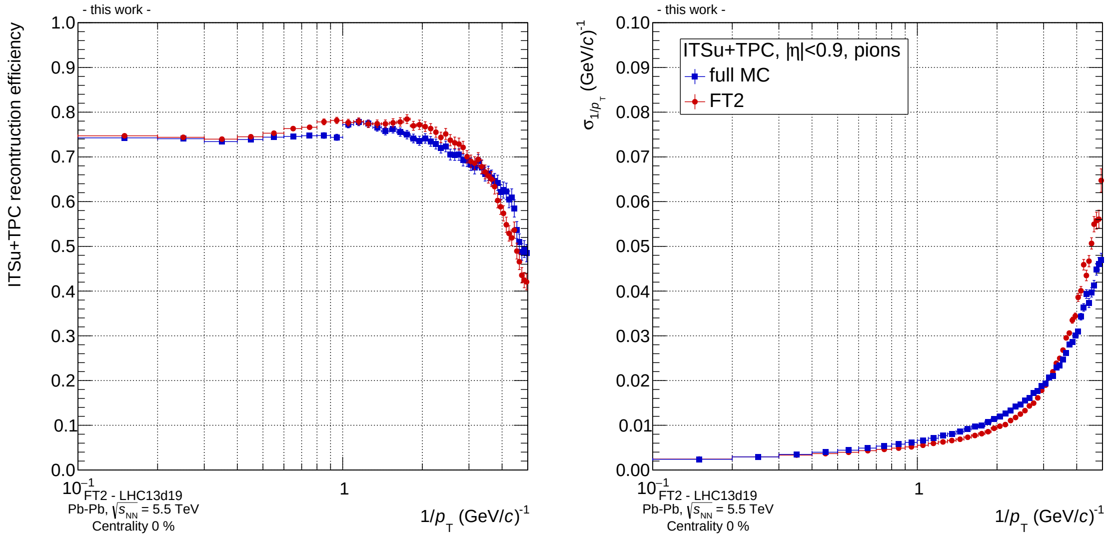

(a) (b)

Figure 4.3.: (a) displays the track finding efficiency for ITS+TPC combined tracks of primary pions within $|\eta| < 0.9$. The corresponding inverse transverse momentum resolution is displayed in (b). In both figures, the performance of the full MC (blue squares) and the FT2 (red circles) are shown respectively.

the complete particle identification information of the various (central barrel) subsystems. Further, all information needed during the physics analyses, such as run and event number as well as the primary vertex are stored. These ESDs are compressed to *analysis object data* (AOD), which is meant as a more general input. These AODs can be accompanied by a so-called *friend*, which contains further case-specific information. For example, a selection of reconstructed secondary vertices with a high probability to originate from heavy-flavor decays of charmed or beauty mesons and baryons may be stored.

The performance of the reconstruction chain is demonstrated in figure 4.3a, where the track finding efficiency for the upgraded ITS and TPC combined tracks for primary pions in simulations of 0 % central Pb–Pb collisions is shown as a function of inverse transverse momentum. Here, full Monte Carlo simulations are compared to the new fast simulation (FT2), which will be explained in detail in section 4.3. The particle identification is performed via the true information from the MC simulation. In both approaches, the efficiency for transverse momentum higher than about 1.0 GeV/c is dominated by cluster losses of a track in the TPC: When the trajectory is projected in the transverse plane onto the endcaps of the TPC, an increasing fraction of clusters is located within the dead zones between the individual TPC sectors, which are not covered by readout pads and correspond to the support structure of the TPC readout chambers. While tracks with lower momentum have a larger curvature and only a fraction of clusters is contained in these gaps, tracks at larger momentum are stiffer and may be lost entirely in these dead zones. In addition, $\vec{\mathrm{E}}\times\vec{\mathrm{B}}$-distortions may shift charge clusters in (and out of) these areas. For momentum below 500 MeV/c, part of the tracks are lost due to the interaction of particles with the detector material. For even lower momentum, the magnetic field strength limits the p_{T} reach as the trajectories do not leave a large enough signal in the TPC to be reconstructed reliably. For

example, primary pions with less than 200 MeV/c just reach the outer radius of the TPC, whereas secondary electrons can be tracked down to $p_{\mathrm{T}} \geq 60\,\mathrm{MeV}/c$.
The inverse transverse momentum resolution for combined ITSu+TPC tracks is displayed in figure 4.3b for full MC and FT2. Here, the difference between the reconstructed track momentum and the true kinematic information in the MC simulation was fitted for each p_{T}-bin with a Gauß-function. Generally, the resolution decreases with inverse transverse momentum due to the reduced curvature of the trajectory in the magnetic field of the experiment. The performance in central Pb–Pb collisions is slightly worse for high momentum than in p+p or p–Pb collisions, due to an increased fraction of cluster overlaps, fake clusters and clusters within ion tails [156]. In addition, energy loss and multiple scattering cause a slight increase of the resolution for low momentum. Despite a small deterioration of the FT2 for low p_{T} tracks, which is due to a slight overestimation of the energy loss, good overall agreement is observed in the comparison to the full MC simulation. The performance of the fast simulation is evaluated at a later stage in section 4.3.9.2.

4.2.1. Kalman filter technique

The *Kalman filter* is one of the most well-known and frequently used mathematical tools for stochastic estimation from (noisy) measurements [211]. It was first published in 1960 by its inventor Rudolph E. Kalman, who described a new, recursive solution to the linear filtering problem of discrete data. The algorithm has been continuously extended and appears these days in a large variety of technological applications, such as navigation, guidance and control of vehicles, et cetera [212]. It was introduced into the field of high-energy and heavy-ion physics in 1987 [209]. Since then it is commonly used for track finding and filtering as well as vertex reconstruction. Especially in the environment of high track densities in (central) heavy-ion collisions, as in the ALICE Experiment, efficient and reliable track finding and reconstruction is among the most challenging tasks. Here, the Kalman filter comes along with substantial advantages [213]:

- It is capable of simultaneous track recognition and fitting.
- Incorrectly selected space points are rejected *on-the-fly* based on the value of the actual calculated χ^2.
- Multiple scattering, energy loss and other distortions of tracks are addressed as simple additions to the track uncertainties (section 4.2.3).
- Significant multiple scattering leads to correlations in the track measurement and eventually to operations on large error matrices. Although calculated separately for each measurement (cluster) of a track, the Kalman filter used in ALICE relies on a five-dimensional vector of the track parameters (section 4.2.2), and thus only needs to manipulate 5×5-matrices for the uncertainty calculation. This approach significantly speeds up the algorithm compared to computations with larger error matrices [214].
- Extrapolation between the sensitive areas of different, sequential detector subsystems is straightforward [209], as the local estimate in the Kalman filter is often more precise in the trajectory prolongation than the averaged, global estimate [214].

Despite these benefits, the approach also suffers from some major disadvantages, which need to be treated carefully [209, 213]:

- In order to provide a reliable performance, the algorithm requires on good initial track seeds.
- Large dead zones, where no cluster information is available, are present between the different detectors as well as within some subsystems, for example between the individual sectors of the TPC. As a consequence the track finding and extrapolation is more complicated and the performance may degrade.

In ALICE these challenges are overcome by starting the track seeding at the outer radii of the TPC, where the track density is reduced compared to radii closer to the beam pipe [213]. This allows for a realistic initial approximation of the state vector and its error matrix at the start of the filtering algorithm [215]. By design of the algorithm presented in figure 4.1, the second problem is addressed intrinsically: The full cluster information of the subsystems is obtained from the raw data (or digits) in the first step of the offline reconstruction, just before tracks are built. Note, that the formulas and explanations in the following section were taken from [209, 211, 216, 213, 214, 215].

The general principle of the Kalman filter is based on a recursive feedback control between the *prediction* and *correction* of a given state vector x_k at a time t_k. Whereas in the former the (time-)forward projection of the current state and corresponding uncertainty is predicted for the next step, the latter serves as a feedback by inclusion of new measurements into the estimate. The optimal result is computed after the addition of the final measurement. The prediction for a given system, e.g. the particle trajectory within a large distribution of clusters, is based on a known deterministic function f_k, which propagates the state vector from time t_{k-1} to t_k, where a new measurement m_k is made:

$$x_k = f_k(x_{k-1}) + \epsilon_k, \text{ and} \tag{4.1}$$

$$m_k = h_k(x_k) + \delta_k. \tag{4.2}$$

Here, ϵ_k describes the noise with zero mean value ($\langle\epsilon_k\rangle = 0$) and the known covariance matrix $Cov(\epsilon_k) = Q_k$. Note, that within ALICE an *extended* Kalman filter is used, which is capable of handling non-linear processes as it linearizes the estimation around the current estimate via partial derivatives of h_k in the Jacobian matrix H_k [211]. The measurement itself is a linear combination of the state vector $h_k(x_k)$ and the noise δ_k, where no bias is assumed ($\langle\delta_k\rangle = 0$) and covariance matrix $Cov(\delta_k) = V_k$. In the case the measurement does depend linearly on x_k it has to be linearized, where x_0 is the point of linearization. Thus equation 4.2 becomes

$$m_k = h_k(x_k) + \delta_k \approx h_k(x_k) + H_k(x_k - x_0) + \delta_k, \tag{4.3}$$

$$\text{where } H_k = \left.\frac{\partial h_k(x_k)}{\partial x_k}\right|_{x_k = x_0}. \tag{4.4}$$

In case the linearization is taking the current solution x_k, the residual is similar to the classical Kalman filter [217]. The true value of x_k is of course not known because the step-wise noise cannot be determined at each iteration, but $\tilde{x}_k$ serves as an estimate with the assumption that the noise is zero. In order to obtain stable and optimal results, the fitting procedure has to be iterated several times, as it is the case for the ALICE inward-outward-inward scheme. In the prediction from t_{k-1} to t_k, the non-linear difference of the current state vector and the covariance matrix ($\tilde{C}_k$) are then estimated as [214]

$$\begin{aligned}\tilde{x}_k^{k-1} &= f_k\left(\tilde{x}_{k-1}\right), \text{ and} && (4.5)\\ \tilde{C}_k^{k-1} &= F_k\tilde{C}_{k-1}F_k^T + Q_k, && (4.6)\\ \text{where } F_k &= \frac{\partial f_k}{\partial x_{k-1}} \text{ is a Jacobian matrix.} && (4.7)\end{aligned}$$

The corresponding predicted χ^2-increment, which is used in ALICE to reject wrongly assigned cluster, is calculated as

$$\begin{aligned}\left(\chi^2\right)_k^{k-1} &= \left(r_k^{k-1}\right)^T\left(R_k^{k-1}\right)^{-1} r_k^{k-1}, && (4.8)\\ \text{where } r_k^{k-1} &= m_k - H_k\tilde{x}_k^{k-1}, && (4.9)\\ \text{and } R_k^{k-1} &= V_k + H_k\tilde{C}_k^{k-1}H_k^T. && (4.10)\end{aligned}$$

In the correction step, after the subsequent measurement is performed, the new information is included in the current prediction to improve the vector estimate:

$$\begin{aligned}\tilde{x}_k &= \tilde{x}_k^{k-1} + K_k\left(m_k - H_k\tilde{x}_k^{k-1}\right) && (4.11)\\ \tilde{C}_k &= \tilde{C}_k^{k-1} - K_kH_k\tilde{C}_k^{k-1}, && (4.12)\\ \text{and } K_k &= \tilde{C}_k^{k-1}H_k^T\left(V_k + H_k\tilde{C}_k^{k-1}H_k^T\right)^{-1} && (4.13)\end{aligned}$$

Here, K_k is the *Kalman gain matrix* and $\left(m_k - H_k\tilde{x}_k^{k-1}\right)$ the *residual* or *innovation.* The gain is an indicator for the behavior of the filter: a low gain indicates that the filter follows a model prediction more precisely, which allows to smooth out noise more effectively, but the filter is less responsive to the measurement updates. The χ^2-increment evolves to

$$\begin{aligned}\chi_k^2 &= \left(r_k\right)^T\left(R_k\right)^{-1} r_k, && (4.14)\\ \text{where } r_k &= m_k - H_k\tilde{x}_k, && (4.15)\\ \text{and } R_k &= V_k - H_k\tilde{C}_kH_k^T. && (4.16)\end{aligned}$$

The recursive behavior of the algorithm described above is summarized in figure 4.4. The application of the Kalman filter in the ALICE tracking procedure is outlined in the subsequent section.

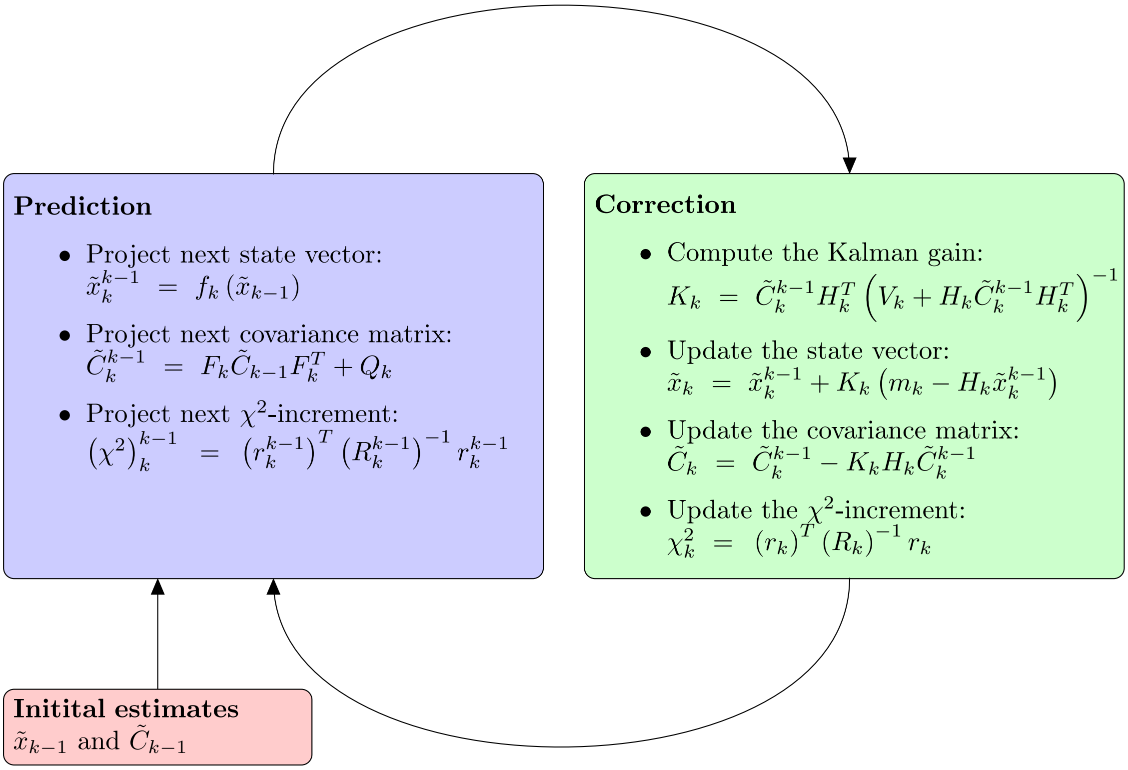

Figure 4.4.: Diagram of the recursive extended Kalman filter algorithm. At the first step, initial estimates of the state vector and the covariance matrix have to be provided. Then, the Kalman filter enters the recursive loop of *prediction* and *correction*, until it was updated with all available measurements. The optimal result is computed after the addition of the final measurement.

4.2.2. ALICE tracking procedure

As described before, the recursive Kalman filter algorithm improves in precision with each measurement (cluster), which is included. For the ALICE tracking, where an inward-outward-inward scheme is employed, this means that in the first inward stage the best estimates of the track state vectors are available after all tracks are propagated to the preliminary primary vertex. Given that the inward tracking was started with the seeds at the outer TPC radii, the uncertainty is largest there, thus a subsequent outward propagation is necessary in order to update also these measurements to their best values. The updated state vector and its covariance matrix can then be used for further prolongation into other central barrel subsystems, such as TRD and TOF. In the final stage, the tracks are propagated inwards again to obtain best possible information for secondary tracks from V^0, kink and cascade decays [156].

4.2.2.1. Track model

Given these considerations, it is clear that the Kalman filter essentially relies on a well defined propagation function with a corresponding state vector. As outlined in section 3, the detectors of the ALICE central barrel are placed in a homogenous, solenoidal magnetic field, typically of strength $\mathrm{B} = 0.5\,\mathrm{T}$. In addition, an electric drift field $\vec{\mathrm{E}}$ in z-direction (parallel to the beam axis) is applied in the TPC. Neglecting material effects, and assuming the propagation in vacuum, the equation of motion of a particle with mass m and charge q can be derived from the Lorentz force [218]:

$$\frac{d\vec{p}}{dt} = \frac{d\left(m\gamma \cdot d\vec{x}/dt\right)}{dt} = c^2\kappa q\left(\vec{v}\left(t\right) \times \vec{B}\left(\vec{x}\left(t\right)\right)\right), \tag{4.17}$$

where γ is the Lorentz factor, $\vec{x}$ the space point of the particle and κ a proportionality factor. Using the path length of the trajectory $s\left(t\right)$ where $ds/dt = v$ and $p = |\vec{p}| = |\gamma m\beta c|$, equation 4.17 is expressed in geometrical quantities as

$$\frac{d^2\vec{x}}{ds^2} = \kappa\left(\frac{q}{p}\right)\left(\frac{d\vec{x}}{ds} \times \vec{B}\left(\vec{x}\left(s\right)\right)\right). \tag{4.18}$$

Further employing the relation

$$\left(\frac{dx}{ds}\right)^2 + \left(\frac{dy}{ds}\right)^2 + \left(\frac{dz}{ds}\right)^2 = 1, \tag{4.19}$$

five free parameters are remaining. Eventually, under these conditions in the experiment, the equation of motion is described by a helix parallel to the beam axis. The free parameters and the state vector are defined such, that the propagation of the helix is performed between any two reference surfaces, which are planes parallel to the global z-axis separated by a given step size. This helix describes a circle in the transverse plane and a straight line in longitudinal direction, which leads to one equation for each coordinate direction in a local coordinate system:

$$\begin{aligned} x^{'} &= x_0^{'} - R\cos\left(t+t_0\right), && (4.20)\\ y^{'} &= y_0^{'} - R\sin\left(t+t_0\right), && (4.21)\\ z^{'} &= z_0^{'} - R\tan\left(\lambda\right)\left(\theta_{k+1}\right), && (4.22)\\ \text{using } \theta &= \frac{\Delta s}{2\pi R_H}, \text{ where } \Delta s \text{ is the arc length}, && (4.23)\\ \phi &\in [-\pi/2, \pi/2] \text{ and } R = \sqrt{x^2+y^2}. && (4.24) \end{aligned}$$

Here, $\left(x_0^{'}, y_0^{'} = y\left(x_0^{'}\right), z_0^{'} = z\left(x_0^{'}\right)\right)$ are the coordinates of the center of the curvature $C = 1/R_H$ and $\tan\left(\lambda\right)$, which corresponds to the pseudo-rapidity of the track and is measured between the slope of the track in z-direction and the transverse plane. Here, λ is the so called *dip angle*. It is more convenient to use the curvature instead of the radius R_H, as the corresponding uncertainties are assumed to follow a Gauß-distribution, independently of the lever arm of the detector and particle momentum [219]. The corresponding five-dimensional state vector

$$\vec{x}^T = \left(y^{'}, z^{'}, \sin\left(\phi\right), \tan\left(\lambda\right), q/p_{\mathrm{T}}\right) \qquad (4.25)$$

needs to be updated in two components during propagation, namely *y'* and *z'*, and has a 5 × 5 covariance matrix attached. Here, q is the charge of the tracked particle. A schematic view of the transverse plane of the coordinate system during propagation is shown for an individual, charged track in figure 4.5. The procedure is as follows [220] [215]: Each cluster is assigned to three global coordinates $\left(X_{cl} = R\cos\left(\phi\right), Y_{cl} = R\sin\left(\phi\right), Z_{cl}\right)$ in the ALICE coordinate system in the reconstruction. In the Kalman filter algorithm, the tracks are propagated across the sensitive detecting areas, e.g. the TPC pad rows, along these clusters. Note, that there is a chance that a cluster is rejected via the χ^2-selection, or is simply missing. For the propagation, the global coordinate system is rotated into a local coordinate system via the angle α, which corresponds to the global Φ position of the center of the TPC sector. The origin of the coordinate system is defined as the *ideal* interaction point of the colliding beams at (0,0), but does not necessarily correspond to the true interaction point and/or particle origin.

As indicated in figure 4.5, and depending on the track curvature, it is possible that a track passes two or more TPC sectors during its propagation. Thus the tracks are updated at the cluster position evaluated in the local coordinate system $\left(x_{cl}^{'}, y_{cl}^{'}\right)$. The track has to be extrapolated by $\Delta x^{'} = x_{k+1}^{'} - x_k^{'}$ for each propagation step with the helix model. From the relation

$$\begin{aligned} \tan\left(\phi\right) &= \frac{\partial y^{'}}{\partial x^{'}} = \frac{\partial y^{'}}{\partial \theta}\Big/\frac{\partial x^{'}}{\partial \theta} = -\frac{1}{\tan\left(\theta\right)} && (4.26)\\ & && (4.27) \end{aligned}$$

it is derived that

$$\sin\left(\phi\right) = -\cos\left(\theta\right). \qquad (4.28)$$

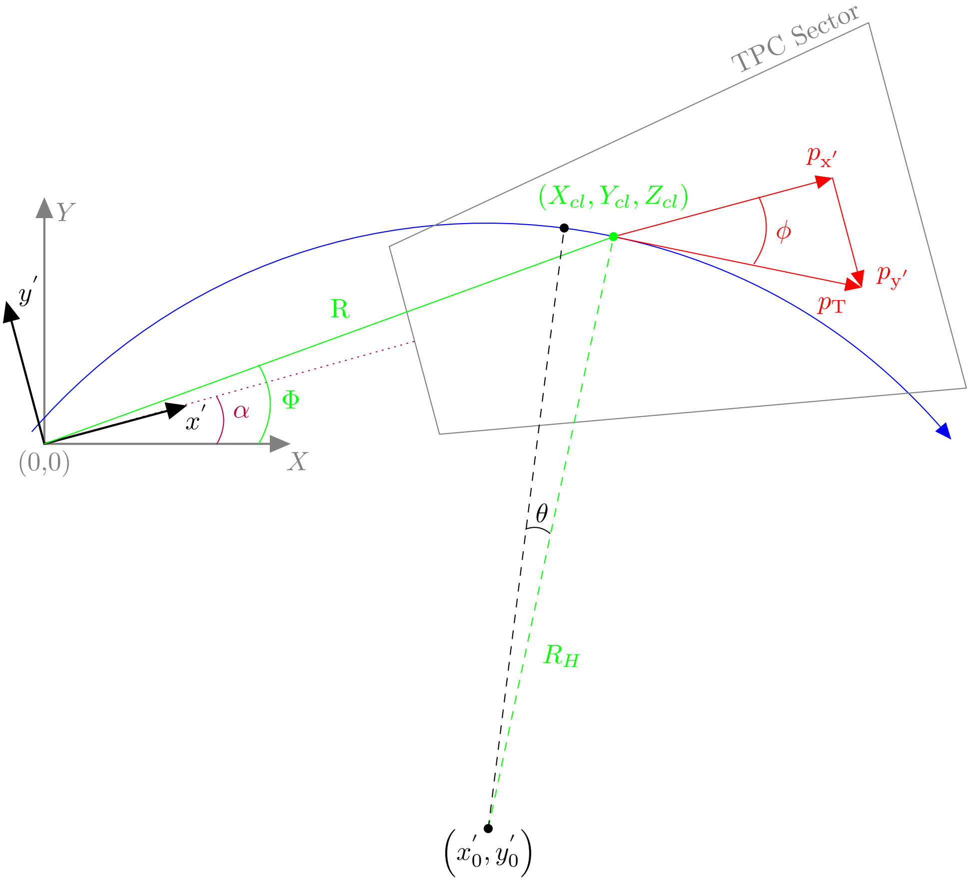

Figure 4.5.: Schematic view of the global and local ALICE coordinate system. The global coordinate system (X, Y, Z) is rotated into the local coordinate system (x', y', z') of a given TPC sector by α. The particle itself is propagated with a given step length along a helix trajectory, which is updated along the space points (X_{cl}, Y_{cl}, Z_{cl}) of the measured clusters.

For each step the complete state vector is thus updated according to

$$\Delta y' = y'_{k+1} - y'_k = R_H \left(\sqrt{1 - \sin(\phi_k)^2} - \sqrt{1 - \sin(\phi_{k+1})^2} \right) \tag{4.29}$$

$$\begin{aligned} \Delta z' &= z'_{k+1} - z'_k = R_H \tan(\lambda) \cdot \theta \\ &= R_H \tan(\lambda) \\ &\quad \cdot \sin \left(\sin(\phi_{k+1}) \sqrt{1 - \sin(\phi_k)^2} - \sin(\phi_k) \sqrt{1 - \sin(\phi_{k+1})^2} \right)^{-1} \end{aligned} \tag{4.30}$$

and

$$\Delta \sin(\phi) = \cos(\theta_k) - \cos(\theta_{k+1}) = \frac{\Delta x'}{R_H}. \tag{4.31}$$

The equations are expressed as a function of $\sin\left(\phi_{k/k+1}\right)$, as it is part of the state vector and makes the computation more performant. The curvature $C = \frac{1}{R_H}$ is measured via the transverse momentum p_{T} in the homogenous magnetic field $B_z = |\vec{B}| \cdot \vec{e}_z$ according to equation 4.17:

$$\begin{aligned} \frac{mv_T^2}{R_H} &= \kappa q v_T B_z && (4.32) \\ \Leftrightarrow\ C &= \left(\frac{q}{p_{\mathrm{T}}}\right) \kappa B_z. && (4.33) \end{aligned}$$

As previously mentioned, the dip angle λ is derived consequently from geometric considerations, further relating the transverse and longitudinal momentum

$$\tan(\lambda) = \frac{\Delta z'}{\sqrt{\Delta x'^2 + \Delta y'^2}} = \frac{p_{\mathrm{z}}}{p_{\mathrm{T}}}. \tag{4.34}$$

The components

$$\begin{aligned} \tan(\lambda) &= const., && (4.35) \\ \frac{q}{p_{\mathrm{T}}} &= const., && (4.36) \end{aligned}$$

are considered constant under propagation in a uniform magnetic field neglecting any distortions or effects from material corrections with a small enough step size, which is in ALICE of the order of a few centimeters.
The values of p_{x}' and p_{y}' are computed from the local ϕ angle, indicated in figure 4.5:

$$p_{\mathrm{x}}' = p_{\mathrm{T}} \cos(\phi) \text{ and } p_{\mathrm{y}}' = p_{\mathrm{T}} \sin(\phi). \tag{4.37}$$

4.2.2.2. Track covariance matrix

As outlined in the previous section, the track covariance matrix plays an important role in the Kalman filter algorithm, because it reflects the predictive power of the approach and the extrapolation is a crucial step in each iteration. The covariance matrix is also part of the corresponding χ^2 calculation, visible in equation 4.10. In case of its application in the ALICE Experiment, it not only reflects the systematic uncertainty of the actual physical propagation of the track, for example stemming from multiple scattering, but also reflects the degree of correlation between the different measured quantities. Generally, the covariance matrix C is defined via its elements

$$C_{ij} = \langle (x_i - \langle x_i \rangle)(x_j - \langle x_j \rangle) \rangle = \sigma_{ij} \tag{4.38}$$

and is thus a generalization of the variance, with the standard deviation σ_i

$$C_{ii} = \langle (x_i - \langle x_i \rangle)^2 \rangle = \sigma_{ii} = \sigma_i^2 \tag{4.39}$$

on the diagonal. Effectively, the off-diagonal matrix elements contain the statistical correlation

$$C_{ij} = \frac{\sigma_{ij}}{\sqrt{(\sigma_i^2 \sigma_j^2)}}, \tag{4.40}$$

which reflect the degree of correlation between two components of the state vector. Here, full (anti-)correlation corresponds to (-)1, and no correlation results in a vanishing value. By construction the covariance matrix is symmetric. In case of the ALICE state vector, the matrix is 5 × 5-dimensional. As outlined in section 4.2.3.1, most off-diagonal elements are un-correlated.

4.2.2.3. Transport matrix

The (ALICE) Kalman filter further requires a transport matrix, which is the Jacobian matrix specified in equation 4.7, for the extrapolation of the state vector from the current position $x_k^{'}$ to the updated position $x_{k+1}^{'}$. Some elements vanish and the remaining off-diagonal elements are:

$$\begin{aligned}
\frac{\partial y_{k+1}}{\partial \sin(\phi_k)} &= \frac{\Delta x}{r_1^3} && (4.41)\\
\frac{\partial y_{k+1}}{\partial C} &= \frac{1}{2}\frac{(\Delta x)^2}{r_1^3} && (4.42)\\
\frac{\partial z_{k+1}}{\partial \sin(\phi_k)} &= \frac{\Delta x \cdot \tan(\lambda) \cdot \sin(\phi_k)}{r_1^3} && (4.43)\\
\frac{\partial z_{k+1}}{\partial \tan(\lambda)} &= \frac{\Delta x}{r_1} && (4.44)\\
\frac{\partial z_{k+1}}{\partial C} &= \frac{1}{2}\frac{(\Delta x)^2 \cdot \tan(\lambda) \cdot \sin(\phi_k)}{r_1^3} && (4.45)\\
\frac{\partial \sin(\phi_k)}{\partial C} &= \Delta x, && (4.46)\\
\text{substituting } r_1 &= \sqrt{1-\sin(\phi_k)^2}. && (4.47)
\end{aligned}$$

Here, the derivatives were Taylor expanded up to first order, which shortens the calculation and thus speeds up the computing algorithm. For those elements, where the first order has vanishing values (equations 4.42 and 4.45), the expansion was extended to second order [199, 200, 202]. With the derivatives above, the symmetry of the covariance matrix is further exploited, such that the calculation of the extrapolation uncertainty is rewritten in a more performant algorithm:

$$\begin{aligned}
F_k \tilde{C}_{k-1} F_k^T &= (F - I + I)\,\tilde{C}_{k-1}\,(F - I + I)^T \\
&= \tilde{C}_{k-1} + f\tilde{C}_{k-1}f^T + f\tilde{C}_{k-1}\tilde{C}_{k-1}f^T, && (4.48)
\end{aligned}$$

using $f = F - I$, where I is the identity matrix.

4.2.2.4. State vector in global coordinates

Eventually, the state vector is updated with measurements in the global coordinate system (X, Y, Z) of the ALICE central barrel, which relates to the track state vector $\vec{x}^T$ as follows:

$$\begin{aligned}
\vec{x}^T &= \left(y^{'}, z^{'}, \sin\left(\phi\right), \tan\left(\lambda\right), \frac{q}{p_{\mathrm{T}}}\right), \text{ with} && (4.49)\\
y^{'} &= -X\sin\left(\alpha\right) + Y\cos\left(\alpha\right), && (4.50)\\
z^{'} &= Z, && (4.51)\\
\sin\left(\phi\right) &= C\left(x^{'} - x_0^{'}\right) = \sin\left(\arctan^2\left(\frac{p_{\mathrm{y}}}{p_{\mathrm{x}}}\right)\right), && (4.52)\\
\tan\left(\lambda\right) &= \frac{p_{\mathrm{z}}}{p_{\mathrm{T}}}, && (4.53)\\
\frac{q}{p_{\mathrm{T}}} &= \pm\frac{1}{p_{\mathrm{T}}} && (4.54)
\end{aligned}$$

at the reference coordinate:

$$x^{'} = X\cos\left(\alpha\right) + Y\sin\left(\alpha\right), \text{ and rotation angle } \alpha. \tag{4.55}$$

This relation of the state vector enables a fast transformation between local and global frame. Further, during propagation, the material effects, such as multiple scattering and energy loss, as well as detector effects, such as residual calibration and alignment, have to be considered.

4.2.3. Transport through material

So far, all considerations are computed in an ideal detector scenario, which does not include the impact of the detector material on the particle trajectory. Such distortions are indeed present and introduced by the sensitive detector elements as well as any other material installed in the experiment and need to be accounted for. Whereas detector effects such as alignment and calibration are determined already before the reconstruction, multiple scattering and energy loss of a particle traversing the material still need to be included. In the following, the latter two effects will be discussed in detail.

4.2.3.1. Multiple scattering

Multiple scattering is a consequence of an electrically charged particle traversing matter and being deflected from its original path, which is determined by the equations of motion in vacuum. The impact of the transverse momentum transfer is the result of an integration of the transverse component of the force interacting between two charged particles, where the first can be considered a moving projectile and the second particle as target at rest [218]. For two point-like and spinless particles the differential cross-section is well described by the Rutherford formula [221]:

$$\frac{\mathrm{d}\sigma_R}{\mathrm{d}\Omega} = \frac{1}{4}q_1^2 q_2^2\left(\frac{e^2}{pv}\right)^2\frac{1}{\sin\left(\theta/2\right)^4} \tag{4.56}$$

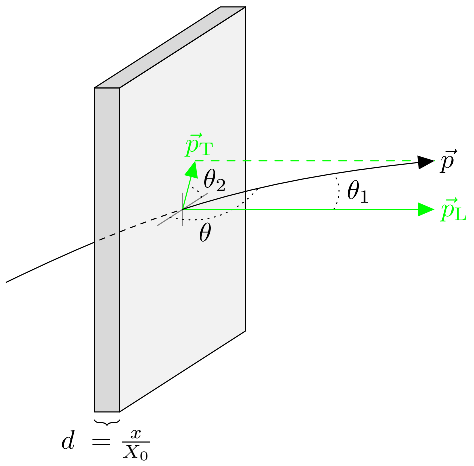

Figure 4.6.: Illustration of the effect of multiple scattering of a particle passing some material with a given thickness thickness d.

where q_1 and q_2 are the respective charges in units of electron charge e, and pv the projectile momentum times velocity. The deflection angle θ describes the angle between the original path in vacuum and its direction after the scattering, as indicated in figure 4.6. Note, that it can be expressed as a combination of two orthogonal and uncorrelated angles θ_1 and θ_2, where $\theta^2 = \theta_1^2 + \theta_2^2$, in a cartesian coordinate system with one axis pointing into the longitudinal momentum direction of the projectile with mass m [222]. Further considering the thickness of the material $d = x/X_0$, expressed in units of radiation lengths, the variance of θ (mean square angle) per scattering process is then given by:

$$\langle\theta^2\rangle = E_s^2 \frac{m^2 + p^2}{p^4} d, \text{ where } E_s = 14.1 \text{ MeV}. \tag{4.57}$$

For θ_1, the angle of deflection on a plane containing the initial trajectory, the mean square value is half of $\langle\theta^2\rangle$:

$$\langle\theta_1^2\rangle = \left(\frac{E_s}{\sqrt{2}}\right)^2 \frac{m^2 + p^2}{p^4} d. \tag{4.58}$$

The values of $\langle\theta_1\rangle$ and $\langle\theta_2\rangle$ coincide because of symmetry [222].
Only the direction of the projectile is changed and the position is assumed to be unaffected: The variance of the track position is proportional to d^3 and in ALICE [222], especially inside the TPC, d $\ll$ 1 for a typical step length of a few centimeters [215]. Irrespective of the material thickness, it was approximated that the angular distribution is following a Gauß-distribution [222], even though this is not true as long tails from single scatterings [223] are present in the distribution. In addition, the assumption is made that the matter in between two subsequent pad rows in the TPC is approximated as infinitely thin scatterer and thus the logarithmic correction as in the *Molière formula* [221] is neglected.
Given the previous definition of the two orthogonal scattering angles θ_1 and θ_2, the impact of multiple scattering on the covariance matrix is expressed as:

$$\vec{Q}_k = \frac{\partial\left(y_k^{'}, z_k^{'}, \sin\left(\phi_k\right), \tan\left(\lambda_k\right), C_k\right)}{\partial\left(\theta_1, \theta_2\right)} \left(\begin{vmatrix} \langle\theta_1^2\rangle & 0 \\ 0 & \langle\theta_2^2\rangle \end{vmatrix}\right). \tag{4.59}$$

In order to express the relation between ϕ and λ and the scattering angles, two unitary orthogonal vectors are expressed as:

$$\vec{e}_1 \,=\, \begin{pmatrix}\cos(\phi)\cos(\lambda)\\ \sin(\phi)\cos(\lambda)\\ \sin(\lambda)\end{pmatrix} \text{ and } \vec{e}_2 \,=\, \begin{pmatrix}-\sin(\phi)\\ \cos(\phi)\\ 0\end{pmatrix}, \tag{4.60}$$

from which

$$\vec{e}_3 \,=\, \vec{e}_1 \times \vec{e}_2 \,=\, \begin{pmatrix}-\cos(\phi)\sin(\lambda)\\ -\sin(\phi)\cos(\lambda)\\ 0\end{pmatrix} \tag{4.61}$$

can be constructed. Thus, the effect of multiple scattering on $\vec{e}_1$ can be expressed as

$$\vec{e}_1^{\,\prime} \,=\, \vec{e}_1 + \theta_2\vec{e}_2 + \theta_1\vec{e}_3, \tag{4.62}$$

and we the desired relation is derived from a Taylor expansion of the second component of the linear combination:

$$\begin{aligned}
\sin(\phi)^{\prime}\cos(\lambda)^{\prime} &= \sin(\phi)\cos(\lambda) + \theta_2\cos(\phi) - \theta_1\sin(\phi)\sin(\lambda) && (4.63)\\
&\approx \sin(\phi)^{\prime}\cos(\lambda) - \sin(\phi)^{\prime}\sin(\lambda)\cdot\delta\lambda\\
&= \sin(\phi)\cos(\lambda) + \delta\phi\cos(\lambda)\cos(\phi) - \theta_1\sin(\phi)\sin(\lambda) + ...\\
\text{and thus } \delta\phi &= \frac{\theta_2}{\cos(\lambda)}. && (4.64)
\end{aligned}$$

Here, we the relation

$$\delta\lambda \,=\, \theta_1 \tag{4.65}$$

is used, which can be derived similarly from the third component of the linear combination. Now, equation 4.59 is evaluated via

$$\begin{aligned}
\vec{Q}_k &= \langle\theta^2\rangle\vec{J}_k \left(\begin{vmatrix}1 & 0\\ 0 & \frac{1}{\cos(\lambda_k)^2}\end{vmatrix}\right)\vec{J}_k^T, && (4.66)\\
\text{using } \vec{J}_k &= \frac{\partial\left(y_k, z_k, \sin(\phi_k), \tan(\lambda_k), C_k\right)}{\partial\left(\lambda_k, \phi_k\right)} \text{ [215].} && (4.67)
\end{aligned}$$

The corresponding terms stemming from multiple scattering, which have to be added to the covariance matrix, then read as:

$$\begin{aligned}
\vec{Q}_{(\sin(\phi_k),\sin(\phi_k))} &= \langle\theta^2\rangle\cdot(1-\sin(\phi_k)^2)\cdot(1+\tan(\lambda_k)^2) && (4.68)\\
\vec{Q}_{(\tan(\lambda_k),\tan(\lambda_k))} &= \langle\theta^2\rangle\cdot(1+\tan(\lambda_k)^2)^2 && (4.69)\\
\vec{Q}_{(\tan(\lambda_k),C_k)} &= \langle\theta^2\rangle\cdot C_k\tan(\lambda_k)\cdot(1+\tan(\lambda_k)^2) && (4.70)\\
\vec{Q}_{(C_k,C_k)} &= \langle\theta^2\rangle\cdot C_k^2\tan(\lambda_k)^2 && (4.71)
\end{aligned}$$

The final multiple scattering correction displayed in equations 4.68–4.71 actually corresponds to the corrections applied during the Kalman filter propagation in the ALICE Experiment [199, 215]. Some of the non-trivial, off-diagonal elements are neglected during the propagation:

- $\vec{Q}_{(\sin(\phi_k),\tan(\lambda_k))}$: It is assumed that multiple scattering in ϕ and λ are uncorrelated.
- $\vec{Q}_{(\sin(\phi_k),C_k)}$: In the small scattering approximation, the energy and momentum of the projectile particle are conserved, thus changing the angle in the transverse plane has no influence on the transverse momentum and curvature determination.

However, applying the same assumption on $\vec{Q}_{(\tan(\lambda_k),C_k)}$, a change in pseudo-rapidity, which corresponds to $\tan(\lambda)$, implies a change of transverse momentum and thus the curvature. The corresponding distortion is considered in equation 4.70.

4.2.3.2. Energy loss

It is expected that the energy loss of a particle traversing some material is not correlated with a particular angle, but only influences the curvature of a track. Thus, a simplified Bethe-Bloch formula is considered for the estimate, which parameterizes the formula used in the calculations in GEANT3 [193]:

$$\langle -\frac{\mathrm{d}E}{\mathrm{d}x}\rangle \approx K \cdot \langle Z/A\rangle \cdot \frac{1+\beta^2\gamma^2}{\beta^2\gamma^2} \cdot \left(\frac{1}{2}\cdot\log\left(\frac{2m_ec^2\beta^2\gamma^2T_{max}}{\langle I\rangle^2}\right) - \frac{\beta^2\gamma^2}{1+\beta^2\gamma^2} - \delta^2\right), \tag{4.72}$$

in units of GeVcm^2/g, where $K = 2\pi r_e^2 m_e c^2 = 0.307\cdot 10^{-3}$ GeVcm^2/g, $\langle Z/A\rangle = 0.498$, electron mass m_e in $\left(\mathrm{GeV}/c^2\right)$, $T_{max} = 2m_ec^2\beta^2\gamma^2$, mean excitation energy $\langle I\rangle = 173\cdot 10^{-9}$ GeV and δ as density effect. The given values are the default parameters for pions traversing silicon, used as first approximation.

Utilizing that

$$E_{new} = E_{old} + \Delta E, \text{ and } p_{new} = \frac{K}{C_{new}}\sqrt{1+\tan(\lambda)^2} \tag{4.73}$$

the updated track curvature is modified such that

$$C_{new} = C_{old}\left(1-\frac{\Delta C}{C_{old}}\right) = C_{old}\left(1-\frac{E_{old}}{p^2}\Delta E\right). \tag{4.74}$$

$C_{old/new}$ are the curvature before and after the crossing of the material layer. In addition, energy loss fluctuations are estimated and taken into account in the covariance matrix element of the curvature via

$$\vec{Q}^{\mathrm{d}E}_{(C_k,C_k)} = \left(\sigma_{\mathrm{d}E}\frac{(p^2+m^2)}{p^2}C_k\right)^2, \tag{4.75}$$

$$\text{where} \quad \sigma_{\mathrm{d}E} = \kappa\sqrt{|\mathrm{d}E|)}$$

$$\text{and} \quad \kappa \text{ tuned to } 0.07.$$

For example, the energy loss for tracks at $|\eta| \approx 0$ passing through the full active volume of the TPC ($\approx$ 170 cm and $\rho^{\mathrm{Ne}} \approx 9\cdot 10^{-3}$ g/cm^3) is about 300 keV. For a pion, this corresponds to a relative change of the resolution of about 1.9 % due to multiple scattering, assuming a momentum resolution of 1.0 %. Note, that additional energy loss through Bremsstrahlung is not considered in the current tracking algorithm. However, studies are ongoing to include this effect for electrons based on parameterizations of the average probability for Bremsstrahlung over a given distance in the detector material [200].

4.3. FT2: Development of a fast estimation tool for primary particles

The ALICE upgrade strategy (section 3.3.2) aims to record a vast amount of data in various collision systems during the LHC Run 3 and 4, beginning in 2020: It is foreseen to record about $\mathrm{L}_{\mathrm{int}} = 10\,\mathrm{nb}^{-1}$ of Pb–Pb collisions, accompanied by the measurement of significant reference data samples of p–Pb (at $\sqrt{s_{NN}} = 8.8\,\mathrm{TeV}$) and p+p (at $\sqrt{s} = 5.5$ and $14\,\mathrm{TeV}$). The analyses of the expected physics measurements, especially with respect to rare signals of charmed and beauty hadrons as well as high-p_{T} jets, require not just a vast amount of data but also demand for large and accurate samples of simulated events. It is also expected, that the large set of recorded data will lead to more advanced, differential analysis, which in turn will also need solidification through Monte Carlo simulations of the corresponding collision system. The ALICE Collaboration therefore aims to simulate about $5 \cdot 10^{8}$ central Pb–Pb collisions, which correspond to about 0.5 % of the expected data sample [189].
In addition, it is foreseen to simulate $5 \cdot 10^{10}$ p+p, and $5 \cdot 10^{9}$ p–Pb collisions as reference, which imposes high demands on the available computing resources in the future. As the complete simulation of a central Pb–Pb event takes approximately 6000 s, the required resources amount to a total of $\mathcal{O}(10^{12})$ CPUs per year, distributed over 5 years.
Whereas the reconstruction is dominated by digitization in p+p collisions, the resource consumption in the reconstruction of (central) Pb–Pb collisions is dictated by the particle transport and propagation through the experiment (as outlined in section 4.2). This includes the particle propagation and interaction with active and passive detector material and the evaluation of the corresponding detector response. These requirements are on the edge of feasibility for the available computing resources by the time of the LHC Run 3 [189].
One way to cope with the available amount of resources, is to invest into sufficiently accurate, fast (parameterized) MC simulations (fast MC), which require smaller sets of full MC simulations only for validation and tuning purposes. The need for fast MC is further demonstrated by the analysis of the rare heavy-flavor decay $\mathrm{B}^{+} \rightarrow \overline{\mathrm{D}}^{0}\pi^{+}$ ($\overline{\mathrm{D}}^{0} \rightarrow \mathrm{K}^{+}\pi^{-}$), presented in this thesis. As it will be explained in section 5, the full MC generation of 10^{6} central Pb–Pb events is not sufficient for a statistically accurate description of the expected combinatorial background. For efficiency and performance studies, the lack of statistics of the generated signals is typically overcome by injecting an artificial amount of the analyzed signal particles into the MC simulation (section 4.1). The available background statistics can be increased by other methods, for example through *event mixing* or *track rotations* (section D). These, however, introduce another significant systematic uncertainty in the specific tuning of selection criteria of the signal decay channel.
Indicated in figure 4.1, and given these considerations, a suitable fast MC tool is needed complementary to the slow and resource-expensive transport of generated particles through the detector environment. Ideally, the tool is embedded in the complete processing chain from *event generation* to *data reconstruction* such, that the actual physics analysis of the generated ESDs (or AODs) is insensitive to the underlying simulation mechanisms, e.g. fast or full MC. Such an approach further allows a comparison of physics analyses on both simulation approaches, with the possibility to further tune the fast simulation. This additionally requires a realistic implementation of the detector response at the hit level, including the most important features of the individual devices installed in ALICE. The

ATLAS and CMS collaborations at the LHC already employ fast simulation techniques in their respective simulation frameworks [224, 225, 226], including most physical effects, such as Bethe-Bloch energy loss in material and Bremsstrahlung. Besides other differences, their respective fast simulation is based on a simplification of the tracking algorithm and the detector geometry, as well as a parameterization of the detector response of individual subsystems. Within this thesis a fast, parameterized simulation tool, specifically tuned for central heavy-ion collisions in the upgraded ALICE detector environment, was developed, which may serve as a baseline for future developments.

The remaining section is structured as follows: After an introduction of already available fast simulation methods within ALICE, the general working principle of the new tool is explained in section 4.3.2. Subsequently, the most important and ALICE-specific requirements are highlighted. The complete simulation framework and its integration into the existing software infrastructure is presented in section 4.3.4, and the comparison of the FT2 performance to full MC simulation, as well as the consumption on CPU resources, is given in section 4.3.9.

4.3.1. Available fast simulation methods

In the following, a brief summary of already available simulation tools in the ALICE Collaboration is presented. It aims to give an overview of existing and recent developments, besides the full simulation framework.

- *covariance matrix parameterization* [220]: Developed for the unit test of vertexing packages used in ALICE, this tool smears the track parameters according to a parameterized covariance matrix evaluated from data. It is capable of generating tracks with realistic kinematic properties and resolution, at a high speed. A similar development was tested for applicability for the demanded task of a global, fast simulation, but failed to reproduce the track-by-track topologies and thus reconstruction efficiency, especially with respect to the impact of fake tracks and material interactions.

- *Fast Estimation Tool* (FET) [20, 227]: This semi-analytical tool is based on a *toy-model*, developed by the STAR heavy-flavor tracker collaboration [228], which was extended to include the Kalman tracking algorithm used in ALICE. Here, for each MC generated particle, charge clusters are generated within a given resolution in the active layers of a simplified ITSu geometry. These are used by the Kalman filter algorithm to calculate the covariance matrix at each step of a measurement, including the impact of multiple scattering. The obtained efficiencies are reliable and verified within 5 %, when compared to full MC simulations. However, the cluster-to-track association efficiency at a given detector layer depends on purely analytical, Gauß-shaped distributions of the track pointing resolution, the cluster resolution and the hit density in that layer. For this reason, fake clusters cannot be modeled. Hence, the evaluated efficiencies are only relative, but quantitative estimate on differences between various detector layouts can be derived.

- *hybrid method* [186]: The hybrid approach applies the upgraded ITS performance on full simulations of the current ITS, such that the scaling factors correspond to the difference between the resolutions of the current and upgraded ITS detector. Based on the reconstructed track parameters with the FET tool, the residuals of the impact parameters in $r\phi$ and z ($d_{0,r\phi}$, $d_{0,z}$) and the transverse momentum p_{T}, are scaled with respect to their true MC value, while all intrinsic correlations of the parameters are kept. This approach is extremely useful for studies of the sensitivity of a measurement with respect to changes in the ITS detector design. However, as it is based on already existing MC samples, there is no benefit in CPU consumption and timing during the full MC production.

- *Fast Monte Carlo Tool* (FMCT) [20]: The FMCT is an extension of the FET. Even though considerably slower, the tool includes a more realistic tracking approach, which is able to differentiate between correct and background clusters and can provide tracks with associated fake clusters (fake tracks). While propagated from the primary vertex to the outer sensitive layers, and taking into account Gauß-shaped multiple scattering and deterministic energy loss, clusters are filled randomly in the sensitive areas within a given resolution. Here, the sensitive ITSu layers are approximated by cylinders of a given material thickness. The Kalman filter is applied in inward direction, starting from the exact outer coordinates of the true MC track. At each step, it is tested whether clusters (good or fake) can be matched to the track candidate, based on the track-to-cluster χ^2. Once propagated back to the primary vertex, the best track candidate for a given true MC particle is selected. This approach allows to differentiate between the performance of specific track-finding algorithms. Conceptually, this tool serves as a baseline of the newly developed *Fast estimation Tool 2* (FT2), which includes several extensions, such as the usage of the fully simulated ITSu geometry. These will be explained in detail in the subsequent section.

The latter three methods were specifically developed for the studies on the performance of the upgraded ITS detector compared to the current device [19, 186, 20].
Even though the conceptual idea of the already available FMCT matches the basic requirements for a fast MC simulation, which is capable of reproducing full MC simulations to a reasonably good extend, the FMCT itself was not designed for that purpose, and is not able to reproduce the absolute reconstructed particle yields [199]. Detector effects, which strongly impact the track quality and thus the reconstruction efficiency, were only taken into account on a simplistic level in the FMCT. However, the aim of having a more realistic approach further requires that the detector response of a fast simulated track is similar to full MC simulations, such that the user analysis remains largely unaffected by the choice of the simulation tool.
These challenges triggered the development of the FT2, which aims for improvement around three essential features:

1. The FT2 must be several orders of magnitude faster than full MC simulations, such that it meets (current and) future restrictions on CPU resources available for simulations in ALICE.

2. The detector response of the central tracking detectors in ALICE, the (upgraded) ITS and the TPC, should be similar to a realistic performance.

3. The sensitivity of ALICE on physics observables must be reproduced to a good precision, such that the systematic uncertainty imposed by the fast simulation remains sufficiently small compared to other uncertainties in the corresponding analyses.

With these properties, the FT2 improves the current fast simulations to a more realistic estimate on the performance of ALICE. In contrast to previous attempts, it includes the full detector geometry, which slows down the algorithm, but significantly improves the estimate of the track parameter uncertainties through a more precise calculation of material effects. Further, it includes parameterizations of the most important device specific features, which enables an absolute comparison of the complete, reconstructed event with full MC simulations and even data. Previous fast simulation approaches could only be used for relative, quantitative studies.

4.3.2. General working principle

The FT2 is designed such, that it uses the MC generated events, for example central Pb–Pb collisions simulated with HIJING, and simulates the detector response in order to realistically reconstruct tracks from the physical particles. As described in section 4.2.2, a Kalman filter is used in ALICE to reconstruct tracks in the central barrel, where the global track reconstruction is mainly performed in the (upgraded) ITS and TPC detectors, which are also the only devices taken into account in the FT2. Including more devices would significantly increase the computing time, as tracks would have to be propagated through the additional material. Further, the detector geometry of devices such as TOF and TRD is complex and their performance not easily parameterized. As explained in section 4.3.7, the complete geometry of the relevant detectors needs to be considered, while the segmentation of the TPC readout can be simplified. Note, that in this approach the tilt of the TPC readout pads is included, as sketched in figure 4.7. As they contribute to the overall material budget, and thus affect the trajectory of a given particle, the beam pipe and the inner wall of the TPC are included as additional passive material. Figure 4.7 displays the algorithm of the track reconstruction of particles from a collision, which is explained in the following:

1. In the FT2, each particle is selected one-by-one at its point of generation in the event. For primary particles, this typically corresponds to a small area around the primary vertex. The FT2 naturally selects particles (e, μ, π, K, p) within the acceptance of the ALICE central barrel detectors as the propagation of a particle is stopped when it exits the ITSu or TPC detectors. Thus particles in the forward region will not generate a reconstructable signal and are discarded.

2. Along its ideal trajectory (blue line), the track candidate is propagated outward with an arbitrary, but small enough step length ($\mathcal{O}(1\,\mathrm{cm})$). As the full geometric information of the ITSu and TPC detectors is available during runtime, in each step the traversed material can be approximated. Using the actual mass of the particle, taken from the MC truth information, the mean energy loss as well as the impact of multiple scattering is considered (purple line) and used to update the track parameters. If the corresponding algorithms are enabled, at each step it is possible for a particle to decay or to be absorbed in the material, which is randomly decided upon the calculated probability based on the traversed material budget (section 4.3.5).

3. In case the particle passes active detector material in the ITSu, or propagates through the active volume of the TPC, a charge cluster is generated within the parameterized resolution of the subsystem (colored circles), which was tuned to match the detector performance.

4. Detector specific features, such as fake hits in the ITSu, and missed or distorted hits in the TPC, can be taken into account. These features are addressed specifically in sections 4.3.7 and 4.3.8.

5. Once the particle is propagated to the point that it exits the TPC, the propagation is stopped.

6. Starting at that exact point, using the same definition of the state vector and assuming an arbitrarily large covariance matrix, the Kalman filter algorithm is used along the generated clusters in the TPC to reconstruct the track (red line) in inwards direction.

7. At the innermost radius of the TPC, so far using the true MC information on the particle species, an assumption on the particle identity of the considered track, based on the TPC performance (section 4.3.8), is used for further propagation through the ITSu. This corresponds to the actual procedure in the data reconstruction. [199, 200].

8. Within the ITSu, a track smoothing algorithm is applied (details in section 4.3.7). The final inward propagation is stopped at the innermost sensitive layer.

In step 2, the effects of multiple scattering and energy loss on the individual particle are considered. Both approaches are inspired by the GEANT3 calculation: Multiple scattering is approximated according to equation 4.58 and the scattering angles are sampled according to a Gauß-distribution. The energy loss itself is calculated according to equation 4.72, where the average proton and mass numbers as well as the average number of radiation lengths of the traversed material are estimated within the given step size.

Originally, the FT2 was designed and tuned to handle primary charged particles only, which includes all secondary particles produced by strong and electromagnetic decays. In the meantime, it was extended to propagate also secondary particles, in particular those stemming from strange weak decays or conversions in the material. However, these still must be generated within an available transport package before they can be reconstructed in the FT2.

After all particles are reconstructed into tracks with the fast simulation, the primary (and secondary) vertex reconstruction is performed by the available standard algorithm in the framework. Here, the vertex position is calculated from a χ^2-optimization of the most probable space point, based on the information and uncertainties of all successfully reconstructed tracks.

4.3.3. Anchoring on full Monte Carlo simulation

In order to match the performance of the fast simulation to that of a fully simulated detector response, the FT2 must be anchored to an available full MC production. In this approach, the performance of the full and FT2 track reconstruction are compared on the exact same fully simulated input data, which typically includes the generation of

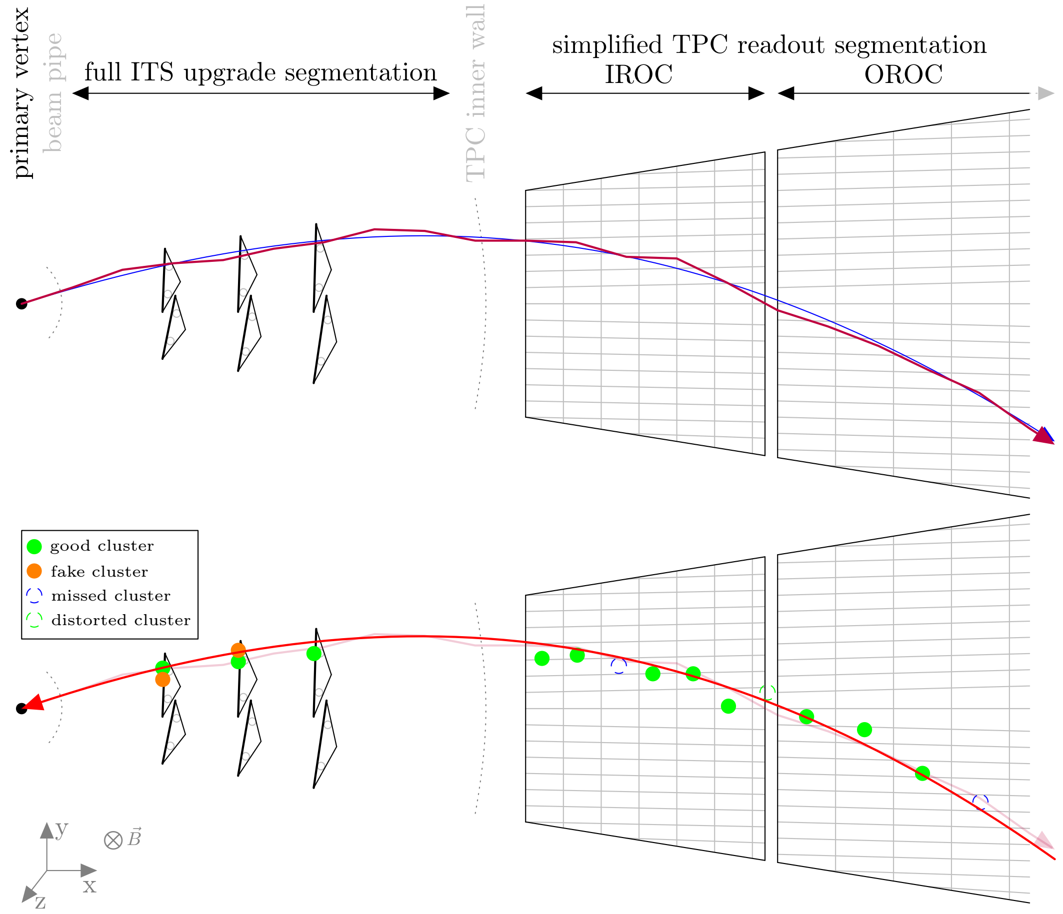

Figure 4.7.: Schematic view of the FT2 working principle. Here the ITSu is sketched with three active layers in front of a TPC sector. The full ITS upgrade and TPC geometry are used, which includes the beam pipe and the TPC inner wall as passive material. In addition, a simplified TPC readout segmentation is applied to include effects specific to the readout of the detector, such as missed clusters in the dead regions of the device through displacement by $\vec{E} \times \vec{B}$-distortions. As shown in the upper figure, the particle is propagated outward from the primary vertex along its ideal trajectory (blue line). For a given step size, energy loss and multiple scattering in the traversed material are approximated and taken into account (purple line). Visible in the lower figure, clusters (colored circles) are placed in the active area of the devices within the specific detector resolution. The final track (red line) is reconstructed using a Kalman filter along these clusters. A realistic implementation of fake clusters in the ITSu and effects on the cluster reconstruction in the TPC are discussed in sections 4.3.7 and 4.3.8, respectively.

all secondary particles and all material interactions. Detector specific effects, such as for example the cluster-pickup probability of a track in the TPC, can then be parameterized using a multi-dimensional, local regression fit on the relevant parameters and variables, developed by [200] and benchmarked throughout this thesis. In this approach, the input for each dimension is divided into a given amount of bins distributed over the relevant range of that specific dimension. Within these bins, a second order polynomial is fit to the input distribution with smooth boundary conditions at the bin edges. As will be shown in the following, fast and reliable parameterizations are obtained using fits on up to three dimensions and at most 10 bins per axis. Here, no significant edge effects were observed at the bin edges, as large statistics in the input samples were used. In this case, increasing the number of dimensions would result in a significantly increased computing time. This powerful approach is continuously extended to increase the computing speed [200].

Throughout this thesis, as will be highlighted in the respective paragraphs, the FT2 was anchored to the full MC production used to evaluate the upgraded ITS detector performance in central Pb–Pb collisions for the technical design report of the new detector [20]. More details on this production can be found in the appendix A.

4.3.4. Embedding into the simulation framework

A detailed, schematic flow chart of the FT2 conceptual design and the integration into the ALICE framework, is presented in figure 4.8. The FT2 is directly operating on particles generated by the physics event generators, and reconstructs these into tracks, in the ALICE ESD format, which can be used for the typical physics analysis.

As usual, particles are generated with the standard physics event generators like HIJING or PYTHIA. In addition, a transport package like GEANT3 can be used to generate additional secondary particles, depending on which processes need to be studied. For example, a subsequent decayer, such as PYTHIA, can be enabled to include strange weak particle decays. After the FT2 was initialized with the desired setup, the generated particles are then inserted one-by-one into the FT2 framework for track reconstruction. This setup is determined from a comparison to an existing full MC simulation. Using the parameterizations of detector specific effects as look-up tables, the particles are propagated and the corresponding tracks are reconstructed. Based on the determined, realistic track parameters, the primary vertex position and resolution are calculated and all information is stored in the ESD, as for a typical full simulation. If required, AODs and for example the complementary analysis file for secondary vertices, can be generated from these ESDs, as usual. Given the structure of the code, the tune of the FT2 to a specific data sample or simulation is easily performed, as all relevant parameterizations are generated before, and are made available at run time in an additional file. In this way, for example the ITSu detector geometry can be simply exchanged by replacement of the corresponding input file.

4.3.5. Decay and absorption of particles

As mentioned above, step 2 includes the calculation of the probability for each propagated particle to decay and/or to be absorbed in the traversed material. The decay probability was estimated with an exponential function, which depends on the true particle lifetime τ and its Lorentz factor γ, as a function of the propagation step size Δs:

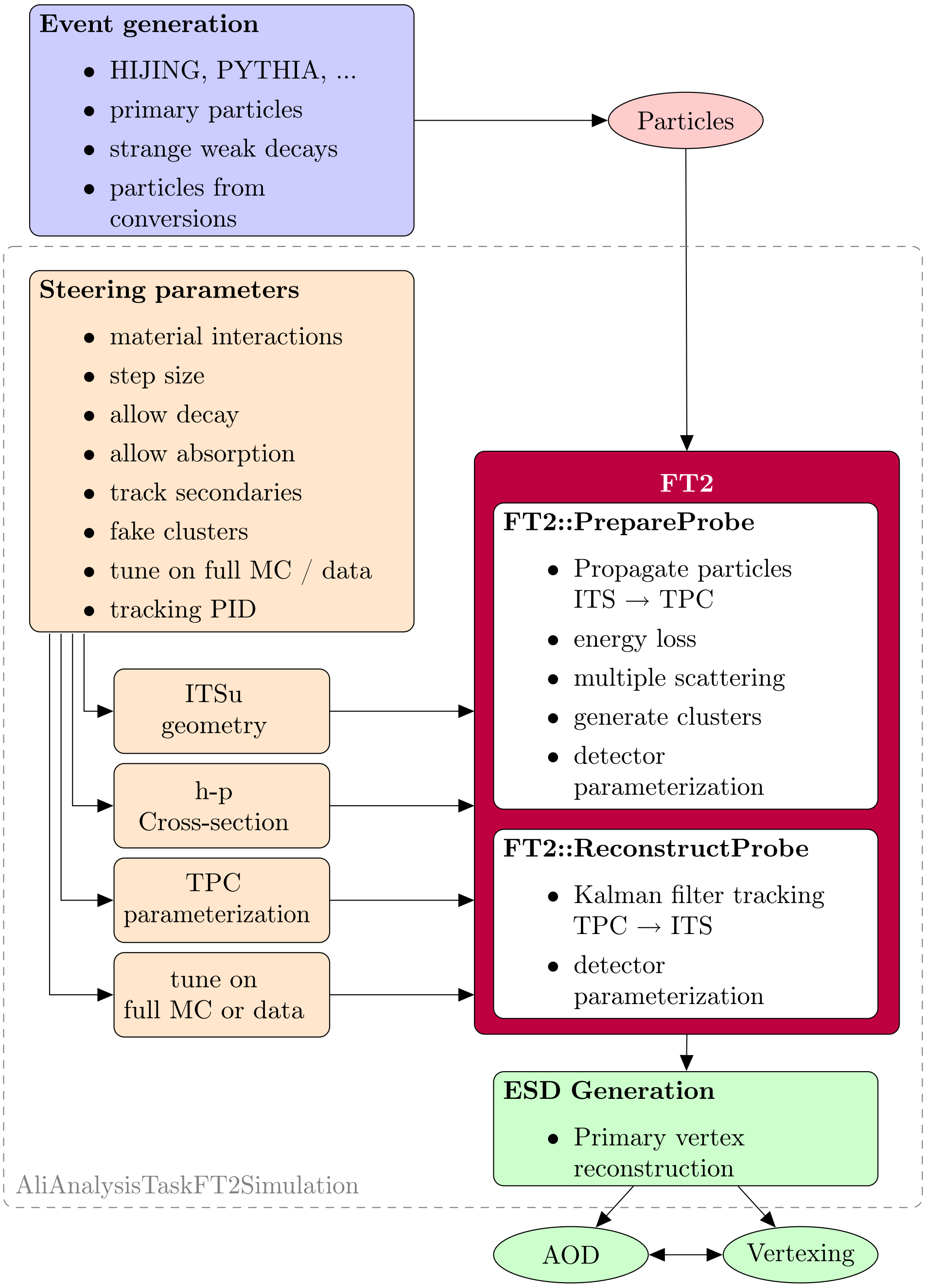

Figure 4.8.: Conceptual design of the full FT2 simulation framework. Parameterizations and for example the ITSu detector geometry specific to an anchored full MC production are evaluated beforehand and stored in accompanying files. Based on the setup in the steering task, the FT2 can use these parameterizations in the cluster simulation and track reconstruction.

$$P_{decayed}\left(\Delta s\right) \quad = \quad 1 - P_{undecayed}\left(\Delta s\right) \;=\; 1 - e^{-\frac{\Delta s}{\gamma c \tau}}. \tag{4.76}$$

The calculation of the absorption probability for a particle is based on available total collision hadron-proton (h-p) cross-section (σ_0) data available over the full kinematic range [10]. Using the data for pions, kaons and protons (and charge conjugates), the nuclear interaction length is calculated via

$$\lambda = \frac{\langle A \rangle^{\frac{1}{3}}}{N_A \sigma_0}, \tag{4.77}$$

where $N_A = 6.022 \times 10^{23}\,\mathrm{mol}^{-1}$ is the Avogadro constant, and $\langle A \rangle$ the mean atomic number of the traversed material within the last step, used for approximate material scaling from the h-p cross-section. Taking into account the mean material density $\langle \rho \rangle$, which the particle passed in the last step Δs, the number of interaction lengths and subsequently the absorption probability are calculated:

$$P^{\pi,K,p}_{abs}\left(\Delta s\right) \quad = \quad 1 - P_{survived}\left(\Delta s\right) \;=\; 1 - e^{-\Delta s \frac{\langle \rho \rangle}{\lambda}}. \tag{4.78}$$

For electrons, the radiation length is approximated according to

$$X_0 \quad = \quad \frac{1432.7 \cdot \langle A \rangle}{\langle Z \rangle \cdot \left(\langle Z \rangle + 1\right) \cdot \left(11.319 - \ln \langle Z \rangle\right)} \;\left[\mathrm{g} \cdot \mathrm{cm}^{-2}\right] \;[10], \tag{4.79}$$

and the probability of energy loss (via Bremsstrahlung) is calculated as

$$P^{e^-}_{abs} = P_{rad}\left(\Delta s\right) \quad = \quad 1 - P_{stable}\left(\Delta s\right) \;=\; 1 - e^{-\Delta s \frac{\langle \rho \rangle}{X_0}}. \tag{4.80}$$

For positrons, an additional annihilation probability P_{an} is multiplied:

$$\begin{aligned} P^{e^+}_{abs} \quad &= \quad P_{rad}\left(\Delta s\right) \cdot P_{an} \;=\; P_{radiation}\left(\Delta s\right) \cdot \left(1 - e^{-\Delta s \frac{\langle \rho \rangle}{\lambda_{an}}}\right), && (4.81) \\ \text{where } \lambda_{an} \quad &= \quad \frac{\langle A \rangle}{N_A \sigma_{an}} \text{ and} && (4.82) \\ \sigma_{an} \quad &= \quad \frac{\langle Z \rangle \pi r_e^2}{\gamma + 1} \cdot \left(\frac{\gamma^2 + 4\gamma + 1}{\gamma^2 - 1} \cdot \ln\left(\gamma + \sqrt{\gamma^2 - 1}\right) - \frac{\gamma + 3}{\sqrt{\gamma^2 - 1}}\right) \;[207] && (4.83) \end{aligned}$$

are the corresponding annihilation length and cross-section [207]. Here, the classical electron radius r_e was used. In general approximation, muons are not considered for decay or absorption.

In case of absorption or decay, the propagation of the particle is stopped and the Kalman filter tries to reconstruct a track from the available clusters. Secondary products from these decays or absorptions are not generated and tracked at all. Note, that particles, which produced enough clusters in the two simulated detectors, can still be reconstructed as tracks, even though they did get absorbed or decayed at some point. The performance of

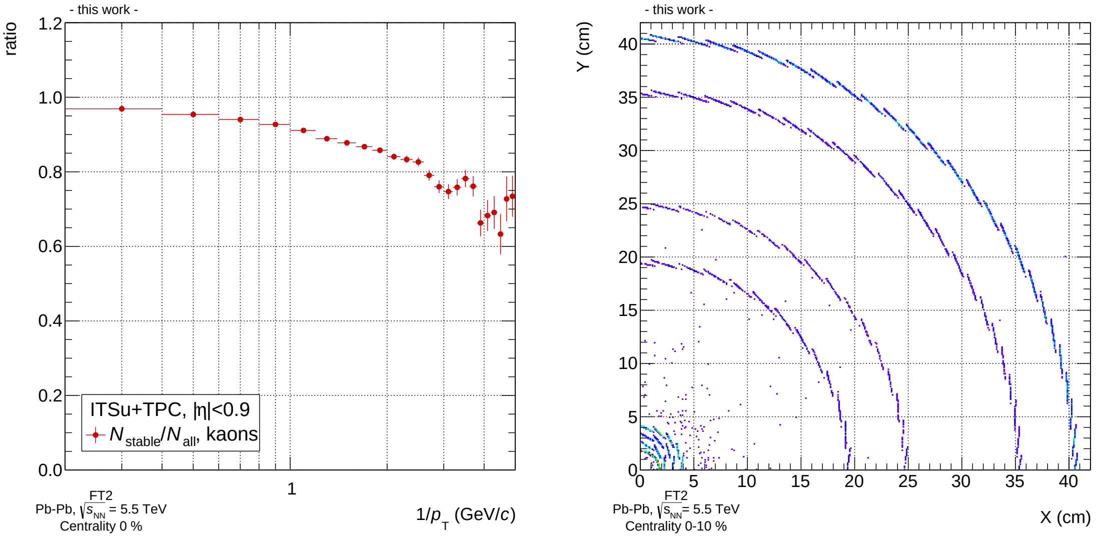

(a) (b)

Figure 4.9.: Effects of the particle decay and absorption mechanisms implemented in the FT2. (a) shows the ratio of undecayed over all kaons as a function of p_T, for tracks reconstructed in the upgraded ITS and TPC detectors. The point of absorption for all stopped particles, not requiring any additional quality or momentum criteria, is shown in global coordinates in (b). The impact of the simulated material of the beam pipe and the upgraded ITS detector is visible. Requiring additional track quality cuts, these tracks would be rejected in the analysis, as their propagation is stopped at the point of absorption and thus for example no TPC clusters associated to them.

the two algorithms is demonstrated in figure 4.9. On the left side, the ratio of "un-decayed" over "all" kaons is shown for tracks reconstructed with the FT2 in the ITSu and TPC, passing certain quality criteria (section 5.1.2.1, without DCA selection). The particle species is identified by a corresponding flag in the MC truth information. The fraction of decayed kaons is visible in the difference of the ratio from unity. For kaons with low transverse momentum, the fraction of decayed particles increases up to 30–40 %, which is in general agreement with equation 4.76 ($\approx 30\%$, assuming $p_T = 250\,\mathrm{MeV}/c$ and a distance of 1.5 m, which roughly corresponds to the track length from the primary vertex, assuming a minimum of 70 generated TPC clusters).

For all particles, and without any momentum or track quality requirements, figure 4.9b displays the point of absorption in global coordinates. Here, the material of the beam pipe (round shape) as well as the seven layers of the inner and outer barrel of the upgraded ITS (turbine shape) are clearly visible. Even though low-p_T particles are dominantly absorbed in the inner barrel, the outer barrel contains more material and the corresponding probability hence increases. Note, that the absorption probability in between the layers is small, but not vanishing, due to the much lower material budget (air).

Both, the material absorption algorithm as well as the decay algorithm can be individually switched on for each particle species separately. This allows for a flexible tuning to match the absolute particle yields of the FT2 to available full MC productions or data samples.

4.3.6. Strange weak decays and particles from material conversions

Up to this point, only primary particles, stemming from the primary vertex in the interaction region inside the beam-pipe, were considered. In ALICE, "primary defines" those particles, which are produced in collisions electromagnetic and strong decays, however exlcuding those from strange weak decays. Even though the definition of primary particles includes heavy-flavor decays, which have vertices displaced by $\mathcal{O}(10^2\,\mu\mathrm{m})$, particles produced in strange weak decays or in interactions with detector material need a more advanced treatment, as they originate far away from the primary vertex. For these particles, the FT2 was extended to correctly start the propagation at the point of particle production, transporting the particle in outward direction. In case a sensitive detector layer is passed, corresponding signal clusters are generated as usual, and reconstructed trajectories can be analyzed with the typically applied track quality selection criteria (section 5.1.2.1).

The FT2 provides realistic, parameterized tracking of the produced particles, but it is not able to generate strange weak decay products, or particles from material interactions itself. If these effects are meant to be included in the simulation, they have to be provided at the stage of the MC generation. Whereas strange weak decays are handled by an external decayer, e.g. HIJING or PYTHIA, GEANT3 is used to simulate the production of secondary particles from material interactions and conversions. However, re-including the material interaction in GEANT3 slows down the complete MC generation sequence considerably, and should only be considered for specific cases such as the analysis low-mass di-electron decays, in which electrons from photon conversions in the detector material yield a significant background source. In heavy-flavor analyses, secondary particles from material interactions are not a significant source of background, as they have a soft momentum spectrum and are typically rejected by analysis cuts.

The fraction of reconstructed primary and secondary tracks in full over fast MC simulations for most central Pb–Pb collisions is shown for electrons and protons in figures 4.10a and 4.10b, respectively. The plots are normalized to the total amount of reconstructable tracks with ITSu+TPC for the given species in the detector acceptance. The relative amount of secondary particles strongly depends on the particle species as well as on the transverse momentum. While only a few percent of the overall reconstructed pion tracks originate from material interaction or strange weak decays (figure A.1c), the fraction of secondary tracks is significant for protons and electrons, as shown in figure 4.10. The amount of reconstructed electron tracks stemming from photon conversions in the detector material reaches about 50 % at transverse momentum below 500 MeV/c, and more than 90 % of the reconstructed proton tracks below 300 MeV/c in central Pb–Pb collisions originate from material interactions or strange weak decays. Here, the particle species and the underlying process of particle generation were identified via MC truth information. The contamination by secondary particles for other species is shown in figure A.1 in appendix A.1.

4.3.7. Implementation of the upgraded Inner Tracking System in the FT2

In contrast to previous attempts of fast simulation (FET, FMCT), where the ITSu detection layers were simulated as a silicon cylinder surrounded by a copper cylinder, respecting the design specifications in terms of radii, material budget, ϕ-segmentation and also the (pixel) resolutions, the FT2 uses the fully simulated, realistic geometric description of the upgraded

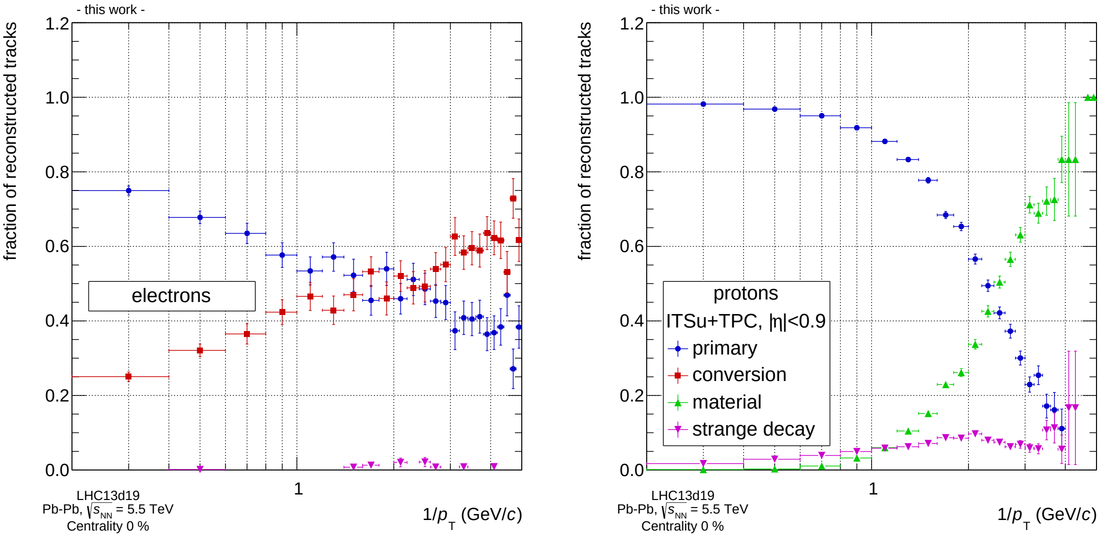

(a) **(b)**

Figure 4.10.: Contamination of ITSu+TPC reconstructed electrons (a) and protons (b) by secondary tracks originating from material interactions or strange weak decays in full MC simulations. The species was identified using MC truth information. A significant fraction of reconstructed electrons stems from photon conversions in the detector material (red squares), which is not observed at all for reconstructed protons. For low p_T, the contamination of protons is dominated by particles from material interactions.

ITS presented in section 3.3.3. After a brief description on the impact of the material budget on the reconstructed particle track, additional important parameters on the ITSu performance in the FT2 are explained in more detail. Here, the single pixel resolution in the local y- and z-coordinate as well as the steering parameter on the amount of random fake clusters in the ITSu are crucial to tune the performance of the FT2 to the anchored full MC or data sample.

Including the full geometric description enables a more precise determination of the material budget a particles traverses. For example, the impact of the energy loss and multiple scattering of the particle on a single element of the covariance matrix is displayed in figure 4.11a. Here, σ_{33} is the square root of the covariance matrix element Cov(3,3) and is displayed as a function of the global ϕ-position, where shaded areas schematically highlight the visible stave of the first layer in the turbine-shape geometry of the ITSu. Note, that the actual standard deviation was normalized to a multi-dimensional fit of the corresponding covariance matrix elements on q/p_T, $|\eta|$ and ϕ, which is used to average out the angular and momentum dependence for better visibility. Clearly, the geometric tilt of the stave is reflected in the value of the covariance, as the extrapolation length to the primary vertex changes. In addition to this modulation, the covariance largely increases, if a particle passes more material, for example at the point where staves overlap ($\phi \approx 2.7$ and 3.1), or going through the cooling pipes of the detector ($\phi \approx 2.9$ and 3.0). Depending on the further path of the particle through the detector and subsequent material interactions, this effect blurs out. Even though only some covariance matrix elements are directly affected by multiple scattering, the uncertainty enters through the correlation of the individual elements during

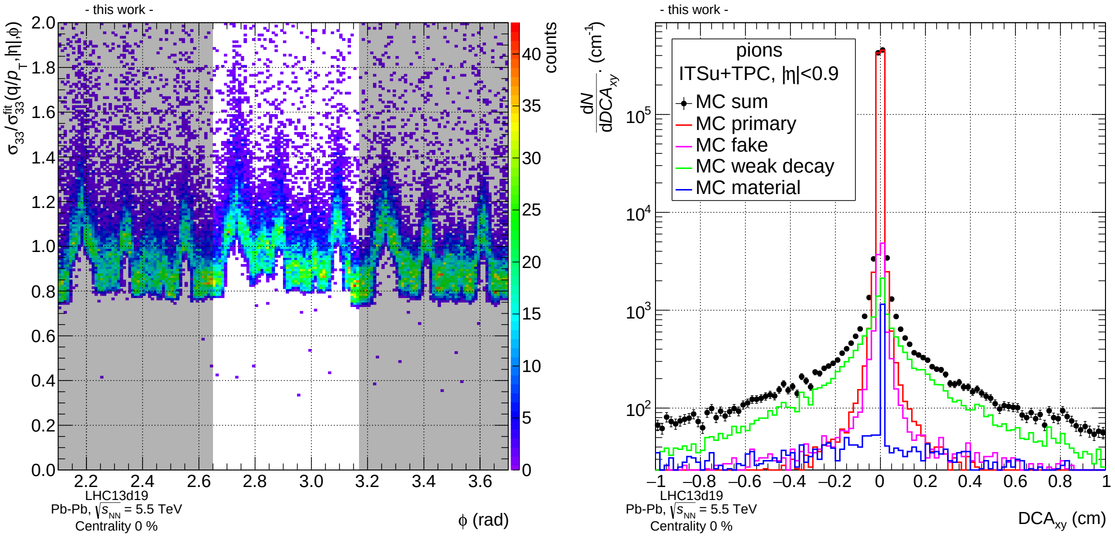

(a) **(b)**

Figure 4.11.: In (a), the correlation between the covariance matrix element $Cov(3,3)$ and the track azimuthal angle is shown. For better visibility, this plot has been normalized to a multi-dimensional fit. The highlighted areas correspond to a single stave of the ITSu detector. A strong dependence of the magnitude of the covariance on the exact track position is observed, further correlated with the material budget traversed by the track. (b) displays the DCA distribution to the primary vertex of generated pions, split into the individual contributions from primary, fake and secondary tracks. Here, only pions which pass the typical track quality cuts with p_{T}> 200 MeV/$c$are considered.

the iterative Kalman propagation into the full covariance matrix, and thus the complete tracking algorithm (see section 4.2.2.2).

4.3.7.1. Single pixel resolution

Although the single pixel resolution of the full MC production of the ITSu detector is well known and could be used in the FT2 simulation, differences in the reconstruction precision are introduced due to the simplified tracking algorithm. Thus the single pixel resolution in the fast simulation does not correspond to the same value as in the full MC production, and should be tuned for an equal performance. In reality, the resolution itself is strongly dependent on the two impact angles of a track (shown in figure 4.6), which passes a sensitive ITSu layer. Also charge sharing between adjacent pixel cells strongly improves the resolution.

In the FT2, these effects are not specifically taken into account, but good correspondence is achieved with a simpler approach: Two parameters, the resolution in the local y- and z-coordinate, are tuned to match the full MC performance. As these parameters also enter the Kalman tracking algorithm during the propagation from one sensitive layer to another, their impact is well visible in the Distance of Closest Approach (DCA) of primary tracks with respect to the primary vertex, as presented in figure 4.11b. Here, they control the width of the central peak region around zero, which was analyzed in small kinematic bins. The relative difference to the full MC values for various resolution parameters in the FT2 is presented for pions in figure 4.12. The transverse (a) and longitudinal (b) directions are

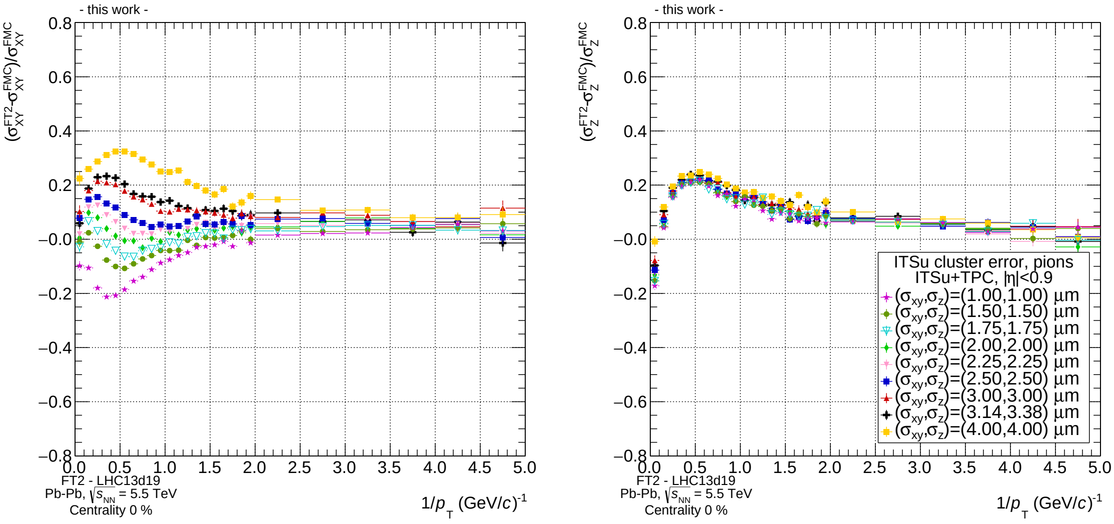

(a) **(b)**

Figure 4.12.: Relative difference of the central DCA peak width in fast and full simulation, obtained from a Gauß-fit to the transverse (a) and longitudinal (b) DCA distribution for various ITSu resolution parameters. In the corresponding full MC simulation, a resolution of $(\sigma_{\rm xy},\sigma_{\rm z})$=(4.00,4.00) μm was used. In the simplified tracking of the FT2, this does not correspond to the optimal value and the setting $(\sigma_{\rm xy},\sigma_{\rm z})$=(2.25,2.25) μm was used, as it resulted in the best performance in the later analysis.

displayed separately. Whereas almost no dependence is observed in longitudinal direction, the transverse DCA resolution is strongly correlated with the resolution parameters at high transverse momentum, where tracks are almost straight, and thus sensitive to the resolution of the detector. For low momentum, the resolution is dominated by multiple scattering, and the different configurations saturate at similar values around $5-10$ %. Whereas the extrapolation error in transverse direction is defined by the contributions from the position, angular and curvature measurements [199], the mild dependence in longitudinal direction, displayed in figure 4.12b, originates from the stronger dependence on the angular measurements. In the transverse plane, the curvature uncertainty is particularly sensitive to the cluster uncertainty, due to the short lever arm of the ITSu. Thus, in the range $0.0 \leq 1/p_{\rm T} \leq 2.0\,({\rm GeV/c})^{-1}$, where the uncertainty from the curvature is dominant, differences between distributions are visible. For both plots, the central peak width was determined via a Gauß-fit in the peak region around zero for primary pions only.

4.3.7.2. Fake cluster generation

As the FT2 is only propagating a single particle at a time, by design only clusters generated by the propagation of this particle are considered in the track fitting procedure. However, as visible in figure 4.11b, which is generated from full MC simulation, the transverse DCA distribution of reconstructed tracks has significant tails towards large values, which originate from strange weak decays and tracks with fake clusters. Here, full reconstructed pions with momentum above $p_{\rm T} > 100$ MeV$/c^2$ are displayed. The daughter particles from strange weak decays naturally have a wide DCA distribution, which results from the large decay length of the mother particle. Depending on the transverse momentum of the

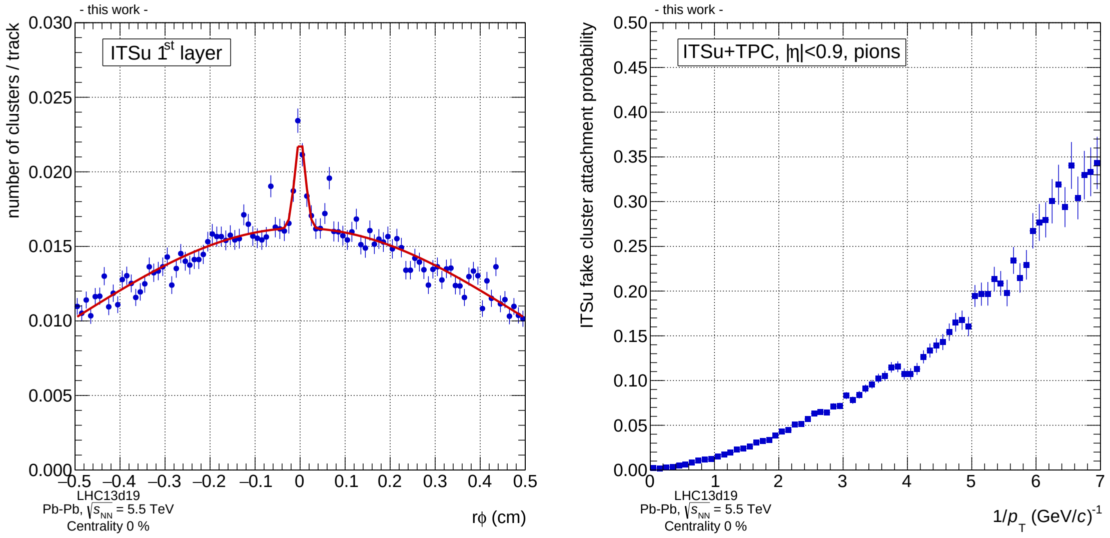

(a) **(b)**

Figure 4.13.: In (a), the fake cluster distributions in $r\phi$-direction in proximity of the true cluster assigned to a track, for the first ITSu layer obtained from full MC simulations. The distributions are fitted by two superimposed Gauß-distributions. The underlying, wide distribution originates from uncorrelated fake clusters, generated by the occupancy in the ITSu detector. The narrow peak at central values is a consequence of correlated fake clusters, generated for example from delta electrons. Two significant narrow peaks are visible symmetrically distributed around the central peak. They originate from the overlap regions in the transverse plane of the inner ITSu staves. In these regions, a track can deposit more than one hit in a single layer, however only one git is taken into account in the reconstruction algorithm. This figure is based on an input by [199]. (b) displays the probability to attach a fake cluster in the ITSu to a fully reconstructed pion track as a function of inverse transverse momentum and identified via MC truth information. For transverse momentum around 1 GeV/c, the probability diminishes to less than 1 %, however it continuously increases up to about 30 % at about 150 MeV/c, where the curvature of a track is larger and the matching becomes increasingly difficult.

decay daughters, they are strongly displaced when propagated in the magnetic field to the primary vertex. Also for tracks with attached fake clusters an increased DCA distribution is observed. An accurate simulation of tracks with attached fake cluster(s) requires an external generation of these clusters, which can then be included in the track reconstruction algorithm of the FT2.

Within the full MC simulation of the ITSu detector, two sources of fake cluster contributions were identified [199]. On the one hand, uncorrelated random hits are widely distributed in the proximity of the cluster attached to the track. As these hits originate from other tracks in an event, the occurrence of random clusters increases linearly with the estimate of the charged particle multiplicity $\mathrm{d}N_{\mathrm{charged}}/\mathrm{d}y$. On the other hand, as visible in the central regions of figure 4.13, correlated clusters are located in close vicinity to the true hit. These originate from secondary particles induced by the probed track, for example delta electrons. In addition, two significant narrow peaks are visible symmetrically distributed around the central peak. They originate from the overlap regions in the transverse plane of the inner ITSu staves. In these regions, a track may generate more than one hit in a single layer, however only one hit is taken into account in the reconstruction algorithm [199]. Also in the FT2, only one hit per layer is considered.

As indicated by the red lines in figure 4.13, the combinatorial and correlated contributions can each be approximated with a Gauß-function. An additional correlation between the layers exists, because the track extrapolation length from one layer to the next changes with the different distances between two layers. Thus in case a fake cluster is picked in a given layer of the ITSu, the probability to pick up a fake cluster in the next layer is increased. For the FT2 these contributions were parameterized and included in a simplistic approach, where the magnitude of uncorrelated random hits is steered via an additional parameter, which is proportional to $\mathrm{d}N_{\mathrm{charged}}/\mathrm{d}y$ [199].

Especially the FT2 reconstruction efficiency of strange weak decays is strongly dependent on these fake clusters: Due to their large decay length of up to several meters, a large fraction of these decays occur outside of the inner ITSu barrel, which implies that there cannot be any true clusters in the inner three ITSu layers associated to the daughters tracks. When selecting primary tracks, typically a track quality cut is applied, which requires a hit in either the first, or in the second and third ITSu layers, and thus suppresses this background from secondaries. However, with an increased number of fake clusters, the probability increases that a fake cluster is wrongly assigned to the secondary track, which could then pass this selection criterion. As a consequence, this steering parameter was tuned to match the full MC production to which the FT2 is anchored. In addition, it can further be used to study the impact of fake clusters in the ITSu.

Note, that noisy pixels do not contribute to the generation of fake clusters in the (upgraded) ITS, and can be fully neglected compared to the signal. The current operation of the ITS detector shows that only individual hot pixels have a high fake firing rate, but all of these can be singled out. Their overall total amount is on per-mille level [199]. These hot pixels are masked correspondingly in full MC simulations, such that the given pixel is fully neglected in the reconstruction. Besides the masking of these pixels, noise in the (upgraded) ITS is not simulated [199].

4.3.7.3. Track smoothing

An additional smoothing algorithm was incorporated in the ITSu tracking [199], such that the simplified tracking code performance of the FT2 corresponds closer to the original ALICE tracking algorithm. At the stage where the track is propagated inward from the TPC to the ITSu, an additional track seed is propagated along the generated ITSu clusters in outward direction, and matched to the original one. For each sensing layer of the ITSu, the inward-going track is updated with the track parameters of the outgoing track, thus the optimal information from all other layers is used at any stage in the propagation of the final track. Note, that this is also the stage, where fake clusters may be attached to the inward-going track: The decision, whether a cluster, true or fake, is attached to a track is based on a χ^2-comparison.

4.3.8. Implementation of the Time Projection Chamber in the FT2

As the main tracking device in the ALICE central barrel, also the TPC needs to be implemented realistically in the fast simulation approach. Albeit its rather simple material distribution, which mainly consists of a large, cylindric gas volume, the segmentation of the TPC readout plane needs to be taken into account for a realistic description of the detector performance, as it includes regions, which are blind to the charge clusters. Visible in figure 3.8a, the support structure of the readout chambers leads to a gap between two adjacent chambers in the azimuthal coverage. These dead regions introduce a loss in acceptance. High-momentum tracks, which are only slightly bent in the magnetic field of the central barrel, may generate a large fraction of charge clusters exactly in the vicinity of these dead regions, and are thus not reconstructable. As a consequence, a simplified segmentation of the readout pad plane, as described in section 3.2.2, was implemented in the FT2.

Additional effects introduced by the detector are parameterized using a multi-dimensional fitting tool [200], and are explained in the following section. Note, that in current full MC simulations of the ALICE Experiment, only single events of hadron-hadron collisions are considered. Beyond Run 3 of the LHC, tracks from multiple-events will be present in the TPC, which will cause additional distortions of the $\vec{\mathrm{E}} \times \vec{\mathrm{B}}$-fields in the detector. However, it is expected that these can be fully corrected and that the TPC performance will remain similar to the current status, which is a crucial design requirement of the upgraded TPC [187].

4.3.8.1. Cluster-pickup probability

In a first step, the probability to find a charge cluster in the TPC is evaluated, which is mainly dependent on two effects: On the one hand, the charge signal induced on the readout pad planes is zero-suppressed by a lower threshold, which some clusters may not exceed. This effect is strongly dependent on the specific energy loss (and fluctuations) of a particle traversing the TPC, as the overall deposited charge must be sufficiently large to exceed the threshold of the cluster finding. This is further correlated with the dimensions of the readout pads, as larger readout pads group more charges into a single channel than smaller ones. On the other hand, high particle rates lead to a shift of the baseline of the overall charge with respect to the threshold, due to the ion tail of the charge clusters and crosstalk between them [200]. Moreover, the probability not to detect a charge cluster increases with increasing drift length, as for example diffusion may spread the charge over several readout pads. The latter effect is closely related to the track multiplicity in the detector, as the additionally generated charges induce distortions in the electric and magnetic fields.

Given these considerations, the probability to find a charge cluster in full MC was parameterized as a function of the inverse expected Bethe-Bloch energy loss based on the ALEPH parameterization, $1/(\mathrm{d}E/\mathrm{d}x)^{\mathrm{ALEPH}}$, the particle pseudo-rapidity η, and the particle multiplicity in the event. The latter was split into 5 bins in the parameterization, while the other two axes were each grouped into 10 bins. The inverse of the specific energy loss is used, as it appears more linear. Conceptually, the overall deposited charge also depends on the azimuthal angle, which was not considered in the multi-dimensional local regression fit, in order to keep the computation time reasonably low.

The probability to pickup a cluster in the TPC is determined from the fraction of found clusters based on the information whether another charge cluster was found in the adjacent readout pads. As the readout pad dimensions are different for the inner readout chamber, and the medium (OROC(medium)) and long (OROC(long)) outer readout chambers, the fit was performed for each chamber type separately.

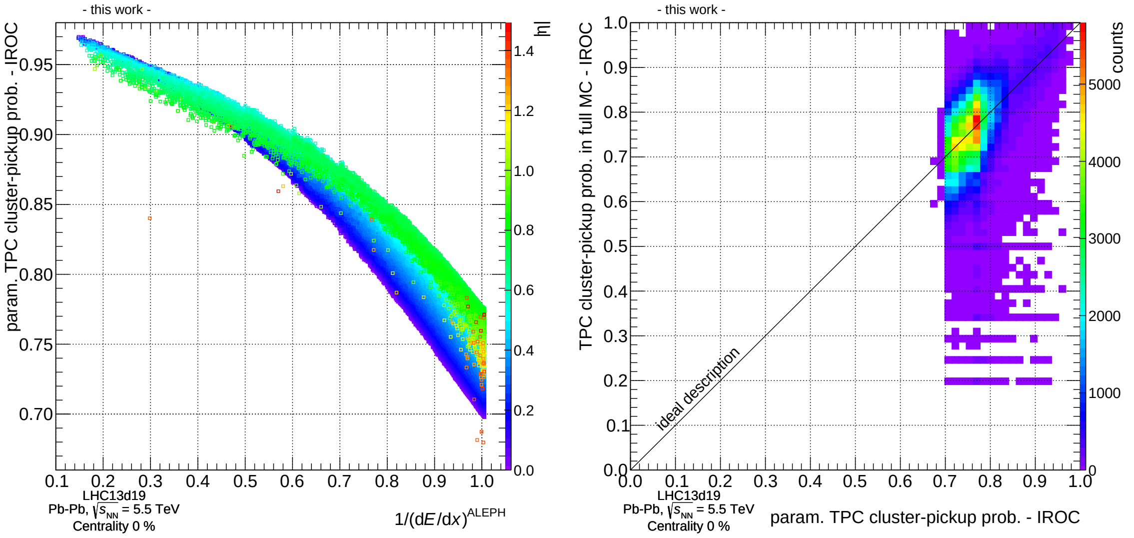

(a) **(b)**

Figure 4.14.: (a) displays the multi-dimensional parameterization of the TPC cluster-pickup probability, defined as the probability to find a cluster in the vicinity of ±1 readout pad around a pad with a detected cluster. A strong dependence on the inverse energy loss as well as pseudo-rapidity is observed. Note, that in this parametrization the true particle properties are used as input to the fit, and only a low momentum threshold at $p_{\mathrm{T}} \geq 150\,\mathrm{MeV}/c$ was applied in order not to bias the results. The comparison between the parameterization and the actual probability in full MC is shown in (b). As indicated by the diagonal line, the parameterization shows good agreement with the observed values in full MC. Individual counts, visible as horizontal bands, originate from the dead regions in $r\phi$-direction. This originates from the exclusion of the azimuthal dependence from the fit, which also causes the spread of the peak around 80 %.

An example of the (parameterized) multi-dimensional dependence of the probability to pick up a charge cluster in the IROC is given in figure 4.14a, where a strong dependence on the pseudo-rapidity and the specific energy loss is visible. Charge clusters generated from tracks around central pseudo-rapidity show a systematically lower probability to be detected, visible by the colored scale. For these tracks, due to the short track length inside the TPC, the overall deposited charge in the TPC is lower than for tracks with large pseudo-rapidity and the probability that the clusters are not found due to lower threshold cuts increases. Corresponding to the change in drift length, the pickup probability of these clusters is about 10–20 % lower at large values of $1/(\mathrm{d}E/\mathrm{d}x)^{\mathrm{ALEPH}}$. The probability for a charge cluster to be above threshold shows a large decrease down to 70 %, decreasing almost entirely linearly with decreasing energy loss, .

The performance of the multi-dimensional fit is displayed in figure 4.14b, where the cluster-pickup probability obtained from full MC simulations is shown. The ideal description is indicated by the diagonal line. The fit performs extremely well, although it returns a slightly lower probability, which is a result of the initial assumption of having a cluster in the adjacent pads. Note, that individual outliers in the full MC, which appear as horizontal lines in the figure, are not described. These stem from tracks along the dead regions in $r\phi$-direction of the IROC, which were not considered in the fitting algorithm. The remaining correlations between the parameterized probability and the different input dimensions are shown in appendix B.1, where also the parameterizations for the TPC OROCs are presented.

4.3.8.2. Parameterization of the cluster acceptance

In the environment of central Pb–Pb collisions, the drift region of the TPC is occupied by many charged clusters from tracks in the high-multiplicity events. During the track reconstruction in the ALICE TPC, a selection on the original position of charge cluster generation can be applied, as shown in figure 4.15a, such that only charge clusters generated by particles stemming from the primary vertex are accepted. This selection was used in older reconstructions but was removed in 2011. However, as the considered full MC simulation is anchored to data from 2010, it still appeared active. This algorithm was applied to reduce the total amount of data to process, and thus to speed up the overall track reconstruction.

At this stage, charge clusters generated at the innermost radius of the TPC were only accepted if they originated from a restricted longitudinal range around the inner electrode of the TPC ($Z = 0\,\mathrm{cm}$). This spatial selection corresponds to the drift time of a charge cluster from its point of generation until the readout chamber, and thus should also consider an additional margin for the delay introduced by the L1 trigger from other detectors. Recently, only a loose selection is applied, as displayed for a newer full MC production in figure 4.15a. Charge clusters generated at the innermost radial position of the TPC are accepted in a Z range of about 0–240 cm, which almost corresponds to the full drift region of the TPC.

However, in the full MC production specifically made for the ITSu performance studies, an error occurred: The selection, indicated by a red line, was too strict. This lead to fewer accepted charge clusters for particle tracks with large pseudo-rapidity, and eventually to a loss in reconstruction efficiency for these tracks, as the number of found TPC clusters is a hard criterion in the track quality selection.

The FT2 includes the selection on the cluster acceptance, which is taken from a parameterization of the corresponding full MC simulation (red lines in figures 4.15). As the impact is fully understood, the cluster acceptance selection can either be included in the FT2 simulation, e.g. for comparisons with existing full MC simulations, or can be set to optimal performance.

4.3.8.3. Parameterization of the cluster resolution

The spatial resolution of the measured charge clusters in local y- and z-direction also needs consideration, as it becomes specifically important in the calculation of the χ^2 of the track refit in the TPC. A simple error parametrization [200] used in the FT2 is visible in figure 4.16. Here, the resolution of the three different readout chamber types is shown as a function of the drift length for two different values of the track inclination angle ($\phi = 0°$ and $\phi = 20°$). With increasing drift length the resolution is degrading, as the charge diffusion increases along the drift path. An increase of the inclination angle, which is measured with respect to the readout pad plane, makes it more difficult to reconstruct the original point of charge generation. The parameterizations scale with the pad length, as visible from the comparison between the inner and outer readout chambers. Note, that these parameterizations were derived from an analytical formula fitted to p+p data [200], thus they do not include any performance degradation due to the high-multiplicity track environment in Pb–Pb collisions. These parameterizations have a precision of about $\pm 5\,\%$ [200]. Albeit the FT2 aims to describe central Pb–Pb collisions, they are nevertheless included as they provide the best

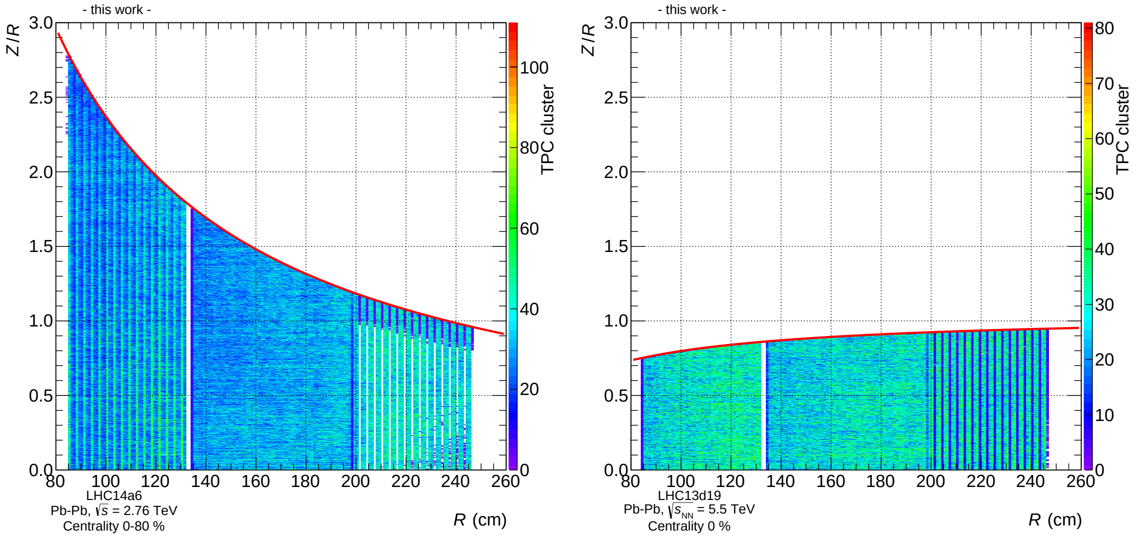

(a) **(b)**

Figure 4.15.: Selection of clusters for the track reconstruction in the ALICE TPC for two MC simulations of Pb–Pb collisions. A fit on the respective threshold is indicated by a red line. In (a), the nominal selection as used since 2011 is visible. In this configuration, almost all TPC clusters are accepted for the track reconstruction, independently on their radial position and distance to the central electrode. (b) shows a configuration, which was supposed to tightly selects those clusters, which are generated from particles near mid-rapidity. However, here, the delay of the L1 trigger was not correctly taken into account, and a more restricted selection was applied, with which a large fraction of tracks was rejected in the range $|\eta| \geq 0.7$. The gaps visible around $\mathrm{R} \approx 135\,\mathrm{cm}$ and $\mathrm{R} > 200\,\mathrm{cm}$ originate from the support structure of the TPC and the increased pad width in the OROC respectively.

available approximation by this time. Parameterizations of the Pb–Pb data could easily replace the current approximation, once provided by the experts.
When anchored to full MC productions, an additional tuning algorithm is applied, which recalculates the χ^2 of the track refit in the TPC obtained with the FT2, to match those values in the corresponding full MC simulation. This is necessary, so that in the subsequent physics analysis no selection criteria need to be re-optimized by the user. Depending on the track quality, this correction factor is typically in the order of 10 %.

4.3.8.4. Parameterization of $\vec{\mathrm{E}} \times \vec{\mathrm{B}}$-distortions

As indicated in figure 3.8a, the electric ($\vec{\mathrm{E}}$) and magnetic ($\vec{\mathrm{B}}$) fields are parallel in the drift region of the TPC, which is part of its fundamental design concepts. In this setup, the magnetic field significantly suppresses the transverse charge diffusion [178]. However, small inhomogeneities in the two fields introduce distortions, which may lead to a displacement of the charge clusters at the readout pad plane in radial and $r\phi$-direction of up to 1.4 cm (visible on the colored z axis in figure 4.18). These local distortions can be mapped to their position in (r, ϕ, Z) obtained from the offline detector calibration [200]. They become critical especially in the areas near the dead regions of the TPC readout plane, as they may transport charge clusters in and out of these regions, and may thus influence the track reconstruction efficiency.

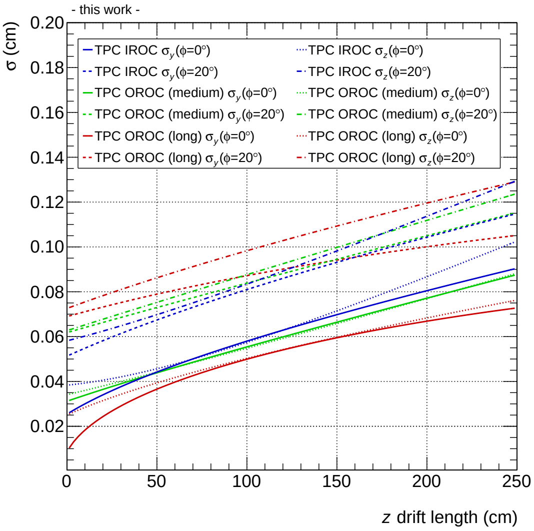

Figure 4.16.: TPC cluster position uncertainty in local y- and z-coordinates for the IROC, OROC(medium) and OROC(long). Generally, resolutions improve with decreasing drift length of the charge clusters, as diffusion decreases. For increasing track inclination as well as increasing pad dimensions, the resolution worsens. They were generated based on input by [200] and the TPC group in ALICE.

Using the multi-dimensional fitting tool on the distortions as a function of their local coordinates, realistic maps of the $\vec{\mathrm{E}} \times \vec{\mathrm{B}}$-distortions for the two (same and opposite direction) magnetic field configurations (B^+ and B^- with a field strength of 0.5 T) in the central barrel were determined and included in the FT2. The comparison between the actual distortions and their parameterization for the B^+ setup are displayed in figure 4.17 in radial (left) and rϕ-direction (right) respectively, showing the good quality of the fit. In case a different magnetic field setup is chosen, e.g. $\mathrm{B} = 0.2\,\mathrm{T}$ as foreseen in the future low-field runs, an additional parameterization would be required. It can be easily included, once the input calibration data is made available by experts.
An example of the actual parameterized distortion maps in radial direction for the B^+ configuration is displayed in figure 4.18. Here, 10 cm thick slices in the TPC are shown, going from one endcap (at $Z = -250\,\mathrm{cm}$) to the other (at $Z = 250\,\mathrm{cm}$). Two significant structures are observed: First, looking at the slices at the endcaps (top left and bottom right), structures with distinct edges are present, which stem from residual mis-alignment of the readout chambers. Note, that this is the only point were mis-alignment enters the fast simulation. Second, at the innermost radii in each slice, significant distortions are visible. These originate from displacements of the conducting TPC foil bands, which make up the TPC field cage (sketched in the top left of figure 3.8b). While in actual data recording these effects have to be corrected, in a realistic description in full MC they are added for each cluster specifically and thus included in the track reconstruction. In a similar approach, these field distortions are fully parameterized and thus available for look-up in the FT2. They are applied in the corresponding direction on each generated cluster. During the track reconstruction stage, these clusters are then taken into account with their updated position. A cluster is neglected in case it was moved into the dead regions of the readout chambers of the TPC. The corresponding parameterizations of the negative magnetic field polarity as

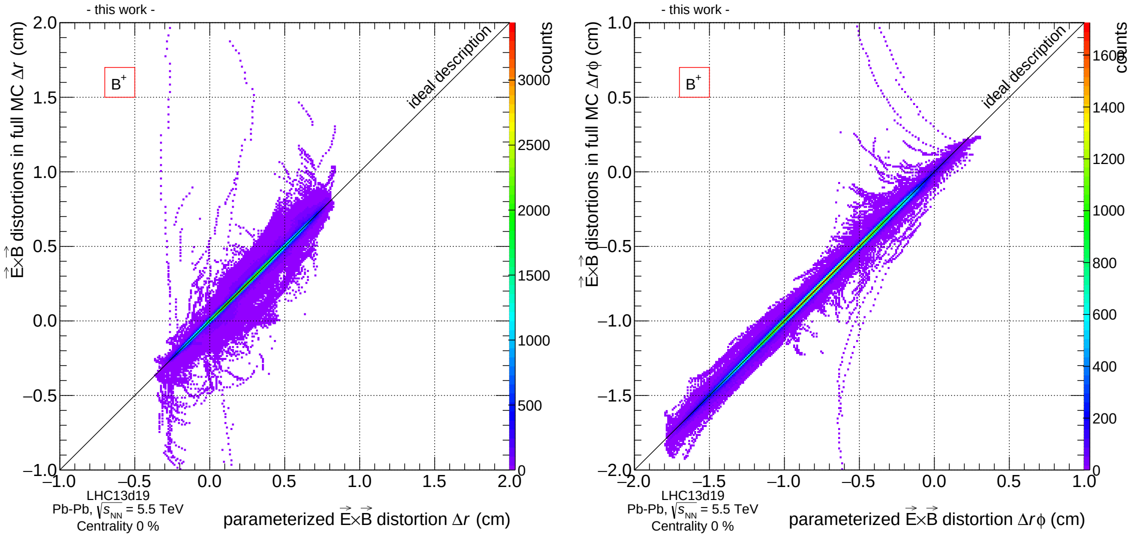

(a) **(b)**

Figure 4.17.: Parameterizations of $\vec{\mathrm{E}} \times \vec{\mathrm{B}}$-distortions in r- and $r\phi$-direction, compared to the results from the offline analysis for the B$^+$ configuration in the ALICE central barrel in (a) and (b), respectively. Except of single outliers, which correspond to less than 1 % of all clusters, the full simulation is well described by the parameterizations. These outliers correspond to single clusters with extreme distortions near the inner radius of the field cage. On average these are correctly parameterized, as visible in figure 4.18. The presented figures were obtained from full MC simulations with a magnetic field strength of $\mathrm{B} = 0.5\,\mathrm{T}$ in the ALICE central barrel.

well as the correlations between the different dimensions of the parameterized distortions and the input dimensions are given in appendix B.2.

4.3.8.5. Parameterization of the mass hypothesis during tracking

As already described in item 7 of the general working principle of the FT2 in section 4.3.2, an assumption of the particle species is made during the track reconstruction in ALICE, based on the specific energy loss of the particle in the TPC. Up to this point, all particles were identified via their MC truth information while traversing the gaseous TPC medium. However, in the tracking within the ITSu, the improved assumption on the particle species is used to estimate the material interactions and multiple scatterings in the ITSu detector. The TPC PID signal, which is proportional to the expected specific energy loss of electrons, muons, pions, kaons and protons is displayed in figure 4.19a for particles identified via their MC truth information. Here, the specific energy loss (ALEPH parameterization) and the expected width σ of the corresponding Gauß-distribution are calculated from the track parameters, such as the momentum, and the number of found charge clusters in the TPC. The PID signal is then randomly sampled from the distribution. These estimates are used to assign a probability to a given particle to be of a given type. The species, which corresponds to the largest probability, is then assigned to the track for further propagation. The species hypothesis obtained from these probabilities is displayed in figure 4.19b for the same input as before. As pions are most abundantly produced, their mass hypothesis is assigned as default (green). Due to their ambiguity, true electrons are always assigned to

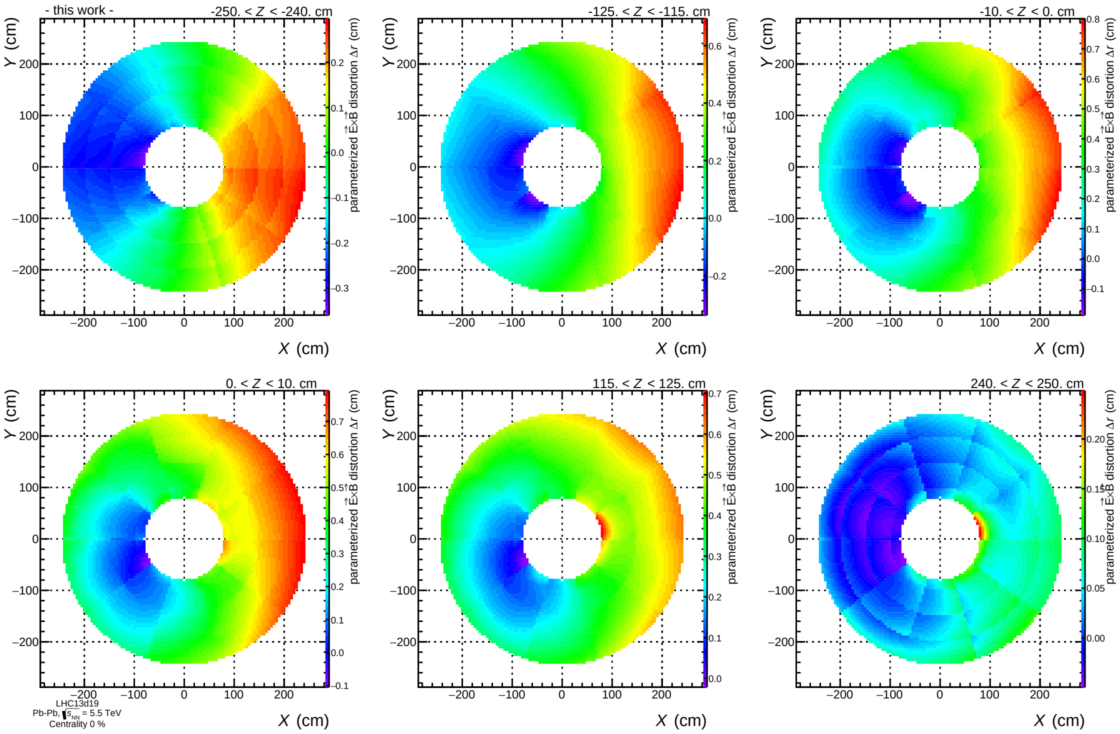

Figure 4.18.: Parameterized map of the r-distortions for the B^{+} setup in the ALICE central barrel. Going from one endcap of the TPC to the other, six slices of the TPC column are depicted. Near the endcaps (top left and bottom right) distortions, induced by mis-alignment of the readout chambers are visible. For the innermost radii inside the TPC, large but local distortions are visible, which originate from misplaced foils of the TPC field cage. The data was obtained from full MC simulations based on the TPC detector performance in the 2010 Pb–Pb data taking period.

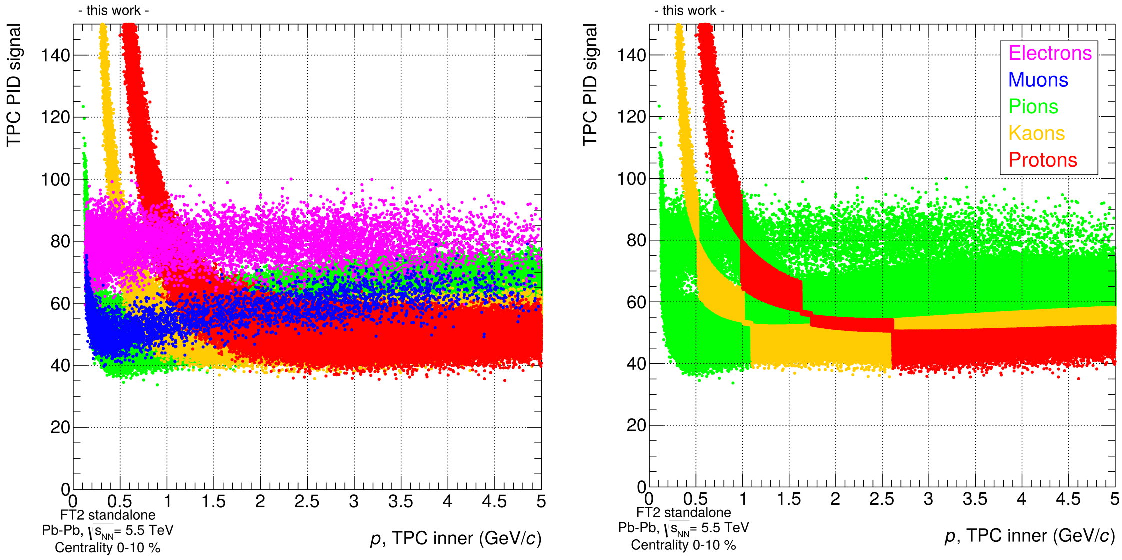

(a) **(b)**

Figure 4.19.: TPC PID signal as a function of momentum evaluated at the innermost radius of the ALICE TPC during the track reconstruction. Particles are identified by MC truth (a) or by probability calculation (b), which is eventually used in the code. As default, particles are identified as pions, because these are produced most abundantly in Pb–Pb collisions. In regions, where the algorithm finds a higher probability for the specific energy loss to originate from another particles species, the kaon or proton mass is assigned. Due to the ambiguity in most regions of the PID signal, electrons and muons are always identified as pions.

the pion mass hypothesis, as well as the true muons. The two signal bands of kaons (yellow) and protons (red) are assigned only in region of large confidence, and are minimized, where the true electron and true muon bands are intersecting (at $p = 0.5$ and $1\,\mathrm{GeV}/c$, as well as $p = 1.1$ and $1.7\,\mathrm{GeV}/c$). This is a valid approximation, as the energy loss of the different species appears similar over a wide momentum range.
Note, that in the full MC production used for the ALICE ITSu production, the TPC PID signal was slightly underestimated, which lead to a shift of the specific energy loss during the track reconstruction, and thus a (partially) wrong tracking mass hypothesis. As a consequence of the wrongly assigned PID assumption, multiple scattering and material interactions in the material of the ITSu are not correctly taken into account, which affects the quality of the Kalman filter propagation, and thus has to be considered. The shift of the PID signal by about 25 % is visible in figure 4.20a, and can be included in the FT2 code via another multi-dimensional parameterization of the PID signal using the local regression fit. Here, the multi-dimensional fit is performed as a function of $1/\left(\mathrm{d}E/\mathrm{d}x^{\mathrm{ALEPH}}\right)$, $|\eta|$, and charged-particle event multiplicity. As before, the multiplicity range was split into 5 bins in the parameterization, while the other two axis were each grouped into 10 bins. Note, that the observed shift in the number of PID clusters does not influence the TPC PID performance used for particle identification in the latter analyses, as the discrimination power is obtained through fits of the ALEPH parameterization to the signal, and not through the measurement directly.

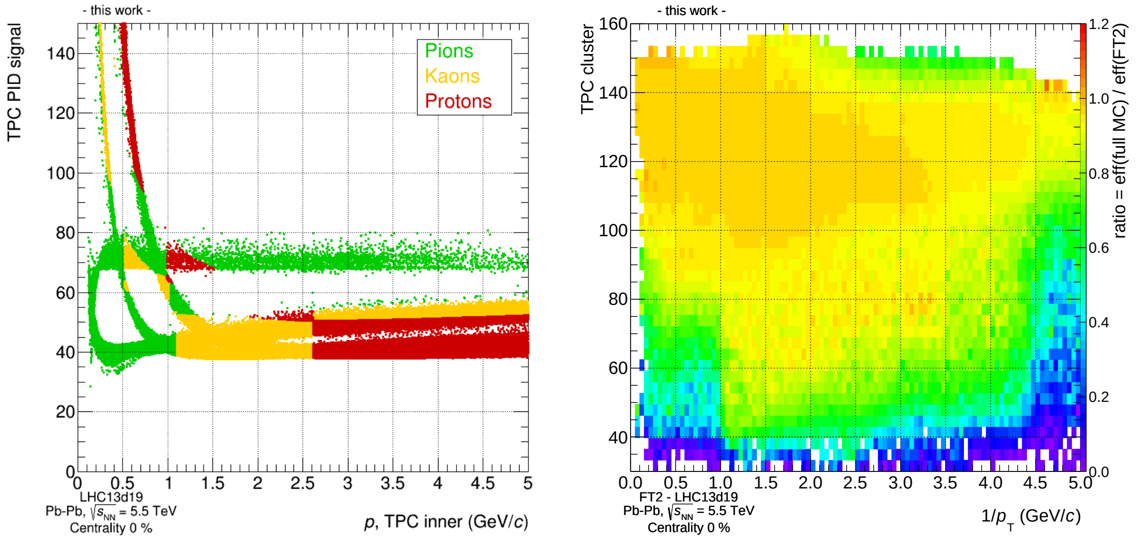

(a) (b)

Figure 4.20.: In (a), the parameterization of the tracking mass hypothesis in the anchored full MC production is displayed. Note, that the expected TPC PID signal of the full MC simulation was parameterized as a function of the inverse specific energy loss, pseudo-rapidity and track multiplicity, and the values appear more narrowly distributed within their bands. Here, the TPC PID signal is lower by about 25 % compared to figure 4.19, which sometimes leads to a false assumption on the particle species. Potential muon or electron candidates are always tracked as pions. (b) displays the ratio of the track prolongation efficiencies between the ITSu and TPC in full and fast MC simulations. For tracks with high quality, visible by their large number of TPC clusters, the FT2 prolongation efficiency reproduces the full MC well. For lower momentum, and/or tracks with less TPC clusters, the FT2 overestimates the prolongation efficiency and the ratio decreases. This is a consequence of the approach taken in the FT2, where tracks are reconstructed one-by-one and less mis-matches with other tracks/clusters can occur when the track is prolongated from the TPC to the ITSu. In heavy-flavor analyses of central Pb–Pb collisions, typically a minimum of 70 TPC clusters per track and a reconstructed track $p_{\mathrm{T}} \geq 500\,\mathrm{MeV}/c$ are required.

4.3.8.6. Parameterization of the prolongation efficiency

The last ingredient for the FT2 is the track prolongation efficiency between the ITSu and the TPC. A small fraction of tracks is lost during the reconstruction, as for some tracks, which are extrapolated during reconstruction from the TPC through the gap between ITSu and TPC, no matching ITSu track can be found. This could be caused by large uncertainties in the covariance matrix, e.g. from energy loss fluctuations, or wrongly matched clusters in the ITSu and TPC in high-occupancy events. As the FT2 uses a simplified tracking algorithm to reconstruct each track individually the track-prolongation capability is over-estimated. The ratio of matched tracks for the full-over-fast MC simulation is presented as a function of assigned TPC clusters and inverse p_{T} in figure 4.20b. Note, that in this comparison only a minimalistic requirement of 30 assigned clusters in the TPC and $p_{\mathrm{T}} > 0.15\,\mathrm{GeV}/c$ on the tracks were placed, such that the ratio remains unbiased by other effects. For high track quality, and tracks with larger momentum, e.g. in the region of $N_{cls}^{\mathrm{TPC}} \geq 120$ and inverse $p_{\mathrm{T}} \geq 2.5\,\mathrm{GeV}/c$, the difference is as low as a few percent. Within this region, tracks typically have a particularly well defined covariance matrix in the TPC, which is described similarly good in the FT2. However, when the track quality slightly decreases in full MC, e.g. for lower N_{cls}^{TPC} ($\approx$ 60) the track prolongation efficiency in the FT2 is increasingly overestimated (still at around 100 %) and the plotted ratio decreases to about 60 %, because the full MC efficiency reduces to around 60 %. For low p_{T}, the curvature of the track increases and the track-matching becomes increasingly difficult in full MC simulations, which leads to decreases in the efficiency. This effect is further enhanced by the dead regions in the TPC detector, which are described on a simplistic level in the FT2. Typically in full MC, for pions with $p_{\mathrm{T}} \geq 500\,\mathrm{MeV}/c$ more than 120 TPC clusters are assigned on average to a track.

4.3.9. Performance of the FT2

The FT2 was generated as a highly performant code, which needs to be fast and reliable, with a reasonable memory consumption. In order to verify these properties, the performance of the tool was analyzed in different stages. For a first characterization, a simple test was performed, which uses the FT2 to evaluate 10 000 particles, randomly and homogeneously distributed in a momentum range between $0.2 - 10.0\,\mathrm{GeV}/c$ within $|\eta| < 0.9$ and the full azimuth. An equal share of pions, kaons, proton, electrons and muons was generated with positive and negative charges. The performance of the code was checked using *callgrind*, which is a cache profiler with call-graph information, based on the *valgrind* tools [229], and *massif* [230], a profiler for allocated memory. With the former tool, an individual slow function call during the propagation of each individual particle inside the active TPC volume was identified and replaced by a significantly faster method (TF1[i] → TFormulaPrimitive[ii]), which improved the relative speed of this step by a factor of six. The result of the total memory consumption as a function of running time measured by *massif* is displayed in figure 4.21. The peak structures at the beginning of the test correspond to the loading of specific settings from the ALICE Offline Condition Data Base (OCDB), in which calibration and status information of the ALICE detector is stored. During the propagation and reconstruction of the 10 000 particles, a constant memory consumption is observed, with a peak value of about 200 MiB ($\approx$ 210 MB), indicating that no harmful memory leaks are present in the code.

4.3.9.1. Performance based on full ITSu simulation

Within the scope of this thesis, the FT2 was tuned on an available full MC simulation using the ALICE ITSu detector, as it is described in section 3.3.3. It should be mentioned, that the TPC detector was simulated with its current performance, which is expected to remain similar after LS2 of the LHC [187]. For a valid comparison between the FT2 and full MC performance, the exact same generated MC events were analyzed and the track reconstruction performance of the two algorithms evaluated. The FT2 was specifically anchored to the full MC production, as presented throughout this section, and some peculiarities of this specific full MC sample had to be considered. First, the ITSu single pixel resolution was set to the (2.25,2.25) μm configuration to account for the simplified tracking in the FT2, as displayed in figure 4.12. Further, as presented in figure 4.15b, an error occurred in the full MC production during the TPC cluster reconstruction, which

---

[i] one-dimensional function class inside the ROOT framework

[ii] helper class to speed up TFormula evaluation inside the ROOT framework

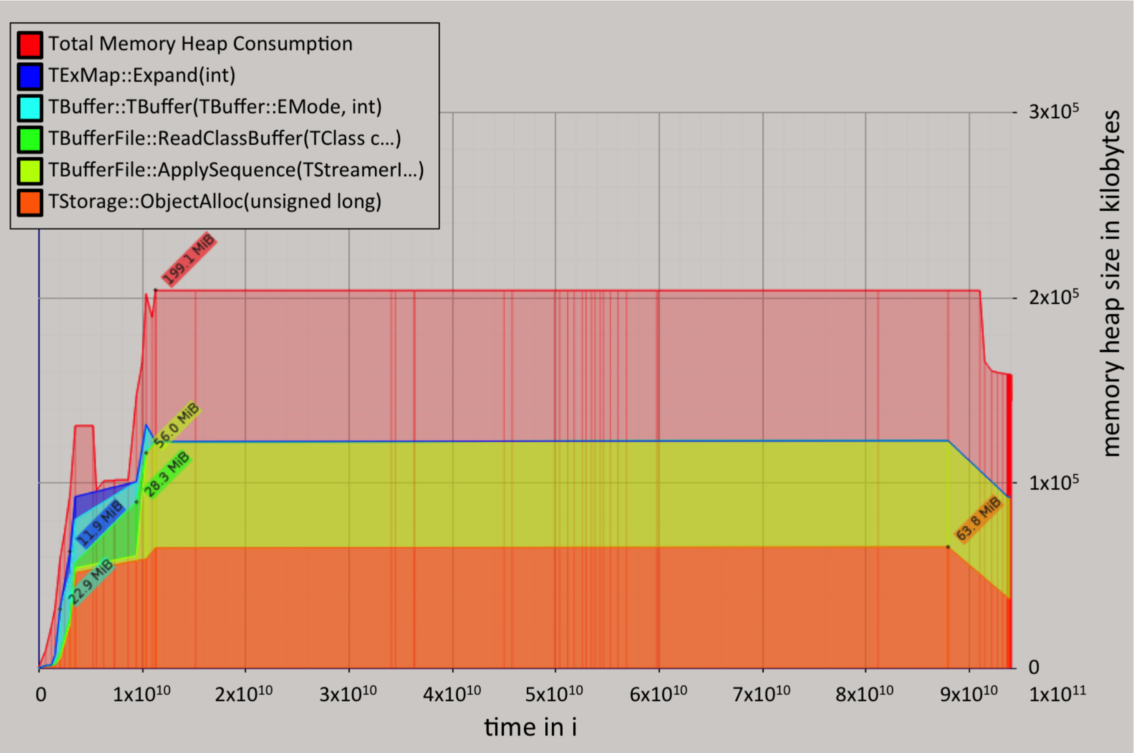

Figure 4.21.: Total memory consumption as a function of processing time of a test production with the FT2 of 10 000 particles, equally distributed over particles species (e, μ, π, K, p) and charge. After initial fluctuations in the memory consumption during the loading of parameters, the distribution is flat at a maximum of 200 MiB during the particle processing, indicating that no unwanted memory leaks are present. The code was analyzed using the massif-visualizer [230].

Parameter	Setting
simulate material	yes
step size	1.0 cm
allow decay	kaons only
allow absorption	no
track secondaries	yes
random fake clusters	dN/dy=1.
correlated fake clusters	yes
tune on anchor	
ITSu pixel resolution	yes
ITSu+TPC matching efficiency	
TPC cluster acceptance	
TPC $\chi^2/\mathrm{N}^{\mathrm{TPC}}_{\mathrm{cluster}}$	
tracking PID	

Table 4.1.: Settings of the FT2 when anchored to the full MC production of ALICE with the ITSu detector (LHC13d19). In this configuration, the performance of the FT2 was characterized throughout this thesis.

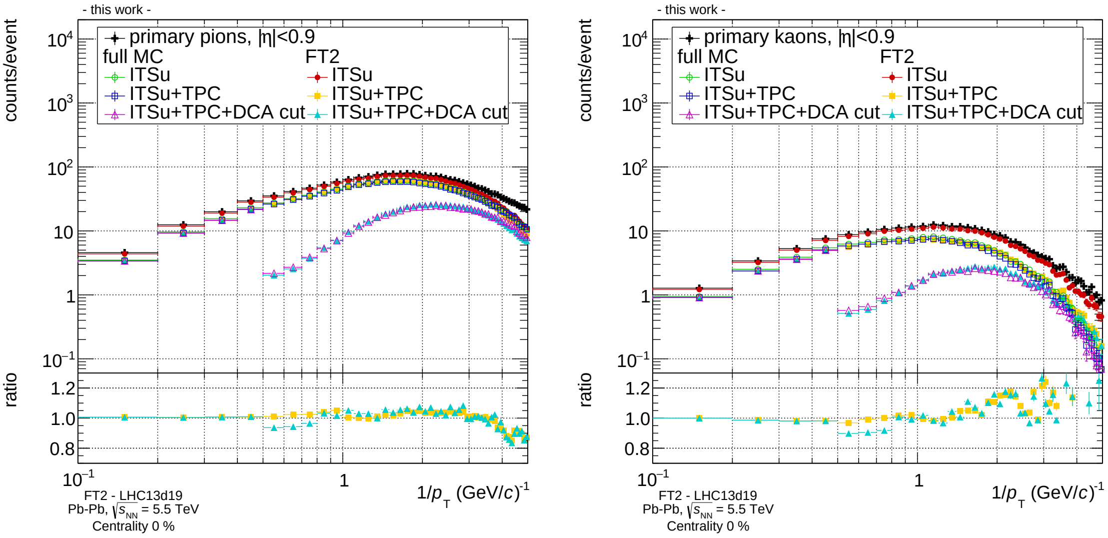

(a) **(b)**

Figure 4.22.: In these figures, the tracking performance of fast and full MC simulations is displayed as a function of p_T for primary pions (a) and kaons (b). Different track selection criteria are applied, requiring ITSu, ITSu+TPC and ITSu+TPC+DCA cuts, as explained in table 4.2.

was included in the FT2. In addition, the mass hypothesis at the innermost radius of the TPC is not correctly determined, and about 25 % less TPC PID cluster were found in the reconstruction (figure 4.20a). This effect leads to a shift in the probability calculation of the species assumption, as displayed in figure 4.20a.

Given the structure of the FT2 framework, these effects were parameterized and stored in the accompanying files of the algorithm, such that they can be loaded during its application. The complete tune of the FT2 is shown in table 4.1. All of these settings were tested and tuned for best performance in the single particle reconstruction, presented in the next section. Here, allowing only the kaon decay and no absorption in the material gave the best description. At low momentum, the FT2 tends to overestimate effects from material interactions, thus a better description of the full MC sample was achieved without these additional algorithms. The extended algorithm to track secondary particles was enabled, such that for example strange weak decays were correctly taken into account, as these were also generated in the full MC simulation. However, uncorrelated fake cluster generation was set to a minimal value, as this delivered the best performance in the strange weak decay reconstruction, which is particularly sensitive to fake clusters.

As the identified detector effects were well under control, the FT2 was set to optimal performance of all included detectors when operated in standalone mode at a later stage, which is explained in section 4.3.9.3.

4.3.9.2. Single track reconstruction

The performance of the signal track reconstruction for primary pions and kaons generated per event is shown in figures 4.22a and 4.22b, respectively.

Track Selection	Settings
ITSu	hits in first or (second and third) ITSu layer minimum of 4 ITSu clusters ITSu refit
ITSu+TPC	ITSu (see above) minimum of 70 TPC clusters TPC refit
ITSu+TPC+DCA cut	ITSu+TPC (see above) $\mathrm{DCA}^{\mathrm{XY}} > 30\,\mu\mathrm{m}$ for $p_{\mathrm{T}} < 2.0\,\mathrm{GeV}/c$ $\mathrm{DCA}^{\mathrm{Z}} < 1.0\,\mathrm{cm}$

Table 4.2.: Track selection criteria as required by the track reconstruction in the ITSu and ITSu+TPC detectors. In addition, a DCA cut was applied, as typically used for the analysis of heavy-flavor decays in ALICE.

Here, different track selection criteria are applied in order to demonstrate their individual impact. In the p_{T}-range above $200\,\mathrm{MeV}/c$, the black crosses represent the total amount of generated primary particles in a pseudo-rapidity interval of $|\eta| < 0.9$. In the upper part of the plot, the different track selection criteria, as summarized in table 4.2, are displayed as open circles (ITSu), squares (ITSu+TPC) and triangles (ITSu+TPC+DCA cut), respectively.

In the full MC reconstruction, TPC standalone track reconstruction was enabled, while no ITSu standalone tracking was active. This explains the observation of the large difference between the generated particle distribution and the ITSu track selection. For the same reason, the difference between ITSu and ITSu+TPC selection is almost negligible, as the tracks which are fully reconstructed in the TPC, are likely to have associated clusters in the ITSu detector as well. In case of the ITSu selection of the FT2 track reconstruction, the situation looks differently. By construction, almost all tracks in the considered pseudo-rapidity range have associated ITSu clusters, except of tracks with low momentum. Further applying the ITSu+TPC selection, reduces the amount of good reconstructed tracks. An additional hard selection on the track distance of closest approach to the primary vertex was applied for comparison, as this is a typical selection criteria in heavy-flavor meson analysis: Large fractions of primary (non-displaced) particles are rejected, while the fraction of particles stemming from heavy-flavor mesons or strange weak decays is enhanced, because their DCA is wider due the increased displacement with respect to the primary vertex.

The ratio of the amount of reconstructed particles in the FT2 over full MC is displayed in the lower part of the plots in figure 4.22. Here, the ITSu+TPC selection as well as the ITSu+TPC+DCA cut selections are compared. For the former, the agreement between the two is within a few percent down to about $250\,\mathrm{MeV}/c$ for pions, and $500\,\mathrm{MeV}/c$ for kaons. For such low momentum, the simplified track reconstruction in the FT2 and a slight overestimation in the energy loss lead to the observed small deficit in the track reconstruction efficiency for pions. In addition, the generation of correlated and combinatorial fake clusters in the ITSu influences tracks at low transverse momentum most (section 4.3.7.2), such that the simplified algorithm in the FT2 introduces some deviations in this kinematic range. Within statistical uncertainties, an opposite trend seems visible for kaons at low p_{T}, where the reconstruction efficiency in the FT2 appears slightly enhanced. This may be a consequence of the simplified implementation of kaon decays in the FT2 (section 4.3.5). However, it is noteworthy that the typical heavy-flavor analysis in ALICE in Pb–Pb collisions uses a kinematic threshold on the reconstructable particles of $p_\mathrm{T} \geq 500\,\mathrm{MeV}/c$, in order to reduce combinatorial background. Also, daughter tracks of heavy-flavor decays there is almost no yield below $p_\mathrm{T} \leq 500\,\mathrm{MeV}/c$. The ratio of the ITSu+TPC+DCA cut selection between full MC and FT2 (turquoise triangles in figures 4.22) reflects the capability of the FT2 to correctly reconstruct not only the track kinematics, but also the topology of the single track spectra. Despite some systematic overestimation of the DCA, and thus lower reconstruction efficiency, around $p_\mathrm{T} = 1.2 - 2.0\,\mathrm{GeV}/c$, the DCA selection does not impose a significant difference between the yields. The small systematic deviation of 5–10 % is a consequence of the simplified tracking and smoothing algorithm in the FT2, which results in slightly wider DCA distributions in this kinematic range, and thus a large rejection of primary particles induced by the threshold cut.

Using similar selection criteria as described above, the track reconstruction performance for particles from strange weak decays is displayed for pions and protons in figures 4.23a and 4.23b, respectively. Two significant features are visible: On the one hand, the ITSu selection significantly reduces the reconstruction efficiency of strange weak decays. For the largely displaced tracks, which may be generated many centimeters away from the primary vertex, the requirement of having a hit in the first (or second and third) ITSu layer is not fulfilled in most cases, while the TPC track reconstruction performs as usual. On the other hand at low momentum the FT2 has a systematically lower reconstruction efficiency due to the simplified application of fake tracks. This could be compensated with an increased amount of fake clusters, which in turn would also lead to an increase of the efficiency at high momentum. This effect is compensated by the DCA selection, as the FT2 tends to overestimate the DCA width, especially at low transverse momentum (figure 4.12). Above $p_\mathrm{T} > 500\,\mathrm{MeV}/c$ good agreement is observed, which is particularly important in heavy-flavor analyses, as the strange weak decays are a significant source of background.

Many additional checks were carried out to verify the excellent performance of the FT2: As it is of particular importance for the presented analysis of the decay $\mathrm{B}^+ \rightarrow \overline{\mathrm{D}}^0\pi^+$ ($\overline{\mathrm{D}}^0 \rightarrow \mathrm{K}^+\pi^-$), these cross-checks are presented together with the full MC results in section 5.1, such as the reproduction of the invariant mass position and resolution, presented in figure 5.5, or the secondary vertex resolution in figure 5.6. In particular, the impact of missing PID information in the ALICE TPC and TOF detectors in the FT2 as well as systematic uncertainty of the FT2 compared to full MC, are discussed for the analysis of $\mathrm{B}^+ \rightarrow \overline{\mathrm{D}}^0\pi^+$ ($\overline{\mathrm{D}}^0 \rightarrow \mathrm{K}^+\pi^-$) in section 5.4.

4.3.9.3. FT2 standalone simulation

Within this thesis a large data sample of central Pb–Pb events was produced with the FT2 for the analysis of the particle background of the signal decay channel $\mathrm{B}^+ \rightarrow \overline{\mathrm{D}}^0\pi^+$ ($\overline{\mathrm{D}}^0 \rightarrow \mathrm{K}^+\pi^-$). Given the statistical limitation of the generated statistics available in full MC for the presented analysis, it was decided to generate a Pb–Pb MC sample of 100 million events with 0–10 % centrality at $\sqrt{s_\mathrm{NN}} = 5.5\,\mathrm{TeV}$, using the available computing facilities at GSI. Even though the application of the FT2 to the analysis will

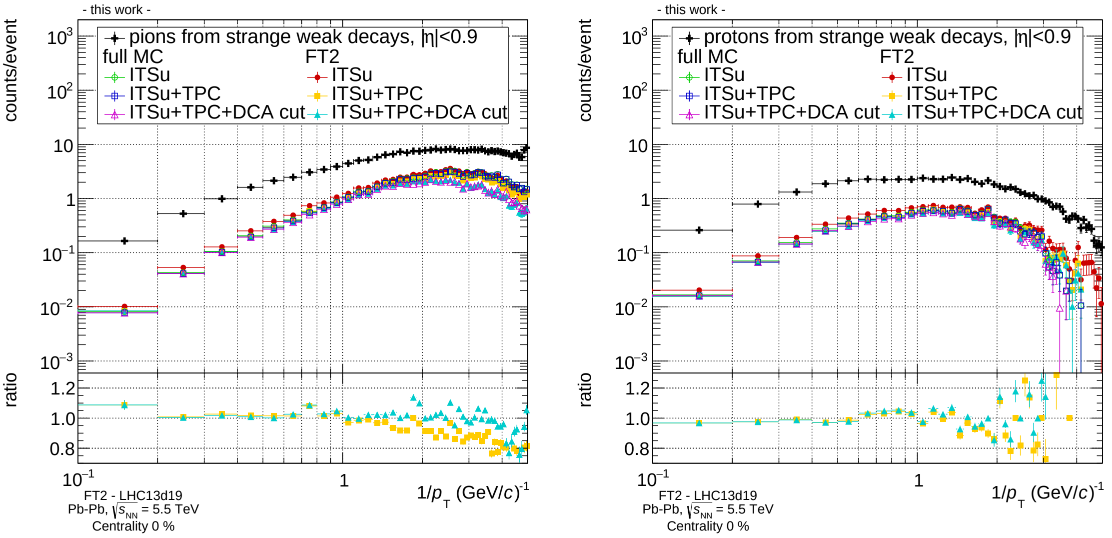

(a) **(b)**

Figure 4.23.: In these figures, the tracking performance of fast and full MC simulations is displayed as a function of p_{T} for pions (a) and protons (b) from weak decays of strange particles. Different stages of track selection criteria are applied, requiring ITSu, ITSu+TPC and ITSu+TPC+DCA cuts, as explained in table 4.2.

only be presented at a later stage in section 5.4, the setup of this standalone FT2 simulation is discussed and summarized in the following.

As shown in the previous section, the full MC production, with which the ITSu detector design was characterized and the performance of different analyses was studied, included some non-ideal effects. For a more realistic description of the ALICE upgrade capabilities, it was decided that the large standalone FT2 MC production should actually be tuned on the best anticipated performance. As these features, namely the shift in the PID mass hypothesis and the limitation in the TPC cluster acceptance, were studied, well understood and incorporated in the FT2 while it was anchored to the full MC production, the algorithm was now tuned to the expected nominal performance, as summarized in table 4.3. After first tests of the code performance and timing on the global ALICE computing GRID, available computing resources were identified at the GSI facility in Darmstadt, where a computing cluster of 200 nodes of Intel Xeon E5-2660 (20 cores · 2 (HyperThreading))128GB RAM processors is available [231]. Given that the full reconstruction of the FT2 is about $\mathcal{O}(10^3 - 10^4)$ faster than a typical full MC production, the ultimate goal of 110 million events was defined as a realistic goal, including a 10 % margin. At most 4000 parallel jobs were available for this purpose at the fast *nyx* cluster at GSI, and the infrastructure was prepared such that the performance for other users was not disturbed. For this reason, the individual jobs were limited to 100 events per job, which lead to an overall running time of about 50 minutes per job. This includes the generation of AOD tracks and pre-filtering the required secondary vertices.

However, despite the significant speed up of the code, the output file size of the generated data was initially unchanged. After a first estimate of a maximum total file size of 1 PB, the total output file size was reduced to about 180 TB. This was achieved by filtering

Parameter	Setting
MC Generation	HIJING, $\sqrt{s_{\mathrm{NN}}} = 5.5\,\mathrm{TeV}$, 0–10 % centrality $+30\ \mathrm{B}^+ \rightarrow \overline{\mathrm{D}}^0\pi^+\ (\overline{\mathrm{D}}^0 \rightarrow \mathrm{K}^+\pi^-)\ ^i$, $\vert y\vert<1.0$ +GEANT3/PYTHIA for strange weak decays
simulate material	yes
step size	1.0 cm
allow decay	kaons only
allow absorption	no
track secondaries	yes
random fake clusters	$\mathrm{d}N/\mathrm{d}y$=1.
correlated fake clusters	yes
tune on anchor	partially
ITSu pixel resolution	tuned on full sim.
ITSu+TPC matching efficiency	tuned on full sim.
TPC $\chi^2/\mathrm{N}^{\mathrm{TPC}}_{\mathrm{cluster}}$	tuned on full sim.
TPC cluster acceptance	nominal performance
tracking PID	nominal performance

Table 4.3.: (^{i} and charge conjugates) Settings of the standalone FT2 simulation. The expected performance of the ITSu detector was tuned on the available full MC simulation, however other specifications were set to the nominal expected performance.

only $\overline{\mathrm{D}}^0$ candidates with some loosely tuned analysis cuts, excluding the analysis of other multi-prong decays. The time measurement on the *nyx*-cluster of the individual processing steps is displayed for 200 random jobs in figure 4.24a. About 68 % of the real time is spent in the generation of the central Pb–Pb events by the event generator, while, after the optimization, less than 7 % are used for the AOD filtering. The FT2 itself, including the complete cluster generation, track reconstruction, ESD generation and primary vertex reconstruction, requires only the remaining 25 % of the real time. The output file size of the same jobs is displayed in figure 4.24b. After the optimization, the file size of the friend file, which contains the secondary vertex information, is reduced to a negligible amount of about 2 % of its initial size. Thus, the AOD file, which includes a copy of all tracks and the corresponding MC truth information, dominates the file storage. Currently, additional efforts are made by the ALICE Collaboration, to reduce the overall files size of the AOD. With an overall average job success rate of about 96 %, 104 million central Pb–Pb events were generated in about three weeks continuous running time at the *nyx* cluster. After cleanup of individual broken files, almost 99 million events were available for the analysis of charged B mesons, presented in this thesis. The low rate of job failures was mainly due to problematic exceptions in the generation of the MC events, and individual tracks which caused problems in the FT2 propagation. The latter problem was not (yet) further investigated, as is caused failures only for a few percent of the overall rate.

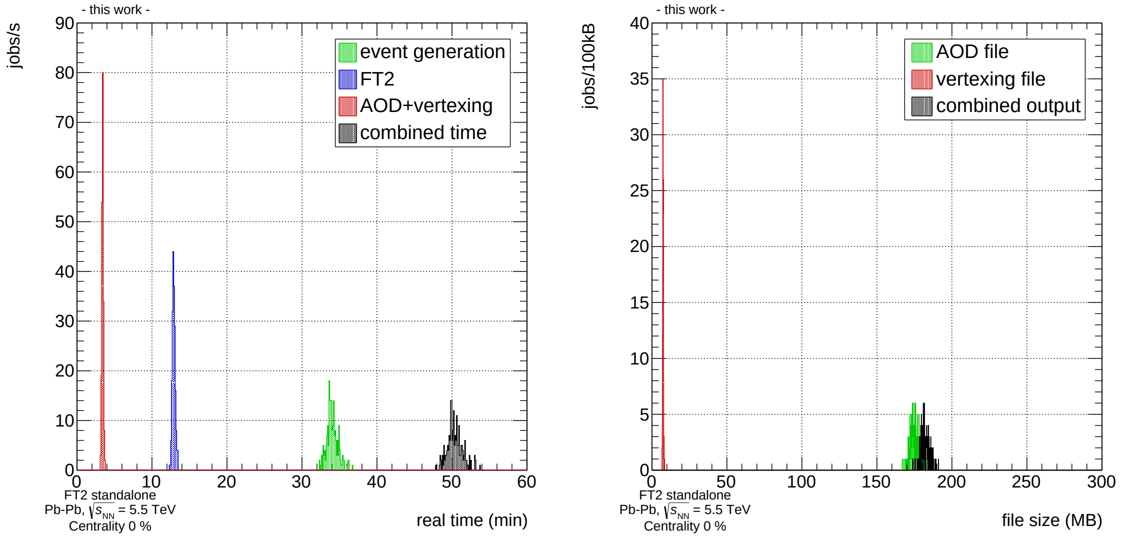

(a) **(b)**

Figure 4.24.: In these figures, the performance of the FT2 standalone simulation on the computing cluster at GSI is presented for 200 randomly chosen, representative jobs. (a) displays the fraction of the running time of the simulation. Most of the time is spent in the MC event generation of the physics event, while the FT2 itself only requires about 25 % of the total time. (b) shows, that the total combined file size is dominated by the AOD file. If all possible candidates are considered the vertexing file is typically even larger. However, though a limit on the reconstruction of two-prong vertices only, and by the application of loose selection criteria already at this filtering stage, the files size was reduced to a negligible amount.

5. Exclusive reconstruction of B^+ mesons in central Pb–Pb collisions

As outlined in section 2.3.4, the measurement of beauty hadrons using the full kinematic reconstruction over a wide p_{T} range at mid-rapidity is a particularly interesting probe to study the QGP in heavy-ion collision. Despite efforts by the CMS Collaboration investigating $\mathrm{B}^+ \rightarrow \mathrm{J}/\psi(1\mathrm{S})\mathrm{K}^+$ ($\mathrm{J}/\psi \rightarrow \mu^+\mu^-$) [18], presented in figure 2.19b, the range in low transverse momentum of the measurement is limited by the muon trigger and selection capabilities as well as the detector acceptance for $\mu^+\mu^-$ pairs in the relevant invariant mass range [232]. At mid-rapidity these criteria restrict the transverse momentum of reconstructed muons in the J/ψ analysis to $p_{\mathrm{T}} > 3.4\,\mathrm{GeV}/c$. As a consequence, the minimum p_{T} of the J/ψ is limited to about $6.5\,\mathrm{GeV}/c$ at $\mathrm{y} = 0$, which scales with the ratio of the invariant masses $\mathrm{m}_{\mathrm{B}^+}/\mathrm{m}_{\mathrm{J}/\psi}$ to a minimal threshold of about $11\,\mathrm{GeV}/c$ for the B^+ mother. In this approach, a nuclear modification factor of $R_{\mathrm{AA}} = 0.37 \pm 0.08\,(\mathrm{stat.}) \pm 0.02\,(\mathrm{syst.})$ was measured for $6.5 < {p_{\mathrm{T}}}^{\mathrm{J}/\psi} < 30\,\mathrm{GeV}/c$ for 0–20 % centrality in Pb–Pb collisions at $\sqrt{s_{\mathrm{NN}}} = 2.76\,\mathrm{TeV}$. At higher momentum, CMS contributed another measurement of the nuclear modification factor of b quarks at mid-rapidity using strongly displaced jets with respect to the primary vertex. Here, a b-jet R_{AA} of about 0.4 for $80 < {p_{\mathrm{T}}}^{\mathrm{jet}} < 250\,\mathrm{GeV}/c$ within $|\eta| < 2$ was observed for 0–10 % centrality in Pb–Pb collisions at $\sqrt{s_{\mathrm{NN}}} = 2.76\,\mathrm{TeV}$ [233], consistent with the measurement of non-prompt J/ψ [232]. However, given the kinematic limitations in these methods, a low p_{T} measurement of R_{AA} and in particular of the elliptic flow v_2 of beauty mesons appear not within reach with the current approach.

In ALICE, it is expected that new (low p_{T}) measurements using full kinematic reconstruction at mid-rapidity in the beauty sector will become possible with the upgrade of the experiment, presented in section 3.3. These will extend current measurements of the beauty sector via heavy-flavor electrons [15] and non-prompt J/ψ mesons [16] in Pb–Pb collisions at the LHC. On the one hand, the analysis will significantly benefit from the improved resolution of the upgraded ITS detector, while on the other hand the enhanced readout capability of the complete experiment will allow to record a large data set of $\mathrm{L}_{\mathrm{int}} = 10\,\mathrm{nb}^{-1}$. It is the aim of this thesis, to demonstrate the performance of the upgraded ALICE detector in open beauty measurement via the decay channel $\mathrm{B}^+ \rightarrow \overline{\mathrm{D}}^0\pi^+$ ($\overline{\mathrm{D}}^0 \rightarrow \mathrm{K}^+\pi^-$). Whenever a particle or its decay are discussed, the charge conjugate is considered and treated similarly.

5.1. Full kinematic reconstruction of B^+ mesons with the upgraded ALICE Experiment

In ALICE, the aim for full kinematic reconstruction of the complete decay chain limits the accessible decay chains in the beauty sector to the cases presented in table 5.1. Only hadronic decays of beauty mesons and baryons are considered, as semi-leptonic decays contain at

Hadron	Mass (MeV/c^2)	Decay Channel	Branching Ratio
B^+	$5\,279.26 \pm 0.17$	$\rightarrow \overline{\mathrm{D}}^0\pi^+$	$(4.81 \pm 0.15) \cdot 10^{-3}$
		$\rightarrow \mathrm{J}/\psi(1\mathrm{S})\mathrm{K}^+$	$(1.027 \pm 0.031) \cdot 10^{-3}$
B^0	$5\,279.58 \pm 0.17$	$\rightarrow \mathrm{D}^{*-}\pi^+$	$(2.76 \pm 0.13) \cdot 10^{-3}$
Λ_b^0	$5\,619.5 \pm 0.4$	$\rightarrow \Lambda_\mathrm{c}^+\pi^-$	$(5.7\,^{+4.0}_{-2.6}) \cdot 10^{-3}$
$\overline{\mathrm{D}}^0$	$1\,864.84 \pm 0.07$	$\rightarrow \mathrm{K}^+\pi^-$	$(3.88 \pm 0.05)\,\%$
J/ψ	$3\,096.916 \pm 0.011$	$\rightarrow \mathrm{e}^+\mathrm{e}^-$	$(5.971 \pm 0.032)\ \%$
D^{*-}	$2\,010.26 \pm 0.07$	$\rightarrow \overline{\mathrm{D}}^0\pi^-$	$(67.7 \pm 0.5)\,\%$
Λ_c^+	$2\,286.46 \pm 0.14$	$\rightarrow \mathrm{p}^+\mathrm{K}^-\pi^+$	$\left(6.84\,^{+0.32}_{-0.40}\right)\,\%$

Table 5.1.: Summary of beauty decay channels studied within the scope of the ALICE ITS upgrade [186]. In addition, electrons from beauty decays and the analysis of non-prompt D and non-prompt J/ψ decays will shed further light on the beauty sector [186]. These are already accessible with the current detector setup, but appear strongly limited by statistical and systematic uncertainties [16]. The data was taken from [10]. Meanwhile, the central value and precision of some of the branching ratios were updated.

least one neutrino, invisible to the experiment. Given the considerations in section 2.3.4.2, B^+, B^0 and Λ_b^0 are the most promising candidates, as the quark predominantly decays into electrically charged and neutral beauty mesons (41 %) and the corresponding beauty baryon (about 8.4%). However, the branching ratios into the hadronic decays and the subsequent decay of the D^0 meson or J/ψ hadron limit the generated yields in the complete decay chain by a factor $\mathcal{O}(10^{-4})$ (or lower), which makes the accessible hadrons rare probes in Pb–Pb collisions at the LHC. For the decay $\mathrm{B}^+ \rightarrow \overline{\mathrm{D}}^0\pi^+$ ($\overline{\mathrm{D}}^0 \rightarrow \mathrm{K}^+\pi^-$) an overall penalty factor, which includes the b quark fragmentation and the branching ratios of the subsequent B^+ and $\overline{\mathrm{D}}^0$ decays, of about $7.65 \cdot 10^{-5}$ must be considered for each produced b quark.

On top of this rate limitation, the detector acceptance and reconstruction efficiency inside the ALICE central barrel further reduce the generated signal yield by up to two orders of magnitude. However, as depicted for $\mathrm{B}^+ \rightarrow \overline{\mathrm{D}}^0\pi^+$ ($\overline{\mathrm{D}}^0 \rightarrow \mathrm{K}^+\pi^-$) in figure 5.1, all beauty hadrons have a distinct decay topology, which allows an efficient reconstruction and enhancement of the signal-to-background ratio. Here, the analysis significantly benefits from the enhanced vertexing capabilities of the ITSu detector.

In this decay, the large invariant mass of the B^+ meson leads to a P value of $P = 2\,308\,\mathrm{MeV}/c$, which means that all decay daughters experience a strong Lorentz-boost. On the one hand, this boost collimates the decay in the acceptance of the detector, while on the other hand the decay daughters have a significantly harder spectrum than particles from the underlying Pb–Pb collision. In addition, the large mean life times $\tau_{\mathrm{B}^+} = (1\,639 \pm 4) \cdot 10^{-15}\,\mathrm{s}$ of the B^+ meson and $\tau_{\overline{\mathrm{D}}^0} = (410.1 \pm 1.5) \cdot 10^{-15}\,\mathrm{s}$ [10] for the subsequent $\overline{\mathrm{D}}^0$ decay strongly displace the secondary and tertiary vertex from the primary vertex. This can be quantified by the reconstructed decay length $\mathrm{L}_{\mathrm{decay}}^{\overline{\mathrm{D}}^0}$ of the $\overline{\mathrm{D}}^0$ meson, which is measured between the primary and tertiary vertex and includes the decay length of the B^+. It is typically several hundred μm long. As a consequence of the big offset between the two vertices, the orientation of the daughter trajectories in the transverse plane

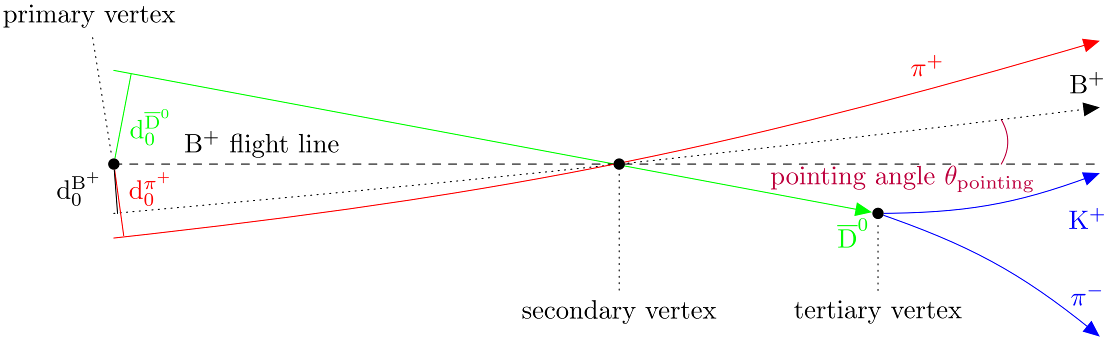

Figure 5.1.: Schematic view of the full decay chain $B^+ \to \overline{D}^0\pi^+$ ($\overline{D}^0 \to K^+\pi^-$) in the transverse plane. The displaced vertices of the beauty and charm mesons as well as some topological definitions, such as the impact parameter of the charged B meson $d_0^{B^+}$, the impact parameters of the two decay daughters $d0^{\overline{D}^0}$ and $d0^{\pi^+}$, as well as the pointing angle $\theta_{\mathrm{pointing}}$ are highlighted.

at the primary vertex typically corresponds to the situation sketched in figure 5.1. Here, the product of the impact parameters of the two decay daughters, $d0^{\overline{D}^0} \cdot d0^{\pi^+}$, is largely shifted towards negative values, as they appear on opposite sides of the primary vertex in the transverse plane. The strong collimation by the Lorentz-boost is further reflected in the distribution of the pointing angle $\theta_{\mathrm{pointing}}$, which is a measure for the deviation between the straight connection line of the primary and secondary vertex and the reconstructed direction of the momentum vector of the B^+ meson. As will be shown in the optimization of these selection criteria in section 5.3, the transverse impact parameter of the B meson $d0_{xy}^{B^+}$ of the signal also appears more narrowly distributed around the primary vertex than for the reconstructed background candidates.
In order to quantify the performance of the ALICE upgrade detectors for the selected decay channel, the expected signal and background yields and their corresponding acceptance and reconstruction efficiencies have to be evaluated using full and fast MC simulations of physics events in the ALICE Experiment. For an estimate of the expected, generated signal yield respecting the full decay chain, the approach of binary scaling [9, 20, 186] was followed. In addition, various sources of expected background candidates were identified, and are specifically discussed in section 5.2, after a more general introduction into the reconstruction strategy in section 5.1.2. The benefit of the distinct topologies of the B^+ decay plays a key role in the efficient signal selection, and corresponding threshold cuts are optimized in section 5.3. Subsequently, the final estimates on the expected statistical significance and the signal-to-background ratio are presented in section 5.5.

5.1.1. Binary scaling approach of the expected signal yield

Based on the previous good agreement between measurements of the charm and beauty quark production cross-sections in p+p collisions by ALICE and FONLL calculations, presented in section 2.3.5, the approach of binary scaling of the FONLL prediction to the Pb–Pb scenario was chosen for the calculation of the expected signal yield S in $B^+ \to \overline{D}^0\pi^+$ ($\overline{D}^0 \to K^+\pi^-$). In this approach, the p_{T}-differential quark production cross-section $\mathrm{d}\sigma/\mathrm{d}p_{\mathrm{T}}$

in p+p collisions is scaled to the anticipated scenario in Pb–Pb collisions, using model and data input. The formula for the full calculation is shown in equation 5.1 [9, 20].

$$\mathrm{S} = 2 \cdot f_{\mathrm{b}\rightarrow\mathrm{B}} \cdot \mathrm{BR} \cdot \int_{p_{\mathrm{T}}^{\max}}^{p_{\mathrm{T}}^{\min}} \left(\frac{\mathrm{d}\sigma}{\mathrm{d}p_{\mathrm{T}}}\right)_{\mathrm{B}^+}^{\mathrm{FONLL}} \mathrm{d}p_{\mathrm{T}} \cdot R_{\mathrm{AA}}^{\mathrm{B}^+} \cdot \langle T_{\mathrm{AA}} \rangle^{0\text{–}10\,\%} \cdot (\mathrm{acc.} \cdot \mathrm{eff.}) \tag{5.1}$$

In this formula, the factor 2 takes into account that particles as well as their anti-particles are reconstructed in the analysis. The signal reduction through the quark to B^+ meson fragmentation $f_{\mathrm{b}\rightarrow\mathrm{B}}$ measured by DELPHI in $\mathrm{e}^+\mathrm{e}^-$ collisions at LEP [79] and the branching ratio of the full decay chain $\mathrm{BR}(\mathrm{B}^+ \rightarrow \overline{\mathrm{D}}^0\pi^+) = (4.81 \pm 0.15) \cdot 10^{-3}$ and $\mathrm{BR}(\overline{\mathrm{D}}^0 \rightarrow \mathrm{K}^+\pi^-) = (3.88 \pm 0.05) \cdot 10^{-2}$ [10] are considered. The measured feed-down rate of (1.1 ± 0.5) % [79] from b baryons was neglected. The branching ratios are multiplied by the p_{T}-differential production cross-section of b quarks in $|\mathrm{y}| < 0.5$, using the CTEQ6.6 NLO parton distribution functions and the Kartvelishvili non-perturbative fragmentation functions for b quark to hadron fragmentation [77]. The rapidity interval of $|\mathrm{y}| < 0.5$ was chosen to maintain consistency with published data of charmed mesons by the ALICE Collaboration [103]. The uncertainty from variations of the scales and masses, as described in section 2.3.4.1, are propagated into the final results.

In order to scale the scenario from p+p to Pb–Pb collisions, the nuclear modification factor $R_{\mathrm{AA}}^{\mathrm{B}^+}$ as predicted by the TAMU model [95] (introduced in section 2.3.4.3) was used. Here, medium effects of the QGP on the b quark spectrum are calculated for Pb–Pb collisions at $\sqrt{s_{\mathrm{NN}}} = 2.76\,\mathrm{TeV}$, 0–10 % centrality. The corresponding R_{AA} is shown in figure 5.2. The actual scaling with binary collisions is included via the nuclear overlap function $\langle T_{\mathrm{AA}} \rangle = N_{\mathrm{coll}}/\sigma_{\mathrm{NN}}^{\mathrm{inel}} = 23.44 \pm 0.77\,\mathrm{mb}^{-1}$, calculated within a Glauber model based on measurements of particle multiplicities in Pb–Pb collisions at $\sqrt{s_{\mathrm{NN}}} = 2.76\,\mathrm{TeV}$ by ALICE [234]. Note, that by the time this thesis was written, published values of measurement and theoretical prediction were used, which were only available at $\sqrt{s_{\mathrm{NN}}} = 2.76\,\mathrm{TeV}$. However, the expected relative changes of R_{AA} and $\langle T_{\mathrm{AA}} \rangle$ with collision energy are expected to be small for $\sqrt{s_{\mathrm{NN}}} = 5.5\,\mathrm{TeV}$ [235], and can be neglected compared to the uncertainty from the FONLL calculation. The expected signal production yield per Pb–Pb collisions at $\sqrt{s_{\mathrm{NN}}} = 5.5\,\mathrm{TeV}$ in 0–10 % centrality is shown as function of transverse momentum in figure 5.2b. The uncertainty band in figure 5.2b includes the variations of the scales and masses in the FONLL calculation at $\sqrt{s_{\mathrm{NN}}} = 5.5\,\mathrm{TeV}$ as well as uncertainties propagated from the TAMU ${R_{\mathrm{AA}}}^{\mathrm{B}^+}$ prediction, shown in figure 5.2a. Additional contributions to the uncertainty of the remaining factors are relatively small. Note, that the TAMU prediction of ${R_{\mathrm{AA}}}^{\mathrm{B}^+}$ and corresponding ${v_2}^{\mathrm{B}^+}$ slightly softens the p_{T} spectrum in Pb–Pb collisions with respect to p+p: Quenched high-p_{T} mesons are shifted to lower p_{T}, and the spectrum peaks around 3–4 GeV/c with a mean transverse momentum of about $\langle p_{\mathrm{T}} \rangle \approx 4.5\,\mathrm{GeV}/c$, compared to $\langle p_{\mathrm{T}}^{\mathrm{p+p}} \rangle \approx 5.4\,\mathrm{GeV}/c$.

In this calculation, a p_{T}-integrated yield of $9.8 \cdot 10^{-5}$ B^+ mesons generated per event in the ALICE central barrel is expected. This accumulates to approximately $7.8 \cdot 10^5$ B^+ mesons and charge conjugates in the complete decay channel for the expected integrated luminosity of $\mathrm{L}_{\mathrm{int}} = 10\,\mathrm{nb}^{-1}$ ($8 \cdot 10^9$ events, $\sigma^{\mathrm{Pb-Pb}} = 8\,\mathrm{b}$ [20]) in 0–10 % centrality. Note, that the total amount of generated charged B mesons visible to the experiment will be reduced by the detector acceptance and signal reconstruction efficiency, which is absorbed in the factor

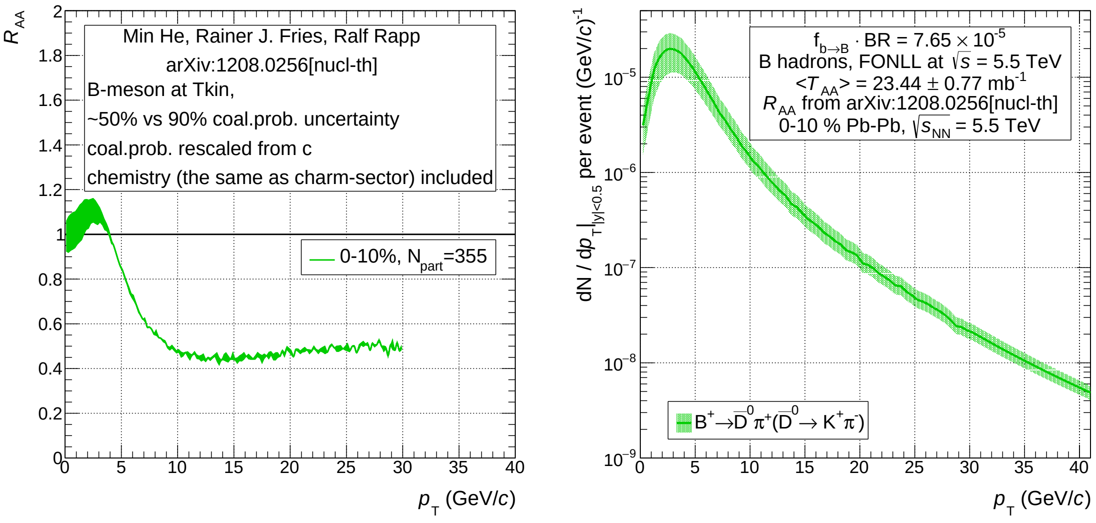

(a) **(b)**

Figure 5.2.: (a) displays the TAMU prediction of the R_{AA} of charged B mesons based on hydrodynamic evolution and coalesence at hadronization in central Pb–Pb collisions at $\sqrt{s_{\mathrm{NN}}} = 2.76\,\mathrm{TeV}$ [95]. It is used to include medium-induced effects of Pb–Pb collisions into the binary scaling calculation of the p_{T}-differential b quark cross-section, calculated in pQCD by FONLL. The result of the expected signal yield per event is shown in (b). The displayed uncertainties are propagated from the FONLL calculations as well as from the R_{AA} prediction.

(acc. · eff.) in equation 5.1. This factor is explained in the following section. The final reconstruction efficiency of the signal is highly dependent on the applied reconstruction strategy and corresponding selection cuts, and will be presented after the evaluation of background sources and the multi-dimensional cut selection optimization in section 5.3.

5.1.1.1. Computation of the acceptance and efficiency

In order to obtain the (acc. · eff.)-factor from Monte Carlo (MC) simulations, and thus the raw yield for fully reconstructed B^+ and B^- mesons, several technical details have to be taken into account, while possible biases must be removed.

Typically two full MC simulations have to be analyzed for this purpose: A signal enriched simulation and a minimum bias simulation. The former approach is necessary in order to have negligible statistical uncertainty in the analyzed signal. For this reason, the additional signals are generated within a given rapidity range, which may however introduce a bias on the signal reconstruction. This bias, and further the restriction of the results to the B^+ range within |y|<0.5, can be corrected via the analysis of the minimum bias simulation, as visible in the right part of equation 5.2:

$$(\text{acc.} \cdot \text{eff.}) = \left(\frac{N^{\mathrm{B}^+}_{\text{rec.}}}{N^{\mathrm{B}^+}_{\text{gen.}}} \right) \Bigg|_{\text{beauty enriched MC}} \cdot \left(\frac{N^{\mathrm{B}^+}_{\text{gen.}}}{N^{\mathrm{B}^+}_{\text{gen. }|y|<0.5}} \right) \Bigg|_{\text{min.bias MC}} \tag{5.2}$$

The first part of equation 5.2 is calculated from the signal enriched simulation. The raw yield, $N^{\mathrm{B}^+}_{\text{rec.}}$ corresponds to the total amount of reconstructed B^+ mesons, including all

applied track quality and analysis cuts, such as the $\overline{\mathrm{D}}^0$ selection, particle identification and topological as well as kinematic selection criteria, as explained in section 5.3. $N^{\mathrm{B}^+}_{\mathrm{gen.}}$ reflects the total amount of B^+ mesons generated and forced into the full sequence of the signal decay channel. Here it is required that all decay daughters (π^+, π^-, K^+) are generated within the acceptance of the experiment ($|\eta| < 0.9$, $p_{\mathrm{T}} > 0.1\,\mathrm{GeV}/c$). In addition, for $N^{\mathrm{B}^+}_{\mathrm{rec.}}$ and $N^{\mathrm{B}^+}_{\mathrm{gen.}}$ a *fiducial volume* selection is applied, as explained in section 5.3.1.
The remaining factor $N^{\mathrm{B}^+}_{\mathrm{gen.}\ |\mathrm{y}|<0.5}$ is derived solely from the minimum bias simulation. In minimum bias productions particles are generated without (or with a wide) restriction on the rapidity. A rapidity bias, as in the signal enhanced simulations, is thus not present. In order to be consistent with the initial FONLL prediction, it is required that all B decays, forced into the complete decay channel, are reconstructed within the rapidity range of $|\mathrm{y}| < 0.5$. Edge effects are overcome by generating the signal in a significantly wider range, e.g. $|\mathrm{y}| < 1.0$. The final reconstruction efficiency is presented in section 5.3, as it strongly depends on the optimized signal selection criteria.

5.1.2. B^+ selection strategy

Conceptually, charged B mesons in ALICE are reconstructed as sketched in figure 5.1. In a first step, $\overline{\mathrm{D}}^0$candidates are selected in the decay chain $\overline{\mathrm{D}}^0 \rightarrow \mathrm{K}^+\pi^-$ via TPC $\mathrm{d}E/\mathrm{d}x$ and TOF time-of-flight particle identification on the daughter tracks, while some topological and kinematic criteria are already applied at this stage. Subsequently, the corresponding reconstructed tertiary decay vertex is combined with a charged track in order to form a candidate secondary vertex, potentially stemming from a B meson in the signal decay chain $\mathrm{B}^+ \rightarrow \overline{\mathrm{D}}^0\pi^+$. Further selection criteria on the candidate B meson and its daughter tracks can then be applied to enhance the signal-to-background ratio, and allow for a significant, visible signal peak in the invariant mass spectrum. Using full (appendix A) and fast MC simulations (section 4.3), the full kinematic reconstruction of the complete decay chain was developed within this thesis: As explained in section 4, signals are injected artificially on top of a realistic HIJING background description and forced into the decay channel under study, in order to obtain a complete correction for the acceptance and efficiency. For this purpose, a dedicated full MC production was launched to simulate the full, upgraded ITS detector in the environment of Pb–Pb collisions, and a total amount of 10^6 central HIJING events was generated (appendix A). The overall size of the simulation is limited by available computing resources, as outlined in the motivation of fast MC simulations in section 4.3. However, as derived from the binary scaling approach in section 5.1.1, only few B^+ mesons are expected to be generated naturally within the available statistics, further diminished to single counts by the acceptance and reconstruction efficiency. Even though this is overcome by the artificial injection of a given amount of signals, which needs to be corrected by the expected yield from the binary scaling calculation, no background yield is neither expected nor observed after the application of additional individual selection criteria in the full MC simulation. As a consequence of the limited number of events, the available full MC simulation is only used as reference to other simulation methods, which are capable to generate sufficiently large statistics for a reliable estimate of the combinatorial background yield. Within this thesis, two approaches were followed: On the one hand, the *track rotation method*, as it is further explained in appendix D, was used to increase the number of background candidates by a factor 13. However, as the precision of the topological description of the full decay chain $\mathrm{B}^+ \rightarrow \overline{\mathrm{D}}^0\pi^+$ ($\overline{\mathrm{D}}^0 \rightarrow \mathrm{K}^+\pi^-$) for background candidates was still limited, this approach introduced an additional systematic uncertainty of 40 % [20], which compromised the quality of the prediction. On the other hand, the newly developed FT2 was used to reconstruct about 100 million central Pb–Pb events using the HIJING event generator, as explained in section 4.3.9.3. The latter approach was used for the final estimate in this thesis, as it has a much lower statistical and systematic uncertainty and can provide higher event statistics. The lack of PID information was overcome by the introduction of scaling factors for the signal and background yields to take into account finite PID efficiencies (see section 5.4). Preliminary results using the track rotation method are presented in [157], where the analysis of the systematic uncertainties was analog to the presented approach in this thesis.

5.1.2.1. Track selection criteria

As pointed out above, the B^+ meson is reconstructed via its hadronic decay daughters, which are visible to the ALICE Experiment. As discussed in full detail in section 4, the tracks in the central barrel are reconstructed through a Kalman filter algorithm along the deposited charge clusters in the active volumes of the individual subsystems. Track quality criteria are applied, which are tuned to select trajectories, which are more probable to originate from heavy-flavor decays. These criteria significantly reduce the number of tracks considered for further analysis in the B^+ reconstruction:

- track refit in the ITSu detector (only available in full MC)
- track refit in the TPC detector (only available in full MC)
- associated clusters in either the first or the second and third layer of the ITSu detector
- minimal amount of reconstructed clusters in the TPC, $\mathrm{N}_{\mathrm{TPC}}^{\mathrm{cluster}} > 70$
- track within $|\eta| < 0.9$
- minimum transverse momentum of $p_{\mathrm{T}} > 0.5\,\mathrm{GeV}/c$
- maximum transverse distance to the primary vertex $\mathrm{DCA}_{\mathrm{xy}} < 1\,\mathrm{cm}$
- minimum transverse distance to the primary vertex $\mathrm{DCA}_{\mathrm{xy}} > 0.003\,\mathrm{cm}$ for $p_{\mathrm{T}} < 2.0\,\mathrm{GeV}/c$
- maximum longitudinal distance to the primary vertex $\mathrm{DCA}_{\mathrm{Z}} < 1\,\mathrm{cm}$

The selection criteria in the ITSu detector are mandatory to maintain a high-quality pointing resolution. This is a crucial ingredient for the presented analysis, as this ensures the capability of differentiating the tracks stemming from the primary, secondary and tertiary vertices. The cuts applied in the TPC ensure that the individual tracks leave a sufficient number of clusters inside the acceptance of the TPC detector, thus allowing for precise momentum determination and particle identification (when available). Typically, pions with $p_{\mathrm{T}} \geq 200\,\mathrm{MeV}/c$ have sufficient transverse momentum to traverse the complete active volume of the TPC in radial direction at a magnetic field strength of $\mathrm{B} = 0.5\,\mathrm{T}$.

However, the kinematic threshold is applied at 500 MeV/c, which enhances the fraction of hard tracks expected from heavy-flavor decays. In addition, a maximum and minimum distance of closest approach between the (propagated) track and the primary vertex in transverse and longitudinal direction are applied in order to suppress the enormous amount of particles generated in (central) Pb–Pb collisions, which are most likely not generated by heavy-flavor decays. These criteria are filtering all tracks on an event-by-event level.
In addition, the position of the primary vertex distribution was smeared at MC generator level in longitudinal and transverse direction within a Gauß-distribution by about $\sigma_z = 3.82\,\text{cm}$ and $\sigma_{xy} = 0.15\,\text{cm}$ respectively. In the simulations, all generated events were considered.

5.1.2.2. $\overline{\mathrm{D}}^0$ meson reconstruction

$\overline{\mathrm{D}}^0$ candidates are reconstructed by a vertexing routine, which identifies and combines those tracks, which could constitute the heavy-flavor meson and pass the previously mentioned track selection criteria. If available in the simulation, the TPC and TOF PID signals (section 3.2) are used to specifically select pion and kaon candidates in order to reduce the overall amount of considered tracks. For the reconstruction of $\overline{\mathrm{D}}^0$ candidates, only tracks are accepted, for which the measured PID signal is within $\pm\,2\sigma$ ($\pm\,3\sigma$) of the expected value in the TPC (TOF), based on the pion and kaon assumption. All pairs of two oppositely charged tracks are combined and propagated through the magnetic field to a distance of closest approach to each other by application of an iterative χ^2-minimization. In case of success, the located coordinates are classified as displaced vertices and are assigned an own covariance matrix. Based on their respective charge, the assumption of the true invariant pion and kaon masses [10] are applied in order to reconstruct the invariant mass of the vertex, and thus the mother $\overline{\mathrm{D}}^0$ candidate, as presented in equation 5.3 (in natural units).

$$M(\overline{\mathrm{D}}^0)^{\text{candidate}} = M(\mathrm{K}^+\pi^-) = \sqrt{\left(\sqrt{(m_{\mathrm{K}}^2 + \vec{p_1}^2)} + \sqrt{(m_\pi^2 + \vec{p_2}^2)}\right)^2 - (\vec{p_1} + \vec{p_2})^2}, \quad (5.3)$$

where $\vec{p_1}$ and $\vec{p_2}$ are the p_{T}-momentum of the two $\overline{\mathrm{D}}^0$ daughter candidates, respectively. The quality of the reconstructed vertex and the potential mother candidate particle are reconstructed based on the track parameters of the two candidate daughter tracks. At this point, the $\overline{\mathrm{D}}^0$-candidate can be evaluated by itself, carrying its own full kinematic and topological information. For a kinematic analysis, the momentum spectrum of heavy-flavor mesons is typically split into individual p_{T}-bins, such that the statistical uncertainty within a bin remains reasonably small. In the presented analysis, the $\overline{\mathrm{D}}^0$ (B^+) spectra are divided into 13 kinematic bins with respect to the mother p_{T}. Here, the shape of the spectrum within a kinematic bin is not further taken into account. Most importantly, the invariant mass range of the reconstructed $\overline{\mathrm{D}}^0$ candidate is required to be within $\pm\,3\sigma$ of the PDG value quoted in table 5.1.
The performance of the invariant mass position reconstruction and its corresponding resolution are determined by a Gauß-fit on the invariant mass spectrum of non-prompt $\overline{\mathrm{D}}^0$ mesons, identified via their MC truth information, and displayed in figure 5.3. In full MC simulations of the current and upgraded ITS detector, the mass position of the

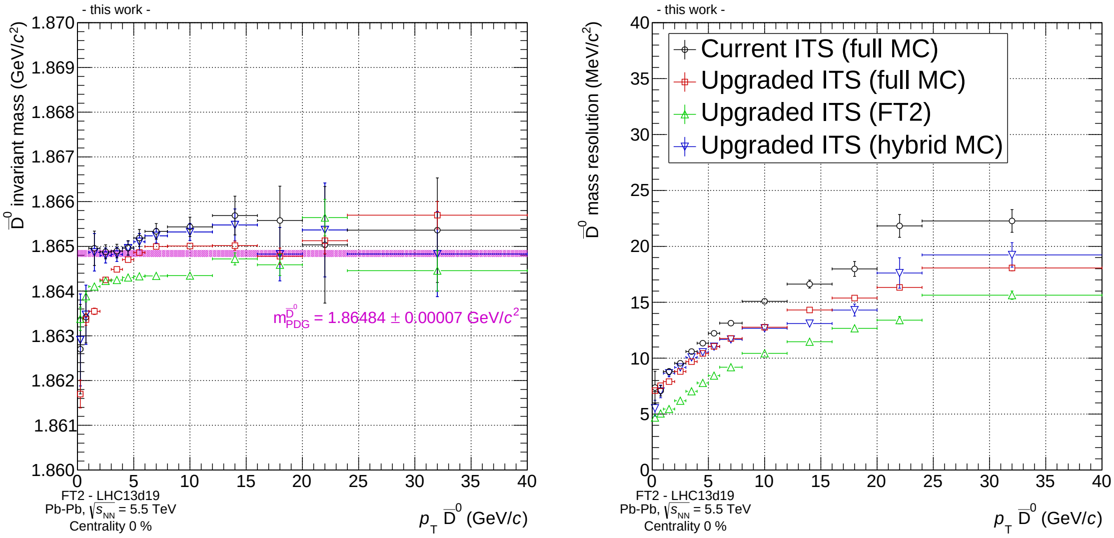

(a) **(b)**

Figure 5.3.: Reconstructed position (a) and invariant mass resolution (b) of $\overline{\mathrm{D}}^0$ mesons in the decay chain $\mathrm{B}^+ \rightarrow \overline{\mathrm{D}}^0\pi^+(\overline{\mathrm{D}}^0 \rightarrow \mathrm{K}^+\pi^-)$, extracted from different MC simulations of central Pb–Pb collisions at $\sqrt{s_{\mathrm{NN}}} = 5.5\,\mathrm{TeV}$. The current ITS performance is shown in black open circles, whereas the performance of the upgraded detector is displayed for full MC (red, open squares), fast MC (green, open triangles) and hybrid MC (blue, open inverse triangles). The magenta band displays the true invariant mass of the $\overline{\mathrm{D}}^0$ meson within the uncertainty [10].

$\overline{\mathrm{D}}^0$meson is correctly reconstructed at the per-mille level, despite a systematic undershoot below $p_{\mathrm{T}} < 5\,\mathrm{GeV}/c$ and an overshoot for larger p_{T}, which are artifacts of the reconstruction algorithm. As simplified tracking as well as energy loss algorithm are applied, simulations with the FT2 systematically underestimate the reconstructed invariant mass. However, the difference remains also on a per-mille level. Similar performance is achieved with the hybrid MC method, which was outlined in section 4.3.1.

The reconstructed invariant mass peak width is displayed in figure 5.3b, and strongly increases with increasing p_{T}, due to the degrading p_{T} resolution with increasing p_{T} of the daughters. Some improvement is observed between the current and upgraded ITS detector. The presented B^+ analysis profits from the slightly better momentum resolution, as the selection on the invariant mass of the $\overline{\mathrm{D}}^0$ largely reduces the amount of background candidates, which are used in the subsequent B^+ reconstruction. In the FT2 simulation, the reconstructed invariant mass peak width is underestimated by about 30 %, which is a consequence of the slightly different momentum resolution, compared to full MC (shown in figure 4.3). This has to be taken into account in the further comparison between the FT2 and full MC simulations, as for a most realistic estimate the signal and background yields should only be compared in a range restricted to the one obtained in full MC simulations. The uncertainties displayed in these figures are propagated from the uncertainty of the corresponding fit parameter.

The resolution in local x- and y-direction, with which the tertiary vertex of the $\overline{\mathrm{D}}^0$ decay is reconstructed, is displayed in figure 5.4. Again, the full decay chain $\mathrm{B}^+ \rightarrow \overline{\mathrm{D}}^0\pi^+$ ($\overline{\mathrm{D}}^0 \rightarrow \mathrm{K}^+\pi^-$) is verified by MC truth. In z-direction, the improvement

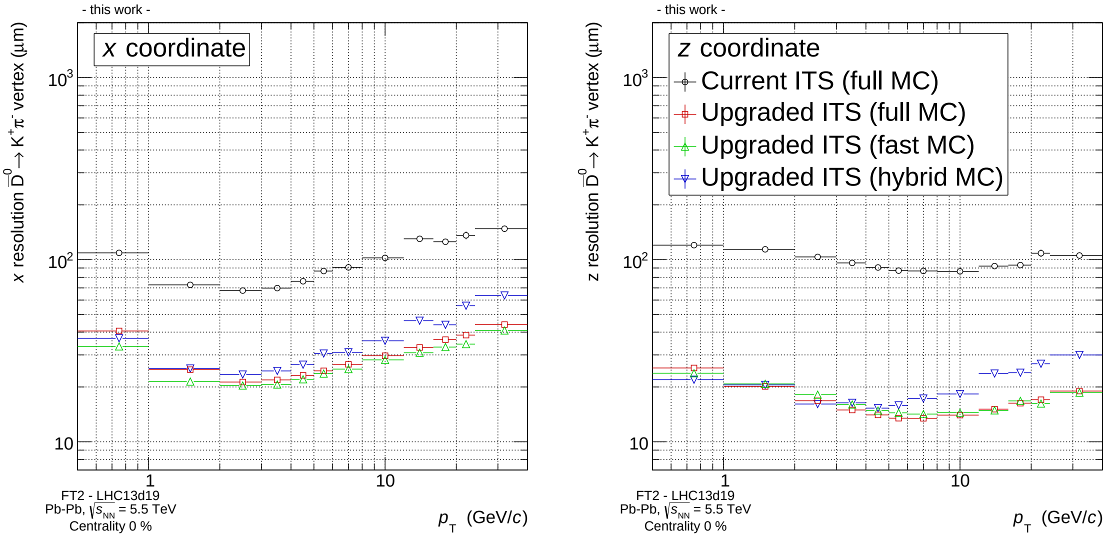

(a) **(b)**

Figure 5.4.: Reconstructed tertiary vertex resolution of $\overline{\mathrm{D}}^0$ mesons in x- and z-direction in the decay chain $\mathrm{B}^+ \rightarrow \overline{\mathrm{D}}^0\pi^+(\overline{\mathrm{D}}^0 \rightarrow \mathrm{K}^+\pi^-)$ for central Pb–Pb collisions at $\sqrt{s_{\mathrm{NN}}} = 5.5\,\mathrm{TeV}$ shown in (a) and (b), respectively. The current ITS performance is shown in black open circles, whereas the performance of the upgraded detector is displayed for full MC (red, open squares), fast MC (green, open triangles) and hybrid MC (blue, open inverse triangles).

from the current to the upgraded ITS detector is up to a factor of five due to the much reduced pixel size of the upgraded ITS. For low transverse momentum in x- (and y-) direction, typically a decreased resolution is expected as a consequence of the larger opening angle between the decay daughters. However, the observed resolution increases, as the single track pointing resolution worsens towards lower track p_{T} [20]. For high momentum, the resolution decreases as the opening angle decreases, making it more difficult to define the intersection point along the decay tracks. Similar arguments can be applied to the resolution in z-direction, which is in general slightly better, as the track opening angle is larger in this direction. Further, it is visible that the hybrid MC approach shows a systematically larger resolution by about 20–30 %. By construction, this originates from the hybrid approach itself, in which the track covariance matrix is not modified with respect to the better tracking precision. The vertex resolution of the full MC simulation are well reproduced by the FT2. The figures are binned in p_{T} of the $\overline{\mathrm{D}}^0$ meson, and the uncertainty bars reflect the determination uncertainty on the displayed root mean square.
Already at this stage, first selection criteria can be applied in order to reduce the number of $\overline{\mathrm{D}}^0$ candidates for further analysis, while it reduces the computational needs and time in the vertex reconstruction of the B^+ candidates. However, in order to maintain a high reconstruction efficiency, only loose kinematic and topological criteria were applied at this stage of the analysis:

- p_{T}-dependent invariant mass selection of $\pm 3\sigma$ (about $21 - 54\,\mathrm{MeV}/c^2$, according to figure 5.3b) around $\mathrm{m}^{\overline{\mathrm{D}}^0}_{\mathrm{PDG}}$

- distance of closest approach between the $\overline{\mathrm{D}}^0$ daughter tracks $\mathrm{DCA}_{K\pi} < 0.035\,\mathrm{cm}$
- upper threshold on the decay angle between the pion momentum vector and the $\overline{\mathrm{D}}^0$ momentum vector $|\cos(\theta^*)| < 0.8$
- minimum transverse momentum of pion and kaon candidates $p_{\mathrm{T}}^{\mathrm{K}}$ and $p_{\mathrm{T}}^{\pi} > 700\,\mathrm{MeV}/c$
- maximum impact parameter of $\overline{\mathrm{D}}^0$ daughters, $|d_{\mathrm{xy}}^{\mathrm{K}}|$ and $|d_{\mathrm{xy}}^{\pi}| < 1\,\mathrm{cm}$
- maximum product of the impact parameters of $\overline{\mathrm{D}}^0$daughters $d_{\mathrm{xy}}^{\mathrm{K}} \cdot d_{\mathrm{xy}}^{\pi} < 0.0\,\mathrm{cm}^2$
- lower threshold on the cosine of the pointing angle of the $\overline{\mathrm{D}}^0$ meson, which is defined analogously to that of the B^+ meson, $\cos(\theta_{\mathrm{pointing}})_{\mathrm{xy}} > 0.5$

A summary of the multi-dimensional optimization of these selection cuts for statistical significance in the $\overline{\mathrm{D}}^0$reconstruction is found here: [66]. However, most cuts, which have a strong dependence on the p_{T} of the $\overline{\mathrm{D}}^0$ meson, were released to preserve more potential B^+ candidates in the next reconstruction step, as the kinematics of non-prompt $\overline{\mathrm{D}}^0$ mesons are harder than for prompt mesons. Specifically the criteria on the impact parameter of the $\overline{\mathrm{D}}^0$ daughters, and the threshold on the pointing angle were loosened, as the daughters of the non-prompt $\overline{\mathrm{D}}^0$ do not necessarily need to point back to the primary vertex at low p_{T}. As the threshold on the decay length of the $\overline{\mathrm{D}}^0$ mesons is optimized later in the analysis cuts, it was also removed at this point of the analysis. Other cuts, for example the lower threshold on the $p_{\mathrm{T}}^{\mathrm{K}}$ and p_{T}^{π}, the upper threshold on $|\cos(\theta^*)|$ and the distance of closest approach between the decay daughters were kept at their original values of the $\overline{\mathrm{D}}^0$ selection.

5.1.2.3. B^+ meson reconstruction

The B^+ meson candidate reconstruction follows the analog principle of the $\overline{\mathrm{D}}^0$ candidates. In order to form a B^+ candidate, the reconstructed $\overline{\mathrm{D}}^0$ particle is combined with all positively charged tracks, which pass the same track selection criteria (section 5.1.2.1) and were not used to build the same $\overline{\mathrm{D}}^0$ candidate. The charge of the specific track corresponds to the charge of the mother meson and uniquely identifies the exact decay channel on top of the PID assumption, whether the reconstructed charmed meson is a $\overline{\mathrm{D}}^0$ or D^0 meson. No PID assumption is applied on the pion track candidate, as the particles species cannot be identified with a high probability, due to the typically large momentum. Again, the true invariant mass of the charmed meson and pion are applied to reconstruct the invariant mass of the mother candidate via the two daughter tracks, as shown in equation 5.4.

$$M(\mathrm{B}^+)^{\mathrm{candidate}} = M(\overline{\mathrm{D}}^0\pi^+) = \sqrt{\left(\sqrt{(m_{\overline{\mathrm{D}}^0}^2 + \vec{p_1}^2)} + \sqrt{(m_{\pi}^2 + \vec{p_1}^2)}\right)^2 - (\vec{p_1} + \vec{p_2})^2}, \quad (5.4)$$

where $\vec{p_1}$ and $\vec{p_2}$ are the p_{T}-momentum of the two B^+ daughter candidates, respectively. The invariant mass calculation itself is already an extremely powerful tool, as it dramatically restricts the amount of potential daughter tracks through its kinematics. In the signal reconstruction only an invariant mass range of $\pm\,3\sigma$ around the B^+ invariant mass of $m_{\mathrm{PDG}}^{\mathrm{B}^+} = 5\,279.26 \pm 0.17\,\mathrm{MeV}$ is considered.

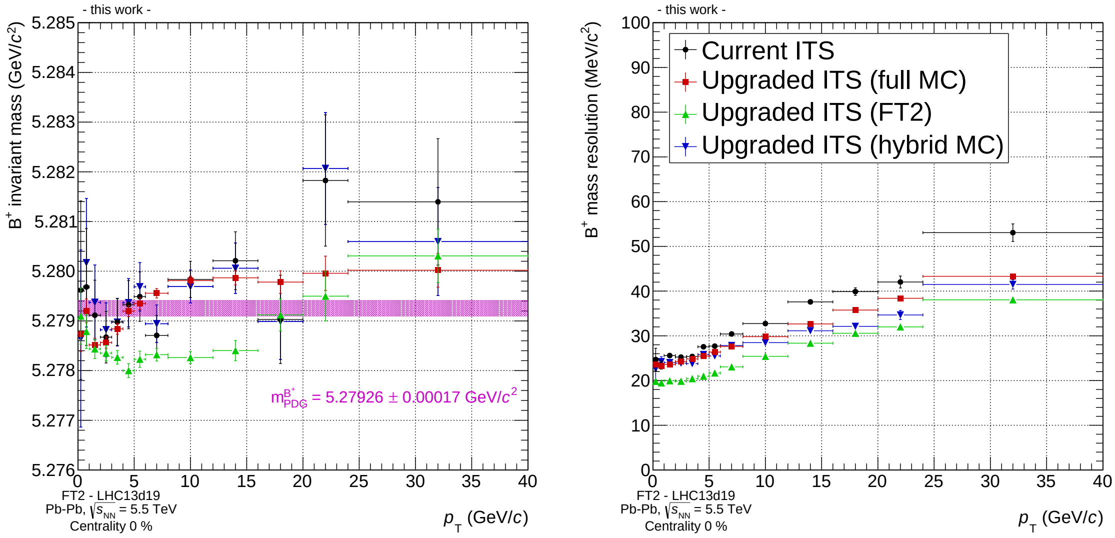

(a) **(b)**

Figure 5.5.: Reconstructed position (a) and invariant mass resolution (b) of open beauty mesons in the decay chain $B^+ \to \overline{D}^0\pi^+(\overline{D}^0 \to K^+\pi^-)$, extracted from different MC simulations of central Pb–Pb collisions at $\sqrt{s_{NN}} = 5.5\,\text{TeV}$. The current ITS performance is shown in black circles, whereas the performance of the upgraded detector is displayed for full MC (red squares), fast MC (green triangles) and hybrid MC (blue inverse triangles). The magenta band display the true invariant mass of the B^+ meson within the uncertainty [10].

The performance of the B^+ invariant mass position reconstruction and the corresponding resolution are shown for the current and upgraded ITS detector in figure 5.5, comparing different MC simulations. As for the $\overline{D}^0$ reconstruction, the B^+ invariant mass is correctly reconstructed at the per-mille level. The invariant mass resolution of the formed B^+ meson is slightly worse compared to the $\overline{D}^0$-meson, which is a consequence of the larger transverse momentum and correspondingly degraded p_T resolution of the daughter particles. Also, the $\overline{D}^0$ daughter itself is a composed object of two daughter tracks, thus effected by detector resolutions of both of its daughter tracks as well. Uncertainties are propagated from the uncertainty of the corresponding fit parameter of a Gauß-fit to the invariant mass peak, verified via MC truth information of the particle identity. The secondary vertex resolution of the B^+ mesons in y- (x-) and z-direction, visible in figure 5.6, shows analog performance as the tertiary vertex reconstruction of the $\overline{D}^0$-meson. Due to the strong Lorentz-boost, the opening angle between the daughter tracks is smaller at low transverse momentum and thus the resolution appears slightly increased. The interplay between track pointing resolution and opening angle between the daughter tracks similarly leads to a dip in resolution at around $p_T \approx 7$ and $15\,\text{GeV}/c$ for the x- and z-coordinates. Note, that the figures are binned in kinematic bins of the B^+ meson. The uncertainty bars reflect the determination uncertainty on the width of the Gauß-fit. At this stage, the full kinematic and topological information of the B^+ candidate is available and kinematic and topological selection criteria can be optimized, as they are necessary to enhance the signal-to-background ratio for a significant measurement.

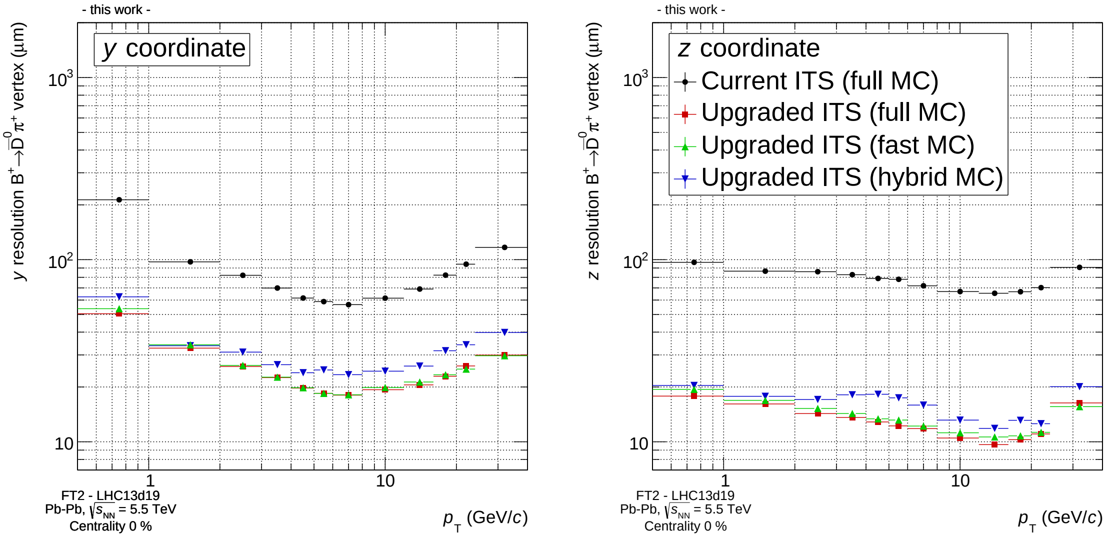

(a) **(b)**

Figure 5.6.: Reconstructed secondary vertex resolution of B^+ mesons in y- and z-direction in the decay chain $\mathrm{B}^+ \rightarrow \overline{\mathrm{D}}^0\pi^+(\overline{\mathrm{D}}^0 \rightarrow \mathrm{K}^+\pi^-)$ for central Pb–Pb collisions at $\sqrt{s_{\mathrm{NN}}} = 5.5\,\mathrm{TeV}$ shown in (a) and (b), respectively. The current ITS performance is shown in black circles, whereas the performance of the upgraded detector is displayed for full MC (red squares), fast MC (green triangles) and hybrid MC (blue inverse triangles).

5.2. Sensitivity to expected background sources

As shown in section 5.1.1, the generated signal rates in the full decay chain $\mathrm{B}^+ \rightarrow \overline{\mathrm{D}}^0\pi^+$ and subsequent $\overline{\mathrm{D}}^0 \rightarrow \mathrm{K}^+\pi^-$ are expected to be of the order of $10^{-5} - 10^{-6}$ B^+ mesons per event, which will be further diminished by the acceptance and reconstruction efficiency. Given the high track multiplicity in central Pb–Pb collisions, the signal will thus make up only a vanishing fraction of the reconstructed candidates, which are dominated by two major sources of background: On the one hand, *combinatorial* background originates from combinations of random uncorrelated tracks with a rather smooth invariant mass distribution, reflecting the inclusive single particle spectra. The background grows up to $\mathcal{O}(10^2)$ reconstructed candidates per event if only the loose $\overline{\mathrm{D}}^0$ selection criteria are applied, as they were described in section 5.1.2.2. On the other hand *correlated* background sources are generated by other heavy-flavor decays, similar to the signal decay channel. These may result in structures in the invariant mass spectrum below the expected signal peak. Both contributions are discussed in the following sections 5.2.1 and 5.2.2.

5.2.1. Combinatorial background

Combinatorial background is typically defined as a combination of random (pairs) of tracks, which fall in the same invariant mass range of the analyzed signal decay and pass all selection criteria due to the finite resolution, as well as seemingly similar topologies, e.g. for strange weak decays. The full decay chain of $\mathrm{B}^+ \rightarrow \overline{\mathrm{D}}^0\pi^+$ $(\overline{\mathrm{D}}^0 \rightarrow \mathrm{K}^+\pi^-)$ is particularly susceptible to combinatorial background, as it involves three prongs visible to the detector and combinatorial background thus enters threefold. On the one hand random, uncorrelated pairs of pion and kaon candidate tracks could be combined as fake $\overline{\mathrm{D}}^0$ candidates, and on the other hand random pion candidate tracks could be combined with real $\overline{\mathrm{D}}^0$ candidates and directly contribute to the background in the invariant mass range of the B^+ meson. Whereas the former background is suppressed by the reconstruction algorithm of the secondary and tertiary vertex, especially through the selection of the invariant mass of the $\overline{\mathrm{D}}^0$, the latter was identified as the dominating source of combinatorial background in the analysis. It is largely suppressed by the application of topological and kinematic selection criteria, explained and optimized in section 5.3. In this analysis, all 100 million events of the fast MC simulation, described in section 4.3.9.3, were used.

5.2.2. Identification of correlated background sources

Typically, correlated background candidates originate from decays with similar kinematics and topologies as the analyzed signal decay, which nevertheless cannot be separated by the means of available particle identification. On the one hand, this could result from ambiguities and subsequent misidentification within the PID capabilities, where particles are assigned the wrong mass hypothesis. On the other hand, as it is the case for the presented analysis, the momentum spectrum of the pion candidate from the potential B^+ decay is with an average transverse momentum of $\langle p_\mathrm{T} \rangle \approx 3.5\,\mathrm{GeV}/c$ too hard for a reliable PID determination in TPC and TOF. Thus, no PID information is used for the charged daughter track, which is combined with the $\overline{\mathrm{D}}^0$ candidate.

Given these considerations, and the large invariant mass of the inspected B^+ meson, contributions to the correlated background are only expected from other open beauty decays of type $\overline{\mathrm{D}}^0 + \mathrm{X}^+$, which may mimimc the distinct decay topology of the analyzed decay chain. Here, X^+ denotes one or more particles with an overall positive charge. This includes leptonic decays, which include a neutral daughter particle, for example as in $\mathrm{B}^+ \rightarrow \overline{\mathrm{D}}^0 l^+ \nu_l$. Based on these considerations, all known beauty decays which involve a $\overline{\mathrm{D}}^0$ meson were identified as potential candidates for correlated background sources. They are presented in table 5.2.

Also the subsequent decays into ρ and ω mesons were considered, where not just the meson itself but their respective hadronic and leptonic daughters were taken into account, including the corresponding branching fraction. The corresponding daughter might as well be combined with the $\overline{\mathrm{D}}^0$ candidate to form a B^+ candidate. Even though it seems unlikely that they yield a significant contribution in the relevant invariant mass range of the B^+ meson, as these are multi-prong decays with strongly different kinematics, they were included in the full simulation, as their combined branching ratio is not negligible. Generally, decay channels with (combined) branching ratios smaller than $\mathcal{O}(10^{-5})$ were not considered, because expected yields would be negligible compared to the expected signal rate.

5.2.2.1. Simulation of correlated background sources

Using dedicated full MC simulations of the individually generated mesons, forced into the decays channels presented in table 5.2, it was studied whether these contribute a significant yield within the acceptance of the ALICE Experiment and in the invariant mass range of

Decay	Branching Ratio
$B^+ \to \overline{D}^0 \pi^+$	$(4.81 \pm 0.15) \cdot 10^{-3}$
$B^+ \to \overline{D}^0 K^+$	$(3.70 \pm 0.17) \cdot 10^{-4}$
$B^+ \to \overline{D}^0 \omega^0 \pi^+$	$(4.1 \pm 0.9) \cdot 10^{-3}$
$B^+ \to \overline{D}^0 \rho^0 \pi^+$	$(4.2 \pm 3.0) \cdot 10^{-3}$
$B^+ \to \overline{D}^0 \rho^+$	$1.34 \pm 0.18\,\%$
$B^+ \to \overline{D}^0 K^*(892)^+$	$(5.3 \pm 0.4) \cdot 10^{-4}$
$B^+ \to \overline{D}^0 l^+ \nu_l$	$2.27 \pm 0.11\,\%$
$B^+ \to \overline{D}^0 \tau^+ \nu_\tau$	$(7.7 \pm 2.5) \cdot 10^{-3}$
$B^+ \to \overline{D}^0 \pi^+ \pi^+ \pi^-$	$(5 \pm 4) \cdot 10^{-3}$ *
$B^+ \to \overline{D}^0 K^+ K^0$	$(5.5 \pm 1.6) \cdot 10^{-4}$
$B^+ \to \overline{D}^0 K^+ \pi^+ \pi^-$	$(5.4 \pm 2.2) \cdot 10^{-4}$
$B^0 \to \overline{D}^0 \pi^+ \pi^-$	$(8.4 \pm 0.9) \cdot 10^{-4}$
$B^0 \to \overline{D}^0 \pi^- l^+ \nu_l$	$(4.3 \pm 0.6) \cdot 10^{-3}$
$B^0 \to \overline{D}^0 \eta^0$	$(2.36 \pm 0.32) \cdot 10^{-4}$
$B^0 \to \overline{D}^0 \eta^{'}$	$(1.38 \pm 0.16) \cdot 10^{-4}$
$B^0 \to \overline{D}^0 \rho^0$	$(3.2 \pm 0.5) \cdot 10^{-4}$
$B^0 \to \overline{D}^0 \omega^0$	$(2.53 \pm 0.16) \cdot 10^{-4}$
$B_s^0 \to \overline{D}^0 K^- \pi^+$	$(9.9 \pm 1.5) \cdot 10^{-4}$

Table 5.2.: (* = non-resonant decay) Decays of potential correlated background candidates, having branching ratios larger than $\mathcal{O}(10^{-5})$. The signal decay channel $B^+ \to \overline{D}^0 \pi^+$ is shown as reference. Numbers are taken from [10].

Decay	Branching Ratio
$\rho(770) \to \pi^+ \pi^-$	~ 1
$\eta \to \pi^+ \pi^- \pi^0$	$(2.292 \pm 0.28) \cdot 10^{-1}$
$\eta^{'}(958) \to \pi^+ \pi^- \eta$	0.429 ± 0.007
$\omega(782) \to \pi^+ \pi^- \pi^0$	0.892 ± 0.007

Table 5.3.: Subsequent decays of neutral particles of the studied correlated background sources. Numbers are taken from [10].

the B^+ meson. In this case, the expected yield of the considered decay was estimated using the binary scaling approach for Pb–Pb collisions, as explained in section 5.1.1.

In these full MC simulations, the complete ALICE geometry with the upgraded ITS detector was taken into account. It was required that all decay products visible to the experiment were propagated in the acceptance of ALICE, while for the limited acceptance correction in equation 5.2, it was sufficient that at least one of the correctly charged daughters appeared within the specified range. For reasons of simplicity, a flat p_T-spectrum of the B^+ (or B^0 or B_s^+) meson was assumed for all of these decays. As a consequence, the kinematics and the related topology of the decays are slightly altered but remain comparable with respect to each other, while sufficient statistics are also generated for high p_T. For a complete comparison, the signal decay $\mathrm{B}^+ \rightarrow \overline{\mathrm{D}}^0\pi^+$was included in the simulations, such that possible effects of this simplification could be singled out. In these simulations, the typical track selection cuts and the previously described $\overline{\mathrm{D}}^0$ selection criteria with PID information were used. As cross check, the generated MC simulations were verified by a comparison of the acceptance of the $\overline{\mathrm{D}}^0 \rightarrow \mathrm{K}^+\pi^-$ to available full MC productions available within ALICE. The final yields and shapes in the invariant mass spectrum of the specific decay channels were scaled by their corresponding branching ratios. In addition, the different branching ratios for the b-quark fragmentation $\mathrm{b} \rightarrow \mathrm{B}^+(= 40.99\,\%$, without baryon feed-down), $\mathrm{b} \rightarrow \mathrm{B}^0(= 40.99\,\%)$ and $\mathrm{b} \rightarrow \mathrm{B}^0_\mathrm{s}(= 8.5\,\%)$ (all from [79]) were taken into account. Uncertainties of the branching fractions were neglected.

In these comparisons, the subsequent decay $\overline{\mathrm{D}}^0 \rightarrow \mathrm{K}^+\pi^-$ is similar for all channels under study and was thus forced in all cases, such that it can be normally reconstructed in the analysis. The corresponding branching ratio $\mathrm{BR}(\overline{\mathrm{D}}^0 \rightarrow \mathrm{K}^+\pi^-) = (3.88 \pm 0.05) \cdot 10^{-2}$ was then included in the binary scaling calculation.

The full information on the configuration of the individual MC simulations and the generated statistics in each channel can be found in the appendix E, tables E.1 and E.2.

5.2.2.2. Determination of the acceptance and efficiency

In a first step, the $\overline{\mathrm{D}}^0$ selection as in section 5.1.2.2 was applied to all generated candidate decays. Despite the fiducial volume selection, explained in section 5.3.1, no additional analysis cuts were applied on the B^+ candidate. Aside the signal decay channel $\mathrm{B}^+ \rightarrow \overline{\mathrm{D}}^0\pi^+$, only six of the simulated candidate decays showed significant contributions in the wide invariant mass range of $\mathrm{m}^{\mathrm{B}^+}_{\mathrm{PDG}} = 5.279 \pm 0.500\,\mathrm{GeV}/c^2$, which are: $\mathrm{B}^+ \rightarrow \overline{\mathrm{D}}^0\mathrm{K}^+$, $\mathrm{B}^+ \rightarrow \overline{\mathrm{D}}^0 l^+\nu_l$, $\mathrm{B}^0 \rightarrow \overline{\mathrm{D}}^0\pi^+\pi^-$, $\mathrm{B}^0 \rightarrow \overline{\mathrm{D}}^0\rho^0$ and $\mathrm{B}^0_s \rightarrow \overline{\mathrm{D}}^0\mathrm{K}^-\pi^+$. Their (acc.·eff.)-factor is presented in figure 5.7a. Note, that each decay is fully corrected for a possible bias from the particle generation within a rapidity window of $|\mathrm{y}|<1.0$ (or $|\mathrm{y}|<7.0$ for the correction factor). The corresponding correction for the limited acceptance can be found in the figure 5.7b.

As can be anticipated from kinematics, the decay channel $\mathrm{B}^+ \rightarrow \overline{\mathrm{D}}^0\mathrm{K}^+$ also contributes significantly in the relevant invariant mass range, because no particle identification can be used on the charged decay daughter of the B^+ meson. Given the small mass difference between the pion and kaon mass assumption, the decay kinematics and topology are similar in the large invariant mass range. For the three three-body decay channels ($\mathrm{B}^+ \rightarrow \overline{\mathrm{D}}^0 l^+\nu_l$, $\mathrm{B}^0 \rightarrow \overline{\mathrm{D}}^0\pi^+\pi^-$, $\mathrm{B}^0_s \rightarrow \overline{\mathrm{D}}^0\mathrm{K}^-\pi^+$) and for $\mathrm{B}^0 \rightarrow \overline{\mathrm{D}}^0\rho^0$ ($\rho(770) \rightarrow \pi^+\pi^-$), in which only the charged decay daughters are visible to the experiment, the acceptance is about one order of magnitude smaller compared to $\mathrm{B}^+ \rightarrow \overline{\mathrm{D}}^0\pi^+$ and $\mathrm{B}^+ \rightarrow \overline{\mathrm{D}}^0\mathrm{K}^+$. This is due to different kinematics of the three-body decays, and the large mass difference between the pion mass hypothesis and the actual mass of the decay daughter. Their invariant mass spectrum appears fundamentally altered, as discussed in section 5.2.2.3.

All of the other channels are rejected because the pion mass assumption on heavier particles in the invariant mass hypothesis of the charged decay daughter $\mathrm{B}^+ \rightarrow \overline{\mathrm{D}}^0 + \mathrm{X}^+$ shifts the considered decay in the invariant mass spectrum of the B^+ candidates, depending on the relative mass difference compared to the pion mass. In addition, for many-body decays such as $\mathrm{B}^+ \rightarrow \overline{\mathrm{D}}^0\pi^+\pi^+\pi^-$ the invariant mass assumption of a two-body decay imposes a kinematic limit at $\mathrm{m}^{\mathrm{B}^+}_{\mathrm{PDG}}$, towards which the reconstructed invariant mass spectrum is

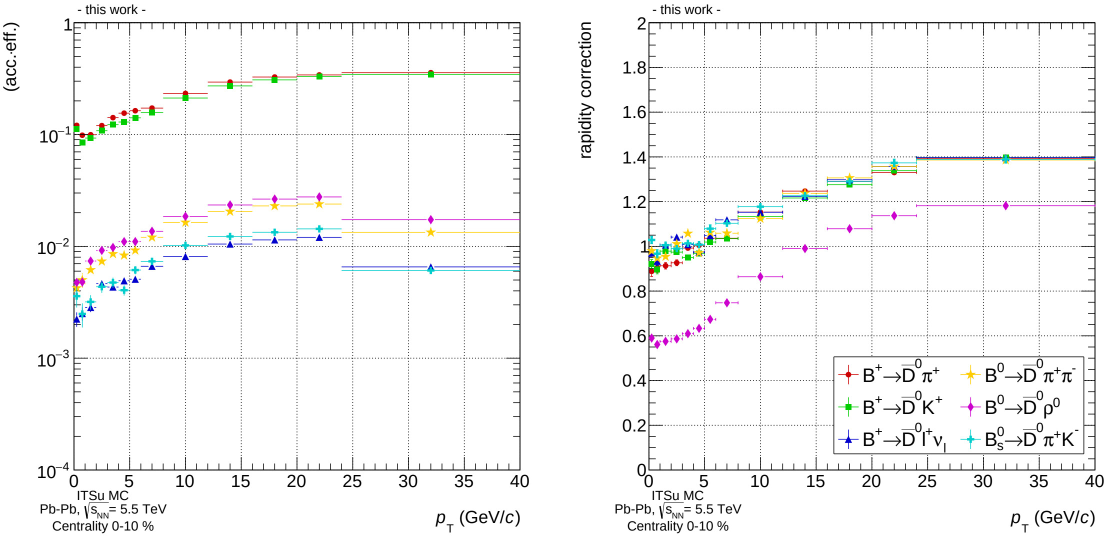

(a) **(b)**

Figure 5.7.: (a) displays the (acc.·eff.)-factor for identified correlated background sources. Note, that for the $B^+ \to \overline{D}^0 \pi^+$ channel the acceptance is always larger compared to figure 5.16, because only the $\overline{D}^0$ and fiducial volume selection were applied. In addition a flat p_T-spectrum was used for simplicity. (b) shows the limited acceptance correction for the same correlated background sources. Note, that the ratio was prepared without a bias on the rapidity ($|y|<7.0$). These additional simulations were performed for identified sources of correlated background only.

exponentially falling. Such kinematic effects further interplay with the low branching ratio compared to the signal decay, and thus do not result in significant yields in the considered invariant mass range. Their acceptance and reconstruction in the relevant invariant mass range is about three orders of magnitude lower, when compared to the signal channel.

5.2.2.3. Invariant mass spectra

Some of the invariant mass spectra of the relevant decay channels for selected kinematic bins are shown in figure 5.8. These spectra were obtained by scaling the results of the MC simulation to the expected yield, using the same approach as in section 5.1.1 and the acceptance from figure 5.7a. As described before, the respective branching ratios and the specific b-quark fragmentation values were included.

The reconstructed signal decay $B^+ \to \overline{D}^0 \pi^+$ appears as a Gauß-shaped structure, centered around the nominal invariant mass $m_{PDG}^{B^+}$. The remaining decay channels have shifted distributions, due to the pion mass assumption in the calculation of the invariant mass in the reconstruction algorithm. For the $B^+ \to \overline{D}^0 K^+$ decay, a peak structure can be identified, which height is roughly smaller by the ratio of the branching fractions compared to the signal decay. As visible in figure 5.8d, a double peak structure emerges with increasing reconstructed p_T of the B^+ candidate, and eventually forms a large tail towards lower values of the invariant mass, which is again a consequence of the false pion invariant mass assumption on the actual kaon daughter. The other decay spectra appear as exponentially falling distributions towards the limit at $m_{PDG}^{B^+}$. This results from the assumption of a

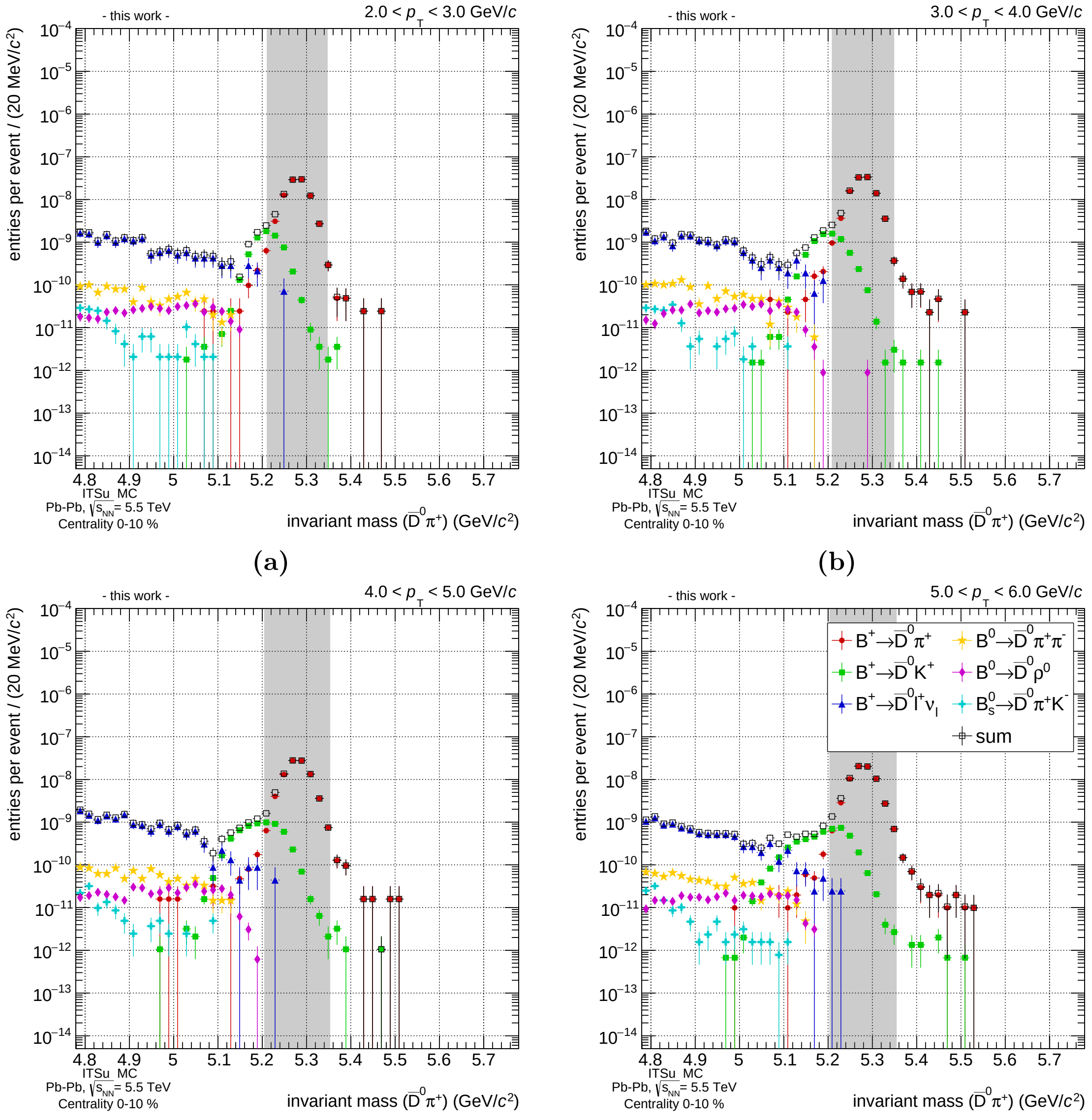

(a) (b) (c) (d)

Figure 5.8.: Invariant mass spectra of correlated background sources for selected kinematic bins. The sum of the combined spectra is displayed using black open boxes, while the gray band indicates the $\pm3\sigma$-range of the signal decay. For these spectra only the loose $\overline{D}^0$ selection criteria and the fiducial volumed cut were on the B$^+$ candidates. No combinatorial background was included in the analysis at this stage. (a), (b), (c) and (d) display a different kinematic bin of the B$^+$ mesons, respectively. The spectra of the remaining kinematic bins can be found in the appendix E, figure E.1.

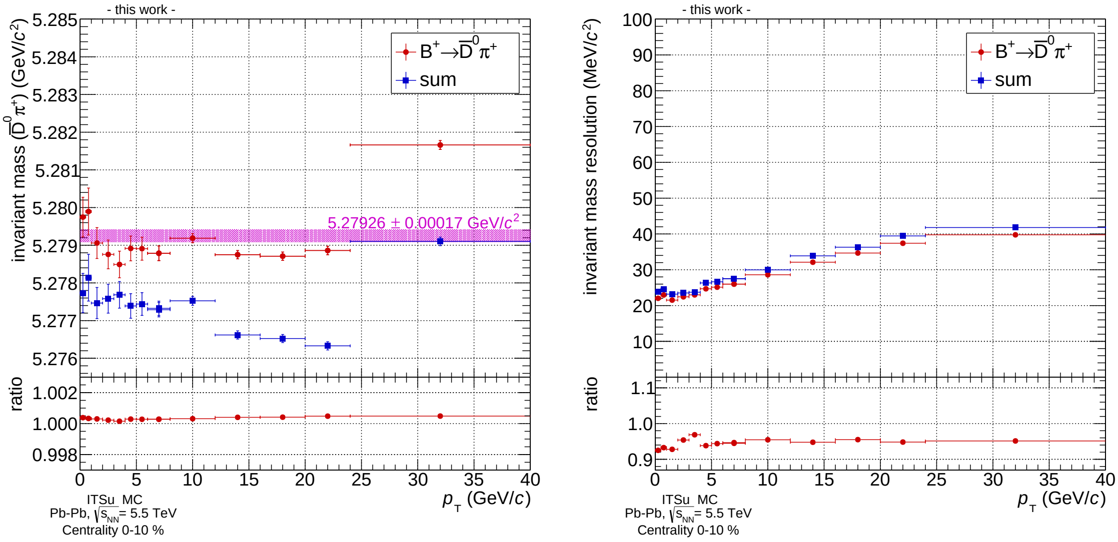

(a) (b)

Figure 5.9.: Results from a Gauß-fit to the peak in the invariant mass spectrum to the signal decay and the summed spectra, respectively. The determined peak position and width are displayed in (a) and (b). In the lower part of the plot, the corresponding ratio of the identified signal over the combined sum is presented.

two-body decay in the reconstruction algorithm, whereas these are true three-body decays with different kinematics. The gray band indicates the $\pm 3\sigma$-range, in which the signal yield is determined in the analysis. Even though it is suppressed by about one order of magnitude, the $B^+ \to \overline{D}^0 K^+$ decay contributes substantially inside this region, while the other decay channels appear smaller by about three orders of magnitude. Because of the rather large branching ratio of $\rho(770) \to \pi^+\pi^-$, $B^0 \to \overline{D}^0\rho^0$ is the only decay, where charged particles from the subsequent decay can be combined with the neutral $\overline{D}^0$ meson to form a potential B^+ candidate. For similar decays such as $B^0 \to \overline{D}^0\eta^0$, $B^0 \to \overline{D}^0\eta'$ and $B^0 \to \overline{D}^0\omega^0$ the subsequent decays also possess a large branching ratio (table 5.3). However, due to the fact that these are three-body decays, the kinematics of the charged daughters are shifted too strongly and thus cannot be formed into a B^+ candidate in this invariant mass range. Note, that no combinatorial background was included in this study.

5.2.2.4. Impact on signal extraction

A Gauß-fit to the invariant mass spectrum of the B^+ decay via $B^+ \to \overline{D}^0\pi^+$ as well as on the summed spectra from all decay channels has been performed in order to evaluate the impact of the additional correlated background sources on the evaluation of the signal yield. For both fits, the initial parameters were set similarly, in order to reduce possible biases. Further, the fit was restricted to a $\pm 3\sigma$-range around the true invariant mass $m^{B^+}_{PDG}$. The differences in the reconstructed position and peak widths are presented in figure 5.9.
As can be seen in the ratio of the identified signal over the combined sum of all decays, presented in the lower part of figure 5.9a, the peak position of the fit to the summed

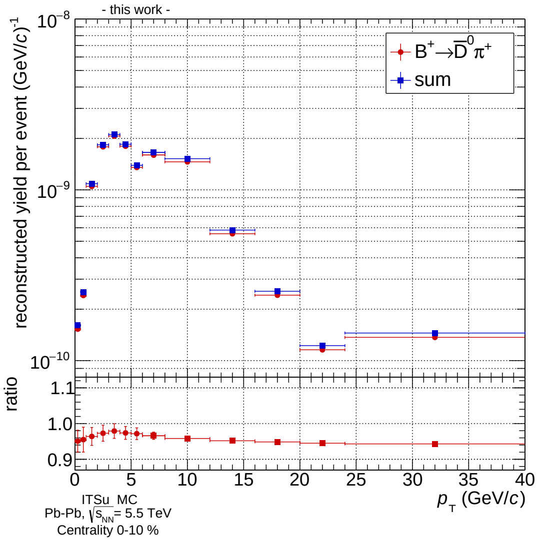

Figure 5.10.: Comparison between the expected yield per event from all summed correlated background sources and the signal decay, both taken from the integration of the corresponding Gauß-fits. The summed signal is systematically higher than the signal decay due to broadened peak width, as shown in figure 5.9b.

spectrum is systematically shifted to lower values, due to the convolution of the invariant mass spectrum. However, the impact is on per-mille level and thus negligible. Nevertheless, the corresponding invariant mass resolution is systematically and constantly larger by up to 10 %. As a consequence, the integral over the Gauß-function fitted to the summed spectra is systematically shifted by up to 6 %, as shown in the lower part of figure 5.10. Considering the foreseen recorded statistics of $L_{\text{int}} = 10\,\text{nb}^{-1}$, the size of this systematic offset is of the same order of magnitude as the expected statistical uncertainty of the $B^+ \to \overline{D}^0\pi^+$ signal, and should be taken into account in the signal extraction uncertainty. In case a template fit is used, the signal can be almost fully recovered, as presented in section 5.4.3.

In addition, it was evaluated, whether the impact from correlated background sources could be further diminished by the application of topological selection criteria, as they are described in section 5.3. As an example, the distribution of the cosine of the pointing angle θ_{pointing}, is shown for two selected kinematic bins in figure 5.11. Here, the signal and background decay channels were scaled to unity in the highest bin for better comparison. Even though for the lower kinematic bin the slopes appear different within the uncertainties, the distributions do not differ significantly for larger p_{T} of the B^+ meson, as visible in figure 5.11b. The distributions of the remaining kinematic bins can be found in the appendix E, figure E.2. From this comparison, it was concluded that the topological selection criteria will have no significant separation power between the signal decay and the correlated background sources.

5.2.3. Feed-down from B^{*+}

Theoretically, the measurement of the kinematics of B^+ mesons is convoluted by feed-down from B^* mesons, which decay dominantly into the correspondingly charged meson via

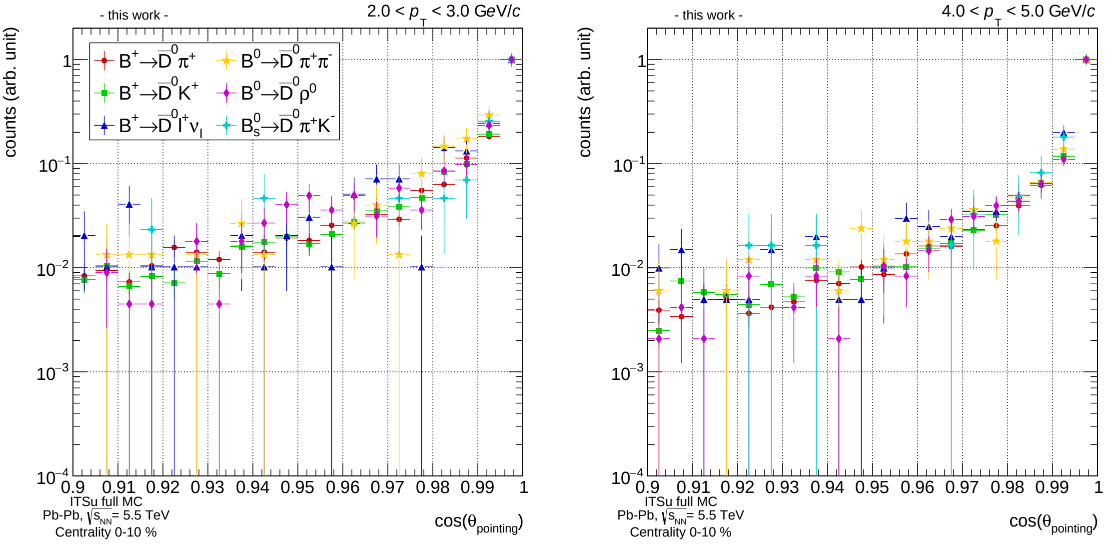

(a) (b)

Figure 5.11.: $\cos(\theta_{\mathrm{pointing}})$ distribution of correlated background sources for selected kinematic bins with statistical uncertainties. All distributions were scaled to unity in the highest bin for better comparability. The distributions of the remaining kinematic bins can be found in the appendix E, figure E.2.

$\mathrm{B}^{*+} \to \mathrm{B}^{+}\gamma$. However, the value $\mathrm{P} = 45\,\mathrm{MeV}/c$ of the decay is, compared to the large mass of the meson, small and does not have an impact on the B^{+} p_{T} shape.

5.3. Analysis cuts

The precise determination of the final detector acceptance and reconstruction efficiency (acc. · eff.) is essential for a reliable raw yield correction. On the one hand, this factor is driven by the actual azimuthal and longitudinal coverage of the detectors in the ALICE central barrel, while on the other hand the track selection criteria and additional topological and kinematic selection cuts further limit the reconstruction efficiency. Thus, optimized criteria are required to enhance the signal-to-background ratio and the statistical significance such that a significant (≥ 5.0) measurement is possible. In the following, the (acc. · eff.)-factor is determined in the full kinematic reconstruction of $\mathrm{B}^{+} \to \overline{\mathrm{D}}^{0}\pi^{+}$ ($\overline{\mathrm{D}}^{0} \to \mathrm{K}^{+}\pi^{-}$).

5.3.1. Fiducial volume selection

The fiducial volume or acceptance of the experiment must be determined from a minimum bias simulation, in order to avoid a possible effect through generation parameters of the MC simulation, such as the rapidity range within which particles are generated. For this purpose, a dedicated full MC simulation of charged B mesons was performed, using the setup of the new ITSu detector. Here, the mesons were generated in wide rapidity range $|\mathrm{y}| < 7.0$, and forced into the studied decay chain. The full decay chain was identified via MC truth information, and a pseudo-rapidity ($|\eta| < 0.9$) and kinematic ($p_{\mathrm{T}} > 0.1\,\mathrm{GeV}/c$) requirement on the charged daughter tracks was imposed, such that the particles propagate

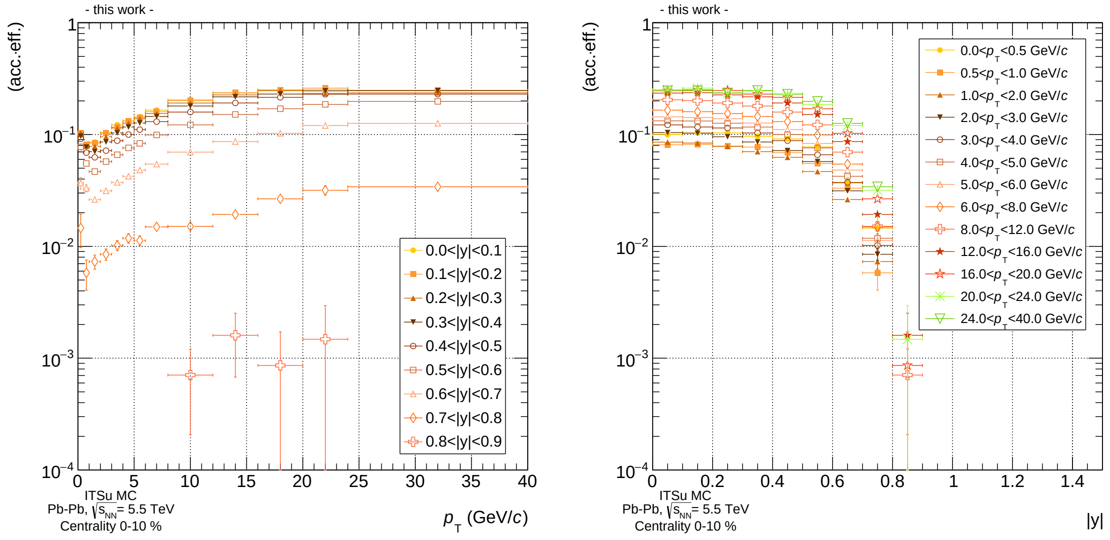

(a) (b)

Figure 5.12.: Acceptance for $B^+ \to \overline{D}^0\pi^+$ ($\overline{D}^0 \to K^+\pi^-$) in bins of rapidity (a) and transverse momentum (b). Despite the homogeneous evolution of the acceptance with rapidity, beyond $y \geq 0.8$ a large drop in the fiducial volume is observed. The fiducial volume cut threshold is applied at $|y| \leq 0.8$. For large momentum the acceptance rises, as the daughter particles appear more Lorentz-boosted and thus collimated into the fiducial region.

within the fiducial region of the experiment. The acceptance, which corresponds to the ratio of charged B mesons generated with these criteria over all generated charged B mesons, was corrected as in equation 5.2, and is presented in figure 5.12. In figure 5.12a, the p_T-dependence is shown in slices of the B meson rapidity, whereas figure 5.12b displays the rapidity dependence, in slices of p_T. For high transverse momentum of the charged B mesons, the daughter particles are strongly Lorentz-boosted and collimated in the acceptance of the detector. For decreasing momentum, the acceptance decreases, as the Lorentz-boost goes down and some of the daughters do not remain in the fiducial volume. For charged B mesons (almost) at rest, the opposite effect is observed, as the acceptance slightly rises. A smooth distribution in the acceptance is observed for all momentum bins with increasing rapidity up to $|y| < 0.8$. However, a rapid reduction of the acceptance is observed beyond $|y| \geq 0.8$, which is problematic for the final correction of the signal yield, and should be avoided. Thus, a p_T-independent selection on the rapidity of the B^+ meson $|y| < 0.8$ was applied and taken into account in the further analysis.

5.3.2. Topological and kinematic selection criteria

As outlined and sketched in section 5.1, the distinct topology of the full decay chain $B^+ \to \overline{D}^0\pi^+$ ($\overline{D}^0 \to K^+\pi^-$) allows to define topological selection criteria, which can efficiently enhance the signal on top of the combinatorial background from the remaining Pb–Pb collision. This enhancement significantly benefits from the improved secondary (and tertiary) as well as p_T resolution of the new ITSu detector, as presented in figures 5.3-5.6. Most efficiently, the invariant mass selection of $\pm 3\sigma$ around the true values of $m_{PDG}^{B^+}$ and

$m_{\overline{\mathrm{D}}^0}$ strongly limits the range of possible kinematic combinations of background candidates. However, given the low expected signal yield, presented in section 5.1.1, additional selection requirements are necessary. The most efficient criteria, which were already introduced in section 5.1, are the $\cos(\theta_{\mathrm{pointing}})$, the decay length of the $\overline{\mathrm{D}}^0$ meson ($\mathrm{L}^{\overline{\mathrm{D}}^0}_{\mathrm{decay}}$), the product of the impact parameters of $\overline{\mathrm{D}}^0$ and π^+ ($\mathrm{d0}^{\overline{\mathrm{D}}^0} \cdot \mathrm{d0}^{\pi^+}$), the transverse impact parameter $\mathrm{d0}^{\mathrm{B}^+}_{\mathrm{xy}}$ and the kinematic thresholds on the daughter momentum $p_{\mathrm{T}}^{\overline{D}^0}$ and $p_{\mathrm{T}}^{\pi^+}$. These cuts were tuned on top of a loose selection, which is applied on the reconstructed $\overline{\mathrm{D}}^0$ candidate, as presented in section 5.1.2.2. Typically, in ALICE the decay length normalized to the detector resolution is used instead of the decay length itself, as it would include the detector resolution. However, better agreement between the fast and full simulation was observed for the decay length itself. Further, in current heavy-flavor analysis in ALICE, usually two-dimensional properties are evaluated, as the resolution along the z-direction is degraded. For the new ITSu detector, the resolutions in transverse and longitudinal direction are similar, thus three-dimensional properties can be analyzed.

As these criteria are strongly correlated with each other, they were all tuned simultaneously in a multi-dimensional, p_{T}-dependent cut optimization, which aimed to achieve the largest possible expected statistical significance in each of the kinematic bins of the charged B meson for $\mathrm{L}_{\mathrm{int}} = 10\,\mathrm{nb}^{-1}$. For example, a tight cut on the $\cos(\theta_{\mathrm{pointing}})$-distribution also enhances the fraction of pions with high p_{T} in the remaining background sample. Out of that reason, each selection criterion was varied within a given range such that all possible combinations were tested. This range was previously determined using only a small fraction of events. In case the boundaries of the range were restricting the optimization, the ranges were readjusted. The statistical significance and the corresponding signal-to-background ratio are a direct indicator of the performance of the upgraded ALICE Experiment in the considered reconstruction. The statistical significance is defined as

$$\mathrm{Significance} = \frac{\mathrm{S}}{\sqrt{\mathrm{S}+\mathrm{B}}}, \tag{5.5}$$

which is the inverse of the statistical uncertainty of the signal, assuming the background is perfectly known. Here, B is the number of background candidates reconstructed in the considered kinematic bin, whereas S corresponds to the signal yield, identified via MC truth information.

In this approach, the full calculation of the binary scaling approach is considered for a realistic description of the signal yield, including the acceptance and reconstruction efficiency. However, the final estimate of the significance is only obtained after the application of additional scaling factors, which rise from the missing PID information and residual deviations in the topological descriptions of the fast simulation. These are presented in section 5.4.

In the following, the outcome of the multi-dimensional cut optimization of the uncorrected significance is presented for two kinematic bins, ranging from $3.0 - 4.0\,\mathrm{GeV}/c$ and $8.0 - 12.0\,\mathrm{GeV}/c$. The remaining figures of the cut optimization in the other kinematic bins are summarized in the appendix F. The correlations between the cut variables are presented in figures 5.13, 5.14 and 5.15, which demonstrate the separation power of all six tuned criteria and are always structured in the same format: The upper two figures display the signal and combinatorial background distributions in the two kinematic bins for the two given selection cuts, while the remaining selection criteria were set to their optimal values. Here, the signal distribution is always normalized to its own integral, and then scaled to the integral of the background distribution for better visibility. The lower two figures represent the correlation of the two considered cuts in two kinematic bins in the cut optimization algorithm, displaying the obtained uncorrected significance. Correlated background sources were not included in this approach, as their impact is included in the systematic uncertainty of the signal extraction in section 5.4.3.

5.3.3. Correlation between $\mathbf{L}^{\overline{\mathrm{D}}^0}_{\mathbf{decay}}$ and $\cos(\boldsymbol{\theta}_{\mathbf{pointing}})$

The reconstructed decay length of $\overline{\mathrm{D}}^0$ mesons for signal and background candidates in the kinematic bin $3.0-4.0\,\mathrm{GeV}/c$ of the B meson is presented in a range from 0 to $2\,000\,\mu m$ in figure 5.13a. Due to the large Lorentz-boost of the B^+ decay, the reconstructed tertiary vertex appears largely displaced, peaking at around $700\,\mu m$. Contrary to the reconstructed signal, the distribution of the background candidates appears as a decreasing exponential function, peaking towards 0 μm. An offset from 0 by $300\,\mu m$ is observed, which is a consequence of the application of the remaining selection criteria. The two distributions intersect around $400-500\,\mu m$, which is also in the region of the largest uncorrected significance (visible along the ordinate in figure 5.13c). Here, a plateau of the uncorrected significance is visible in the correlation between the two cuts, within which the variations of both cuts only impose negligible changes.

The distribution of the $\cos(\theta_{\mathrm{pointing}})$ for signal and background in the kinematic bin $8.0-12.0\,\mathrm{GeV}/c$ is presented in figure 5.13b. Whereas the background distribution only slowly increases towards unity, the signal distribution shows a dramatic increase. This is a consequence of the large Lorentz-boost of the B^+ decay, which collimates the daughter particles along the flight direction of the mother particle. As indicated in figure 5.13d, the best uncorrected significance in this kinematic bin is observed at a lower threshold cut at $\cos(\theta_{\mathrm{pointing}}) = 0.99985$, which marks the point where the signal and background distributions intersect: A much tighter cut a larger values would reject more signal, but only a small fraction of the remaining background candidates. Note, that despite the large statistics of 100 million events generated with the new fast simulation tool, some fluctuation in the background statistics remains present.

5.3.4. Correlation between $\boldsymbol{p}_{\mathbf{T}}^{\overline{\mathrm{D}}^0}$ and $\boldsymbol{p}_{\mathbf{T}}^{\pi^+}$

A strong correlation between the transverse momentum of the B^+ decay daughters is expected, as their kinematics define the reconstructed invariant mass and momentum of the mother particles. The momentum distribution of the $\overline{\mathrm{D}}^0$ meson in the kinematic bin $3.0-4.0\,\mathrm{GeV}/c$ is displayed in figure 5.14a. Here, an interesting feature is observed at low momentum in the background candidate distribution: A large peak at low momentum emerges, which is a consequence of the missing PID information in the fast simulation data sample, which is usually used for identification of the $\overline{\mathrm{D}}^0$ daughters. Here, an interplay of a wrong mass hypothesis and the particle momentum combine to a valid background candidate in the invariant mass region of the B meson. These false combinations are rejected by a lower threshold cut on $p_{\mathrm{T}}^{\overline{D}^0}$. The correlation with the $p_{\mathrm{T}}^{\pi^+}$ is presented in figure 5.14c.

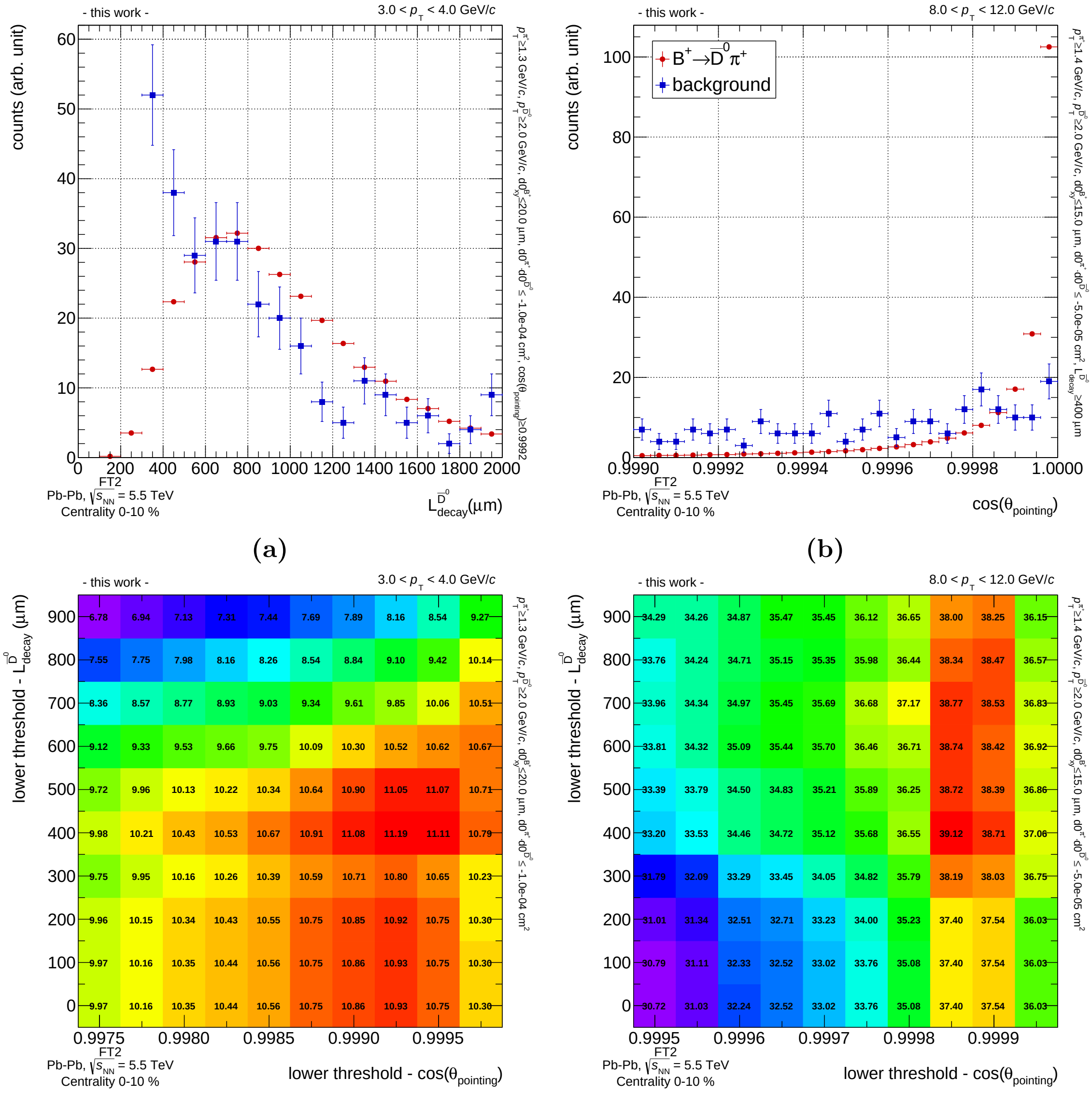

(a)

(b)

lower threshold - $L_{decay}^{\bar{D}^0}$ (µm)	0.9975		0.9980		0.9985		0.9990		0.9995	
900	6.78	6.94	7.13	7.31	7.44	7.69	7.89	8.16	8.54	9.27
800	7.55	7.75	7.98	8.16	8.26	8.54	8.84	9.10	9.42	10.14
700	8.36	8.57	8.77	8.93	9.03	9.34	9.61	9.85	10.06	10.51
600	9.12	9.33	9.53	9.66	9.75	10.09	10.30	10.52	10.62	10.67
500	9.72	9.96	10.13	10.22	10.34	10.64	10.90	11.05	11.07	10.71
400	9.98	10.21	10.43	10.53	10.67	10.91	11.08	11.19	11.11	10.79
300	9.75	9.95	10.16	10.26	10.39	10.59	10.71	10.80	10.65	10.23
200	9.96	10.15	10.34	10.43	10.55	10.75	10.85	10.92	10.75	10.30
100	9.97	10.16	10.35	10.44	10.56	10.75	10.86	10.93	10.75	10.30
0	9.97	10.16	10.35	10.44	10.56	10.75	10.86	10.93	10.75	10.30

(c)

lower threshold - $L_{decay}^{\bar{D}^0}$ (µm)	0.9995		0.9996		0.9997		0.9998		0.9999	
900	34.29	34.26	34.87	35.47	35.45	36.12	36.65	38.00	38.25	36.15
800	33.76	34.24	34.71	35.15	35.35	35.98	36.44	38.34	38.47	36.57
700	33.96	34.34	34.97	35.45	35.69	36.68	37.17	38.77	38.53	36.83
600	33.81	34.32	35.09	35.44	35.70	36.46	36.71	38.74	38.42	36.92
500	33.39	33.79	34.50	34.83	35.21	35.89	36.25	38.72	38.39	36.86
400	33.20	33.53	34.46	34.72	35.12	35.68	36.55	39.12	38.71	37.06
300	31.79	32.09	33.29	33.45	34.05	34.82	35.79	38.19	38.03	36.75
200	31.01	31.34	32.51	32.71	33.23	34.00	35.23	37.40	37.54	36.03
100	30.79	31.11	32.33	32.52	33.02	33.76	35.08	37.40	37.54	36.03
0	30.72	31.03	32.24	32.52	33.02	33.76	35.08	37.40	37.54	36.03

(d)

Figure 5.13.: The upper two figures display the distributions of $L_{decay}^{\overline{D}^0}$ and $\cos(\theta_{pointing})$ in the kinematic bins $3.0-4.0\,\mathrm{GeV}/c$ and $8.0-12.0\,\mathrm{GeV}/c$, respectively. Here, the signal distribution is normalized to its own integral, and then scaled to the integral of the background distribution for better visibility. The large displacement of the tertiary vertex in the signal decay is clearly visible in (a). The distributions in (b) are different, as the daughter particles in the signal decay channel appear strongly Lorentz-boosted. The lower figures display the significance as a function of the correlation between the lower threshold cuts on $L_{decay}^{\overline{D}^0}$ and $\cos(\theta_{pointing})$. The smooth transitions between the cut values and the plateau region of the uncorrected significance indicate a negligible systematic uncertainty from the actual thresholds applied. Other topological and kinematic cuts are set to their optimal value, summarized in table 5.4.

Again, a defined region of large uncorrected significance values is observed around the optimal cut values of $p_{\mathrm{T}}^{\pi^+} = 1.3$ and $p_{\mathrm{T}}^{\overline{D}^0} = 2.0\,\mathrm{GeV}/c$. A large difference between the signal and background distributions is observed at higher B^+ momentum, shown in figure 5.14d. Soft, combinatorial background candidates are efficiently rejected via a low threshold cut around $p_{\mathrm{T}}^{\pi^+} = 1.4\,\mathrm{GeV}/c$.

5.3.5. Correlation between $\mathrm{d0}^{\overline{\mathrm{D}}^0} \cdot \mathrm{d0}^{\pi^+}$ and $\mathrm{d0}_{\mathrm{xy}}^{\mathrm{B}^+}$

The remaining two of the considered selection criteria are presented in figure 5.15. As visible in the upper left figure, the transverse impact parameter distribution appears wider for background candidates. The excellent resolution of the upgraded ITS detector allows to place an upper threshold cut at $20\,\mu m$, rejecting the tail of the background distribution. The statistical fluctuations of the background do not allow for a more precise determination, however, no strong dependence of the uncorrected significance is observed up to $50\,\mu m$. This is different for the signal and background distributions of $\mathrm{d0}^{\overline{\mathrm{D}}^0} \cdot \mathrm{d0}^{\pi^+}$, displayed in figure 5.15b: Whereas the signal does not have any entries above zero and is strongly shifted towards large negative values, the background distribution peaks symmetrically at $0\,\mathrm{cm}^{-2}$. The intersection between the two distributions suggest an upper threshold cut around $-2.0 \cdot 10^{-6}\,\mathrm{cm}^2$. However, as visible in figure 5.15d, a much looser value was selected. The tight cut would result in a reduced reconstruction efficiency, which is not desired, as the raw yield correction becomes increasingly difficult. The threshold was thus limited to the displayed range, which results in lower values of the uncorrected significance, but maintains a reasonable reconstruction efficiency.

All of the selection cuts, optimized for uncorrected significance, are summarized in table 5.4. Some fluctuations are observed within the evolution of individual thresholds in the kinematic bins. These are a consequence from correlations between the individual selection criteria, slightly different ranges used in the multi-dimensional cut optimization, and residual statistical fluctuations in the background candidate distributions. A vanishing systematic uncertainty with varying cut values was observed for all criteria, as the uncorrected significance is rather insensitive to small variations of the thresholds.
In the two lowest kinematic bins ranging from $0.0 - 1.0\,\mathrm{GeV}/c$, the cut optimization was not successful: Given the hard momentum spectrum of the B^+ meson, a vanishing signal yield was observed, and no reasonable signal-to-background ratio was achieved using the topological and kinematic selection criteria. The (acc. · eff.)-factor was calculated analogue to equation 5.2, and is presented in figure 5.16. The statistical uncertainty is vanishing and hardly visible. Note, that some fluctuations are present, for example in the range from $5.0 - 8.0\,\mathrm{GeV}/c$. Here, the multi-dimensional cut optimization, which was tuned to maximize the uncorrected significance, aimed for more tight selection criteria. Albeit the improvement in uncorrected significance with these tight cuts would have been less than $10\,\%$, the signal reconstruction efficiency was strongly reduced. This was overcome by limiting the cut range to less tight thresholds. However, in this p_{T} range the (acc. · eff.) appears slightly lower. The total (acc. · eff.)-factor is larger than for current open charm measurements [236], and is thus expected to be well under control. The scaling factor of the limited acceptance of $|\mathrm{y}| < 0.5$, as shown in equation 5.2, is displayed in figure 5.16b.

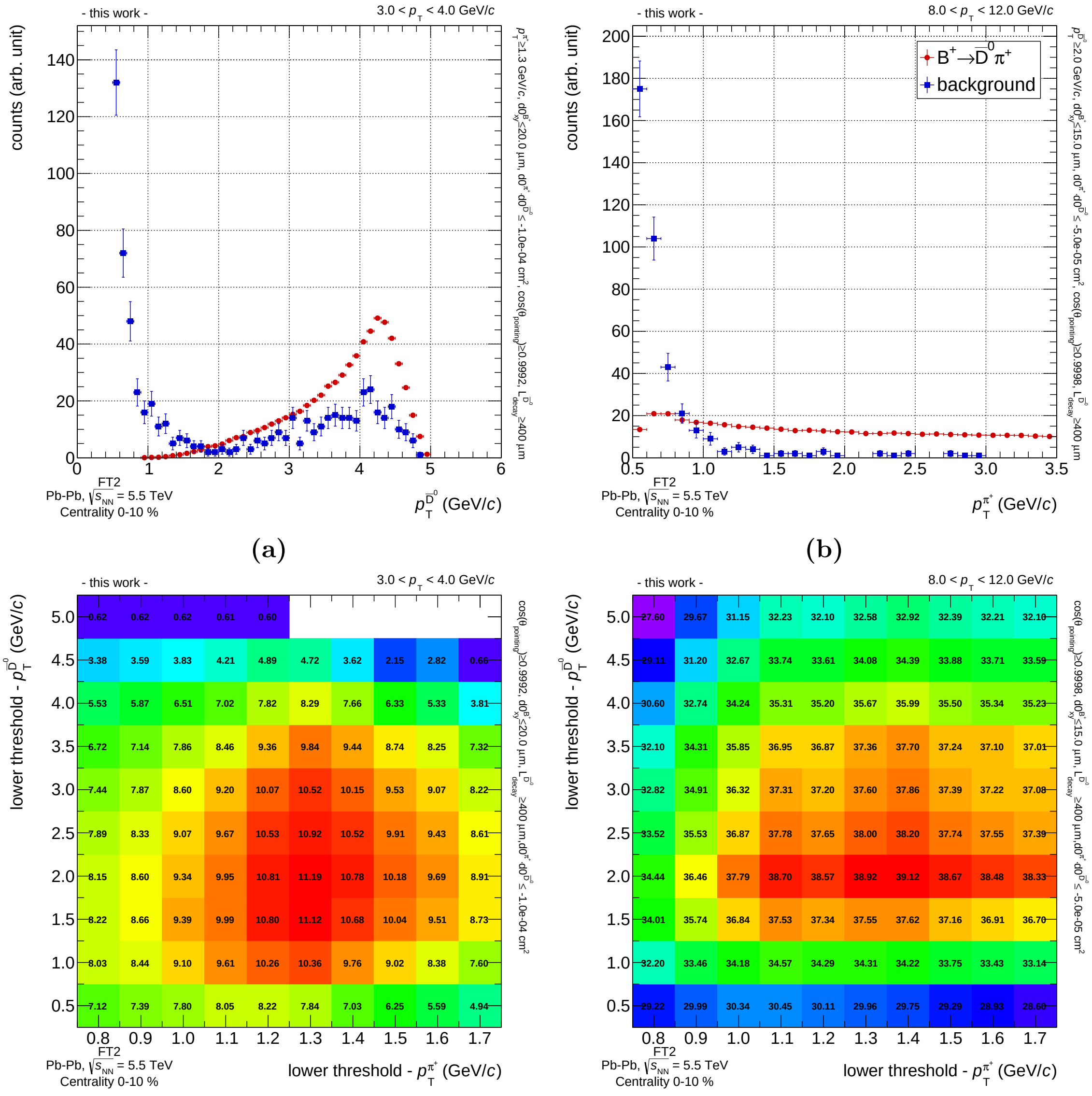

(a) **(b)**

(c) **(d)**

Figure 5.14.: The upper two figures display the distributions of $p_T^{\overline{D}^0}$ and $p_T^{\pi^+}$ in the kinematic bins $3.0 - 4.0\,\mathrm{GeV}/c$ and $8.0 - 12.0\,\mathrm{GeV}/c$, respectively. Here, the signal distribution is normalized to its own integral, and then scaled to the integral of the background distribution for better visibility. A strong correlation between the daughter momentum is observed, as these are combined to the reconstructed invariant mass of the mother B^+ meson. The peak at low momentum in the background distribution in (a) results from missing PID information, and an interplay between invariant mass hypothesis and measured p_T. The pion candidate p_T distributions in (b) appears much harder for particles from the signal decay chain. The lower figures display the significance as a function of the correlation between the lower threshold cuts on $p_T^{\overline{D}^0}$ and $p_T^{\pi^+}$. Other topological and kinematic cuts are set to their optimal value, summarized in table 5.4.

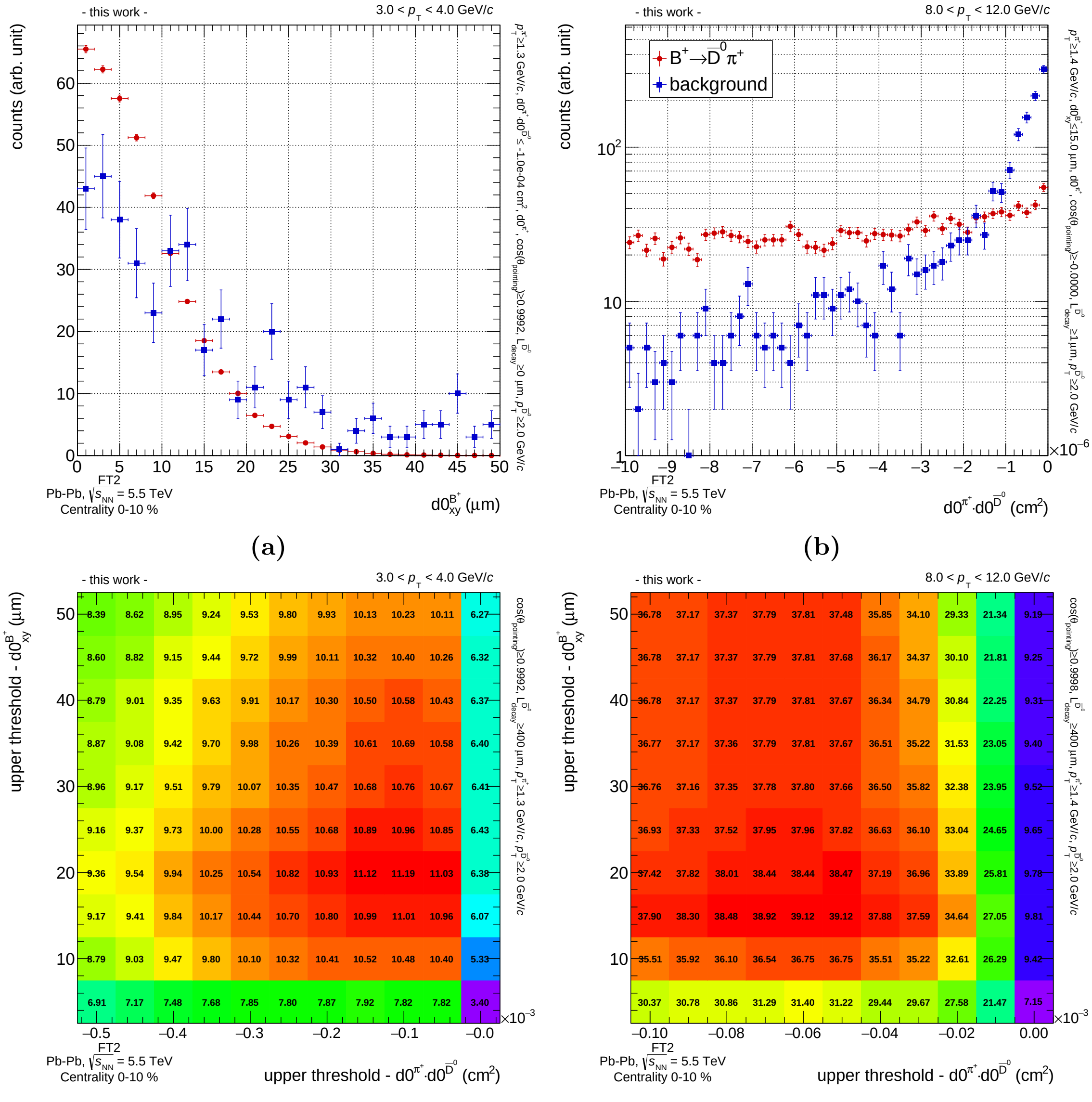

(a) (b)

(c) (d)

Figure 5.15.: The upper two figures display the distributions of $d0^{\overline{D}^0} \cdot d0^{\pi^+}$ and $d0^{B^+}_{xy}$ in the kinematic bins $3.0 - 4.0\,\mathrm{GeV}/c$ and $8.0 - 12.0\,\mathrm{GeV}/c$, respectively. Here, the signal distribution is normalized to its own integral, and then scaled to the integral of the background distribution for better visibility. The transverse impact parameter of the B^+mesons appears more collimated around $0\,\mu m$ than for the reconstructed background candidates, where some statistical fluctuations are visible. The distributions in figure 5.15b suggest an upper thresholds cut around $2.0 \cdot 10^{-6}\,\mathrm{cm}^2$, which, however, would diminish the signal reconstruction efficiency to low values. The cut is just forced to stay within the full range displayed in (b). The lower figures display the significance as a function of the correlation between the upper threshold cuts on $d0^{\overline{D}^0} \cdot d0^{\pi^+}$ and $d0^{B^+}_{xy}$. Other topological and kinematic cuts are set to their optimal value, summarized in table 5.4.

$p_{\mathrm{T}}^{\mathrm{B}^+}$	$\Delta\mathrm{m}^{\overline{\mathrm{D}}^0}$	$\cos\left(\theta_{\text{pointing}}\right)$	$p_{\mathrm{T}}^{\pi^+}$	$p_{\mathrm{T}}^{\overline{D}^0}$	$\mathrm{L}_{\text{decay}}^{\overline{\mathrm{D}}^0}$	$\mathrm{d0}_{\mathrm{xy}}^{\mathrm{B}^+}$	$\mathrm{d0}^{\pi^+}\mathrm{d0}^{\overline{\mathrm{D}}^0}$
(GeV/c)	$\left(\mathrm{MeV}/c^2\right)$		(GeV/c)		μm		cm^{-2}
0.0 – 0.5	16	-	-	-	-	-	-
0.5 – 1.0	21	-	-	-	-	-	-
1.0 – 2.0	26	0.99600	1.7	2.0	300	30	$-2.5\cdot10^{-5}$
2.0 – 3.0	28	0.99800	1.5	2.0	300	20	$-5.0\cdot10^{-5}$
3.0 – 4.0	30	0.99925	1.3	2.0	400	20	$-1.0\cdot10^{-4}$
4.0 – 5.0	32	0.99960	1.1	2.0	500	20	$-1.5\cdot10^{-4}$
5.0 – 6.0	33	0.99960	1.4	2.0	500	15	$-2.5\cdot10^{-4}$
6.0 – 8.0	35	0.99985	1.3	3.0	500	20	$-2.5\cdot10^{-4}$
8.0 – 12.0	38	0.99985	1.4	2.0	400	15	$-5.0\cdot10^{-5}$
12.0 – 16.0	39	0.99950	1.6	3.5	600	60	$-5.0\cdot10^{-6}$
16.0 – 20.0	43	0.99940	1.1	2.5	600	10	$-1.0\cdot10^{-5}$
20.0 – 24.0	53	0.99970	0.9	4.0	400	10	$-1.0\cdot10^{-5}$
24.0 – 40.0	58	0.99970	1.3	3.5	700	10	$-5.0\cdot10^{-6}$

Table 5.4.: Results of the multi-dimensional cut optimization of the uncorrected significance for each p_{T} bin. The applied selection on the reconstructed invariant mass corresponds to $\Delta\mathrm{m}^{\overline{\mathrm{D}}^0} = \mathrm{m}_{\mathrm{PDG}}^{\overline{\mathrm{D}}^0} \pm 3\sigma$. Some fluctuations are observed, which are a consequence from correlations between the individual section criteria, slightly different precision used in the multi-dimensional cut optimization, and statistical fluctuations in the background candidate distributions. No systematic uncertainty from varying thresholds is applied, as the cuts appear within a smooth plateau region of the uncorrected significance, within which only a small dependence on the actual cut value is observed.

5.4. Systematic and statistical uncertainties

Several scaling factors and systematic uncertainties have to be included in order to fully correct the expected statistical significance and to estimate the precision of the measurement. A statistically reliable background analysis was only possible through the analysis of the fast simulation MC production, which, despite careful tuning and setup, imposes residual differences in the topological and kinematic description of the decays compared to full MC. In addition, the fast MC production did not include the PID capabilities of the ALICE Experiment, which can be estimated by other means, described in the following. After the evaluation of the impact of the FT2 on the analysis, uncertainties arising from the signal yield extraction (including correlated background sources) are estimated.

5.4.1. Systematic uncertainty and scaling factors from cut optimization

The FT2 was specifically set up in a standalone configuration (section 4.3.9.3) for the analysis presented above, for which no statistically comparable full MC simulation exists. The performance of the FT2 was thus extracted from a comparison to another full MC simulation of the upgraded ITSu detector, where the fast simulation was specifically anchored to (section 4.3.9.1). Under the assumption that the performance in the topological reconstruction in the FT2 does not change between the two configurations, uncertainties from the comparison to the available full MC production were assigned to the standalone production.

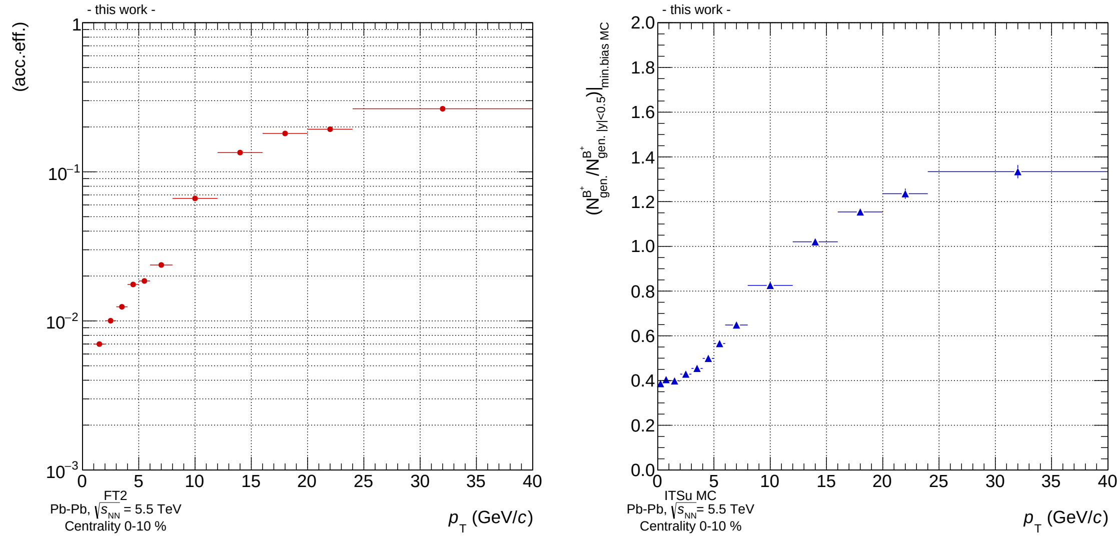

(a) **(b)**

Figure 5.16.: In (a), the (acc. · eff.)-factor is presented as function of p_T for the full decay chain $B^+ \rightarrow \overline{D}^0\pi^+$ ($\overline{D}^0 \rightarrow K^+\pi^-$). Some fluctuations are observed, for example around $5.0 - 8.0\,\mathrm{GeV}/c$, where the cut optimization was aiming for better values of the uncorrected significance. In these bins, the range of the cut optimization was limited to maintain a reasonable reconstruction efficiency. The limited acceptance correction, as shown on the right side of equation 5.2 is presented in (b).

These uncertainties rise from residual differences in the FT2 performance compared to the full MC simulation. On the one hand, these originate from missing background sources in the fast simulation, for example secondary particles generated in interactions of the primary particles with the detector material, which were not included in the fast simulation. On the other hand, residual deviations in the momentum resolution (shown in figure 4.3) and in the reconstructed topologies (e.g. visible after the application of the DCA selection in figure 4.22) introduce deviations in the reconstructed particle yields. An example is presented in figure 5.17a, where the product of impact parameters for background candidates $d0^{\overline{D}^0} \cdot d0^{\pi^+}$ in the FT2 and full MC simulation is presented for the transverse momentum bin between $3.0 - 4.0\,\mathrm{GeV}/c$, and residual differences are visible in the tails of the two distributions.

Given the statistical limitation of the available full MC production, not all cuts could be set simultaneously to their optimal values for the estimation of the systematic differences, as this approach would fully deplete the background candidate statistics. In order to keep the statistical uncertainty small, only a single selection cut was set at a time on top of the lower threshold on the $\cos(\theta_{\mathrm{pointing}})$, and the impact was measured via the ratio of the integrals over the remaining counts in the two simulations. This analysis was repeated for all selection criteria individually. From these variations, an uncertainty range was derived, as presented in figure 5.17b for signal and background candidates (boxes), respectively. The central value of the uncertainty band was used to correct the signal or background candidate yield individually, while the uncertainty band itself was propagated as systematic uncertainty of the FT2. In the presented example in figure 5.17b, the background yield is systematically lower at about $87 \pm 17\,\%$, only loosely dependent on the actual threshold

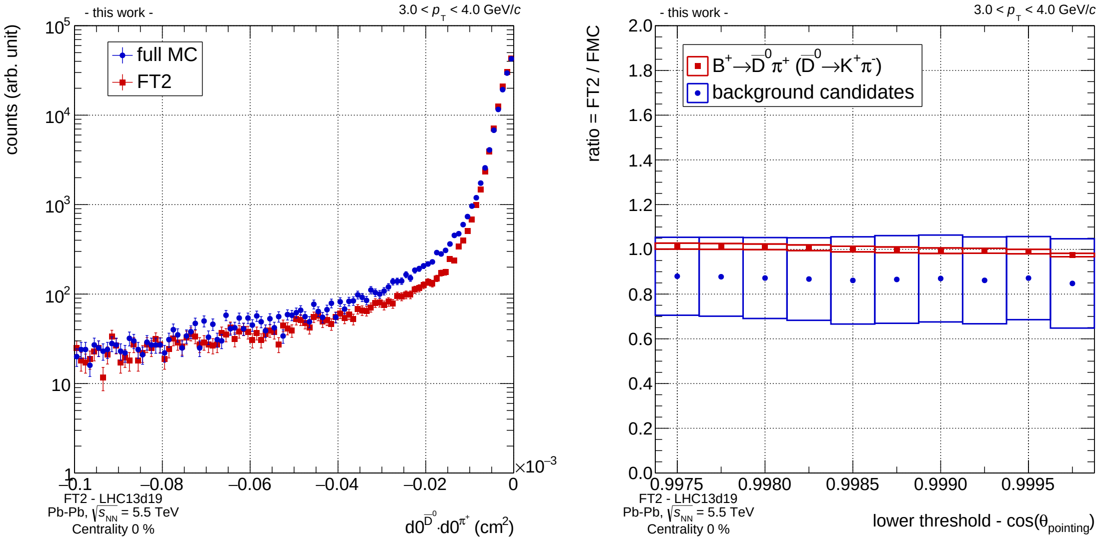

(a) **(b)**

Figure 5.17.: In (a), the distribution of $d0^{\overline{D}^0} \cdot d0^{\pi^+}$ for the background candidates in a full MC simulation and a similarly tuned FT2 simulation is displayed. For a given cut, the integral of the remaining yield is compared, and residual differences are propagated as systematic uncertainty of the FT2, as shown in (b). For signal and background candidates separately, each selection criterion is set to its optimized value one-by-one. The difference of the integral on the remaining yield is then displayed as uncertainty boxes. The actual uncertainty is evaluated for the exact cut in the $\cos(\theta_{\mathrm{pointing}})$ distribution. In addition, signal and background are scaled accordingly by the central value of the uncertainty band.

value of the $\cos(\theta_{\mathrm{pointing}})$ cut. The exact value of the correction and the uncertainty for each kinematic bin then depends on the exact optimized cut values. The largest uncertainties originate from differences between the product of the impact parameters and the decay length of the $\overline{\mathrm{D}}^0$ meson. Note, that in these comparisons the invariant mass resolutions obtained in full MC simulations were used in order not to bias the FT2 results due to the slightly overestimated resolution. This evaluation was performed for all kinematic bins individually, where the remaining bins are shown in appendix C.

5.4.2. Particle identification performance scaling

The missing PID information in the FT2 was addressed via a comparison of performance of the full B meson reconstruction with and without PID selection in full MC. The TPC and TOF PID performance of ALICE only enters in the selection of $\overline{\mathrm{D}}^0$ candidates into the analysis of the full decay chain $\mathrm{B}^+ \to \overline{\mathrm{D}}^0\pi^+$ ($\overline{\mathrm{D}}^0 \to \mathrm{K}^+\pi^-$), when pion and kaon daughters are identified to reconstruct the charmed meson. As shown throughout section 3.2, the PID separation power is strongly dependent on the momentum of the considered particle, which, in this case, is correlated with the momentum of the $\overline{\mathrm{D}}^0$ meson. Thus, using the available full MC simulation, the change in signal and background candidate yield with and without PID was evaluated as function of the applied $p_{\mathrm{T}}^{\overline{D}^0}$ cut in the corresponding kinematic bin. Their reduction is presented in figure 5.18. For large momentum around $16.0 - 24.0\,\mathrm{GeV}/c$, some fluctuations in the PID scaling factor of the background candidates are observed, which

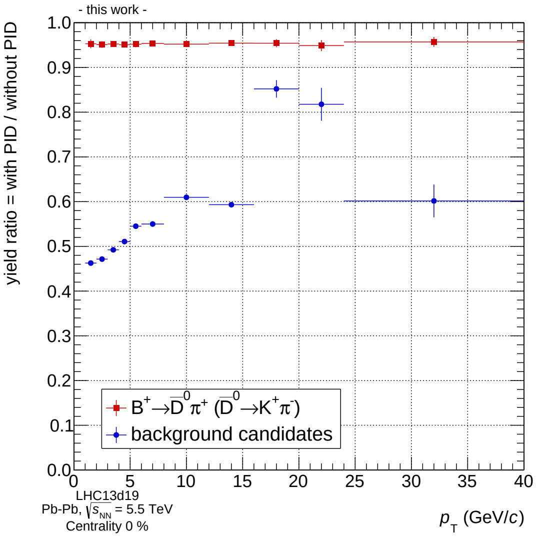

Figure 5.18.: Ratio of the expected reconstructed raw yield with and without the application of TPC and TOF PID for signal and background. PID is applied only on the daughters of the $\overline{D}^0$ candidate, and is thus dependent on the threshold cut of $p_T^{\overline{D}^0}$, which is applied in this analysis on top of some other, loose selection criteria. Both scaling factors are included in the final estimate of the significance.

may be introduced by the application of loose thresholds on the remaining selection criteria. For decreasing momentum the separation power of TPC and TOF becomes increasingly important, as more than 50 % of the background candidates are rejected, while only a 5 % loss in the signal yield is observed. The MC identified signal decay daughters are always narrowly distributed around the TPC and TOF expectation values, and a constant faction is removed for all momentum by the PID selection. The scaling factors of the signal and background candidate yields were propagated in the calculation of the fully corrected significance.

5.4.3. Systematic uncertainty of signal yield extraction

The expected signal, combinatorial and correlated background yields can be combined to sample the shape of an invariant mass spectrum, as it may look like after the entire data set of $L_{int} = 10\,\mathrm{nb}^{-1}$ is recorded beyond Run 3. For this purpose, the *Toolkit for Data Modeling with ROOT* (RooFit)[i] package was used, which is a toolkit distributed within ROOT. These invariant mass spectra can then be used to test the expected performance of the signal yield extraction, including the impact of the correlated background sources. With this approach, a corresponding systematic uncertainty was determined from the difference between true and recovered raw signal yield.
The expected reconstructed yields of signal and combinatorial background were scaled from the so far considered $\pm 3\sigma$-invariant mass range around the true B^+ meson mass to a wide invariant mass range of $\pm 500\,\mathrm{MeV}/c^2$. The shape of the spectra was sampled from the B^+ analysis of the HIJING background, performed with a loose selection criteria, such that statistical uncertainties are negligible. In addition, the shapes of the correlated background

---

[i] https://root.cern.ch/roofit

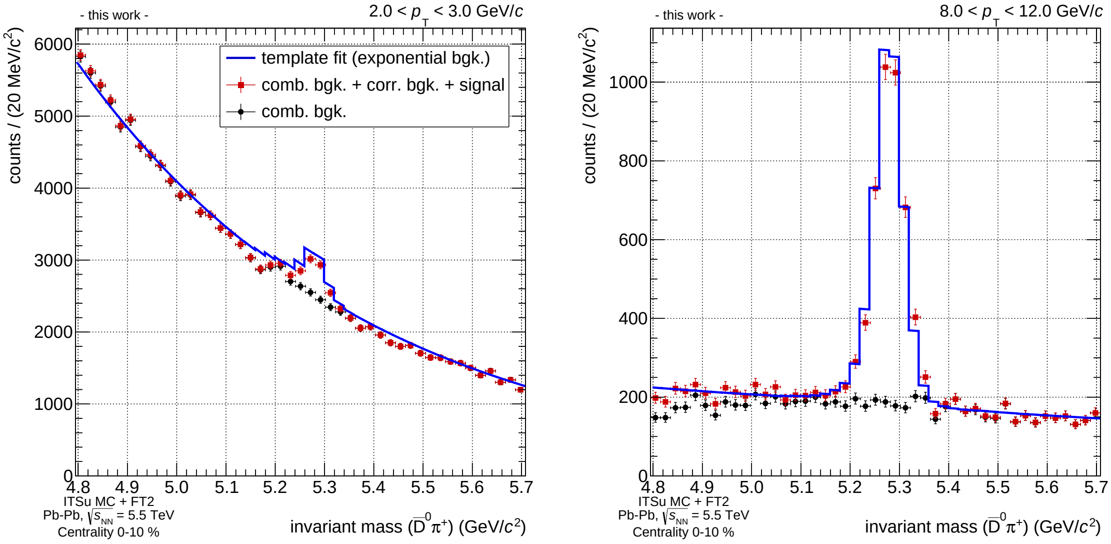

(a) (b)

Figure 5.19.: Invariant mass spectra for two kinematic bins, sampled from distributions obtained in the B^+ analysis with loose cuts and the correlated background analysis. The generated yields correspond to the reported central values in table 5.5 for the full available statistics of $L_{int} = 10\,nb^{-1}$. Combinatorial background (black circles) and the combination of combinatorial and correlated background as well as the signal yield (red squares), are shown separately. A template fit (blue line), which includes the signal as well as the correlated and combinatorial background distributions, is fit bin-by-bin on the spectra.

sources, described in section 5.2.2.3, were scaled to the expected overall yield, relative to the yield in the signal decay channel. Note, that in this approach, the central yield expectation values, as they are presented in table 5.5, were considered without additional systematic uncertainty.

Two examples of the generated invariant mass distributions are presented in figure 5.19. The spectra of the remaining kinematic bins can be found in appendix G. In these figures, the combinatorial background (black circles), as well as the combination of combinatorial and correlated background as well as signal counts (red squares) are displayed individually. On top of the generated spectra, a template fit is presented. This template includes the invariant mass spectra of the signal decay channel and the six relevant correlated background sources, as well as an exponential function for the combinatorial background. Each component of the template has an individual fit parameter, which correspond to the expected yield of that specific component. The complete template is fit bin-by-bin to the invariant mass spectrum, and the eight yield parameters are determined. This approach largely depends on the precision and relative size of the individual template components. Conceptually, it allows to extract not only the signal yield, which will be the only component further considered, but also the contribution of each background source, which could be further analyzed.

The comparison between the reconstructed signal yield identified via MC truth information (red circle) and the template fit (blue square) is presented in figure 5.20. Within some fluctuations, the template fit is capable to fully recover the correct signal yield within a precision better than 5 %. Even for the kinematic bin from $1-2\,\mathrm{GeV}/c$, where only a low

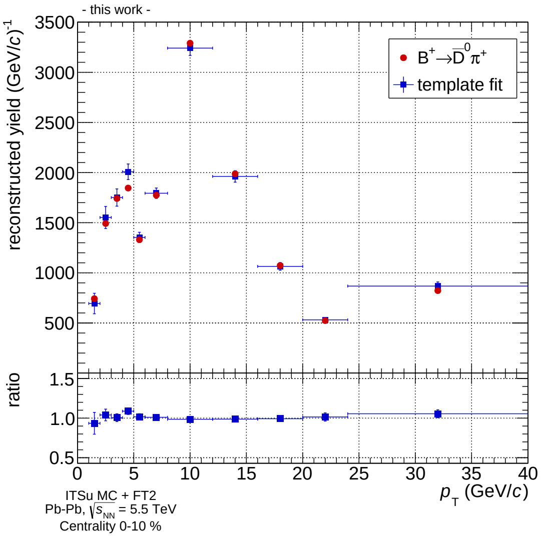

Figure 5.20.: Reconstructed signal yield, identified via MC truth information and the template fit respectively. The template fit is capable to recover almost all signal counts to a precision better than 5 %. Only for the bin from $1.0 - 2.0\,\mathrm{GeV}/c$, where no significant measurement is possible, a deviation of about 18 % is observed. The deviation of the ratio from unity was propagated as uncertainty of the signal yield extraction.

statistical significance is expected (see section 5.5), the template correctly finds more than 82 % of the original signal yield. This deviation originates from the statistical fluctuations of the low expected signal yield. The ratio presented in the lower part of figure 5.20 is further propagated into the systematic uncertainty of the expected signal yield.

5.4.4. Uncertainties for reconstructed signal and background yields

Given all of the presented considerations, the final, combined statistical and systematic uncertainties of the signal and background yields are presented in this section. The full uncertainty of the background yield is shown as a function of the reconstructed transverse momentum in figure 5.21a. Here, the combined uncertainty is displayed as open boxes, which consists of the systematic uncertainty from the FT2 (shaded area) and the statistical uncertainty (error bar) of the reconstructed candidate yield. For momentum up to $12\,\mathrm{GeV}/c$, the combined uncertainty is dominated by the contribution from the FT2 simulation, ranging between 20–40 %. For higher p_T, the statistical uncertainty becomes increasingly relevant. Even though the statistical uncertainty is high for larger p_T, without the fast simulation a reliable cut optimization would not have been possible at all. The uncertainties of the signal yield are much more complex. Here, the combined uncertainty is fully dominated by the FONLL prediction, which ranges within 50 % for low p_T, and 20 % for high p_T. Note, that within the FONLL uncertainties results are equally probable, as they are a consequence of the variations of the scale variables and masses in the calculation. No uncertainties of the parton distributions functions were available in the calculation at all center-of-mass energies. The statistical uncertainty remains below 5 % over the full momentum range, which is the intention of the original concept of injecting a large amount of signal decays into the simulation for negligible statistical uncertainty. Other sources of uncertainties in

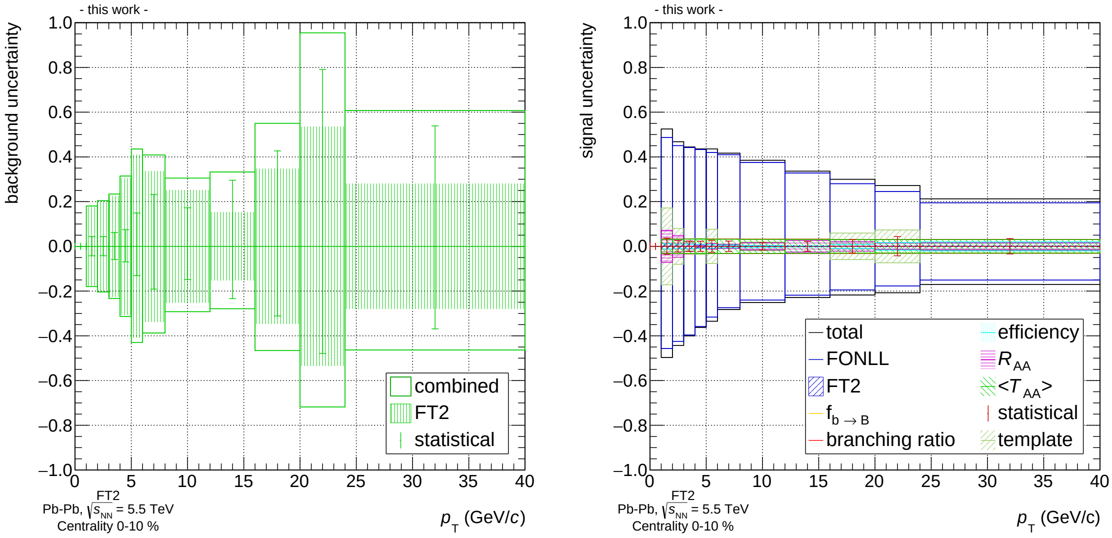

(a) **(b)**

Figure 5.21.: Combined uncertainty of the expected background and signal yield for $L_{int} = 10\,nb^{-1}$. (a) displays the combined (open boxes) uncertainty of the combinatorial background yield, which consists of the uncertainty from the FT2 (shaded area) and the statistical uncertainty (error bar) added in quadrature. The uncertainty of the expected signal yield is presented in (b). It is fully dominated by the uncertainty propagated from the FONLL calculation, used in the binary scaling approach.

the binary scaling approach, such as the contributions from the efficiency, the branching ratios or the R_{AA} estimate, remain small.

5.4.5. Uncertainties for significance and signal-to-background ratio

The uncertainties of the signal and background yields were directly propagated into the calculation of the statistical significance and signal-to-background ratio. They are presented in figures 5.22a and 5.22b respectively. Here, the individual contributions of the FT2 (shaded area), the statistical (error bar) and systematical uncertainties (error bracket) were added in quadrature for the combined uncertainty (open box). Both combined uncertainties are fully dominated by the systematic uncertainty of the signal, which originates from the FONLL calculation. Again statistical uncertainties of the background yield grow relevant only for transverse momentum above 16 GeV/c.

5.5. Significance and signal-to-background ratio

In the following, the final, fully corrected expected signal and background candidate yields in the full kinematic reconstruction of the decay channel $B^+ \to \overline{D}^0\pi^+$ ($\overline{D}^0 \to K^+\pi^-$) are presented for the upgraded ALICE Experiment. The fully corrected, expected yields in the invariant mass range of $\pm 3\sigma$ around the true B^+ mass are presented in table 5.5, together with all evaluated uncertainties. All scaling factors from the FT2 and PID were included. In addition, the yield per Pb–Pb event is indicated together with the combined uncertainty. The corresponding statistical significance and signal-to-background ratio

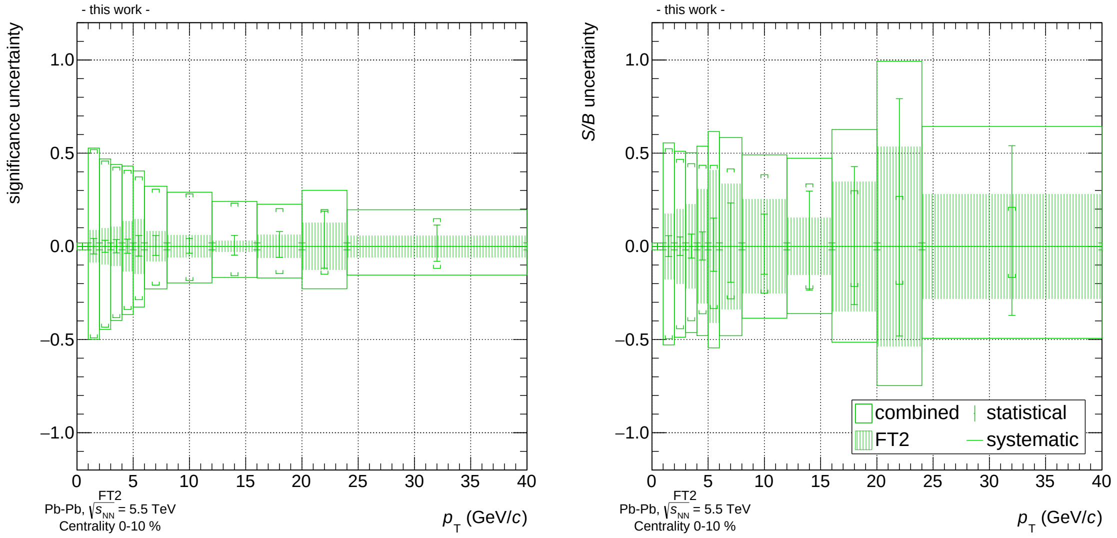

(a) **(b)**

Figure 5.22.: (a) displays the combined uncertainty (open boxes) expected significance, which consists of the uncertainty from the FT2 (shaded area), the statistical uncertainty (error bar) and the systematic uncertainty of the signal yield (error bracket), added in quadrature. The corresponding uncertainty of the signal-to-background ratio is presented in (b). While for transverse momentum below 16.0 GeV/c the propagated uncertainty from FONLL is the dominating contribution, for higher p_T the statistical uncertainty of the background imposes the largest error.

are presented in figure 5.23a and 5.23b, separately showing the performance with and without PID information. The final values are summarized in table H in appendix H. The statistical uncertainty (error bar), the FT2 uncertainty (shaded area) and the remaining systematic uncertainties (error bracket) are uncorrelated and thus added in quadrature to estimate the combined error (open box). In both plots, a large improvement through the usage of the PID information is observed for momentum between 1.0 − 8.0 GeV/c. Within uncertainties, a statistically significant measurement larger than 5 down to 2 GeV/c (with PID) or 3 GeV/c (without PID) is expected for the foreseen integrated luminosity of $L_{int} = 10\,\text{nb}^{-1}$ in ALICE. This corresponds to about 88 % (72 % without PID) of the expected full p_T spectrum of charged B mesons. Note, that previous measurements of the $c\bar{c}$ and $b\bar{b}$ cross-section tend to be on the upper side of current state-of-the-art calculations, as shown in figure 2.17, which would also result in an increase within the uncertainties in these plots. As a consequence of the efficient topological and kinematic selection criteria the signal-to-background ratio appears similar to current measurements of charmed mesons [236]. However, the small b quark production cross-section and the corresponding branching ratios reduce the significance to the limited range of up to about 50.

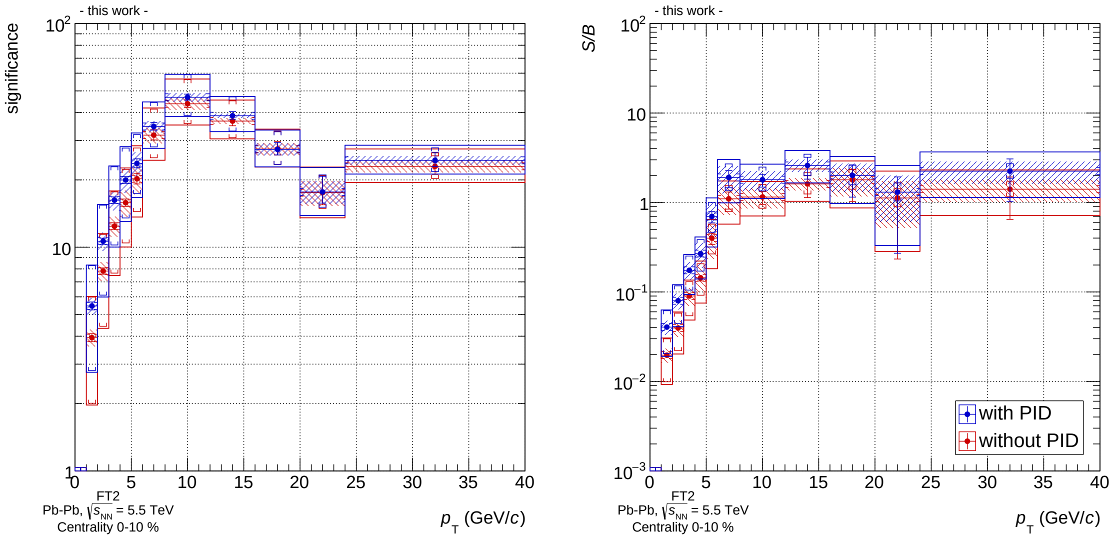

(a) **(b)**

Figure 5.23.: The fully corrected significance and signal-to-background ratio for the expected full available statistics $\mathrm{L}_{\mathrm{int}} = 10\,\mathrm{nb}^{-1}$ in Pb–Pb collisions of 0–10 % centrality are presented with (blue circles) and without (red circles) PID information. The combined error (open box) consists of the systematic (error bracket), FT2 (shaded area) and statistical (error bar) uncertainty. The impact of correlated background sources is included via the signal extraction uncertainty. All remaining uncertainties on the signal and background yields are fully propagated. The scaling factors from the FT2 on the signal and background yield are included as well. As visible in (a), a significant measurement (≥ 5) is possible down to $2.0\,\mathrm{GeV}/c$, using the PID information. This corresponds to about 88 % of the kinematic spectrum of B^+ mesons. The corresponding signal-to-background ratio is presented in (b). It is of similar size as current open charm measurements [236].

$p_{\mathrm{T}}^{\mathrm{B}^+}$ (GeV/c)	$\Delta \mathrm{m}^{\mathrm{B}^+}$ $\left(\mathrm{MeV}/c^2\right)$	signal and background yields	stat.	syst.	FT2	comb.	yield/event ± comb. unc.
				uncertainty			
0.0 – 0.5	68	-	-	-	-	-	-
0.5 – 1.0	73	-	-	-	-	-	-
1.0 – 2.0	72	768	$^{+28}_{-27}$	$^{+402}_{-380}$	± 7	$^{+403}_{-381}$	$\left(0.96^{+0.50}_{-0.43}\right) \cdot 10^{-7}$
		18971	$^{+834}_{-800}$	-	± 3323	$^{+3426}_{-3418}$	$\left(2.37^{+0.43}_{-0.43}\right) \cdot 10^{-6}$
2.0 – 3.0	72	1531	$^{+39}_{-38}$	$^{+715}_{-677}$	± 11	$^{+716}_{-678}$	$\left(1.91^{+0.90}_{-0.85}\right) \cdot 10^{-7}$
		19211	$^{+839}_{-805}$	-	± 3833	$^{+3923}_{-3916}$	$\left(2.40^{+0.49}_{-0.49}\right) \cdot 10^{-6}$
3.0 – 4.0	71	1772	$^{+42}_{-41}$	$^{+786}_{-708}$	± 20	$^{+788}_{-709}$	$\left(2.21^{+0.98}_{-0.89}\right) \cdot 10^{-7}$
		10159	$^{+627}_{-591}$	-	± 2290	$^{+2374}_{-2365}$	$\left(1.27^{+0.30}_{-0.30}\right) \cdot 10^{-6}$
4.0 – 5.0	77	1889	$^{+43}_{-42}$	$^{+822}_{-683}$	± 20	$^{+824}_{-685}$	$\left(2.36^{+1.03}_{-0.86}\right) \cdot 10^{-7}$
		7049	$^{+525}_{-490}$	-	± 2153	$^{+2216}_{-2208}$	$\left(8.81^{+2.77}_{-2.76}\right) \cdot 10^{-7}$
5.0 – 6.0	77	1366	$^{+37}_{-36}$	$^{+594}_{-456}$	± 12	$^{+595}_{-457}$	$\left(1.71^{+0.74}_{-0.57}\right) \cdot 10^{-7}$
		1958	$^{+293}_{-256}$	-	± 801	$^{+852}_{-841}$	$\left(2.45^{+1.07}_{-1.05}\right) \cdot 10^{-7}$
6.0 – 8.0	84	1831	$^{+43}_{-42}$	$^{+762}_{-516}$	± 12	$^{+763}_{-517}$	$\left(2.29^{+0.95}_{-0.65}\right) \cdot 10^{-7}$
		961	$^{+223}_{-184}$	-	± 324	$^{+393}_{-372}$	$\left(1.20^{+0.49}_{-0.47}\right) \cdot 10^{-7}$
8.0 – 12.0	85	3412	$^{+58}_{-57}$	$^{+1312}_{-856}$	± 12	$^{+1313}_{-858}$	$\left(4.26^{+1.64}_{-1.07}\right) \cdot 10^{-7}$
		1899	$^{+328}_{-282}$	-	± 478	$^{+579}_{-555}$	$\left(2.37^{+0.72}_{-0.69}\right) \cdot 10^{-7}$
12.0 – 16.0	93	2077	$^{+46}_{-45}$	$^{+696}_{-473}$	± 8	$^{+698}_{-475}$	$\left(2.60^{+0.87}_{-0.59}\right) \cdot 10^{-7}$
		800	$^{+237}_{-187}$	-	± 122	$^{+266}_{-223}$	$\left(1.00^{+0.33}_{-0.28}\right) \cdot 10^{-7}$
16.0 – 20.0	96	1123	$^{+34}_{-33}$	$^{+335}_{-242}$	± 3	$^{+337}_{-244}$	$\left(1.40^{+0.42}_{-0.31}\right) \cdot 10^{-7}$
		559	$^{+239}_{-174}$	-	± 194	$^{+308}_{-261}$	$\left(6.99^{+3.85}_{-3.26}\right) \cdot 10^{-8}$
20.0 – 24.0	104	551	$^{+24}_{-23}$	$^{+148}_{-112}$	± 2	$^{+150}_{-114}$	$\left(0.69^{+0.19}_{-0.14}\right) \cdot 10^{-7}$
		423	$^{+334}_{-202}$	-	± 226	$^{+403}_{-303}$	$\left(5.28^{+5.04}_{-3.79}\right) \cdot 10^{-8}$
24.0 – 40.0	124	866	$^{+30}_{-29}$	$^{+182}_{-144}$	± 3	$^{+184}_{-147}$	$\left(1.08^{+0.23}_{-0.18}\right) \cdot 10^{-7}$
		387	$^{+208}_{-142}$	-	± 108	$^{+235}_{-179}$	$\left(4.83^{+2.93}_{-2.24}\right) \cdot 10^{-8}$

Table 5.5.: Expected reconstructed signal and background yields for $\mathrm{L}_{\mathrm{int}} = 10\,\mathrm{nb}^{-1}$ ($8 \cdot 10^9$ events) together with their uncertainties. The yields were estimated within $\Delta \mathrm{m}^{\mathrm{B}^+} = \mathrm{m}_{\mathrm{PDG}}^{\mathrm{B}^+} \pm 3\sigma$. In order to highlight the performance of the fast simulation, the uncertainty of the FT2 simulation is quoted separately from the other systematic errors. In addition, the expected yield per central Pb–Pb event is presented together with its full, combined uncertainty. Below $p_{\mathrm{T}}^{\mathrm{B}^+} \leq 1.0\,\mathrm{GeV}/c$, no significant measurement was obtained with the presented cut selection, as the background yield increases and the p_{T} spectrum of the signal strongly decreases with decreasing p_{T}.

6. Recording of p+p reference data for B^+ reconstruction

In the previous section, the expected performance of the full kinematic reconstruction of B^+ mesons in the decay channel $\mathrm{B}^+ \to \overline{\mathrm{D}}^0\pi^+$ ($\overline{\mathrm{D}}^0 \to \mathrm{K}^+\pi^-$) was evaluated for central Pb–Pb colisions. In order to asses the effects of the strongly interacting medium, in particular the measurement of the nuclear modification factor R_{AA}, a high-statistics reference data sample of p+p collisions is needed at similar center-of-mass energy. The ALICE upgrade strategy foresees to record $6\,\mathrm{pb}^{-1}$ at a similar center-of-mass energy $\sqrt{\mathrm{s}} = 5.5\,\mathrm{TeV}$ [19]. In a complimentary approach to the foreseen data recording, an estimate on the required p+p reference statistics is calculated from the expected signal-to-background ratio of charged B mesons in Pb–Pb.

6.1. Expected integrated luminosity in p+p collisions

Based on the expected signal-to-background ratio and the statistical significance of the measurement of B^+ mesons, the range of the required integrated luminosity of the p+p reference data can be evaluated. This limit is evaluated based on the combined relative statistical uncertainty of the two measurements, in which the contribution from the p+p reference should be negligible. Within the scope of the upgrade studies, the choice was made that the combined relative statistical uncertainty should maximally increase by about 20 %, compared to the uncertainty of the Pb–Pb measurement [186]. This restricts the relative statistical uncertainty of the p+p measurement in each p_{T}-bin to be $\sqrt{2}$ times smaller, compared to the Pb–Pb measurement [20]. Here, the expected signal-to-background ratio and the significance, which is the inverse of the relative statistical uncertainty, of the B^+ reconstruction in central Pb–Pb collisions serve as a baseline:

$$\sqrt{2}\cdot\mathcal{S}^{\mathrm{Pb-Pb}} = \mathcal{S}^{\mathrm{p+p}} = \frac{S^{\mathrm{p+p}}}{\sqrt{S^{\mathrm{p+p}}+B^{\mathrm{p+p}}}} = \frac{\sqrt{S^{\mathrm{p+p}}}}{\sqrt{1+\left(\frac{B}{S}\right)^{\mathrm{p+p}}}} \tag{6.1}$$

$$\Rightarrow \mathcal{L}_{\mathrm{B}^+}^{\mathrm{p+p}} = \frac{(\mathcal{S}^{\mathrm{p+p}})^2}{\sigma_{\mathrm{B}^+}^{\mathrm{p+p}}}\cdot\left(1+\mathcal{C}\cdot\left(\frac{B}{S}\right)^{\mathrm{Pb-Pb}}\right) \tag{6.2}$$

$$\text{with}\quad \mathcal{L}_{\mathrm{B}^+}^{\mathrm{p+p}} = \frac{S^{\mathrm{p+p}}}{\sigma_{\mathrm{B}^+}^{\mathrm{p+p}}}, \tag{6.3}$$

$$\text{and}\quad \left(\frac{B}{S}\right)^{\mathrm{p+p}} = \mathcal{C}\cdot\left(\frac{B}{S}\right)^{\mathrm{Pb-Pb}} \tag{6.4}$$

The complete scaling from p+p to Pb–Pb collisions, including a possible scaling of the center-of-mass energy for p+p collisions, is absorbed in the factor $\mathcal{C}$, which is explained

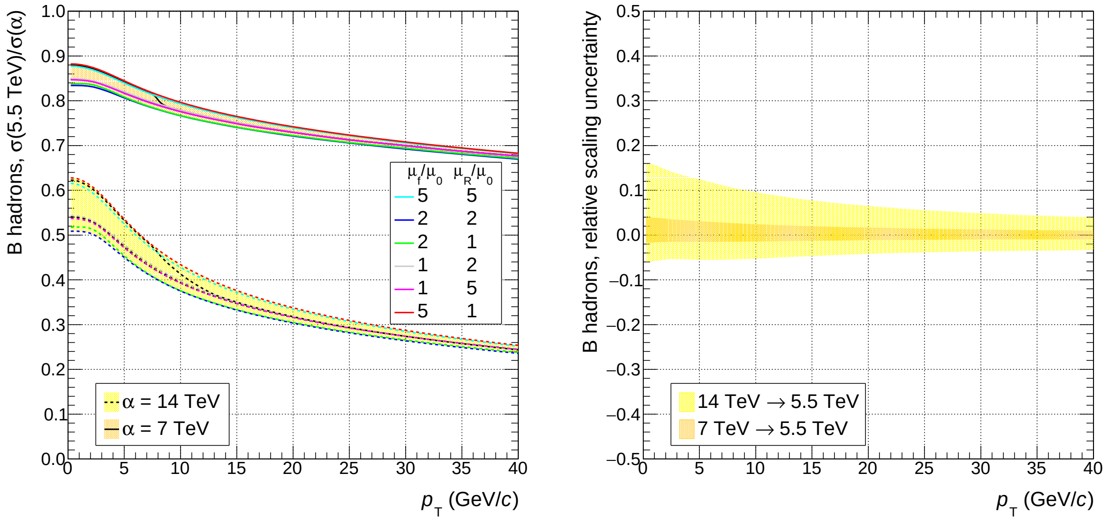

(a) **(b)**

Figure 6.1.: In (a), the energy scaling factor from the FONLL pQCD calculation for 14 to 5.5 TeV and 7 TeV to 5.5 TeV (dotted and solid lines respectively) are presented. The minimal and maximal uncertainty of the central value (black) and the scaling variations (different colors) are displayed for both ratios. The maximal uncertainty spread is indicated as yellow and orange shading, respectively. The relative spread of the scaling uncertainty is shown in (b).

in full detail in the appendix I.0.2. Further, it is assumed that signal and background multiplicity scale similarly with energy and event multiplicity. In this approximation, the signal and background reconstruction efficiencies were kept fixed to the values in the Pb–Pb scenario, which can be considered a worst case assumption. Typically, the selection cuts of the heavy-flavor decays are strongly loosened when moving from Pb–Pb to p+p collisions and the signal efficiency increases accordingly. In current open charm measurements, a factor 3 improvement of the p+p reconstruction efficiencies compared to Pb–Pb is observed [103, 236].

In order to estimate the reduction factor of background candidates, the number of reconstructed candidates in a fixed invariant mass range of $\Delta \mathrm{m}^{\mathrm{B}^+} = 5.279 \pm 0.100\,\mathrm{GeV}/c^2$, are compared for full MC production of p+p and Pb–Pb collisions (details in appendix I.0.1). Here, the reconstructed background candidates generated with HIJING (Pb–Pb at $\sqrt{s_{\mathrm{NN}}} = 5.5\,\mathrm{TeV}$) and PYTHIA (p+p at $\sqrt{s} = 7.0\,\mathrm{TeV}$) were compared for an estimate on the decrease of the background yield in p+p collisions. For both, the hybrid MC (section 4.3.1) approach was employed to include the improved performance of the ITSu. It was assumed that the background yield decreases independently of the analysis cuts, and no B^+ analysis cuts were applied on top of the $\overline{\mathrm{D}}^0$ selection because both data samples would otherwise be limited in event statistics. In addition, a scaling factor between the two center-of-mass energies $\varepsilon^{B}_{7\,\mathrm{TeV}}$ was calculated from FONLL. The scaling factors for $\sqrt{\mathrm{s}} = 7$ to 5.5 TeV and $\sqrt{\mathrm{s}} = 14$ to 5.5 TeV are displayed in figure 6.1, together with their uncertainties.

Despite the large uncertainties from variations of the factorization and renormalization scales and the heavy quarks masses in the FONLL calculation itself, as for example visible in

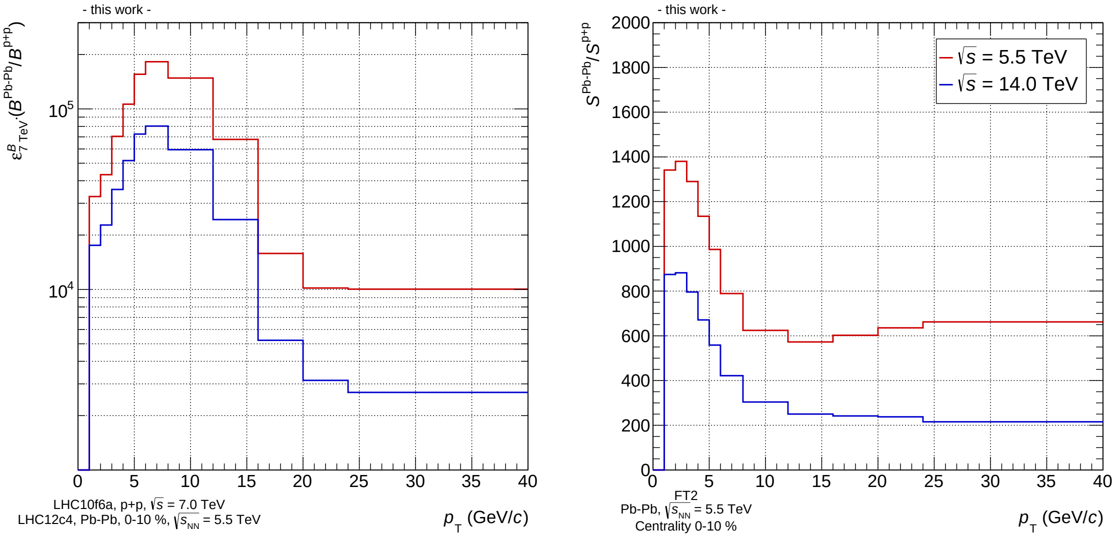

(a) **(b)**

Figure 6.2.: Scaling factors of expected background and signal yields per event in p+p compared to Pb–Pb collisions for different center-of-mass energies. (a) shows the scaling factor of the background yield per event, which was estimated using the ratio of reconstructed background candidates in the B^+ analysis from two different full MC simulations, indicated below the figure. These were scaled to the same center-of-mass energy by an additional factor derived from FONLL. The corresponding factor for the signal yield per event is displayed in (b). Here, the expected signal yield in p+p collisions was calculated for B^+ hadrons in the full decay chain based on FONLL and compared to the minimum-bias triggered cross-section in p+p collisions, as explained in the text.

figure 2.11, many uncertainties (partially) cancel in the ratio, as they are strongly correlated at different energies. As presented in figure 6.1, the central value of the ratio was used as scaling factor between the different center-of-mass energies, whereas the total uncertainty was computed from the envelope created by the systematic variation of the parameters [105]. Here, the factorization scale μ_F, the renormalization scale μ_R and the beauty quark mass $\mathrm{m_b}$ were varied around their central value ($\mu_F = \mu_R = 1.0$ and $\mathrm{m_b} = 4.75\,\mathrm{GeV}/c^2$) in the following ranges:

- $0.5 < \mu_F/\mu_0 < 2.0$ and $0.5 < \mu_R/\mu_0 < 2.0$, with the constraint $0.5 < \mu_F/\mu_R < 2.0$
- $4.5 < \mathrm{m_b} < 5.0\,\mathrm{GeV}/c^2$

using $\mu_0 = \sqrt{\mathrm{m_b^2} + \mathrm{p^2_{T,b}}} = \mathrm{m_{T,b}}$. Uncertainties from the parton distributions functions were not considered, as these were not available for all center-of-mass energies in the framework. As uncertainty of the corresponding energy scaling factor, the full envelope of the ratio was propagated. This uncertainty band is indicated by yellow and orange shaded areas in figure 6.1b.

The results of the comparison of the background candidate yield per event scaled from Pb–Pb collisions at $\sqrt{s_{\mathrm{NN}}} = 5.5\,\mathrm{TeV}$ to p+p collisions at $\sqrt{s} = 5.5$ and $14.0\,\mathrm{TeV}$, corrected for the difference in center-of-mass energy, are presented in figure 6.2a. No uncertainty is displayed, as it partially cancels in the full calculation of the expected signal-to-background ratio and the luminosity estimate in p+p. Depending on the specific kinematic bin, the background per event decreases by almost a factor $2.0 \cdot 10^5$.

The estimate of the raw signal yield per event in p+p collisions was derived from a comparison between the production cross-section of B^+ hadrons in the full decay chain obtained from FONLL and the minimum bias triggered reference cross-section $\sigma_{\mathrm{VBAND}}(7.0\,\mathrm{TeV}) = 54.34 \pm 1.90\,(\mathit{syst.})$ in ALICE [237, 56]. It was determined in dedicated luminosity calibration runs at the LHC (van der Meer scans), using a logical *AND* between the two V0 detectors [237]. Here, the difference to the cross-section at $\sqrt{s} = 5.5\,\mathrm{TeV}$ can be neglected, as it is small compared to other uncertainties. However, in order to estimate the minimum-bias cross-section at $\sqrt{s} = 14.0\,\mathrm{TeV}$, an additional scaling factor was introduced, based on the assumption that it scales similarly as the measured inelastic cross-section:

$$\sigma_{\mathrm{VBAND}}(14.0\,\mathrm{TeV}) = \sigma_{\mathrm{VBAND}}(7.0\,\mathrm{TeV}) \cdot \frac{\sigma_{\mathrm{inel}}(14.0\,\mathrm{TeV})}{\sigma_{\mathrm{inel}}(7.0\,\mathrm{TeV})} \tag{6.5}$$

Here, the measurements of $\sigma_{\mathrm{inel}}(7.0\,\mathrm{TeV}) = 60.2 \pm 0.2\,(\mathrm{stat.}) \pm 1.1\,(\mathrm{syst.}) \pm 2.4\,(\mathrm{lum.})\,\mathrm{mb}$ by CMS [238] and of $\sigma_{\mathrm{inel}}(13.0\,\mathrm{TeV}) = 73.1 \pm 0.9\,(\mathrm{exp.}) \pm 6.6\,(\mathrm{lum.}) \pm 3.8\,(\mathrm{extr.})\,\mathrm{mb}$ by ATLAS [239] were used. The final calculated scaling factors from Pb–Pb collisions at $\sqrt{s_{\mathrm{NN}}} = 5.5\,\mathrm{TeV}$ to p+p collisions at $\sqrt{s} = 5.5$ or $14.0\,\mathrm{TeV}$ are presented in figure 6.2. The uncertainty is omitted in the figure, as it largely cancels in the remaining calculation, but was further propagated as explained in section I.0.2.

As observed before in section 5.5, the errors are dominated by the uncertainty of the FONLL prediction and the background statistics. They are added in quadrature for an estimate on the total expected error. In this plot it is visible that the expected signal-to-background ratio rises significantly in p+p collisions, which originates from the large decrease of the background yield in p+p collisions. This scaling factor also introduces a peak structure in the range $5.0 < p_{\mathrm{T}} < 15.0\,\mathrm{GeV}/c$. The final estimate on the required p+p reference luminosity calculated with equation 6.1 is displayed in figure 6.4a. The corresponding uncertainties are outlined in figure 6.4b, where S and B stand for the signal and background yield respectively. Essentially, the uncertainties appear similar to those of the signal-to-background ratio presented in figure 5.22b. Originally, it was foreseen to record the required $6\,\mathrm{pb}^{-1}$ of reference data in a one month period with the luminosity leveled to $6 \cdot 10^{30}\,\mathrm{cm}^{-1}\mathrm{s}^{-1}$ at equivalent Pb nucleon energy. This limit is indicated in figure 6.4a. However, the data will not be sufficient to meet the goals on the increase of the statistical uncertainty, as the B^+ analysis requires an integrated luminosity of around $100\,\mathrm{pb}^{-1}$.

Nevertheless, in order to collect a sufficiently large data sample, the data could be recorded at a different center-of-mass energy, namely at the nominal design energy of the LHC at $\sqrt{\mathrm{s}} = 14\,\mathrm{TeV}$, which is expected as default configuration of the collider throughout the upcoming years. In order to maintain comparability in the R_{AA} measurement, the data must be scaled to similar center-of-mass energy as in Pb–Pb collisions, where the corresponding scaling factors are typically taken from different FONLL calculations [105], as previously described. As visible in figure 6.1, the uncertainty of this scaling factor does not exceed 16 % at low momentum, and reduces down to 5 % with increasing p_{T}. Given the relatively small size of this additional error, the p+p reference data may as well be taken at $\sqrt{\mathrm{s}} = 14\,\mathrm{TeV}$. The corresponding expected reference luminosity and its uncertainties are

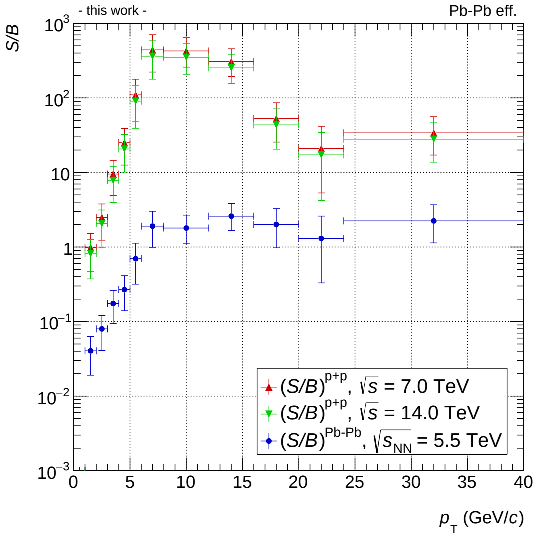

Figure 6.3.: Expected signal-to-background ratio for p+p collisions at $\sqrt{s} = 7$ TeV and $\sqrt{s} = 13$ TeV scaled from the expected results in central Pb–Pb collisions. The expectation values in p+p were estimated using equation 6.4. Their uncertainties were propagated accordingly.

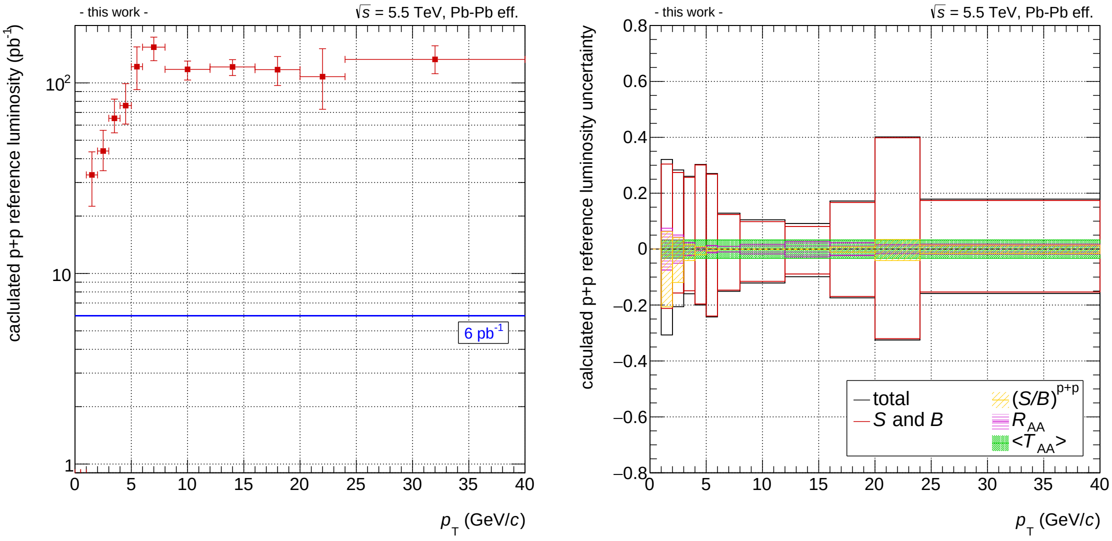

(a) **(b)**

Figure 6.4.: In (a), the required integrated luminosity of the p+p reference at $\sqrt{s} = 5.5$ TeV is displayed. It was calculated from the expected signal-to-background ratio in Pb–Pb collisions based on equation 6.1, using the same reconstruction efficiencies for signal and background. The foreseen reference statistics of 6 pb^{-1} are indicated by the horizontal blue line. It will not be sufficient to statisfy the statistical precision in the B$^+$ analysis. The propagated uncertainties from different contributions are displayed in (b). As before, the R_{AA} and $\langle T_{\mathrm{AA}} \rangle$ were taken from the TAMU prediction [95] and the ALICE centrality measurement [234], respectively. The uncertainty "S and B" corresponds to the error of the signal-to-background ratio in figure 5.22b. A detailed derivation on the displayed uncertainties is given in appendix I.0.2.

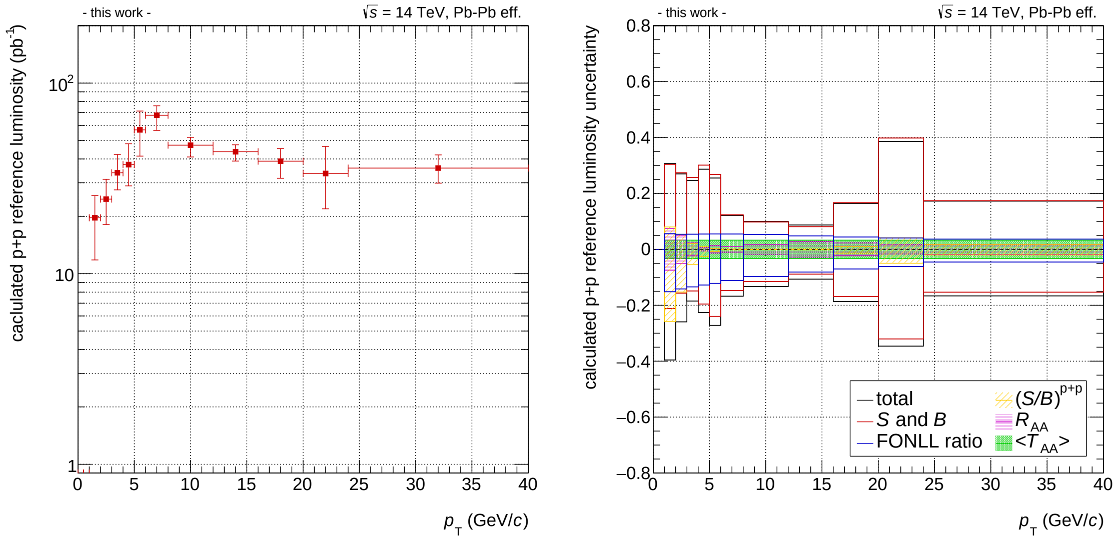

(a) **(b)**

Figure 6.5.: In (a), the expected integrated luminosity of p+p reference statistics at $\sqrt{s} = 14\,\text{TeV}$ using the Pb–Pb reconstruction efficiencies for the signal and background, based on equation 6.1, is displayed. The propagated uncertainties from different contributions are displayed in (b), and correspond to those errors shown in figure 6.4b. In addition the systematic uncertainty propagated from the energy scaling is displayed, which has only a minor effect on the overall precision.

displayed in figures 6.4a and 6.4b, respectively. The overall required integrated luminosity is reduced by about a factor 2–3 to approximately $50\,\text{pb}^{-1}$. This would correspond to about seven month of data taking at the nominal LHC design energy, depending on the performance of the LHC and availability of the ALICE detector. As indicated in figure 6.5b, the additional systematic uncertainty propagated from the energy scaling has only a minor effect on the overall precision.

7. Expected sensitivity on v_2 and R_{AA} in Pb–Pb collisions

In this section, the final results on the expected sensitivity of the nuclear modification factor R_{AA} and the elliptic flow v_2 in central Pb–Pb collisions in the full kinematic reconstruction of $\mathrm{B}^+ \rightarrow \overline{\mathrm{D}}^0\pi^+$ ($\overline{\mathrm{D}}^0 \rightarrow \mathrm{K}^+\pi^-$) and charge conjugates in ALICE measured at mid-rapidity are presented for the full statistic of $\mathrm{L}_{\mathrm{int}} = 10\,\mathrm{nb}^{-1}$ in Run 3 and 4 of the LHC. In addition, these results are put into context with the published R_{AA} measurement of non-prompt J/ψ by CMS [232] as well as the theoretical models introduced in section 2.3.4.3 [87, 93].

7.1. Nuclear modification factor

The nuclear modification factor of B^+ mesons predicted by the TAMU model [95] and the corresponding softening of the Pb–Pb p_{T} spectrum has been included in the binary scaling approach to calculate the expected signal yield (section 5.1.1) throughout this thesis, and is thus reflected in the calculation of the expected significance with PID information and its uncertainties in Pb–Pb collisions. Assuming that the background yield is precisely known, the relative statistical uncertainty corresponds to the inverse of the statistical significance of a measurement. The inverse of the statistical significance of the full kinematic reconstruction of B^+ mesons obtained in p+p and Pb–Pb collisions were thus propagated for an estimate of the expected sensitivity in the R_{AA} measurement.

Given the presented approach to obtain the predictions on the expected p+p reference statistics in section 6, the uncertainties of the two collisions systems should hence be treated fully correlated. Thus, in case maximal or minimal expected significance is assumed in Pb–Pb collisions, the same assumption must be valid for the significance in p+p collisions. As presented in section 5.4, a combined uncertainty of the significance was derived within the binary scaling approach, which is dominated by the propagated error from the FONLL calculation for $p_{\mathrm{T}} \leq 16\,\mathrm{GeV}/c$ and by statistical uncertainties of the expected reconstructed background yield for higher transverse momentum. As was explained in section 5.3, no relevant uncertainty from cut variations is expected and it was thus neglected. In current data analysis of charmed mesons in central Pb–Pb collisions at $\sqrt{s_{\mathrm{NN}}} = 2.76\,\mathrm{TeV}$, the PID efficiency was smaller than 15 %, while the tracking efficiency was 5 % per track [236], which is small compared to previously described uncertainties of the binary scaling approach. Hence, no additional error were assigned to the PID selection efficiency or the tracking efficiency in the following.

The inverse of the maximal and minimal expected significance in p+p and Pb–Pb collisions were added in quadrature respectively, such that an estimate on the best and the worst expected sensitivity in the R_{AA} measurement can be evaluated. As the uncertainty from the additional energy scaling factor is small, the results is insensitive to the difference between the two center-of-mass energies, at which the p+p reference data could be recorded.

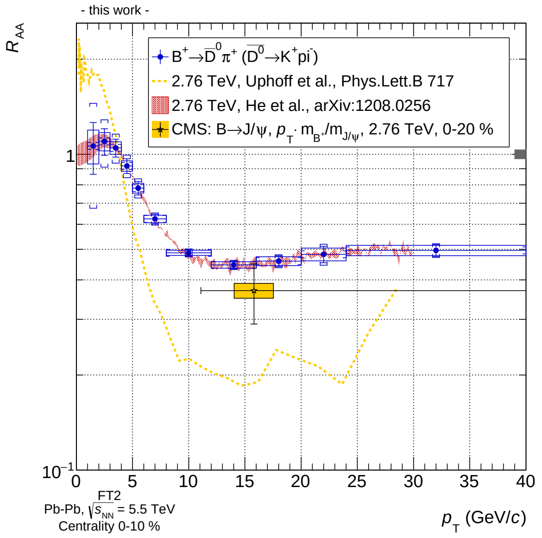

Figure 7.1.: Expected precision of the R_{AA} measurement with the upgraded ALICE Experiment in Pb–Pb collisions at $\sqrt{s_{NN}} = 5.5\,\text{TeV}$, 0–10 % centrality, for $L_{int} = 10\,\text{nb}^{-1}$. The results from simulation are plotted on top of the TAMU prediction [95], which was used in the binary scaling approach. The error bar corresponds to the central values of the expected significance, while the uncertainty box and the error bracket display the uncertainties of the minimal and maximal significance uncertainty, respectively. In this calculation the uncertainty of the R_{AA} is presented together with the model prediction and excluded from the uncertainty of the significance. In addition, a different model prediction by BAMPS [91] and the published CMS measurement of non-prompt J/ψ are presented [232].

The expected precision on the R_{AA} of fully reconstructed B^+ mesons is displayed in figure 7.1, on top of the model prediction by TAMU (He *et al.* [95]) for Pb–Pb collisions at $\sqrt{s_{NN}} = 2.76\,\text{TeV}$, 0–10 % centrality, which was presented in section 2.3.4.3. For the central value, the averaged model prediction in the corresponding kinematic bin was used. The indicated error bar corresponds to the central expectation of the significance estimate, while the uncertainty box and the error bracket display the uncertainties of the minimal and maximal significance, respectively. In this calculation the uncertainties of the R_{AA} and $\langle T_{AA} \rangle$ were excluded from the combined uncertainty of the significance. The overall error of $\langle T_{AA} \rangle$ of 3.3 % [234] is displayed separately as a gray shaded area, while the error of the R_{AA} calculation is indicated as red shaded area.

In addition, the corresponding prediction by BAMPS (Uphoff *et al.* [91]) and the published measurement by CMS of $R_{AA} = 0.37 \pm 0.08\,(\text{stat.}) \pm 0.02\,(\text{syst.})$ [232] are shown. For a valid comparison at similar transverse momentum, the momentum of the non-prompt J/ψ was scaled with the ratio of masses of B^+ and J/ψ [240], assuming that

$$p_T^{B^+} \approx p_T^{J/\psi} \cdot \frac{m^{B^+}}{m^{J/\psi}}. \tag{7.1}$$

The theoretical predictions and the expected sensitivity in the channel $B^+ \to \overline{D}^0 \pi^+$ ($\overline{D}^0 \to K^+ \pi^-$) are summarized in table 7.1. Note, that the observed jitter in the BAMPS prediction is a consequence of low statistics in the calculation [241]. Given the small uncertainties for the transverse momentum above 5 GeV/c and using the full expected statistics, ALICE will be sensitive to the suppression of the p_T spectrum by the QGP,

$p_{\mathrm{T}}^{\mathrm{B}^+}$ (GeV/c)	$\langle R_{\mathrm{AA}}^{\mathrm{TAMU}} \rangle$	$\langle R_{\mathrm{AA}}^{\mathrm{BAMPS}} \rangle$	Expected sensitivity
$0.0 - 0.5$	-	-	-
$0.5 - 1.0$	-	-	-
$1.0 - 2.0$	1.062 ± 0.079	1.780	$12 - 36\,\%$
$2.0 - 3.0$	1.098 ± 0.055	1.539	$7 - 17\,\%$
$3.0 - 4.0$	1.048 ± 0.024	1.119	$5 - 11\,\%$
$4.0 - 5.0$	0.918 ± 0.005	0.727	$4 - 8\,\%$
$5.0 - 6.0$	0.781 ± 0.010	0.522	$4 - 7\,\%$
$6.0 - 8.0$	0.624 ± 0.006	0.353	$3 - 4\,\%$
$8.0 - 12.0$	0.487 ± 0.008	0.231	$2 - 3\,\%$
$12.0 - 16.0$	0.446 ± 0.012	0.195	$2 - 3\,\%$
$16.0 - 20.0$	0.459 ± 0.011	0.219	$3 - 5\,\%$
$20.0 - 24.0$	0.482 ± 0.008	0.200	$5 - 8\,\%$
$24.0 - 40.0$	0.496 ± 0.009	0.327	$4 - 5\,\%$

Table 7.1.: Theoretically predicted R_{AA} for 0–10 % central Pb–Pb collisions at $\sqrt{s_{\mathrm{NN}}} = 2.76\,\mathrm{TeV}$ by TAMU (He *et al.* [95]) and BAMPS (Uphoff *et al.* [91]) compared to the derived sensitivity for the highest and lowest expected significance in the full kinematic reconstruction via $\mathrm{B}^+ \rightarrow \overline{\mathrm{D}}^0 \pi^+$ ($\overline{\mathrm{D}}^0 \rightarrow \mathrm{K}^+ \pi^-$).

independent on the actual theoretical model. For lower momentum, it is more difficult to draw a conclusive answer, as it is strongly model dependent: As both presented models include QGP and shadowing effects, it is implied that large p_{T} beauty quarks are quenched by the medium to lower momentum, thus the spectra in Pb–Pb collisions appear softer than in p+p collisions. According to the TAMU model, which predicts a suppression of the R_{AA} just below 0.5 for $p_{\mathrm{T}} \geq 8\,\mathrm{GeV}/c$, an increase of R_{AA} by up to 10 % above unity around $p_{\mathrm{T}} \approx 3\,\mathrm{GeV}/c$ is estimated. Even for the maximal expected significance ALICE will not be able to obtain a measurement which can distinguish this enhancement from unity. However, for the BAMPS model, a much stronger suppression of up to a factor five ($R_{\mathrm{AA}} \approx 0.2$) is predicted in the region $p_{\mathrm{T}} \geq 8\,\mathrm{GeV}/c$, which in turn means that more beauty quarks are quenched to low p_{T}. Subsequently, the expected rise above unity at low p_{T} is significantly larger by almost up to a factor of two. In this case, ALICE can distinguish the increase from unity with a separation power between $\langle R_{\mathrm{AA}}^{\mathrm{BAMPS}} \rangle / \sigma_{R_{\mathrm{AA}}} \approx 2.1 - 5.0$ at $p_{\mathrm{T}} = 2.5\,\mathrm{GeV}/c$, considering the lowest and highest possible expected significance. Note, that both theoretical models are for $\sqrt{s_{\mathrm{NN}}} = 2.76\,\mathrm{TeV}$, but expected changes of the R_{AA} of heavy-flavor mesons with center-of-mass energy are vanishing [235].

As visible in figure 7.1, the measurement by ALICE will be of similar or even higher precision and complementary to the published CMS data. As outlined in section 5 the analysis of non-prompt J/ψ is limited to a ${p_{\mathrm{T}}}^{\mathrm{B}^+}$-range larger than about 10 GeV by the acceptance and trigger capabilities of the CMS detector, and a differentiation between the model descriptions remains a challenge. With a similar reconstruction strategy of charged B^+ mesons in p+p collisions, a measurement down to $p_{\mathrm{T}} \geq 5.0\,\mathrm{GeV}/c$ was obtained by CMS [242]. Thus in case CMS can improve its signal selection strategy in Pb–Pb collisions, a measurement at lower momentum could be possible. In either case, ALICE will be capable to contribute a precise measurement of beauty R_{AA} down to $p_{\mathrm{T}} \geq 2.0\,\mathrm{GeV}/c$.

7.2. Elliptic flow

The expected precision of the elliptic flow measurement was evaluated using the raw signal yield in two intervals of the azimuthal angle ϕ, where the event plane direction Ψ_{EP} is assumed to be known on even-by-event basis. Conceptually, the procedure is analogue to the one presented in [186]: The reconstructed raw yield is sampled according to equations 2.14-2.16, using theoretical predictions by TAMU and BAMPS of v_2 at different centralities of Pb–Pb collisions at $\sqrt{s_{\mathrm{NN}}} = 2.76\,\mathrm{TeV}$. Again, the expected change of the elliptic flow at $\sqrt{s_{\mathrm{NN}}} = 5.5\,\mathrm{TeV}$ is expected to be less than $10\,\%$ and was neglected [243].
The combined uncertainty of the raw yields in $N_{\mathrm{in-plane}}$ and $N_{\mathrm{out-of-plane}}$ are then equal to $\sqrt{2/\left(1 \pm v_2\right)}$, relative to the initial raw yield. These uncertainties are propagated and added in quadrature. In current D meson measurements, uncertainties for the determination of the event plane resolution rise up to $20\,\%$ for low p_{T} [66]. Likely, similar uncertainties will rise for the future measurement in $\mathrm{B}^+ \rightarrow \overline{\mathrm{D}}^0\pi^+$ ($\overline{\mathrm{D}}^0 \rightarrow \mathrm{K}^+\pi^-$), but they are small compared to the error of the raw yield prediction (figure 5.21b) and can thus be neglected in this estimate. Other uncertainties, for example from the tracking, are not considered as they are fully negligible compared to the magnitude of the presented uncertainties and it is expected that these would (partially) cancel in the ratio of the v_2 calculation [20].
Similar to the previously presented R_{AA} sensitivity, the central, minimal and maximal expected raw signal yields in Pb–Pb collisions were used to evaluate the sensitivity to the observable. For the scaling between different centralities 20–40 % ↔ 0–10 % ↔ 30–50 %, it was assumed that the same significance per event is observed, as it is seen in current open charm measurements [236]. The statistical uncertainties of the signal were then scaled with change of the number of events and the number of binary collisions $\langle N_{\mathrm{coll}}\rangle$ in the given centrality class, using averaged values from [54]: $\langle N_{\mathrm{coll}}^{0-10\,\%}\rangle = 1\,499.8 \pm 94.6$, $\langle N_{\mathrm{coll}}^{0-10\,\%}\rangle = 558.4 \pm 62.5$ and $\langle N_{\mathrm{coll}}^{30-50\,\%}\rangle = 321.6 \pm 44.5$. The theoretical predictions and the expected sensitivity in the channel $\mathrm{B}^+ \rightarrow \overline{\mathrm{D}}^0\pi^+$ ($\overline{\mathrm{D}}^0 \rightarrow \mathrm{K}^+\pi^-$) are summarized in table K.1 in appendix K.
Figure 7.2a displays the expected precision of the v_2 measurement on top of a prediction for B^+ mesons by BAMPS (Uphoff *et al.* [91]) for 0–10 % centrality, $\sqrt{s_{\mathrm{NN}}} = 2.76\,\mathrm{TeV}$. Again, uncertainties are displayed based on the central (error bar), minimal (uncertainty box) and maximal (error bracket) values of the expected raw signal yield (table 5.5). For the bins where no prediction is available at high p_{T}, which corresponds to the region where the elliptic flow originates from the path length dependence in the medium, the absolute uncertainty was centered on zero. This approach was also applied in the first bin for at 0–10 % centrality, where no prediction is given by BAMPS. As elliptic flow is a direct consequence of the asymmetry of the macroscopic overlap region of the two Pb nuclei the relative magnitude in central collisions is smaller compared to more peripheral collisions, as can be seen for example by the increase of the predicted v_2 by BAMPS in figure 7.2b. Here, the precision of the measurement was estimated on top of the TAMU prediction (He *et al.*, 20–40 % (beauty)), which predicts a slightly lower v_2 than BAMPS. However, the BAMPS calculations were performed on low statistics only [241] and show some significant variations. It may also be possible that the actual v_2 of beauty quarks and mesons is even larger than expected by model predictions. Such an estimate is shown in figure 7.3, which displays the precision with respect to the predicted flow of charm quarks by TAMU (He

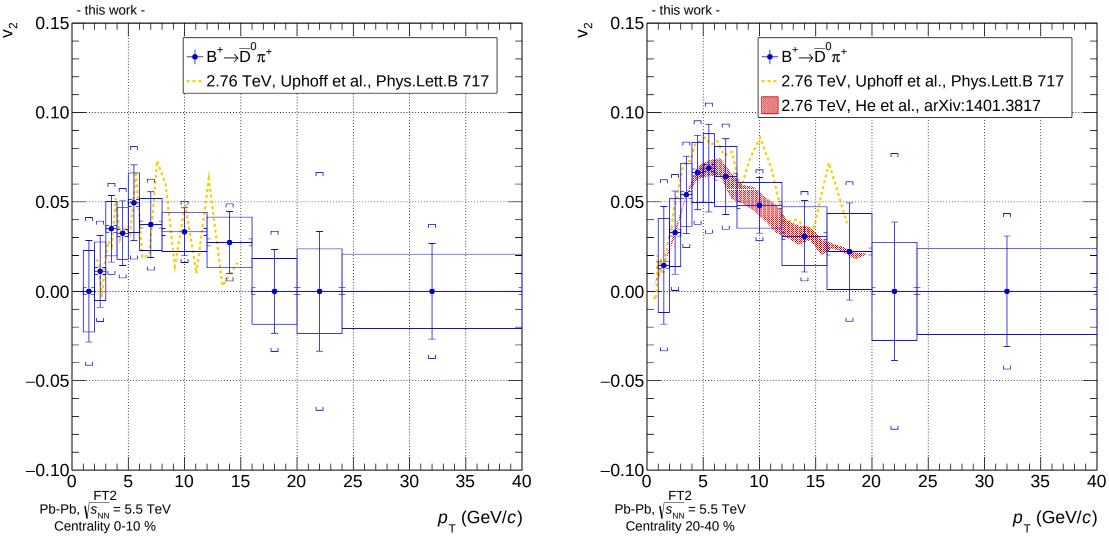

(a) **(b)**

Figure 7.2.: Expected precision of the v_2 measurement with the upgraded ALICE Experiment with full statistics of $L_{\mathrm{int}} = 10\,\mathrm{nb}^{-1}$ for Pb–Pb collisions at $\sqrt{s_{\mathrm{NN}}} = 5.5$ TeV, 0–10 % and 20–40 % centrality. Here, the precision for the expected central (bars), minimal (boxes) and maximal (brackets) raw yield is considered. In (a), the prediction by BAMPS (Uphoff *et al.*, 0–10 %) [91] is used, while for (b) the sensitivity was calculated with a prediction by TAMU (He *et al.*, 20–40 % (beauty)) [98]. As expected from the asymmetry of the nuclear overlap region, an increase of v_2 for more peripheral collisions is visible, e.g. by comparison of the BAMPS predictions in the two figures.

et al., 30–50 % (charm)) [98]. Due to the lower charm-quark mass, the kinematic range of the model is limited to $p_T \leq 10$ GeV/c and v_2 is maximal at lower p_T, but this approach is just meant to illustrate the separation power of the measurement.
Given the presented uncertainties in figures 7.2a, 7.2b and 7.3 the highest expected separation power of the v_2 measurements was evaluated within the minimal and maximal expected signal raw yield calculated in section 5.5:

- 0–10 % centrality: $v_2/\sigma_{v_2} = 1.6$–3.0 at $p_T = 5.5$ GeV/c (BAMPS)
- 20–40 % centrality: $v_2/\sigma_{v_2} = 2.3$–4.0 at $p_T = 4.5$ GeV/c (TAMU)
- 30–50 % centrality: $v_2/\sigma_{v_2} = 3.2$–5.3 at $p_T = 2.5$ GeV/c (TAMU, charm).

The obtained separation power corresponds to the current performance of the v_2 measurement of the D^{*+} mesons [66], which is limited by systematic and statistical uncertainties. If beauty quarks participate in the collective motion of the medium, the separation power of the analysis of $B^+ \to \overline{D}^0\pi^+$ ($\overline{D}^0 \to K^+\pi^-$) depends on the actual magnitude of v_2. For the given theoretical predictions in figures 7.2a and 7.2b, v_2 is measured up to about 15–20 GeV/c, above which it originates from the path-length dependence in the medium. Given the lower kinematic bound of the CMS measurement of non-prompt J/ψ mesons at about 10 GeV/c, ALICE will provide crucial information at mid-rapidity wether beauty quarks participate in flow, in addition to the foreseen improved high-precision measurement of v_2 for charm quarks [66, 20].

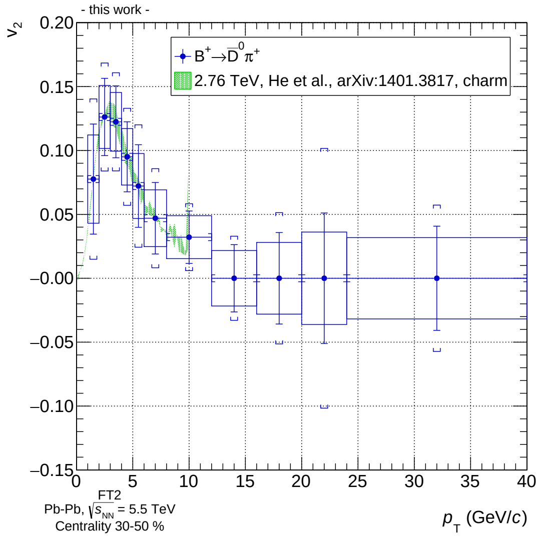

Figure 7.3.: Expected precision of the B^+ v_2 measurement with the upgraded ALICE Experiment at 30–50 % centrality, assuming charm quark v_2. As the calculation is made for charm quarks, the kinematic range of v_2 is limited to $p_{\mathrm{T}} \leq 10\,\mathrm{GeV}/c$. In case beauty v_2 is of similar magnitude as for charm or light-flavor quarks, a larger separation power to zero elliptic flow is obtained.

8. Summary and outlook

In this thesis the analysis of the full kinematic reconstruction of B^+ mesons in the decay channel $\mathrm{B}^+ \rightarrow \overline{\mathrm{D}}^0\pi^+$ ($\overline{\mathrm{D}}^0 \rightarrow \mathrm{K}^+\pi^-$) and charge conjugates with the upgraded ALICE detector was developed. Further, its performance was evaluated using fast and full MC simulations of Pb–Pb collisions at $\sqrt{s_{\mathrm{NN}}} = 5.5\,\mathrm{TeV}$, 0–10 % centrality, for the expected integrated luminosity of $\mathrm{L}_{\mathrm{int}} = 10\,\mathrm{nb}^{-1}$ in Run 3 and 4 of the LHC .
During the second Long Shutdown (LS2) of the LHC, the ALICE Collaboration foresees to undergo significant detector and readout upgrades in preparation of the increased instantaneous luminosity $\mathcal{L} = 6 \cdot 10^{27}\,\mathrm{cm}^{-2}\mathrm{s}^{-1}$ at an interaction rate of about 50 kHz in Pb–Pb collisions, which will allow the collaboration to accumulate $10\,\mathrm{nb}^{-1}$ of Pb–Pb collisions in Run 3 and 4 of the LHC. Among these upgrades is the replacement of the current ITS with a new, high-granularity silicon pixel inner tracker with a single-hit resolution of $4\,\mu$m and a readout rate capability of 50 kHz in Pb–Pb collisions, which will enhance the pointing resolution by a factor 3 (5) in $r\phi$ (z) direction to about $50\,\mu$m and the momentum resolution to about 0.4 % for ITSu+TPC combined tracks at $p_{\mathrm{T}} = 400\,\mathrm{MeV}/c$.
In line with the upgrade strategy of ALICE, new rate limited measurements in the beauty sector will become accessible for the first time over a wide transverse momentum range at mid-rapidity in Pb–Pb collisions.
Within this thesis a new fast simulation tool (FT2) was developed from existing simulation methods and extended to include the full detector geometries of the ALICE subsystems in order to generate reliable and large statistics MC simulations for the analyses of these new probes. Such fast simulations are essential to overcome the statistical limitations of full MC simulations, set by computational resources. After careful parameterization of existing full MC simulations of the upgraded ALICE subsystems, key specifications of the upgraded ITS (ITSu) and TPC detectors were identified and included in the FT2. Here, a precise determination of the pixel resolution as well as generation of random and correlated clusters in the ITSu, and the tracking mass hypothesis, the cluster reconstruction efficiency and $\vec{E} \times \vec{B}$-distortions in the TPC, proved to be essential for a realistic description of the track reconstruction performance in the two detectors. Within this context, the particle reconstruction and tracking algorithm used in ALICE were reviewed in this thesis.
With the current implementation, the FT2 is capable to described the single track reconstruction efficiencies in full MC simulation with a precision better than 10 % for $p_{\mathrm{T}} \geq 500\,\mathrm{MeV}/c$, including the application of topological cuts on the distance of closest approach to the primary vertex, while the FT2 is a factor 10^3–10^4 faster than corresponding full MC simulations.
As such, the FT2 was added into the ALICE computing framework and serves as a central tool for future fast simulation approaches foreseen in ALICE. Already now, the high simulation speed of the FT2 allows fast studies on the impact of newly developed ITSu geometries and beyond. For example, new possibilities in silicon fabrication processes may enable the construction of even more advanced silicon pixel layers, e.g. of cylindrical shape.

Here, the FT2 is used to study the impact on the different analyses compared to the current turbine-shaped implementations of the detector.

Certainly, the tool is foreseen to include a realistic description of particle identification capabilities of TPC and TOF, which both can be parameterized based on calculations of the expected energy loss $\mathrm{d}E/\mathrm{d}x$ and time-of-flight for particles with a given p_{T} and (η, ϕ)-coordinates. It may also be extended to include other subsystems in general, such as the TOF and TRD detectors, which however could considerably slow down the track reconstruction as more propagation steps are introduced though the additional detector material. This may be overcome by a generally improved loading algorithm of the detector geometries. As the processing time is dominated by the MC event generation, which takes about 70 % of the total real time, the FT2 could also be applied on existing generated MC events. With such an approach, the available statistics for upgrade studies could be rapidly increased.

The analysis presented in this thesis demonstrates the needs of fast and reliable MC simulations for precise data analysis. It can now be easily used for the analyses of other rare beauty decays, such that for example the low p_{T} reach of the analysis of $\Lambda_b^0 \to \Lambda_c^+\pi^-$ ($\Lambda_c^+ \to p^+\mathrm{K}^-\pi^+$) may be re-evaluated for an improved signal selection [19, 20].

Within the developments of the FT2, several unwanted but unnoticed features, such as wrongly applied selection on the cluster acceptance in the TPC, were found in full MC simulations through the comparison with the fast simulation. In this sense, the FT2 also serves as cross-reference and quality assurance tool for full MC simulations, and can thus help to improve the MC description of the data. For example, it could also be used for detailed studies on the energy loss algorithms within the tracking code. For these purposes, the FT2 integration into the available simulation framework should be advanced, such that a given fraction of events in full MC simulations is also evaluated by the FT2. This would enable the possibility to inspect the exact same events with the different approaches. Here, the integration of the FT2 would profit from a more automatized handling of its parameterization and anchoring to full MC productions. In addition, if applied on already existing generated MC data, the FT2 processing time would increase by another factor of three.

Already now the development of the FT2 allowed to generate about 100 million Pb–Pb events at $\sqrt{s_{\mathrm{NN}}} = 5.5\,\mathrm{TeV}$, 0–10 % centrality, with the HIJING event generator in a standalone simulation. This corresponds to the largest MC production available within the ALICE Collaboration and to about one fifth of the statistics foreseen in future MC simulation in the collaboration for Run 3 and 4 at the LHC. These events were used for a detailed analysis and evaluation of the combinatorial background sources in the hadronic open beauty decay $\mathrm{B}^+ \to \overline{\mathrm{D}}^0\pi^+$ ($\overline{\mathrm{D}}^0 \to \mathrm{K}^+\pi^-$), which appears rate limited by fragmentation and branching ratios ($f_{\mathrm{b}\to\mathrm{B}} \cdot \mathrm{BR} = 7.65 \cdot 10^{-5}$) to about $9.8 \cdot 10^{-5}$ B^+ and B^- mesons generated per event within the acceptance of the ALICE central barrel, which will be further reduced by acceptance cuts and reconstruction efficiencies. The signal yield was determined using a binary scaling approach [20, 201] based on FONLL calculations of p+p collisions.

The large lifetimes of $\tau_{\mathrm{B}^+} = (1\,639 \pm 4) \cdot 10^{-15}\,\mathrm{s}$ for the B^+ meson and $\tau_{\overline{\mathrm{D}}^0} = (410.1 \pm 1.5) \cdot 10^{-15}\,\mathrm{s}$ [10] for the subsequent $\overline{\mathrm{D}}^0$ decay strongly displace the secondary and tertiary vertex from the primary vertex. Based on the available high-statistics of the fast MC simulation, the most-efficient signal selection criteria ($\cos(\theta_{\mathrm{pointing}})$, $\mathrm{L}_{\mathrm{decay}}^{\overline{\mathrm{D}}^0}$, $p_{\mathrm{T}}^{\overline{D}^0}$, $p_{\mathrm{T}}^{\pi^+}$,

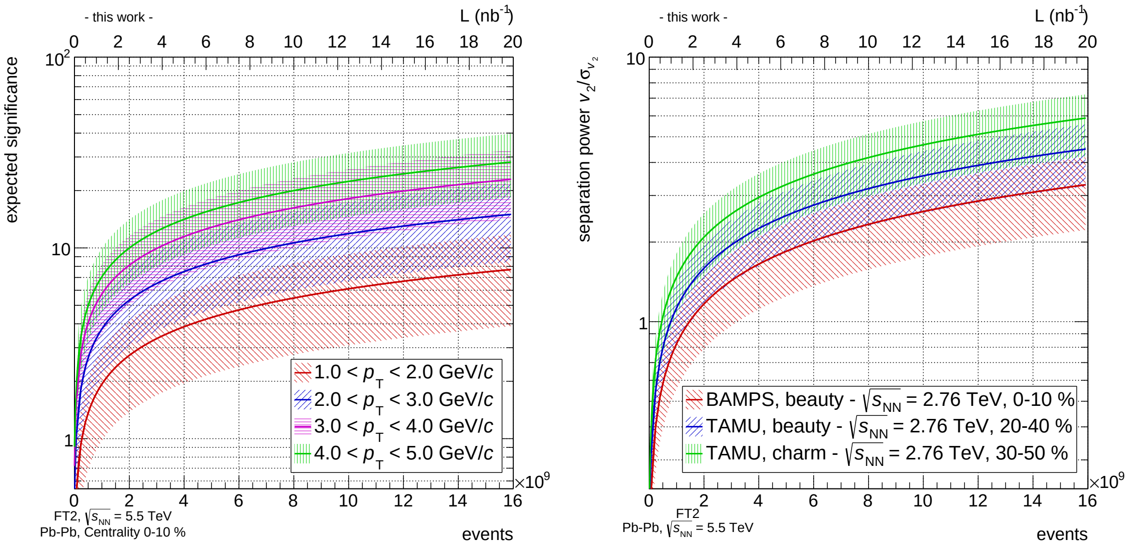

(a) **(b)**

Figure 8.1.: Evolution of the expected significance and the separation power in the v_2 measurement with the number of recorded events (or integrated luminosity). (a) describes the change of the expected significance for the first four kinematic bins, which demonstrate the low momentum reach of the full kinematic reconstruction. The separation power in the v_2 measurement in (b) is displayed for three different centralities and theoretical predictions [91, 98], generally assuming beauty flow, or beauty flow as large as charm flow. Here, the evolution is displayed for the kinematic bins with the largest expected separation power for a given centrality: $5.0 < p_T < 6.0$ for 0–10 %, $4.0 < p_T < 5.0$ for 20–40 % and $2.0 < p_T < 3.0$ for 30–50 %. In both figures, the solid lines represent the central expectation values, while the shaded areas indicate the maximal and minimal expected significance or separation power.

$\mathrm{d0}^{\overline{\mathrm{D}}^0}\cdot\mathrm{d0}^{\pi^+}$ and $\mathrm{d0}^{\mathrm{B}^+}_{\mathrm{xy}}$) were identified and optimized in a simultaneous multi-dimensional cut optimization in order to enhance the signal-to-background ratio and statistical significance of the full kinematic reconstruction of $\mathrm{B}^+ \rightarrow \overline{\mathrm{D}}^0\pi^+$ ($\overline{\mathrm{D}}^0 \rightarrow \mathrm{K}^+\pi^-$) on top of the invariant mass selection. Here, the analysis significantly profits from the installation of the upgraded ITS, as the secondary and tertiary vertex resolution increase by up to a factor of five. Given the distinct topology of the full decay scheme, in principle it should also be possible to perform the full kinematic reconstruction of the decay daughters with the current detector resolutions, too. However, based on the rate limitation of the generated signal yield within the acceptance of the ALICE central barrel at mid-rapidity in Pb–Pb collisions, the measurement relies on the improved readout capabilities of the full ALICE Experiment.

Additional correlated background sources were studied with dedicated full MC simulations. These do not impose a strong impact on the signal extraction as the true signal yield can be recovered though the application of template fits with a precision of better than 5 %.

Based on the FT2 simulations and including a scaling factor to account for the particle identification capabilities of ALICE, within uncertainties of up to 40 % a significant measurement of B^+ mesons and charge conjugates will be possible down to 2 GeV/c, which corresponds to about 88 % of the complete p_T spectrum. For momentum up to 12 GeV/c, the combined uncertainty is dominated by the contribution from the FT2 simulation, ranging between 20–40 %, while for higher p_T, the statistical uncertainty of the background grows largest to up to 70 %. The highest expected statistical significance for $\mathrm{L}_{\mathrm{int}} = 10\,\mathrm{nb}^{-1}$

of $46.82^{+12.50}_{-8.36}$ is found in the range $8.0 < p_{\mathrm{T}} < 12.0\,\mathrm{GeV}/c$. The corresponding signal-to-background ratio increases with p_{T} from about 0.01 to 4.0. The evolution of the statistical significance as a function of the recorded number of events (or integrated luminosity) is depicted for the kinematic bins of the B^{+} within $1.0 < p_{\mathrm{T}} < 5.0\,\mathrm{GeV}/c$ in figure 8.1a. In order to maintain a significant measurement down to $p_{\mathrm{T}} \geq 2.0\,\mathrm{GeV}/c$, within uncertainties at least about $6.0 \cdot 10^{9}$ central Pb–Pb events ($\mathrm{L_{int}} \approx 7.5\,\mathrm{nb}^{-1}$) need to be recorded. This corresponds to the kinematic region with the lowest expected significance, thus a measurement for higher p_{T} will be possible as well.

The expected statistical significance and signal-to-background ratio were propagated into an estimate on the integrated luminosity of the required p+p reference statistics, such that the combined statistical uncertainty in the R_{AA} measurement increases only by about 20 %. It was found, that the foreseen $6\,\mathrm{pb}^{-1}$ at similar center-of-mass energy will not be sufficient, but about $100\,\mathrm{pb}^{-1}$ at $\sqrt{s} = 5.5$ TeV would be required for large enough references statistics in this measurement. The reference data could also be recorded at $\sqrt{s} = 14.0$ TeV. Here, taking into account an additional scaling factor for the different center-of-mass energies derived from FONLL, about $50\,\mathrm{pb}^{-1}$ would be sufficient to obtain the foreseen statistical precision due to the higher center-of-mass energy.

The expected yields and their uncertainties were further propagated to anticipate the expected precision in the measurements of R_{AA} and v_2, estimated on top of the theoretical predictions of BAMPS [91] and TAMU [98] for central Pb–Pb collisions at $\sqrt{s_{\mathrm{NN}}} = 2.76$ TeV. These prediction can be used, as the difference of the observables between the two center-of-mass energies is neglectable [235, 243]. The models were chosen, as both are capable to simultaneously calculate expectation values of R_{AA} and v_2 with reasonably good agreement with data [91, 98].

With ALICE, the predicted suppression of $R_{\mathrm{AA}} \approx 0.2 - 0.5$ for $p_{\mathrm{T}} \geq 8\,\mathrm{GeV}/c$ [91, 98] will be visible with a precision of up to 2–8 %. For lower momentum, the obtained sensitivity is within 7–17 % and would be sufficient to observe the predicted enhancement of about 1.5 by BAMPS, but would not be good enough to detect the average R_{AA} of about 1.1 predicted by TAMU. This momentum region is particularly interesting, as the quenched high-p_{T} b quarks must be recovered at low p_{T}, which will be accessible to a large extend by ALICE. The actual observation of elliptic flow of B^{+} mesons is strongly model dependent, and relies on the true magnitude of v_2. The evolution of the predicted separation power compared to a non-flow scenario is presented for different centralities and models [91, 98] in figure 8.1b. Here, the evolution is displayed for the kinematic bins with the largest expected separation power for a given centrality, which are $5.0 < p_{\mathrm{T}} < 6.0$ for 0–10 %, $4.0 < p_{\mathrm{T}} < 5.0$ for 20–40 % and $2.0 < p_{\mathrm{T}} < 3.0$ for 30–50 % centrality. For $\mathrm{L_{int}} = 10\,\mathrm{nb}^{-1}$, an expected sensitivity within about 20–60 % is expected. For central collisions, a separation power of $v_2/\sigma_{v_2} = 1.6 - 3.0$ could be obtained, where the range is given by the minimal and maximal uncertainty of the expected significance of the measurement. However, in case beauty flow is as large as charm flow, a separation power of $v_2/\sigma_{v_2} = 3.2 - 5.3$ could be obtained for 30–50 % centrality. As visible in figure 8.1b, less recorded data would strongly limit the sensitivity of the measurement.

At this stage, the prediction of the measurement sensitivity is essentially limited by the uncertainty of the FONLL calculation in the binary scaling approach, while for momentum $p_{\mathrm{T}} \geq 16\,\mathrm{GeV}/c$ statistical uncertainties of the expected reconstructed combinatorial background are dominating. For transverse momentum below $3\,\mathrm{GeV}/c$, the topological and kinematic selection of the signal will not be capable to find a significant signal yield as the efficiency is too low and because the FONLL calculation predicts a steeply falling p_{T} spectrum, such that only a very low signal yield is expected. Here, other approaches for the signal extraction could be developed, for example based on a reconstruction without topological selection, which was demonstrated for charmed mesons in p+p collisions [244]. With the foreseen statistics expected at the LHC, ALICE will provide a new and unique measurement of fully reconstructed B^+ mesons and charge conjugates ranging from low to moderate p_{T}. As the beauty mesons are particularly sensitive to the medium, the measurement of collectivity and energy loss of b quarks in the QGP will provide a new probe at the LHC. Also additional measurements using the full kinematic reconstruction in the beauty sector via $\mathrm{B}^+ \to \mathrm{J}/\psi(1\mathrm{S})\mathrm{K}^+$ ($\mathrm{J}/\psi(1\mathrm{S}) \to e^+e^-$) or $\mathrm{B}^0 \to \mathrm{D}^{*-}\pi^+$ ($\mathrm{D}^{*-} \to \overline{\mathrm{D}}^0\pi^-$), are foreseen in ALICE and it is expected that they have a similar sensitivity as the presented $\mathrm{B}^+ \to \overline{\mathrm{D}}^0\pi^+$ ($\overline{\mathrm{D}}^0 \to \mathrm{K}^+\pi^-$). As the signal extraction via template fits appears as an effective tool to determine the reconstructed signal yield, it could be further extended to recover the yield of correlated background candidates, e.g. from $\mathrm{B}^+ \to \overline{\mathrm{D}}^0\mathrm{K}^+$ ($\overline{\mathrm{D}}^0 \to \mathrm{K}^+\pi^-$), which may be used as an actual measurement by itself. It would be particularly interesting to combine the B^+ measurement with the full kinematic reconstruction of $\Lambda_b^0 \to \Lambda_c^+\pi^-$ ($\Lambda_c^+ \to p^+\mathrm{K}^-\pi^+$) or even $\mathrm{B}_s^0 \to \overline{\mathrm{D}}^0\mathrm{K}^-\pi^+$ ($\overline{\mathrm{D}}^0 \to \mathrm{K}^+\pi^-$), such that the ratio of the production cross-sections could be studied and compared to the production ratio of light flavor and strange baryons, where an enhancement was observed at intermediate transverse momentum [245]. These comparisons would further help to asses the hadronization mechanisms and thermalization of heavy-flavor hadrons in the Quark-Gluon Plasma [20]. Through these measurements of full kinematic reconstruction of beauty hadrons in Pb–Pb collisions at mid-rapidity, ALICE will contribute new insight to the underlying mechanisms of the QGP in the near future and advance the experimental and theoretical understanding.

A. LHC13d19: Full Monte Carlo simulation setup

About 1 million Pb–Pb events were generated in a full MC simulation to characterize the upgraded ITS detector, as described in the technical design report [20]. The underlying Pb–Pb event was setup at a center of mass energy of $\sqrt{s_{\mathrm{NN}}} = 5.5\,\mathrm{TeV}$ with an impact parameter of $\mathrm{b} < 0\,\mathrm{fm}$, which corresponds to $0\,\%$ centrality. In addition, 60 PYTHIA signals per event were generated at 5.5 TeV using the Perugia-0 tune, which are setup as listed:

- $16\,\%$ probability for a $\mathrm{c\overline{c}}$ pair, with at least one within $|\mathrm{y}| < 1.5$ and D mesons decaying only hadronically.
- $16\,\%$ probability for a $\mathrm{b\overline{b}}$ pair, with at least one within $|\mathrm{y}| < 1.5$ and D mesons decaying only hadronically.
- $16\,\%$ probability for a $\mathrm{c\overline{c}}$ pair and no decays forced, however at least one electron from charm is required in $|y| < 1.2$.
- $16\,\%$ probability for a $\mathrm{b\overline{b}}$ pair and no decays forced, however at least one electron from charm or beauty is required in $|y| < 1.2$.
- $16\,\%$ probability for a $\mathrm{J}/\psi \rightarrow \mathrm{e}^{+}\mathrm{e}^{-}$ decay and the J/ψ within $|y| < 1.0$.
- $20\,\%$ probability for a $\mathrm{B} \rightarrow \mathrm{J}/\psi \rightarrow \mathrm{e}^{+}\mathrm{e}^{-}$ decay while the B meson and the J/ψ are required within $|y| < 2.0$.

Another set of 30 signal decays, equally distributed over particle and anti-particle, were injected per event for performance studies of the ITSu detector:

- $\mathrm{D}_s^{+} \rightarrow \mathrm{K}^{+}\mathrm{K}^{-}\pi^{+}$
- $\mathrm{D}^{+} \rightarrow \mathrm{K}^{-}\pi^{+}\pi^{+}$
- $\mathrm{B}^{+} \rightarrow \overline{\mathrm{D}}^{0}\pi^{+}$
- $\mathrm{B}^{0} \rightarrow \mathrm{D}^{*}(2010)^{-}\pi^{+}$
- $\Lambda_c^{+} \rightarrow p^{+}\mathrm{K}^{-}\pi^{+}$
- $\Lambda_b^{0} \rightarrow \Lambda_c^{+}\pi^{-}$
- χ_c

The mother particles are simulated according to p_{T}-distributions, obtained from fits to data in an interval 0–30 GeV/c, which are however slightly overestimated for high p_{T}. In order to study the signals from hypernuclei, another 10 nuclei (= 5 particles + 5 anti-particles) per event per type were injected for ${}^{3}_{\Lambda}\mathrm{H}$ (Hypertriton), ${}^{4}_{\Lambda}\mathrm{H}$ (Hyperhydrogen) and ${}^{4}\mathrm{He}$ (Hyperhelium-4).

A.1. Contamination of reconstructed tracks

In these figures, the contamination of the reconstructed particles by secondary particle generation in material or from strange weak decays is presented. Here, the fraction of reconstructed tracks is determined as the ratio over all reconstructed tracks for a given species, which was identified via MC truth information. While only electrons show a contamination from photon conversions in material, presented in section 4.3.6 figure 4.10a, kaons are almost exclusively generated at the primary vertex (figure A.1b). For pions, only a small amount of secondary particles is reconstructed: For transverse momentum around 200 MeV/c, about 85 % of all reconstructed pions are generated at the primary vertex, while 10 % originate from strange weak decays. Only 5 % of the reconstructed yield is stemming from material interactions. Within large statistical uncertainties, muons appear largely contaminated by up 100 % for momentum below 500 MeV/c.

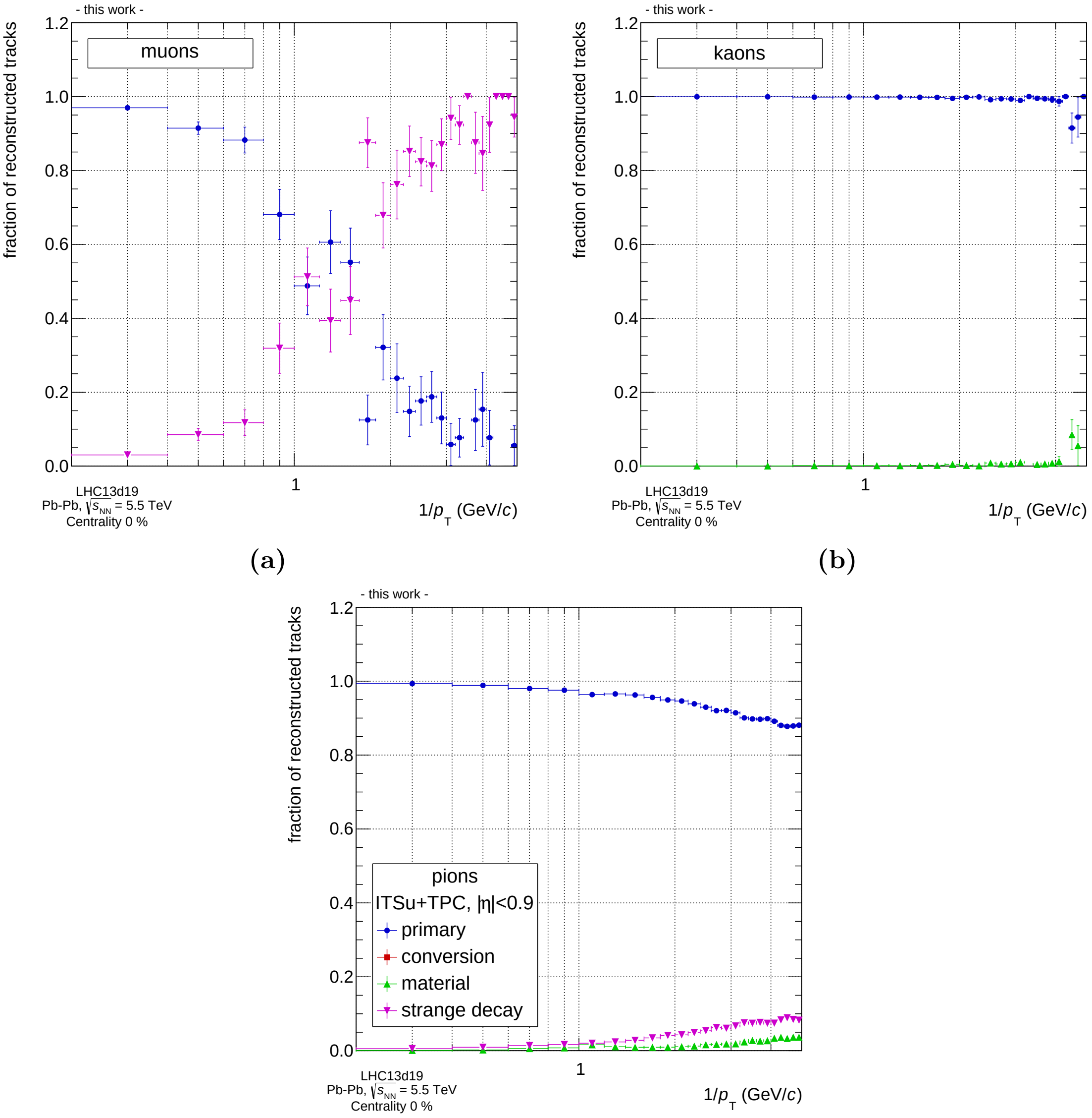

(a) **(b)**

(c)

Figure A.1.: Contamination of reconstructed muon, kaons and pions.

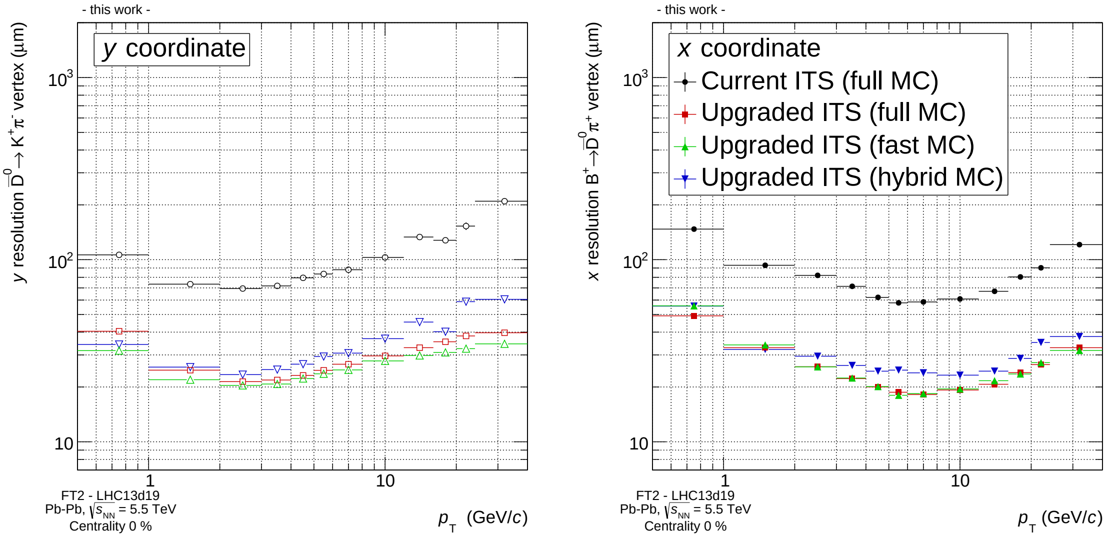

(a) (b)

Figure A.2.: Reconstructed secondary vertex resolution of $\overline{\mathrm{D}}^0$ (a) and B^+ (b) mesons in y- and x-direction respectively, identified via MC truth in the decay chain $\mathrm{B}^+ \rightarrow \overline{\mathrm{D}}^0\pi^+(\overline{\mathrm{D}}^0 \rightarrow \mathrm{K}^+\pi^-)$ for central Pb–Pb collisions at $\sqrt{s_{\mathrm{NN}}} = 5.5\,\mathrm{TeV}$. Note that the mesons are shown in bins of their corresponding reconstructed transverse momentum. The current ITS performance is shown in black circles, whereas the performance of the upgraded detector is displayed for full MC (red squares), fast MC (green triangles) and hybrid MC (blue inverse triangles)

A.2. Secondary vertex resolution

Here, the remaining dimensions of the secondary vertex resolution of reconstructed $\overline{\mathrm{D}}^0$and B^+ candidates are shown. Note that the x and y resolutions are similar in the respective channels.

B. FT2: Parameterizations and performance

In this section, supporting figures of the multi-dimensional regression fits used in the FT2 are presented.

B.1. Parameterizations of the cluster-pickup probability

The TPC cluster-pickup probability corresponds to the probability for a cluster to be above noise-canceling thresholds, and is thus dependent on the overall collected charge in a cluster. It was parameterized as a function of the inverse specific energy loss $1/(\mathrm{d}E/\mathrm{d}x)^{\mathrm{ALEPH}}$ of a particle, $|\eta|$ and charged particle multiplicity. It is also dependent on the azimuthal angle ϕ, which was left out of the fit for computing time reasons. In addition the cluster-pickup probability also increases with increasing pad size of the readout chamber, as for example visible from comparisons of figures 4.14 (IROC), B.3 (OROC, medium pads) and B.4 (OROC, long pads).

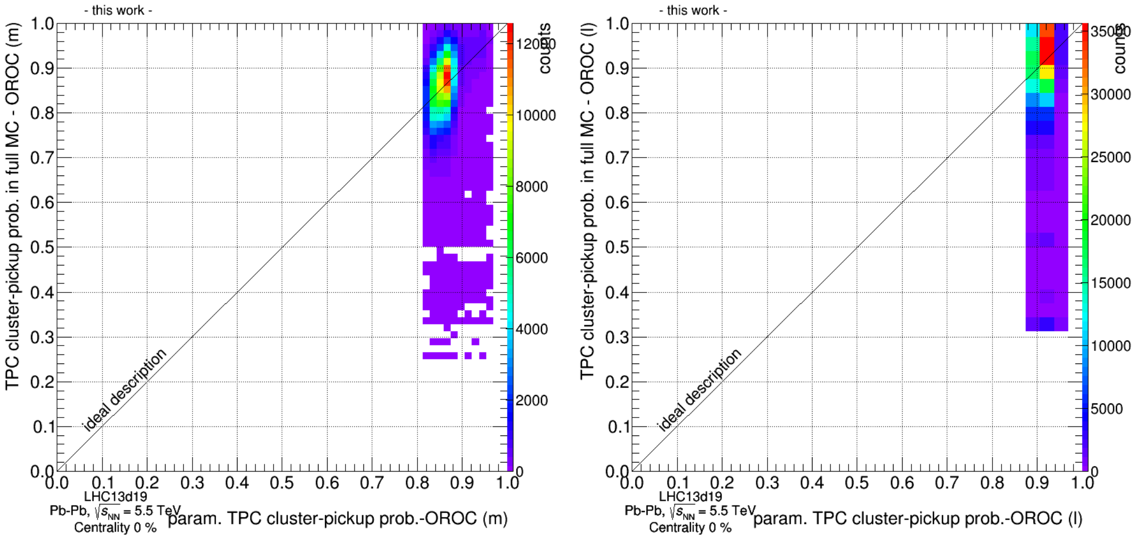

(a)

(b)

Figure B.1.: In these figures, the comparison between the parameterizations of the cluster-pickup probability and the true full MC information of the OROC with medium (a) and long (b) pad sizes are shown. Optimal agreement is indicated by the diagonal line. As explained in section 4.3.8, the residual difference is a consequence of the azimuthal dependence, which is not included in the multi-dimensional regression fit. With increasing pad size, the probability to detect clusters above threshold, and thus the cluster-pickup probability, increases.

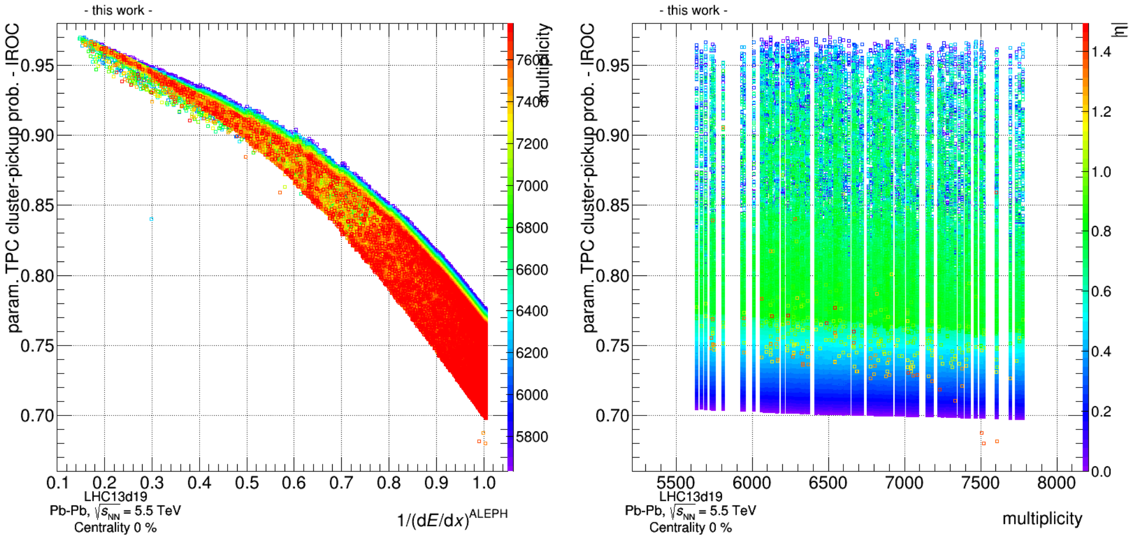

(a)

(b)

Figure B.2.: (a) displays the parameterized TPC cluster-pickup probability of the IROC as a function of $1/(\mathrm{d}E/\mathrm{d}x)^{\mathrm{ALEPH}}$ and charged particle multiplicity. With increasing energy loss, it is more probable that a cluster is above the zero-suppression threshold. For higher multiplicity, the probability is slightly shifted towards lower values, as the high occupancy in the detector makes it more difficult to correctly assign the clusters to the correct track. This dependence is similar for different $|\eta|$, as visible in (b).

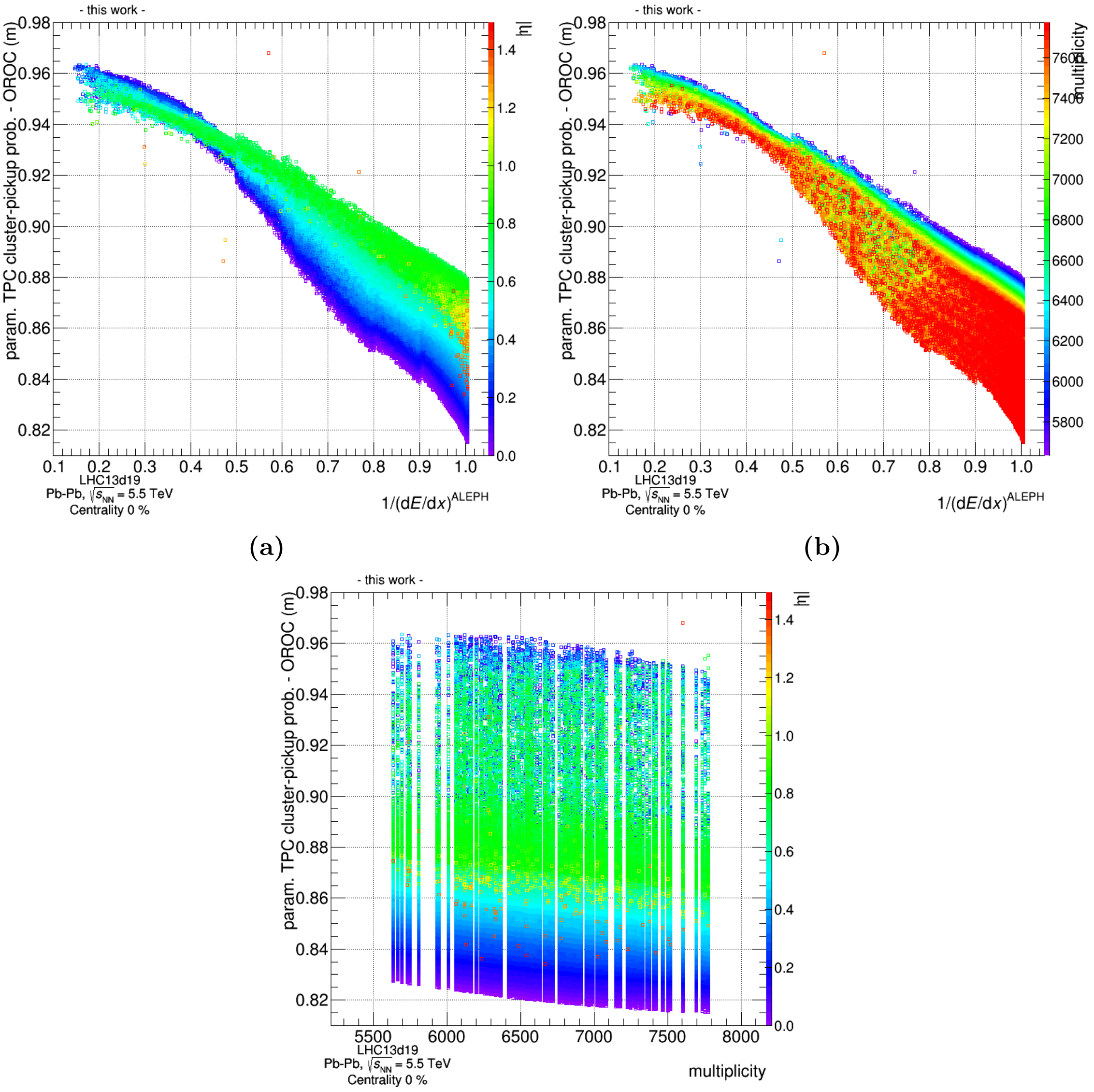

(a) **(b)**

(c)

Figure B.3.: Compared to figure 4.14a, an increased probability is observed in (a) as a consequence of the increased pad sized in the OROC. In addition, smaller spread with $|\eta|$ is visible. Around $1/(\mathrm{d}E/\mathrm{d}x)^{\mathrm{ALEPH}} \approx 0.8$ and 0.9 small edges are visible, which correspond to the bin edges used in the multi-dimensional regression fit. (b) displays the parameterized cluster-pickup probability as a function of $1/(\mathrm{d}E/\mathrm{d}x)^{\mathrm{ALEPH}}$ and multiplicity. The observations are in line with those of the IROC. The correlation between the multiplicity and $|\eta|$ is shown in (c).

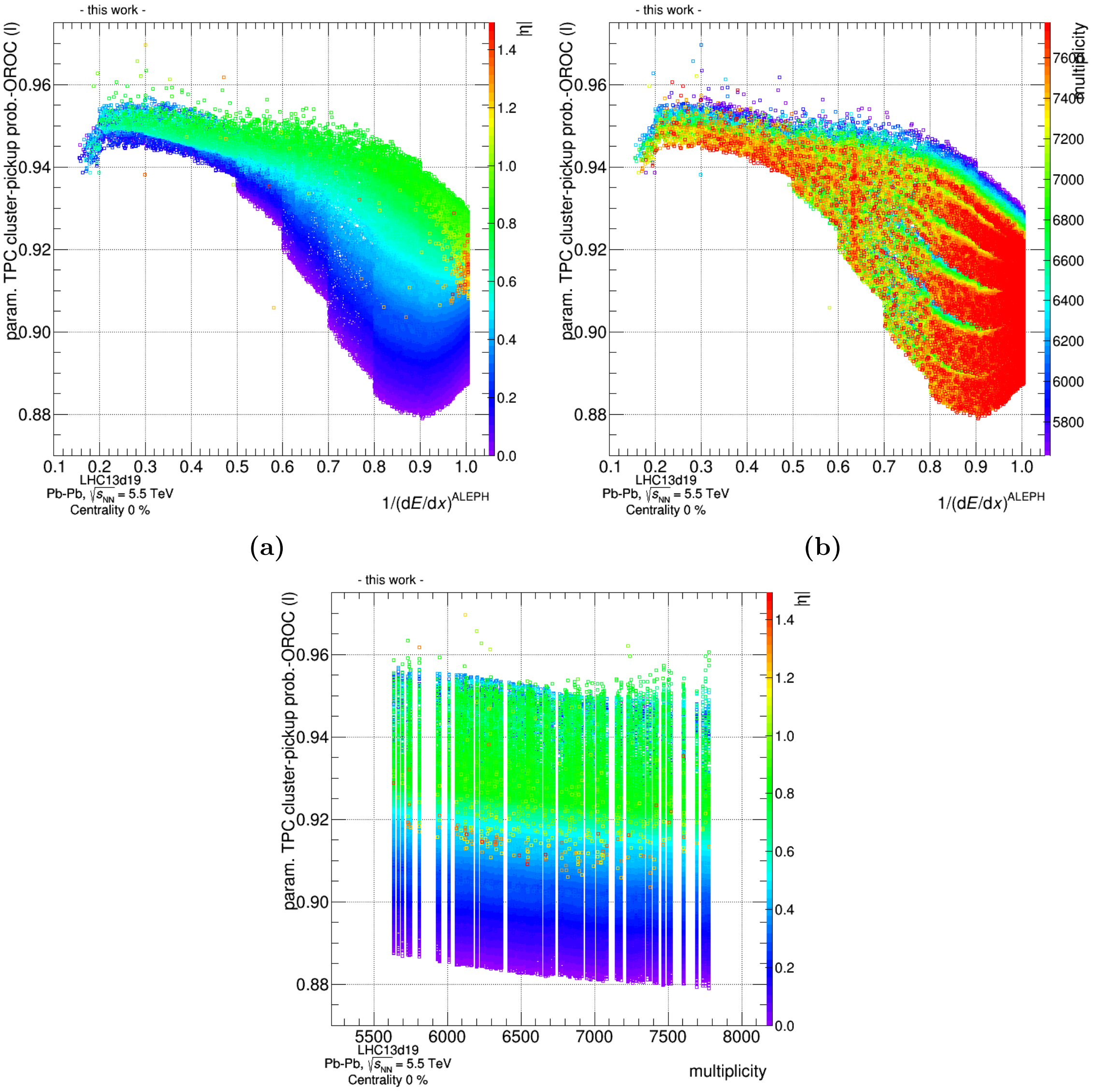

(a) **(b)**

(c)

Figure B.4.: Similar observations as in figure B.3, but with increased probability due to the larger pad size. For lower specific energy loss, distinct bands of the probability become visible: As the OROC contains only 32 pads with increased length, the distribution appears not smooth any more due to the limited number of combinations in the ratio of the pickup probability [200]. In principle, this effect is also present for the IROC and OROC (medium), however there the number of pads is higher (IROC: 63, OROC (medium): 64, compared to OROC (long): 32) and the bands blur out.

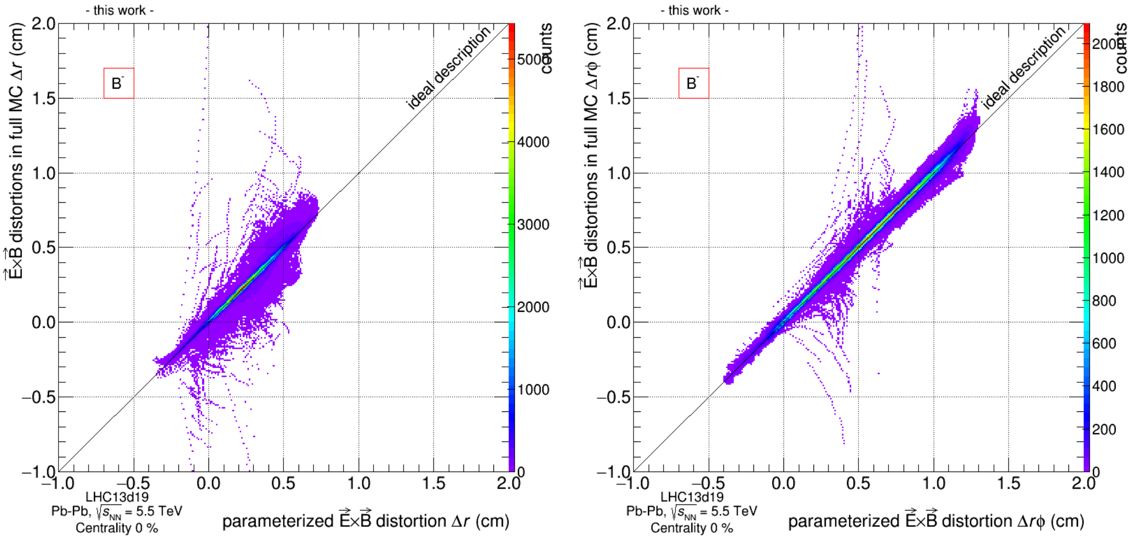

(a) **(b)**

Figure B.5.: Parameterizations of $\vec{\mathrm{E}}\times\vec{\mathrm{B}}$ distortions in r- and $r\phi$-direction, compared to the results from the offline analysis for the B^- configuration in the ALICE central barrel. Except for single outliers, the full simulation is described extremely well by the parameterizations. These outliers correspond to single clusters with very extreme distortions near the inner radius of the field cage. On average these are correctly parameterized, as visible for example in (a). The presented figures were obtained from full MC simulations with a magnetic field strength of $\mathrm{B} = 0.5\,\mathrm{T}$ in the ALICE central barrel.

B.2. Parameterizations of $\vec{E}\times\vec{B}$-distortions

The parameterization of the $\vec{E}\times\vec{B}$-distortions were obtained from a multi-dimensional regression fit on cluster information determined in the offline calibration of the TPC. In these fits, 5 bins along the r-direction were used for the parameterization, while the z- and r-direction were each grouped into 10 bins. The field strength was 0.5 T. Small edge effects from the finite binning are visible, for example in figure B.6b. Generally, the largest distortions are observed for clusters with the largest drift length, thus distributed around $Z = 0\,\mathrm{cm}$ in the plots. For each side of the field cage ($Z < 0\,\mathrm{cm}$ and $Z > 0\,\mathrm{cm}$) no strong correlation of the distortions were observed along Z for a fixed ϕ position, except near the readout chambers, where residual mis-alignment becomes visible. These are best visible in the top left or lower right graphics in figures B.8, B.9 and B.10.

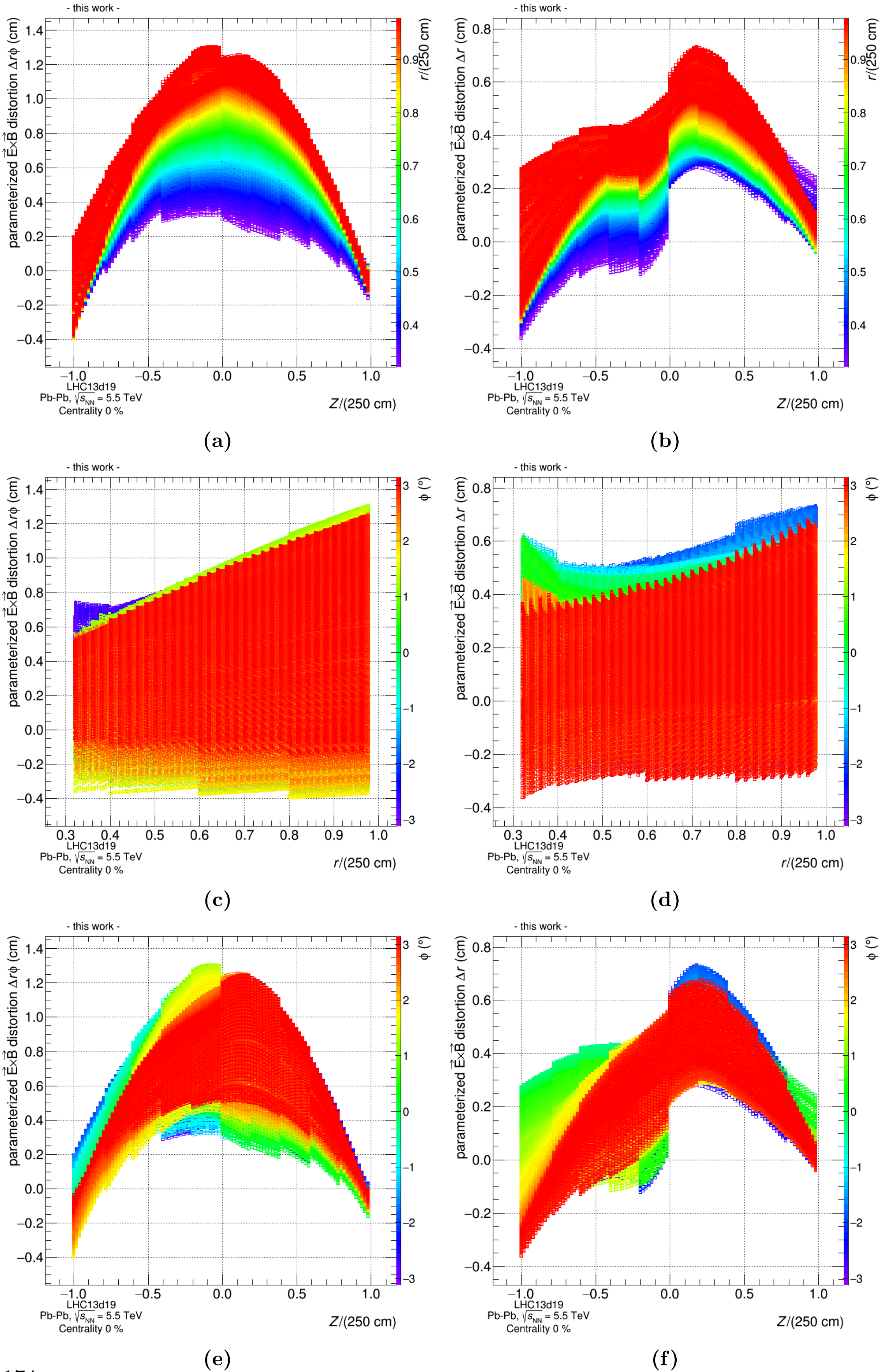

(a) (b) (c) (d) (e) (f)

Figure B.6.: In these figures the multi-dimensional parameterization of the $\vec{E} \times \vec{B}$-distortions in r and $r\phi$ are shown as a function of the r, Z and ϕ.

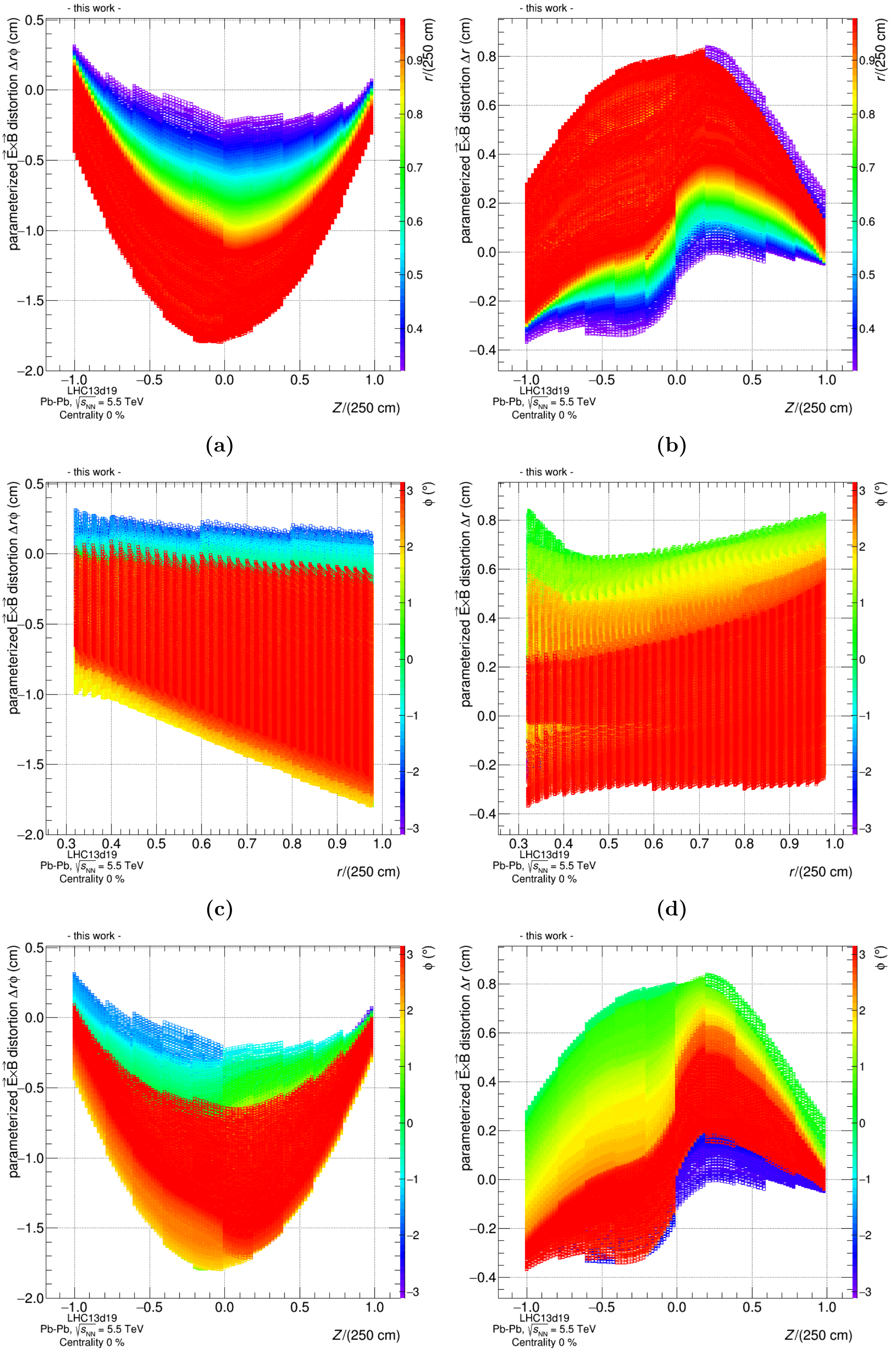

(a)

(b)

(c)

(d)

(e)

(f)

Figure B.7.: In these figures the multi-dimensional parameterization of the $\vec{E}\times\vec{B}$-distortions in r and $r\phi$ are shown as a function of the r, Z and ϕ. Small edge effects from the finite binning of the dimensions are visible, for example in (b).

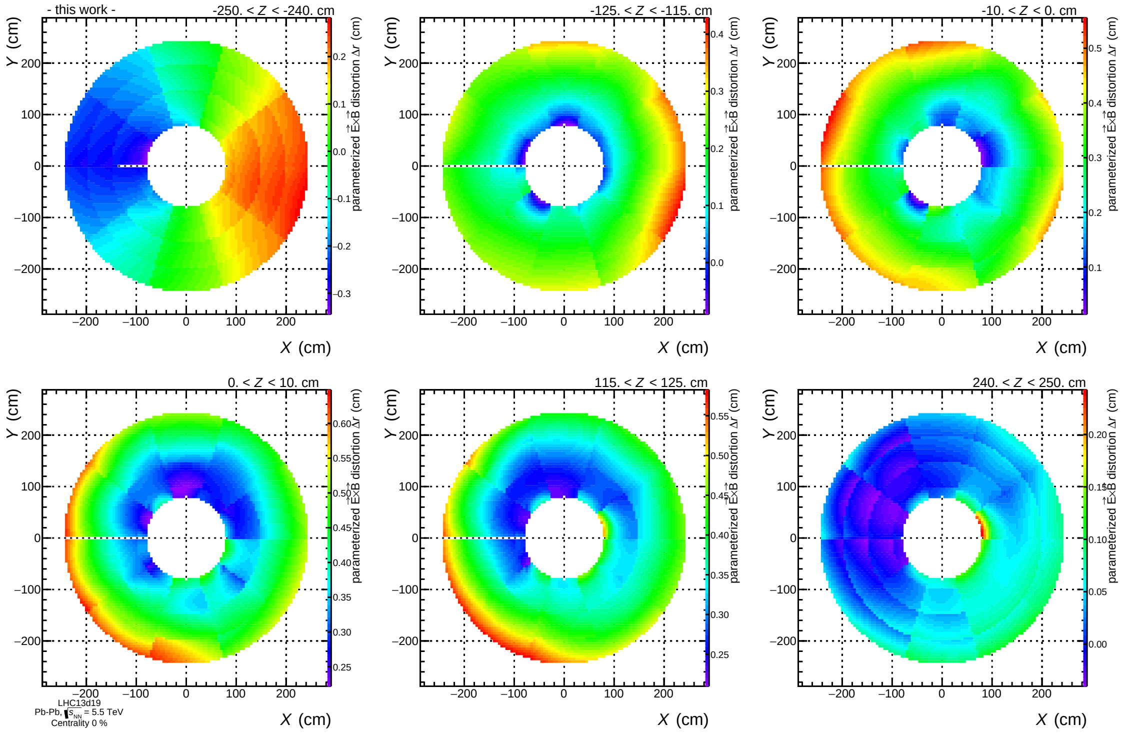

Figure B.8.: Parameterized map of the r-distortions for the B^{-} setup in the ALICE central barrel. Going from one endcap of the TPC to the other, six slices of the TPC column are depicted. Near the endcaps (top left and bottom right) distortions, induced by mis-alignment of the readout chambers are visible. For the innermost radii inside the TPC, large but local distortions are visible, which originate from misplaced foils of the TPC field cage.

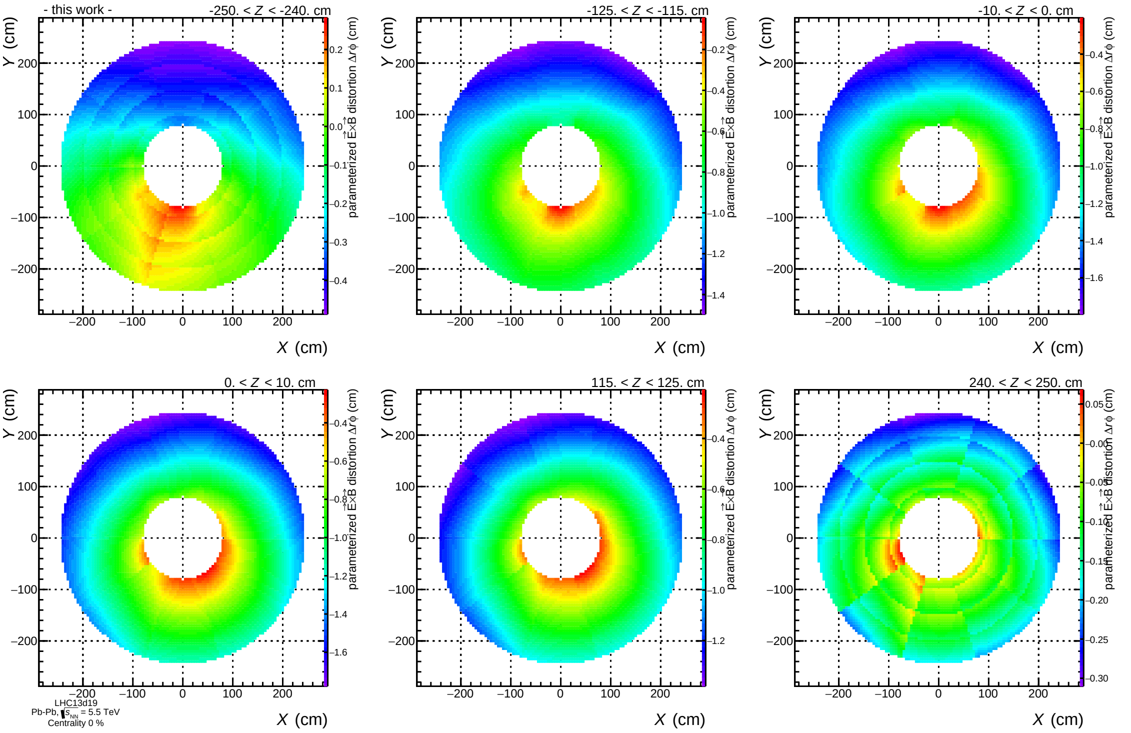

Figure B.9.: Parameterized map of the $r\phi$-distortions for the B$^+$ setup in the ALICE central barrel. Going from one endcap of the TPC to the other, six slices of the TPC column are depicted. Near the endcaps (top left and bottom right) distortions, induced by mis-alignment of the readout chambers are visible. For the innermost radii inside the TPC, large but local distortions are visible, which originate from misplaced foils of the TPC field cage.

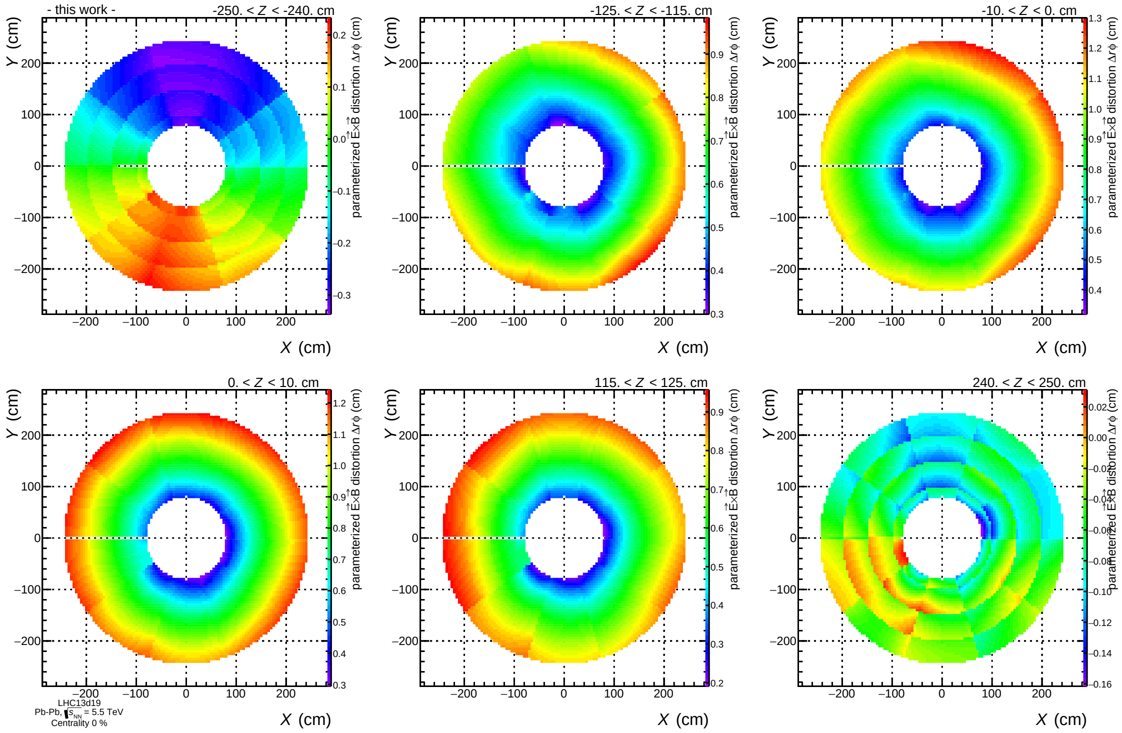

Figure B.10.: Parameterized map of the $r\phi$-distortions for the B^- setup in the ALICE central barrel. Going from one endcap of the TPC to the other, six slices of the TPC column are depicted. Near the endcaps (top left and bottom right) distortions, induced by mis-alignment of the readout chambers are visible. For the innermost radii inside the TPC, large but local distortions are visible, which originate from misplaced foils of the TPC field cage.

B.3. Single-track reconstruction

In this section, the track reconstruction efficiencies for primary protons, electrons and muons (figure B.11) as well for electrons and muons from strange weak decays (figure B.12) are presented. Different stages of the track selection cuts are applied, similar to those presented in section 4.3.9.2.

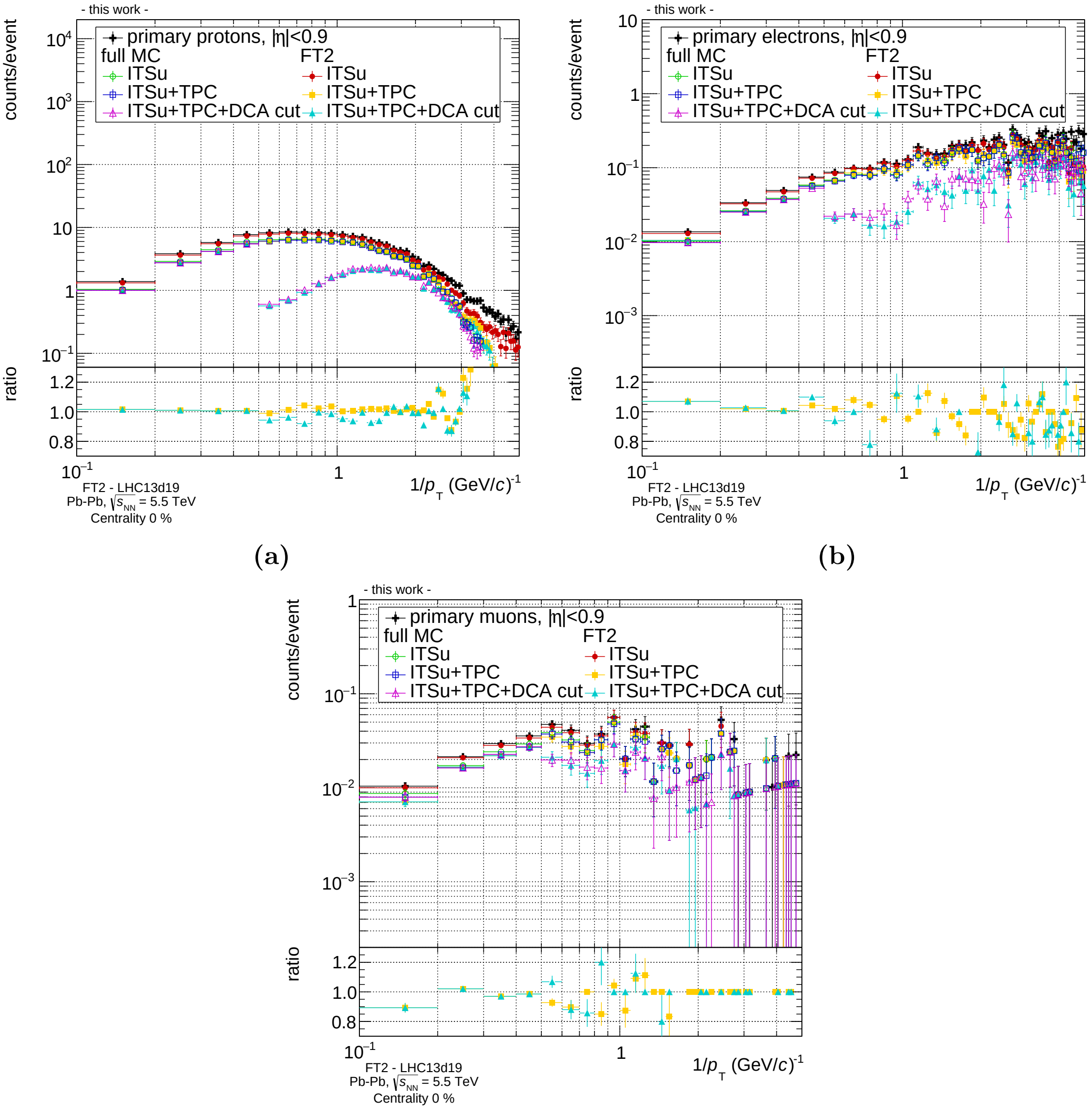

(a)

(b)

(c)

Figure B.11.: Generated and reconstructed particle yields as a function of p_T for primary protons (a), electrons (b) and muons (c) using the FT2 and full MC reconstruction algorithms. Different stages of track selection criteria are applied, requiring ITSu, ITSu+TPC and ITSu+TPC+DCA cuts, as explained in table 4.2.

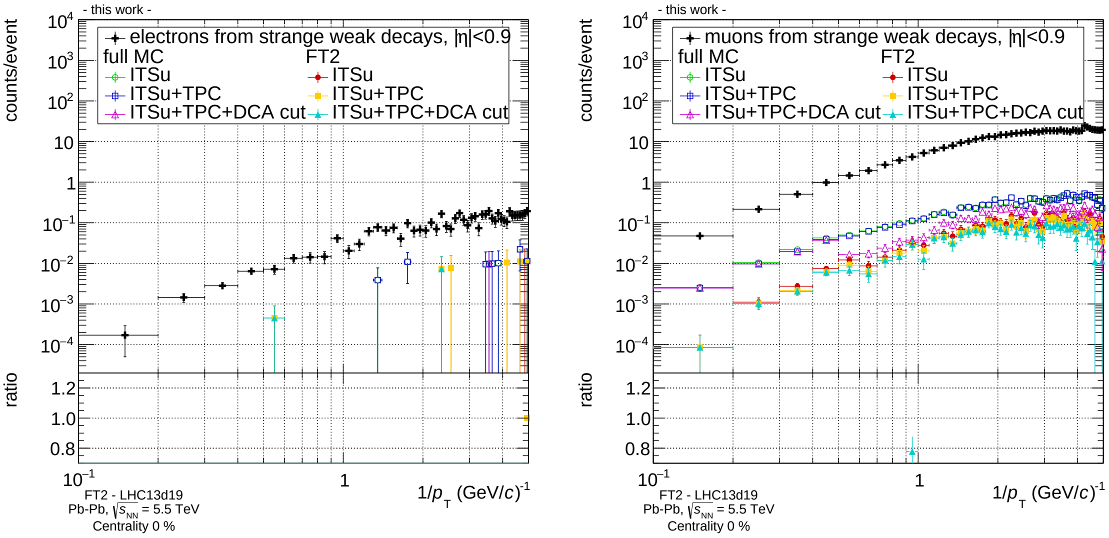

(a) **(b)**

Figure B.12.: Generated and reconstructed particle yields as a function of p_{T} for electrons (a) and muons (b) from strange weak decays using the FT2 and full MC reconstruction algorithms. Different stages of track selection criteria are applied, requiring ITSu, ITSu+TPC and ITSu+TPC+DCA cuts, as explained in table 4.2. Almost no electrons from weak decays pass the track selection criteria and are reconstructed to tracks. For muons from strange weak decays, a large deviations between FT2 and full MC tracks is observed. The origin of this difference remains unclear, as for all other particles species (no matter if primary or secondary particles) excellent agreement was observed and no obvious problem in the algorithm was found. Nevertheless, the fraction of reconstructed muons from strange weak decays in a Pb–Pb collision is smaller by at least three orders of magnitude compared to the remaining particle yields, and can thus be neglected.

C. FT2: Systematic uncertainties and scalers

In this section, the uncertainty of the reconstructed background and signal yields in the full kinematic reconstruction of $B^+ \rightarrow \overline{D}^0\pi^+$ ($\overline{D}^0 \rightarrow K^+\pi^-$) in the FT2 are evaluated in the remaining kinematic bins of the reconstructed B^+ candidates. After the application of the $\cos(\theta_{\text{pointing}})$-cut in combination with a different single selection criterium, a scaling factor was assigned to the central value of the ratio of the remaining yields in the invariant mass range $\pm 3\sigma$ around the PDG value. The open boxes reflect the spread of the combinations of the cuts. In these comparisons, the invariant mass resolutions obtained in full MC simulations were used in order not to bias the FT2 results due to the slightly improved resolution.

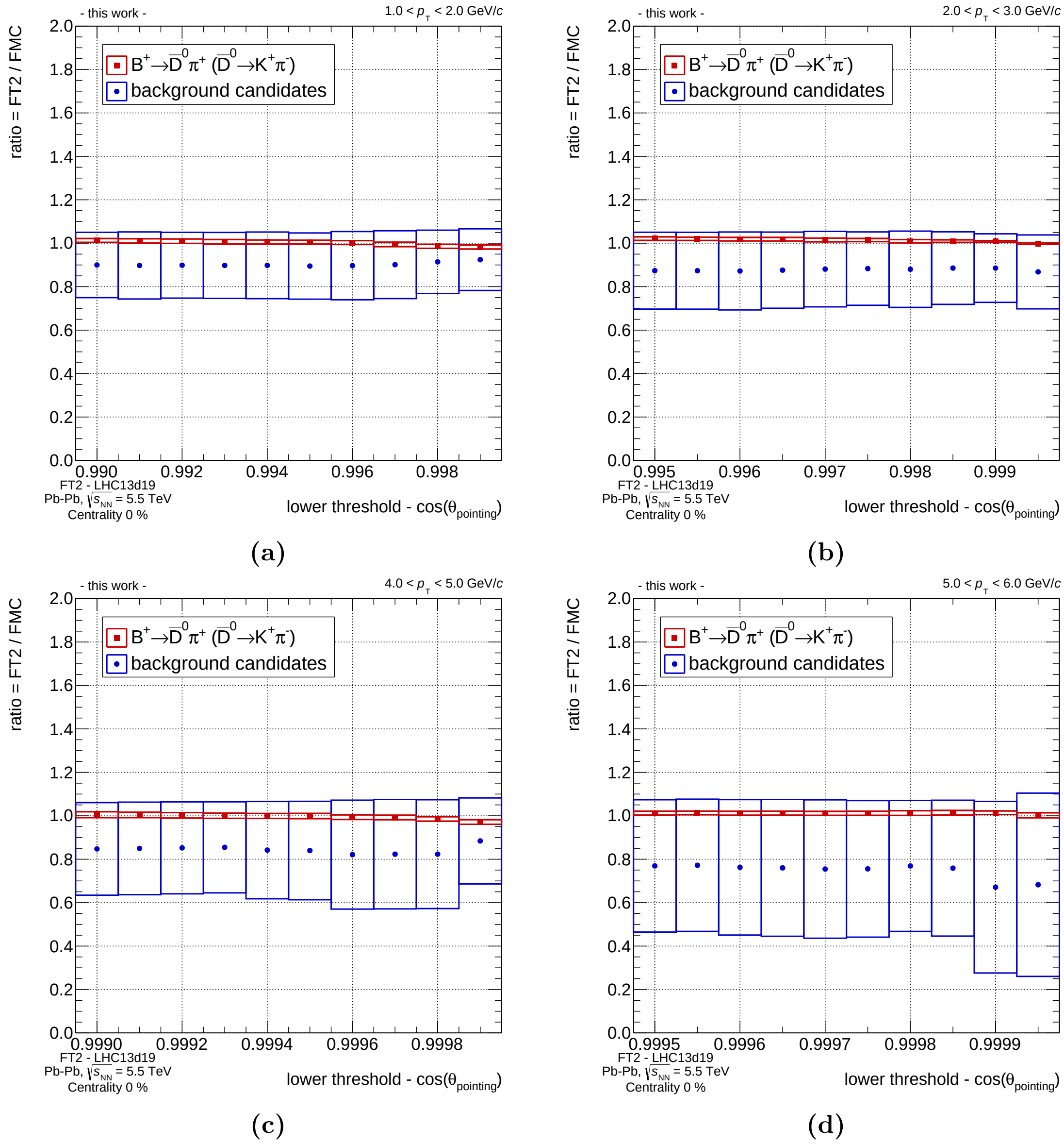

(a) **(b)**

(c) **(d)**

Figure C.1.: Systematic uncertainties evaluated for the FT2 in the remaining p_T-bins.

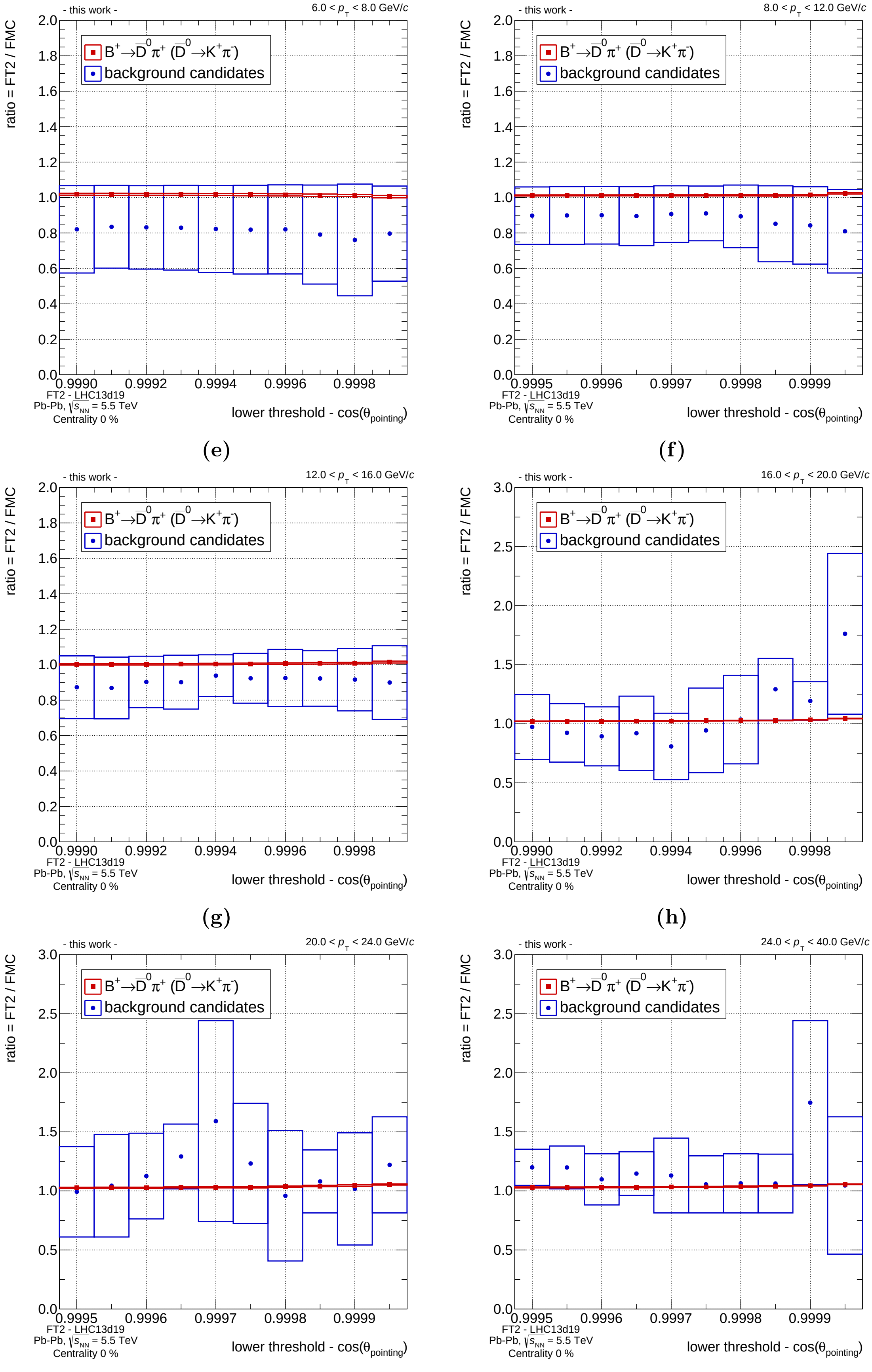
- this work -
6.0 < p_T < 8.0 GeV/c
8.0 < p_T < 12.0 GeV/c
12.0 < p_T < 16.0 GeV/c
16.0 < p_T < 20.0 GeV/c
20.0 < p_T < 24.0 GeV/c
24.0 < p_T < 40.0 GeV/c
ratio = FT2 / FMC
B⁺→D̄⁰π⁺ (D̄⁰→K⁺π⁻)
background candidates
FT2 - LHC13d19
Pb-Pb, √s_NN = 5.5 TeV
Centrality 0 %
lower threshold - cos(θ_pointing)
0.9990
0.9992
0.9994
0.9996
0.9998
0.9995
0.9996
0.9997
0.9998
0.9999
0.0
0.2
0.4
0.6
0.8
1.0
1.2
1.4
1.6
1.8
2.0
0.5
1.5
2.5
3.0

(e) (f) (g) (h) (i) (j)

D. Enhancement of combinatorial background statistics using the track rotation method

The track rotation method is applied on the pion candidate track which is to be paired with the $\overline{\mathrm{D}}^0$ candidate in order to reproduce the background of the B^+ invariant mass distribution. This method was selected, as it appears as most promising candidate reproducing the event, and even more important, the decay topology. Other techniques, for example in case of *event mixing*, suffer from the fact that the primary vertex would have to be moved to the exact same position within a very high resolution, to be able to compare different events to each other. The concept behind the track rotation method is to break possible correlation between existing track pairs by the rotation of a given track momentum vector in the detectors transverse plane around the z-axis. This redistribution of tracks should mimic the random combination of uncorrelated tracks pairs and can be used to further calculate the invariant mass spectrum. The benefit is, that no additional particles need to be generated, while the rotated candidates already correspond to realistically reconstructed tracks in the experiment. However, also in this approach computational resources are quickly exhausted, as the additionally rotated tracks need to be written into temporary memory. The working principle of the track rotation method for the generation of background candidates for the decay $\mathrm{B}^+ \to \overline{\mathrm{D}}^0\pi^+$ is schematically displayed in figure D.1. In order to form a B^+ candidate, all correctly charged tracks are rotated around a base angle $\phi_{\mathrm{B}} = 180°$ in the xy-plane. For an additional decrease of the statistical uncertainty, an additional interval angle ϕ_{interval} is chosen relative to ϕ_{B}, which allows to rotate several times over different angles:

$$\phi_{\mathrm{total}} = \phi_{\mathrm{B}} + N \cdot \phi_{\mathrm{interval}} \tag{D.1}$$

Obviously, the two angles and the number of rotations (N) have to be chosen carefully, as it is required that each rotation is independent of the others. In addition, for a given amount of computing power, the number of rotations will largely increase the processing time of the analysis, as visible in figure D.2a. The relative processing time increases linearly with an increased number of rotations for a given amount of computational power, reaching up to 4.4 times the initial analysis time for 30 rotations. Figure D.2b displays the reduction of background fluctuations as a function of the number of rotations. With increasing number of rotations, the normalized standard deviations steeply decreases with approximately $0.41/\sqrt{N}$ until a saturation is visible at around eight rotations. Beyond this point, the gain in statistical precision is rather limited. From these consideration the number of rotations was fixed to $\mathrm{N} = 13$.

The base angle ϕ_{B} was set to 180°. Displayed in figure D.3, where the normalized standard deviation of the background is shown as a function of the interval angle, the tune of the

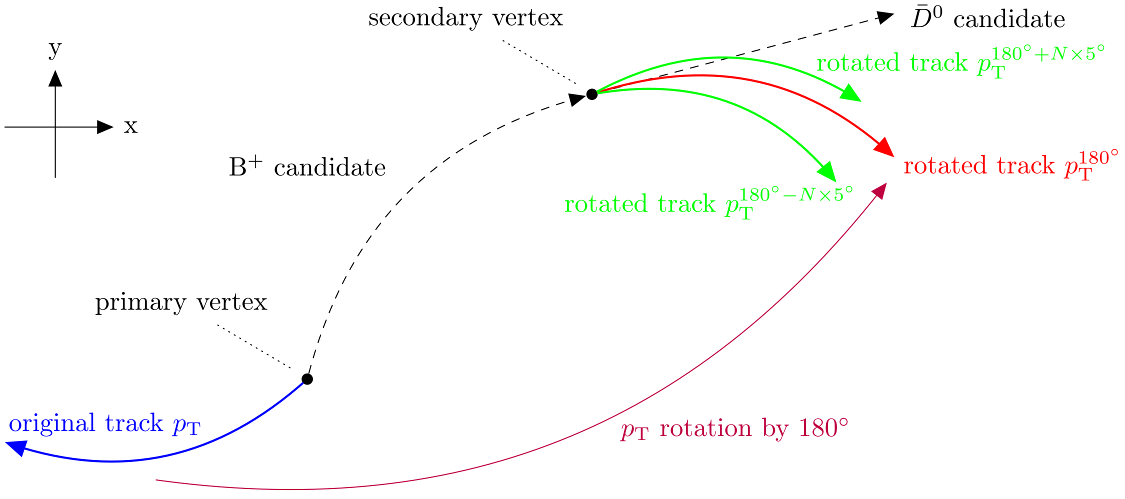

Figure D.1.: Schematic view of the woking principle of the track rotation method for the pion candidate track in the decay $B^+ \to \overline{D}^0\pi^+$.

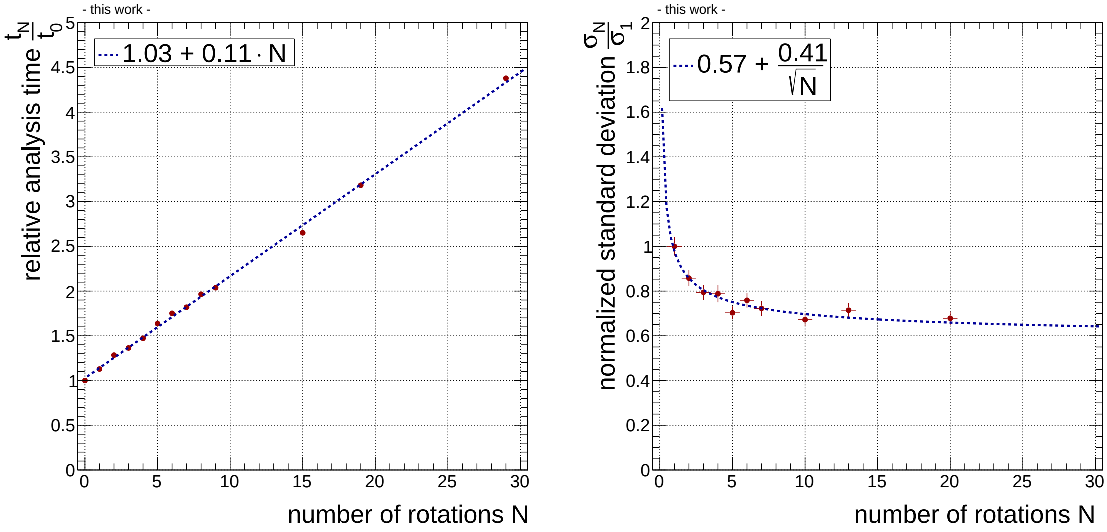

(a) (b)

Figure D.2.: Relative analysis time and normalized standard deviation of the track rotation method.

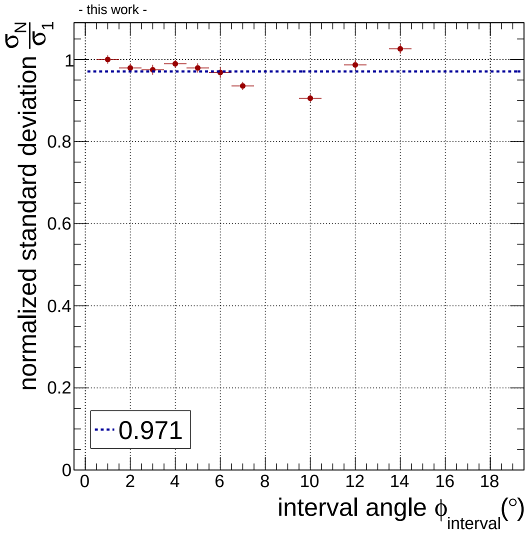

Figure D.3.: Dependence of the normalized standard deviation on the interval angle ϕ_{interval} in the track rotation method.

interval angle was performed independently. However, there is an interplay between the normalized standard deviation, the interval angle and the bin width of the B^+ invariant mass histogram, as the opening angle between the two daughter tracks is changed:

$$M(\text{B}^+)^{\text{candidate}} = M(\overline{\text{D}}^0\pi^+) = \sqrt{\left(m^2_{\overline{\text{D}}^0} + m^2_\pi + 2|p_{\overline{\text{D}}^0}||p_\pi|\cos(\theta)\right)}. \tag{D.2}$$

Reducing the interval angle will increase the probability that the candidate mass will lie in the correct mass range and thus for large bin widths an increased fluctuation of the normalized standard deviation is observed. However, for the chosen width of the B^+ analysis displayed in D.3, no strong dependence was found and the angle was fixed to $\phi_{\text{interval}} = 5°$. With these settings the track rotation method is performing 13 rotations in the range of $150° < \phi_{\text{total}} < 210°$ around the z-axis.

E. Correlated background analysis

In this appendix the settings of the MC simulations of the correlated background sources are provided in Section E.1. Further, the efficiency correction factor, the Invariant mass spectra and the distributions of the $cos(\theta_{pointing})$ for the identified correlated background sources are shown for additional kinematic bins in Section E.2.

E.1. Settings of the Monte Carlo simulations

All of the dedicated MC simulations were based on the generation of the final state of the interaction. A flat p_{T} spectrum was assumed for simplicity and the particles were generated within |y|<1. In order to remove a possible bias from this assumption, identified sources of correlated background were generated within |y|<7 and considered in the calculation. The *AliGenBox*[i]-generator was used.

The particle decays were forced using an implementation of the *EvtGen*-package [246] inside the ALICE software framework. The ideal geometry of the upgraded ALICE detector (as in MC production LHC13d19) was used, anchored on the run 138871 (period LHC10h). The analysis was performed on *AOD*s. The statistics of the generated decay channels is shown in table E.1. Here, it was required that the B meson passes the fiducial acceptance selection. In addition, at least one decay daughter detectable by the experiment was required to be within $|\eta| < 0.9$ and p_{T}>0.1 GeV/c. Table E.2 displays the statistics for the productions dedicated to the analysis of the potential bias effect described before. Here, only B mesons within |y|<0.5 were considered.

In addition, for all productions it was required that decay daughters visible to the experiment are within the fiducial acceptance of the ALICE central barrel detectors (|y|<1 and $40° < \theta < 140°$).

The reconstructed raw yield describes the number of successfully reconstructed B mesons in the analysis, identified via the MC truth information. Here, only the D^0-selection criteria and the fiducial acceptance criterion on the B meson were applied. An invariant mass range of $\Delta m_{\mathrm{B}^+} = 5.279 \pm 0.500\,\mathrm{GeV}/c^2$ was studied.

In order to reduce the statistical uncertainty additional MC productions with a similar setup but in a more restricted kinematic range were evaluated, too.

E.2. Additional results

In this section, the invariant mass spectra as well as the $\cos(\theta_{\mathrm{pointing}})$-distributions of the correlated background sources in the remaining kinematic bins are presented.

---

[i] http://aliroot-docs.web.cern.ch/aliroot-docs/AliGenBox.html

Decay generated in $\|y\|<1$	Generated in p_{T}-range (GeV/c)	Generated raw yield B^+ in fiducial acceptance daus. in $\|\eta\|<0.9$, $p_{\mathrm{T}} > 0.1\,\mathrm{GeV}/c$	Reconstructed raw yield
$\mathrm{B}^+ \to \overline{\mathrm{D}}^0 \pi^+$	0 - 24	2 291 085	529 662
$\mathrm{B}^+ \to \overline{\mathrm{D}}^0 \mathrm{K}^+$	0 - 24	2 561 622	561 850
$\mathrm{B}^+ \to \overline{\mathrm{D}}^0 \omega^0 \pi^+$	0 - 24	2 163 436	3
$\mathrm{B}^+ \to \overline{\mathrm{D}}^0 \rho^0 \pi^+$	0 -24	2 411 942	184
$\mathrm{B}^+ \to \overline{\mathrm{D}}^0 \rho^+$	0 - 24	1 351 718	2 621
$\mathrm{B}^+ \to \overline{\mathrm{D}}^0 K^*(892)^+$	0 - 24	1 375 378	709
$\mathrm{B}^+ \to \overline{\mathrm{D}}^0 l^+ \nu_l$	0 - 24 (0 - 8)	3 865 446 (3 281 703)	27 722 (13 862)
$\mathrm{B}^+ \to \overline{\mathrm{D}}^0 \tau^+ \nu_\tau$	0 - 24	1 823 151	1
$\mathrm{B}^+ \to \overline{\mathrm{D}}^0 \pi^+ \pi^+ \pi^-$	0 - 24	2 341 888	575
$\mathrm{B}^+ \to \overline{\mathrm{D}}^0 \mathrm{K}^+ \mathrm{K}^0$	0 - 24	1 422 425	131
$\mathrm{B}^+ \to \overline{\mathrm{D}}^0 \mathrm{K}^+ \pi^+ \pi^-$	0 - 24	2 380 753	131
$\mathrm{B}^0 \to \overline{\mathrm{D}}^0 \pi^+ \pi^-$	0 - 24 (0 - 8)	1 619 466 (3 473 769)	22 923 (27 911)
$\mathrm{B}^0 \to \overline{\mathrm{D}}^0 \pi^- l^+ \nu_l$	0 - 24	924 682	1
$\mathrm{B}^0 \to \overline{\mathrm{D}}^0 \eta^0$	0 - 24	797 102	126
$\mathrm{B}^0 \to \overline{\mathrm{D}}^0 \eta'$	0 - 24	1 205 761	4
$\mathrm{B}^0 \to \overline{\mathrm{D}}^0 \rho^0$	0 - 24	2 522 925	52 563
$\mathrm{B}^0 \to \overline{\mathrm{D}}^0 \omega^0$	0 - 24	1 238 256	393
$\mathrm{B}_s^0 \to \overline{\mathrm{D}}^0 \mathrm{K}^- \pi^+$	0 - 24 (0 - 8)	1 230 858 (1 837 565)	10 042 (8 247)

Table E.1.: Statistics of the simulated raw yields of all studied correlated background sources.

Decay generated in $\|y\| < 7$	Generated in p_{T}-range (GeV/c)	Generated with B^+ in $\|y\|<0.5$	Generated raw yield with B^+ in fiducial acceptance and daughters in $\|\eta\|<0.9$, $p_{\mathrm{T}} > 0.1\,\mathrm{GeV}/c$
$\mathrm{B}^+ \to \overline{\mathrm{D}}^0 \pi^+$	0 - 24	17 495	21 766
$\mathrm{B}^+ \to \overline{\mathrm{D}}^0 \mathrm{K}^+$	0 - 24	21 191	26 223
$\mathrm{B}^+ \to \overline{\mathrm{D}}^0 l^+ \nu_l$	0 - 24	17 749	22 287
$\mathrm{B}^0 \to \overline{\mathrm{D}}^0 \pi^+ \pi^-$	0 - 24	17 851	22 265
$\mathrm{B}^0 \to \overline{\mathrm{D}}^0 \rho^0$	0 - 24	234 033	229.702
$\mathrm{B}_s^0 \to \overline{\mathrm{D}}^0 \mathrm{K}^- \pi^+$	0 - 24	10 289	12.954

Table E.2.: Statistics of the simulated raw yields of all studied correlated background sources without a bias on the rapidity of the generated B meson.

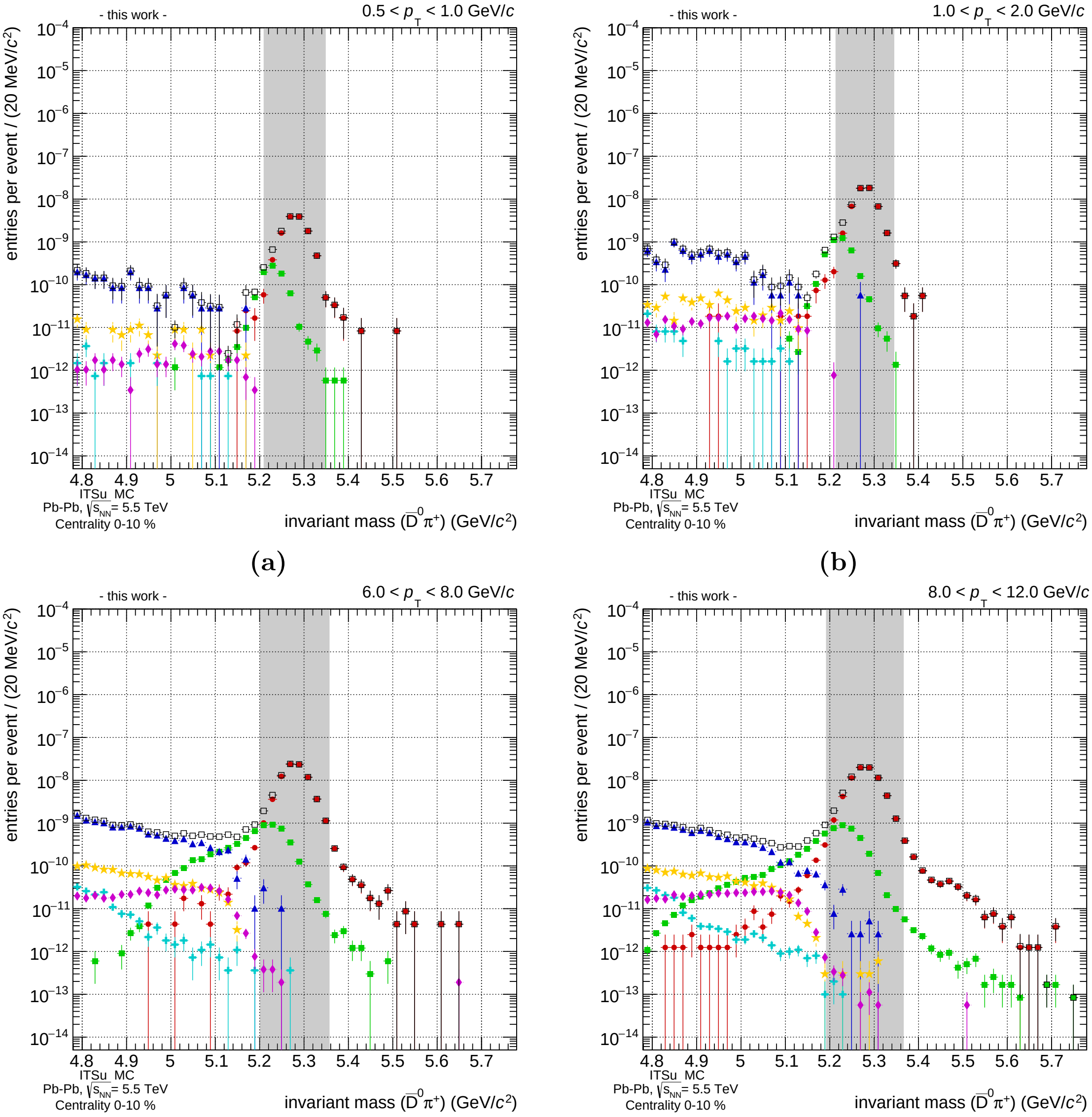

(a) (b)

(c) (d)

Figure E.1.: Invariant mass spectra of correlated background sources in the remaining kinematic bins. The gray band indicates the 3σ-range of the signal decay.

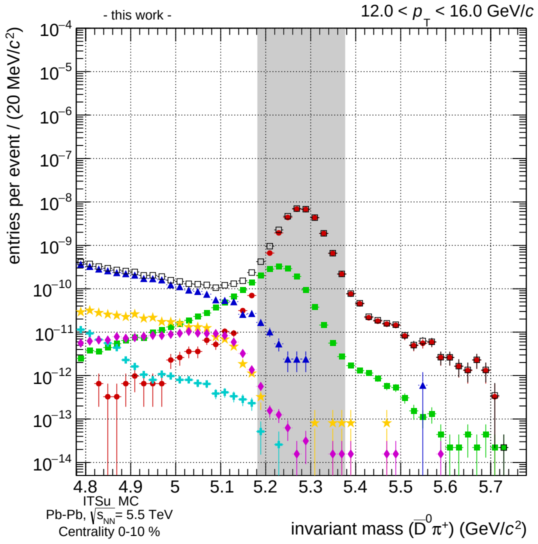
- this work -
12.0 < p_T < 16.0 GeV/c
entries per event / (20 MeV/c^2)
10^{-4}
10^{-5}
10^{-6}
10^{-7}
10^{-8}
10^{-9}
10^{-10}
10^{-11}
10^{-12}
10^{-13}
10^{-14}
4.8
4.9
5
5.1
5.2
5.3
5.4
5.5
5.6
5.7
ITSu_MC
Pb-Pb, $\sqrt{s_{NN}}$= 5.5 TeV
Centrality 0-10 %
invariant mass ($\overline{D}^0\pi^+$) (GeV/c^2)

(e)

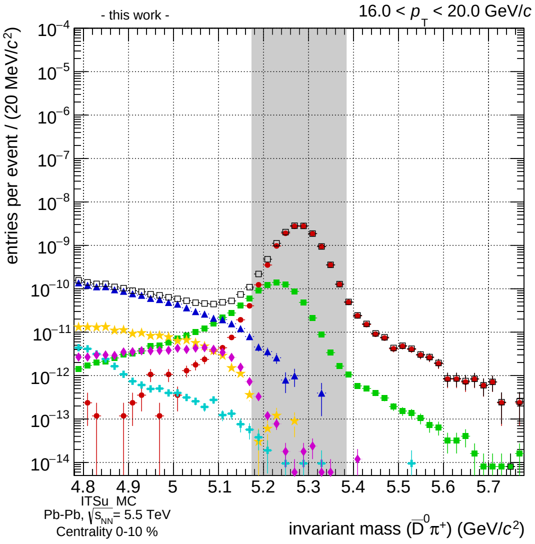
- this work -
16.0 < p_T < 20.0 GeV/c
entries per event / (20 MeV/c^2)
10^{-4}
10^{-5}
10^{-6}
10^{-7}
10^{-8}
10^{-9}
10^{-10}
10^{-11}
10^{-12}
10^{-13}
10^{-14}
4.8
4.9
5
5.1
5.2
5.3
5.4
5.5
5.6
5.7
ITSu_MC
Pb-Pb, $\sqrt{s_{NN}}$= 5.5 TeV
Centrality 0-10 %
invariant mass ($\overline{D}^0\pi^+$) (GeV/c^2)

(f)

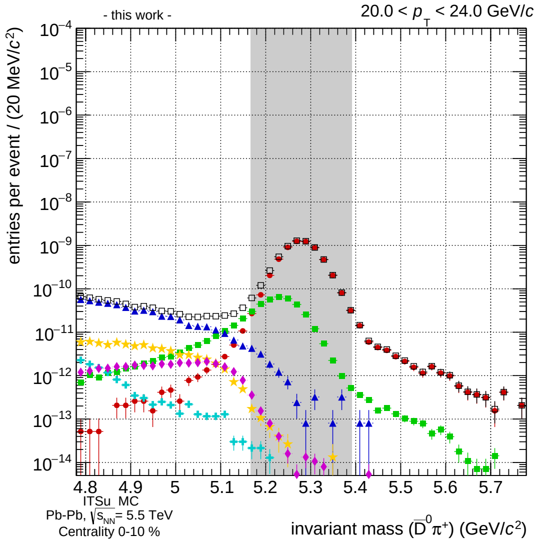
- this work -
20.0 < p_T < 24.0 GeV/c
entries per event / (20 MeV/c^2)
10^{-4}
10^{-5}
10^{-6}
10^{-7}
10^{-8}
10^{-9}
10^{-10}
10^{-11}
10^{-12}
10^{-13}
10^{-14}
4.8
4.9
5
5.1
5.2
5.3
5.4
5.5
5.6
5.7
ITSu_MC
Pb-Pb, $\sqrt{s_{NN}}$= 5.5 TeV
Centrality 0-10 %
invariant mass ($\overline{D}^0\pi^+$) (GeV/c^2)

(g)

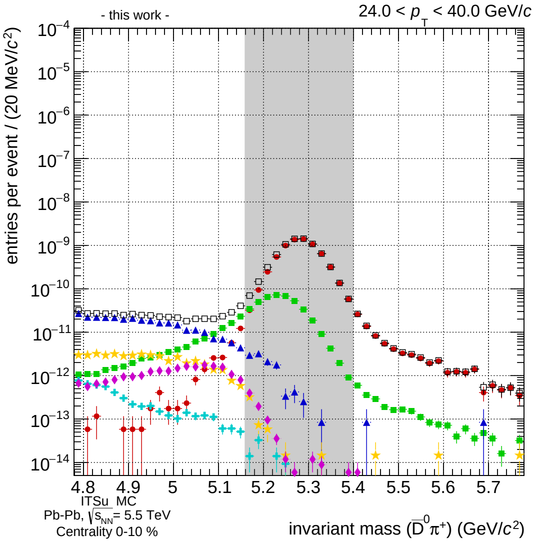
- this work -
24.0 < p_T < 40.0 GeV/c
entries per event / (20 MeV/c^2)
10^{-4}
10^{-5}
10^{-6}
10^{-7}
10^{-8}
10^{-9}
10^{-10}
10^{-11}
10^{-12}
10^{-13}
10^{-14}
4.8
4.9
5
5.1
5.2
5.3
5.4
5.5
5.6
5.7
ITSu_MC
Pb-Pb, $\sqrt{s_{NN}}$= 5.5 TeV
Centrality 0-10 %
invariant mass ($\overline{D}^0\pi^+$) (GeV/c^2)

(h)

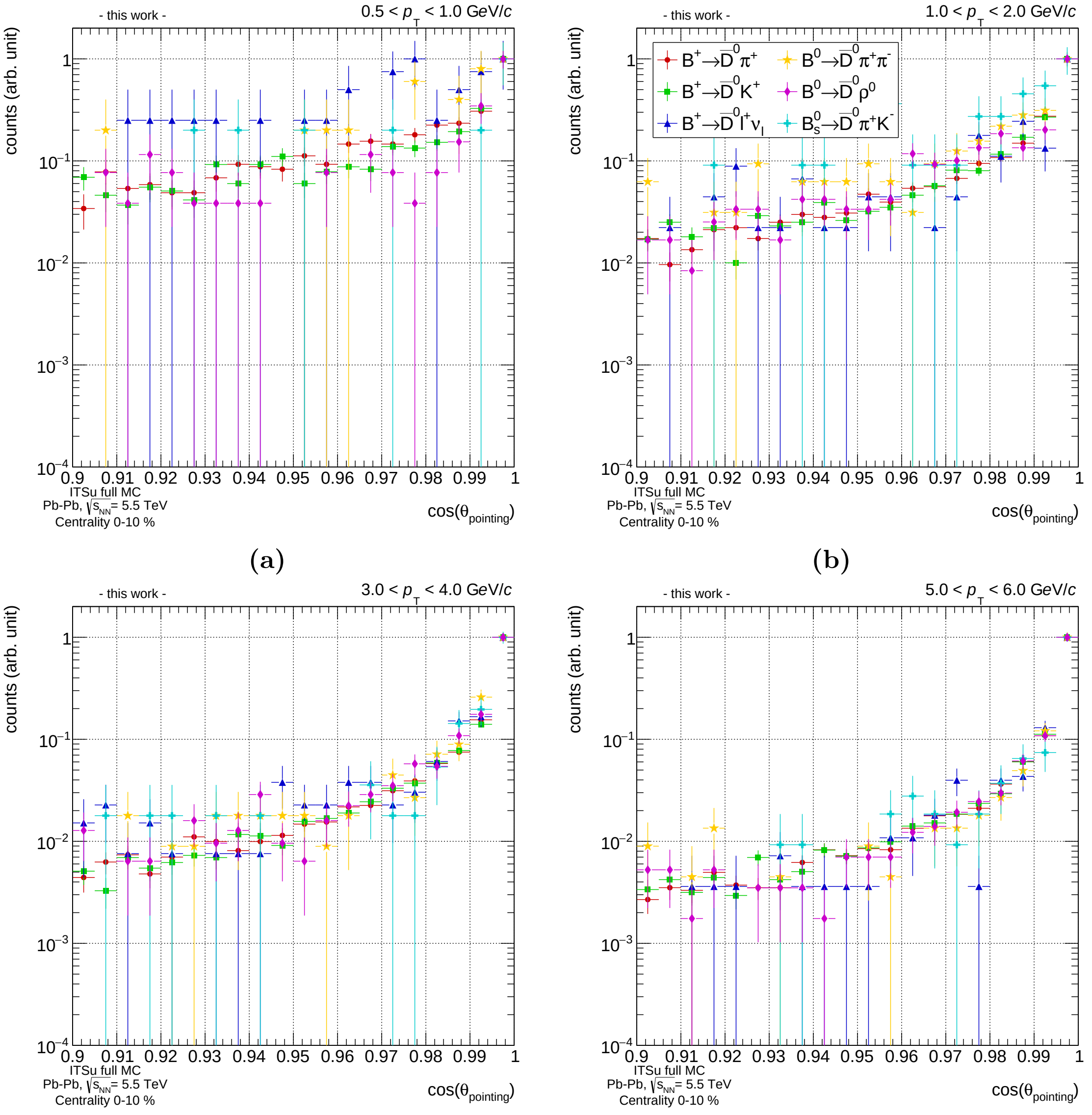

(a)

(b)

(c)

(d)

Figure E.2.: $\cos\left(\theta_{pointing}\right)$ distribution of correlated background sources in the remaining kinematic bins. All distributions were scaled to unity in the bin with the highest content for better comparability.

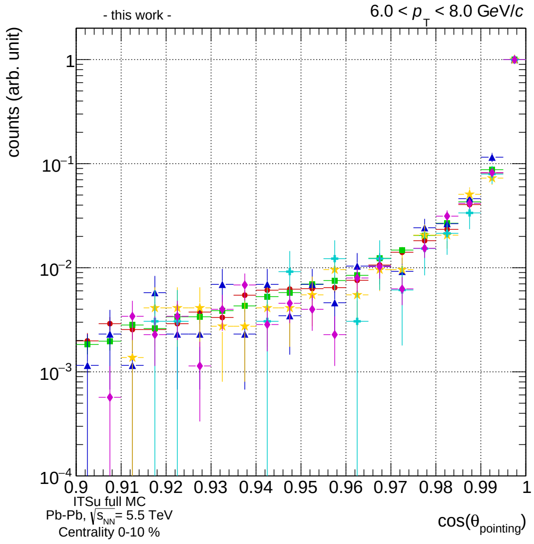
- this work -
6.0 < p_T < 8.0 GeV/c
counts (arb. unit)
1
10^-1
10^-2
10^-3
10^-4
0.9 0.91 0.92 0.93 0.94 0.95 0.96 0.97 0.98 0.99 1
ITSu full MC
Pb-Pb, √s_NN = 5.5 TeV
Centrality 0-10 %
cos(θ_pointing)

(e)

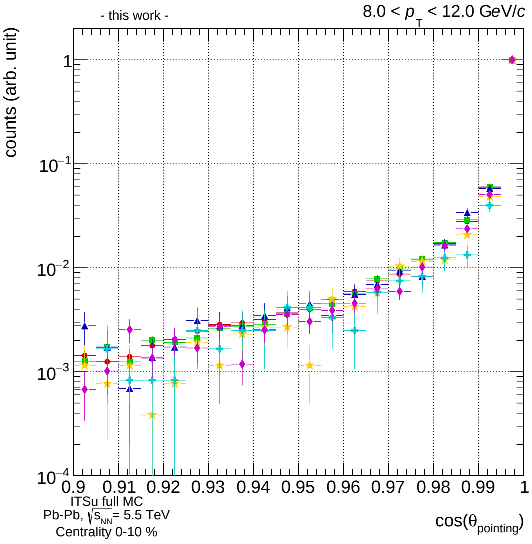
- this work -
8.0 < p_T < 12.0 GeV/c
counts (arb. unit)
1
10^-1
10^-2
10^-3
10^-4
0.9 0.91 0.92 0.93 0.94 0.95 0.96 0.97 0.98 0.99 1
ITSu full MC
Pb-Pb, √s_NN = 5.5 TeV
Centrality 0-10 %
cos(θ_pointing)

(f)

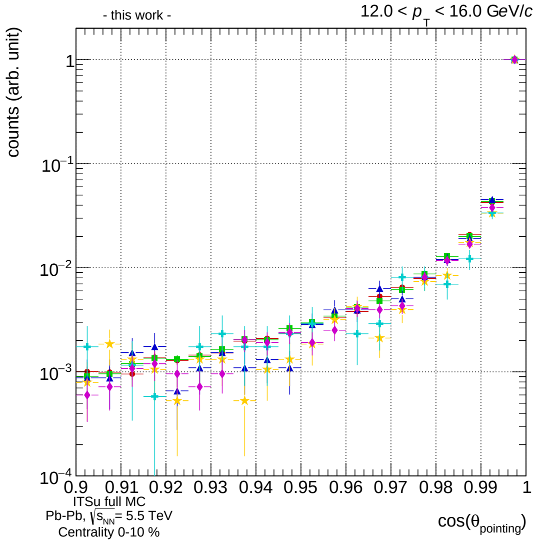
- this work -
12.0 < p_T < 16.0 GeV/c
counts (arb. unit)
1
10^-1
10^-2
10^-3
10^-4
0.9 0.91 0.92 0.93 0.94 0.95 0.96 0.97 0.98 0.99 1
ITSu full MC
Pb-Pb, √s_NN = 5.5 TeV
Centrality 0-10 %
cos(θ_pointing)

(g)

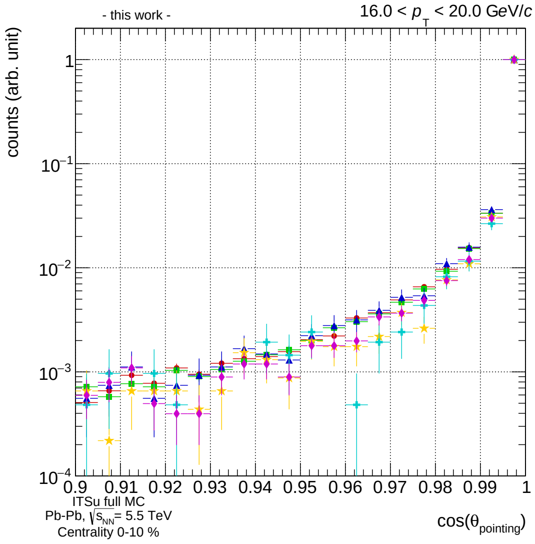
- this work -
16.0 < p_T < 20.0 GeV/c
counts (arb. unit)
1
10^-1
10^-2
10^-3
10^-4
0.9 0.91 0.92 0.93 0.94 0.95 0.96 0.97 0.98 0.99 1
ITSu full MC
Pb-Pb, √s_NN = 5.5 TeV
Centrality 0-10 %
cos(θ_pointing)

(h)

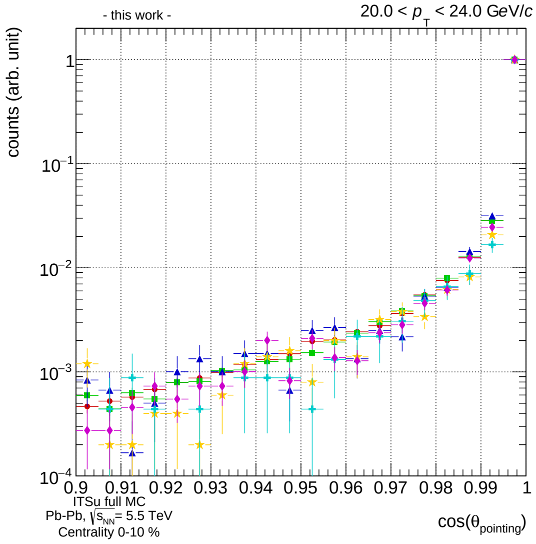
- this work -
20.0 < p_T < 24.0 GeV/c
counts (arb. unit)
1
10^-1
10^-2
10^-3
10^-4
0.9 0.91 0.92 0.93 0.94 0.95 0.96 0.97 0.98 0.99 1
ITSu full MC
Pb-Pb, √s_NN = 5.5 TeV
Centrality 0-10 %
cos(θ_pointing)

(i)

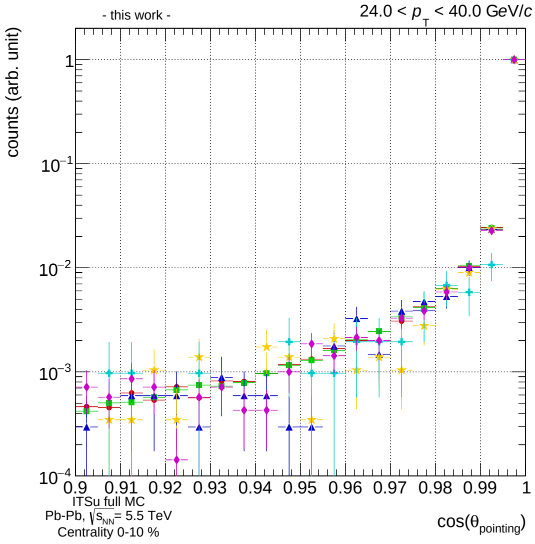
- this work -
24.0 < p_T < 40.0 GeV/c
counts (arb. unit)
1
10^-1
10^-2
10^-3
10^-4
0.9 0.91 0.92 0.93 0.94 0.95 0.96 0.97 0.98 0.99 1
ITSu full MC
Pb-Pb, √s_NN = 5.5 TeV
Centrality 0-10 %
cos(θ_pointing)

(j)

F. Multi-dimensional cut optimization

In this section, the remaining figures of the multi-dimensional cut optimization are presented, complementary to section 5.3.

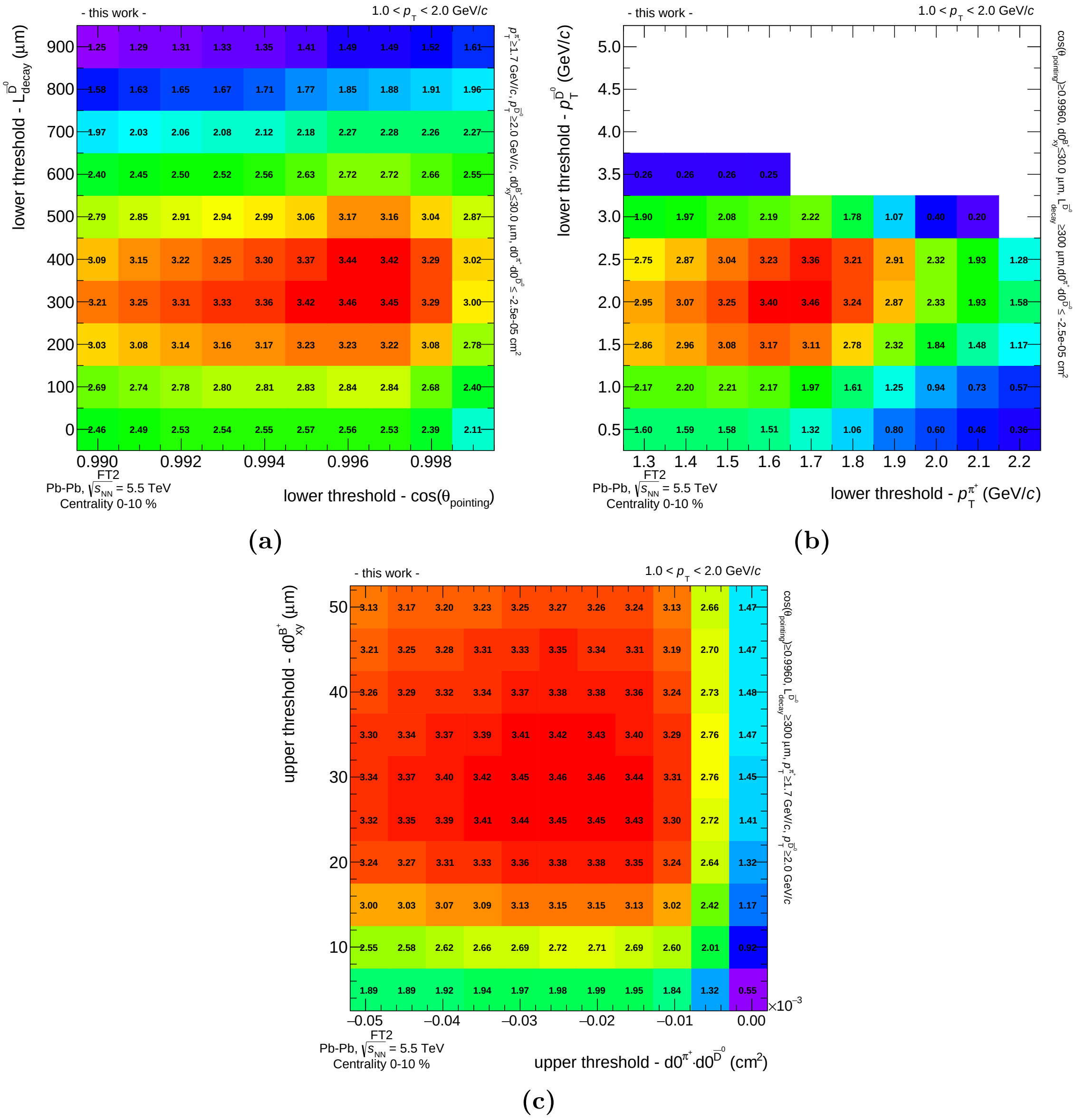

(a)

(b)

(c)

Figure F.1.: Multi-dimensional cut optimization in the remaining p_T-bins.

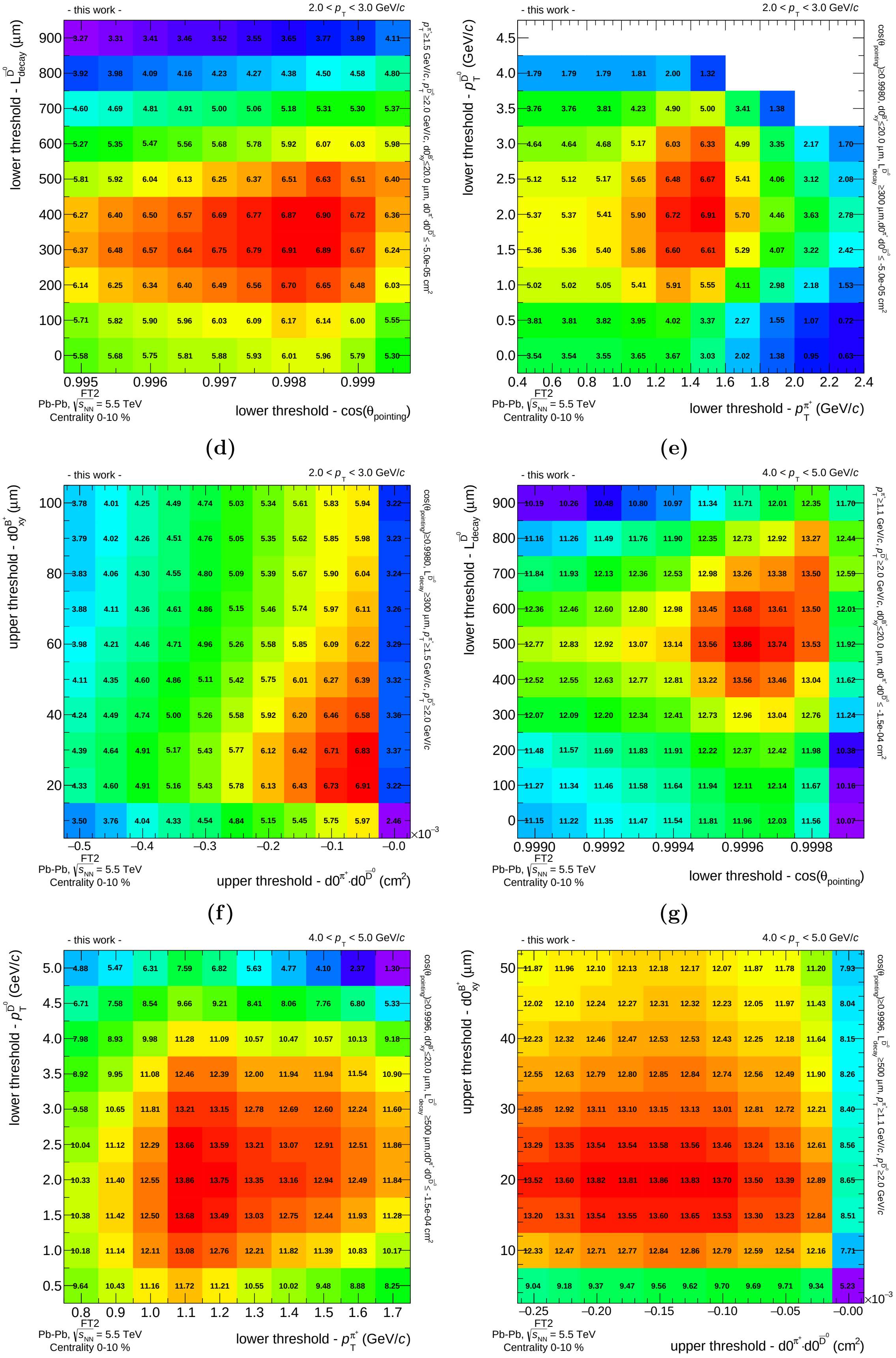
- this work -
2.0 < p_T < 3.0 GeV/c
lower threshold - L_decay^D̄0 (μm)
900 800 700 600 500 400 300 200 100 0
3.27 3.31 3.41 3.46 3.52 3.55 3.65 3.77 3.89 4.11
3.92 3.98 4.09 4.16 4.23 4.27 4.38 4.50 4.58 4.80
4.60 4.69 4.81 4.91 5.00 5.06 5.18 5.31 5.30 5.37
5.27 5.35 5.47 5.56 5.68 5.78 5.92 6.07 6.03 5.98
5.81 5.92 6.04 6.13 6.25 6.37 6.51 6.63 6.51 6.40
6.27 6.40 6.50 6.57 6.69 6.77 6.87 6.90 6.72 6.36
6.37 6.48 6.57 6.64 6.75 6.79 6.91 6.89 6.67 6.24
6.14 6.25 6.34 6.40 6.49 6.56 6.70 6.65 6.48 6.03
5.71 5.82 5.90 5.96 6.03 6.09 6.17 6.14 6.00 5.55
5.58 5.68 5.75 5.81 5.88 5.93 6.01 5.96 5.79 5.30
0.995 0.996 0.997 0.998 0.999
lower threshold - cos(θ_pointing)
p_T^π+ ≥1.5 GeV/c, p_T^D̄0 ≥2.0 GeV/c, d0_xy^B+ ≤20.0 μm, d0^π+·d0^D̄0 ≤ -5.0e-05 cm²
FT2
Pb-Pb, √s_NN = 5.5 TeV
Centrality 0-10 %
- this work -
2.0 < p_T < 3.0 GeV/c
lower threshold - p_T^D̄0 (GeV/c)
4.5 4.0 3.5 3.0 2.5 2.0 1.5 1.0 0.5 0.0
1.79 1.79 1.79 1.81 2.00 1.32
3.76 3.76 3.81 4.23 4.90 5.00 3.41 1.38
4.64 4.64 4.68 5.17 6.03 6.33 4.99 3.35 2.17 1.70
5.12 5.12 5.17 5.65 6.48 6.67 5.41 4.06 3.12 2.08
5.37 5.37 5.41 5.90 6.72 6.91 5.70 4.46 3.63 2.78
5.36 5.36 5.40 5.86 6.60 6.61 5.29 4.07 3.22 2.42
5.02 5.02 5.05 5.41 5.91 5.55 4.11 2.98 2.18 1.53
3.81 3.81 3.82 3.95 4.02 3.37 2.27 1.55 1.07 0.72
3.54 3.54 3.55 3.65 3.67 3.03 2.02 1.38 0.95 0.63
0.4 0.6 0.8 1.0 1.2 1.4 1.6 1.8 2.0 2.2 2.4
lower threshold - p_T^π+ (GeV/c)
cos(θ_pointing)≥0.9980, d0_xy^B+ ≤20.0 μm, L_decay^D̄0 ≥300 μm, d0^π+·d0^D̄0 ≤ -5.0e-05 cm²
FT2
Pb-Pb, √s_NN = 5.5 TeV
Centrality 0-10 %
- this work -
2.0 < p_T < 3.0 GeV/c
upper threshold - d0_xy^B+ (μm)
100 80 60 40 20
3.78 4.01 4.25 4.49 4.74 5.03 5.34 5.61 5.83 5.94 3.22
3.79 4.02 4.26 4.51 4.76 5.05 5.35 5.62 5.85 5.98 3.23
3.83 4.06 4.30 4.55 4.80 5.09 5.39 5.67 5.90 6.04 3.24
3.88 4.11 4.36 4.61 4.86 5.15 5.46 5.74 5.97 6.11 3.26
3.98 4.21 4.46 4.71 4.96 5.26 5.58 5.85 6.09 6.22 3.29
4.11 4.35 4.60 4.86 5.11 5.42 5.75 6.01 6.27 6.39 3.32
4.24 4.49 4.74 5.00 5.26 5.58 5.92 6.20 6.46 6.58 3.36
4.39 4.64 4.91 5.17 5.43 5.77 6.12 6.42 6.71 6.83 3.37
4.33 4.60 4.91 5.16 5.43 5.78 6.13 6.43 6.73 6.91 3.22
3.50 3.76 4.04 4.33 4.54 4.84 5.15 5.45 5.75 5.97 2.46
×10⁻³
−0.5 −0.4 −0.3 −0.2 −0.1 −0.0
upper threshold - d0^π+·d0^D̄0 (cm²)
cos(θ_pointing)≥0.9980, L_decay^D̄0 ≥300 μm, p_T^π+ ≥1.5 GeV/c, p_T^D̄0 ≥2.0 GeV/c
FT2
Pb-Pb, √s_NN = 5.5 TeV
Centrality 0-10 %
- this work -
4.0 < p_T < 5.0 GeV/c
lower threshold - L_decay^D̄0 (μm)
900 800 700 600 500 400 300 200 100 0
10.19 10.26 10.49 10.80 10.97 11.34 11.71 12.01 12.35 11.70
11.16 11.26 11.49 11.76 11.90 12.35 12.73 12.92 13.27 12.44
11.84 11.93 12.13 12.36 12.53 12.98 13.26 13.38 13.50 12.59
12.36 12.46 12.60 12.80 12.98 13.45 13.68 13.61 13.50 12.01
12.77 12.83 12.92 13.07 13.14 13.56 13.86 13.74 13.53 11.92
12.52 12.55 12.63 12.77 12.81 13.22 13.56 13.46 13.04 11.62
12.07 12.09 12.20 12.34 12.41 12.73 12.96 13.04 12.76 11.24
11.48 11.57 11.69 11.83 11.91 12.22 12.37 12.42 11.98 10.38
11.27 11.34 11.46 11.58 11.64 11.94 12.11 12.14 11.67 10.16
11.15 11.22 11.35 11.47 11.54 11.81 11.96 12.03 11.56 10.07
0.9990 0.9992 0.9994 0.9996 0.9998
lower threshold - cos(θ_pointing)
p_T^π+ ≥1.1 GeV/c, p_T^D̄0 ≥2.0 GeV/c, d0_xy^B+ ≤20.0 μm, d0^π+·d0^D̄0 ≤ -1.5e-04 cm²
FT2
Pb-Pb, √s_NN = 5.5 TeV
Centrality 0-10 %
- this work -
4.0 < p_T < 5.0 GeV/c
lower threshold - p_T^D̄0 (GeV/c)
5.0 4.5 4.0 3.5 3.0 2.5 2.0 1.5 1.0 0.5
4.88 5.47 6.31 7.59 6.82 5.63 4.77 4.10 2.37 1.30
6.71 7.58 8.54 9.66 9.21 8.41 8.06 7.76 6.80 5.33
7.98 8.93 9.98 11.28 11.09 10.57 10.47 10.57 10.13 9.18
8.92 9.95 11.08 12.46 12.39 12.00 11.94 11.94 11.54 10.90
9.58 10.65 11.81 13.21 13.15 12.78 12.69 12.60 12.24 11.60
10.04 11.12 12.29 13.66 13.59 13.21 13.07 12.91 12.51 11.86
10.33 11.40 12.55 13.86 13.75 13.35 13.16 12.94 12.49 11.84
10.38 11.42 12.50 13.68 13.49 13.03 12.75 12.44 11.93 11.28
10.18 11.14 12.11 13.08 12.76 12.21 11.82 11.39 10.83 10.17
9.64 10.43 11.16 11.72 11.21 10.55 10.02 9.48 8.88 8.25
0.8 0.9 1.0 1.1 1.2 1.3 1.4 1.5 1.6 1.7
lower threshold - p_T^π+ (GeV/c)
cos(θ_pointing)≥0.9996, d0_xy^B+ ≤20.0 μm, L_decay^D̄0 ≥500 μm, d0^π+·d0^D̄0 ≤ -1.5e-04 cm²
FT2
Pb-Pb, √s_NN = 5.5 TeV
Centrality 0-10 %
- this work -
4.0 < p_T < 5.0 GeV/c
upper threshold - d0_xy^B+ (μm)
50 40 30 20 10
11.87 11.96 12.10 12.13 12.18 12.17 12.07 11.87 11.78 11.20 7.93
12.02 12.10 12.24 12.27 12.31 12.32 12.23 12.05 11.97 11.43 8.04
12.23 12.32 12.46 12.47 12.53 12.53 12.43 12.25 12.18 11.64 8.15
12.55 12.63 12.79 12.80 12.85 12.84 12.74 12.56 12.49 11.90 8.26
12.85 12.92 13.11 13.10 13.15 13.13 13.01 12.81 12.72 12.21 8.40
13.29 13.35 13.54 13.54 13.58 13.56 13.46 13.24 13.16 12.61 8.56
13.52 13.60 13.82 13.81 13.86 13.83 13.70 13.50 13.39 12.89 8.65
13.20 13.31 13.54 13.55 13.60 13.65 13.53 13.30 13.23 12.84 8.51
12.33 12.47 12.71 12.77 12.84 12.86 12.79 12.59 12.54 12.16 7.71
9.04 9.18 9.37 9.47 9.56 9.62 9.70 9.69 9.71 9.34 5.23
×10⁻³
−0.25 −0.20 −0.15 −0.10 −0.05 −0.00
upper threshold - d0^π+·d0^D̄0 (cm²)
cos(θ_pointing)≥0.9996, L_decay^D̄0 ≥500 μm, p_T^π+ ≥1.1 GeV/c, p_T^D̄0 ≥2.0 GeV/c
FT2
Pb-Pb, √s_NN = 5.5 TeV
Centrality 0-10 %

(d)

(e)

(f)

(g)

(h)

(i)

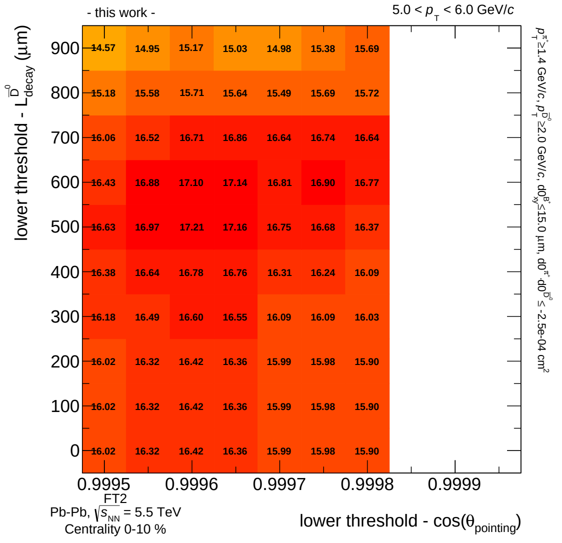
- this work -
5.0 < p_T < 6.0 GeV/c
lower threshold - $L^{D^0}_{decay}$ (μm)
900: 14.57 14.95 15.17 15.03 14.98 15.38 15.69
800: 15.18 15.58 15.71 15.64 15.49 15.69 15.72
700: 16.06 16.52 16.71 16.86 16.64 16.74 16.64
600: 16.43 16.88 17.10 17.14 16.81 16.90 16.77
500: 16.63 16.97 17.21 17.16 16.75 16.68 16.37
400: 16.38 16.64 16.78 16.76 16.31 16.24 16.09
300: 16.18 16.49 16.60 16.55 16.09 16.09 16.03
200: 16.02 16.32 16.42 16.36 15.99 15.98 15.90
100: 16.02 16.32 16.42 16.36 15.99 15.98 15.90
0: 16.02 16.32 16.42 16.36 15.99 15.98 15.90
0.9995 0.9996 0.9997 0.9998 0.9999
lower threshold - cos($\theta_{pointing}$)
$p_T^{\pi^+}$≥1.4 GeV/c, $p_T^{\bar{D}^0}$≥2.0 GeV/c, $d0^{B^+}_{xy}$≤15.0 μm, $d0^{\pi^+}\cdot d0^{\bar{D}^0}$ ≤ -2.5e-04 cm^2
FT2
Pb-Pb, $\sqrt{s_{NN}}$ = 5.5 TeV
Centrality 0-10 %

(j)

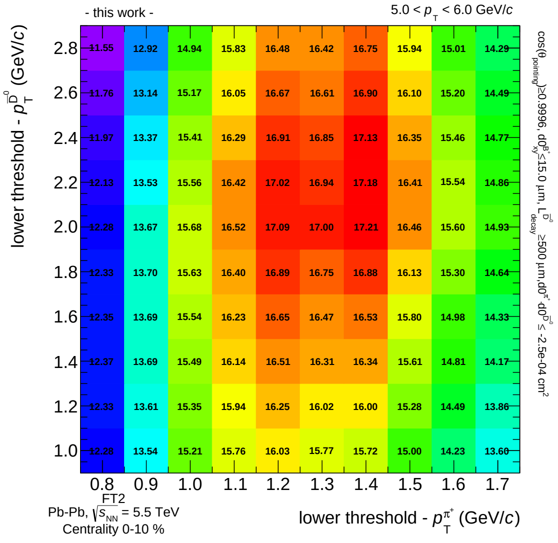
- this work -
5.0 < p_T < 6.0 GeV/c
lower threshold - $p_T^{\bar{D}^0}$ (GeV/c)
2.8: 11.55 12.92 14.94 15.83 16.48 16.42 16.75 15.94 15.01 14.29
2.6: 11.76 13.14 15.17 16.05 16.67 16.61 16.90 16.10 15.20 14.49
2.4: 11.97 13.37 15.41 16.29 16.91 16.85 17.13 16.35 15.46 14.77
2.2: 12.13 13.53 15.56 16.42 17.02 16.94 17.18 16.41 15.54 14.86
2.0: 12.23 13.67 15.68 16.52 17.09 17.00 17.21 16.46 15.60 14.93
1.8: 12.33 13.70 15.63 16.40 16.89 16.75 16.88 16.13 15.30 14.64
1.6: 12.35 13.69 15.54 16.23 16.65 16.47 16.53 15.80 14.98 14.33
1.4: 12.37 13.69 15.49 16.14 16.51 16.31 16.34 15.61 14.81 14.17
1.2: 12.33 13.61 15.35 15.94 16.25 16.02 16.00 15.28 14.49 13.86
1.0: 12.28 13.54 15.21 15.76 16.03 15.77 15.72 15.00 14.23 13.60
0.8 0.9 1.0 1.1 1.2 1.3 1.4 1.5 1.6 1.7
lower threshold - $p_T^{\pi^+}$ (GeV/c)
cos($\theta_{pointing}$)≥0.9996, $d0^{B^+}_{xy}$≤15.0 μm, $L^{D^0}_{decay}$ ≥500 μm, $d0^{\pi^+}\cdot d0^{\bar{D}^0}$ ≤ -2.5e-04 cm^2
FT2
Pb-Pb, $\sqrt{s_{NN}}$ = 5.5 TeV
Centrality 0-10 %

(k)

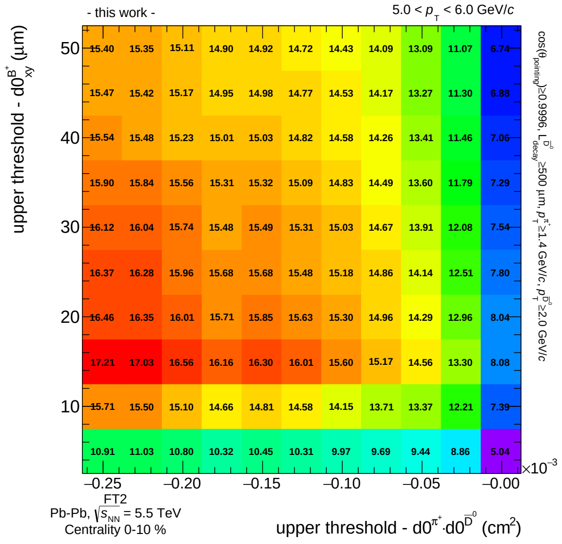
- this work -
5.0 < p_T < 6.0 GeV/c
upper threshold - $d0^{B^+}_{xy}$ (μm)
50 40 30 20 10
15.40 15.35 15.11 14.90 14.92 14.72 14.43 14.09 13.09 11.07 6.74
15.47 15.42 15.17 14.95 14.98 14.77 14.53 14.17 13.27 11.30 6.88
15.54 15.48 15.23 15.01 15.03 14.82 14.58 14.26 13.41 11.46 7.06
15.90 15.84 15.56 15.31 15.32 15.09 14.83 14.49 13.60 11.79 7.29
16.12 16.04 15.74 15.48 15.49 15.31 15.03 14.67 13.91 12.08 7.54
16.37 16.28 15.96 15.68 15.68 15.48 15.18 14.86 14.14 12.51 7.80
16.46 16.35 16.01 15.71 15.85 15.63 15.30 14.96 14.29 12.96 8.04
17.21 17.03 16.56 16.16 16.30 16.01 15.60 15.17 14.56 13.30 8.08
15.71 15.50 15.10 14.66 14.81 14.58 14.15 13.71 13.37 12.21 7.39
10.91 11.03 10.80 10.32 10.45 10.31 9.97 9.69 9.44 8.86 5.04
−0.25 −0.20 −0.15 −0.10 −0.05 −0.00 ×10^{-3}
upper threshold - $d0^{\pi^+}\cdot d0^{\bar{D}^0}$ (cm^2)
cos($\theta_{pointing}$)≥0.9996, $L^{D^0}_{decay}$ ≥500 μm, $p_T^{\pi^+}$≥1.4 GeV/c, $p_T^{\bar{D}^0}$≥2.0 GeV/c
FT2
Pb-Pb, $\sqrt{s_{NN}}$ = 5.5 TeV
Centrality 0-10 %

(l)

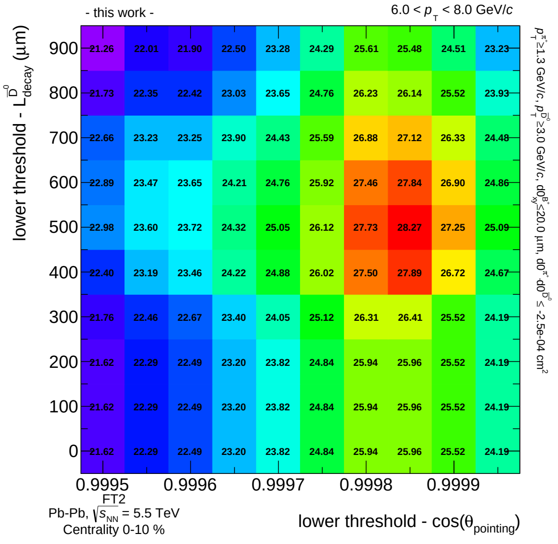
- this work -
6.0 < p_T < 8.0 GeV/c
lower threshold - $L^{D^0}_{decay}$ (μm)
900: 21.26 22.01 21.90 22.50 23.28 24.29 25.61 25.48 24.51 23.23
800: 21.73 22.35 22.42 23.03 23.65 24.76 26.23 26.14 25.52 23.93
700: 22.66 23.23 23.25 23.90 24.43 25.59 26.88 27.12 26.33 24.48
600: 22.89 23.47 23.65 24.21 24.76 25.92 27.46 27.84 26.90 24.86
500: 22.98 23.60 23.72 24.32 25.05 26.12 27.73 28.27 27.25 25.09
400: 22.40 23.19 23.46 24.22 24.88 26.02 27.50 27.89 26.72 24.67
300: 21.76 22.46 22.67 23.40 24.05 25.12 26.31 26.41 25.52 24.19
200: 21.62 22.29 22.49 23.20 23.82 24.84 25.94 25.96 25.52 24.19
100: 21.62 22.29 22.49 23.20 23.82 24.84 25.94 25.96 25.52 24.19
0: 21.62 22.29 22.49 23.20 23.82 24.84 25.94 25.96 25.52 24.19
0.9995 0.9996 0.9997 0.9998 0.9999
lower threshold - cos($\theta_{pointing}$)
$p_T^{\pi^+}$≥1.3 GeV/c, $p_T^{\bar{D}^0}$≥3.0 GeV/c, $d0^{B^+}_{xy}$≤20.0 μm, $d0^{\pi^+}\cdot d0^{\bar{D}^0}$ ≤ -2.5e-04 cm^2
FT2
Pb-Pb, $\sqrt{s_{NN}}$ = 5.5 TeV
Centrality 0-10 %

(m)

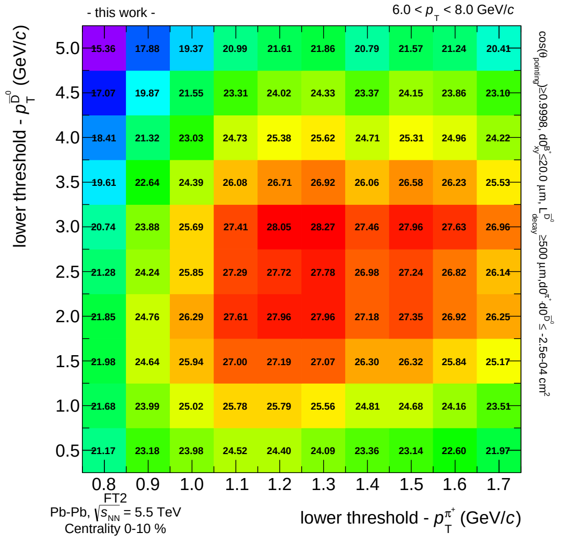
- this work -
6.0 < p_T < 8.0 GeV/c
lower threshold - $p_T^{\bar{D}^0}$ (GeV/c)
5.0: 15.36 17.88 19.37 20.99 21.61 21.86 20.79 21.57 21.24 20.41
4.5: 17.07 19.87 21.55 23.31 24.02 24.33 23.37 24.15 23.86 23.10
4.0: 18.41 21.32 23.03 24.73 25.38 25.62 24.71 25.31 24.96 24.22
3.5: 19.61 22.64 24.39 26.08 26.71 26.92 26.06 26.58 26.23 25.53
3.0: 20.74 23.88 25.69 27.41 28.05 28.27 27.46 27.96 27.63 26.96
2.5: 21.28 24.24 25.85 27.29 27.72 27.78 26.98 27.24 26.82 26.14
2.0: 21.85 24.76 26.29 27.61 27.96 27.96 27.18 27.35 26.92 26.25
1.5: 21.98 24.64 25.94 27.00 27.19 27.07 26.30 26.32 25.84 25.17
1.0: 21.68 23.99 25.02 25.78 25.79 25.56 24.81 24.68 24.16 23.51
0.5: 21.17 23.18 23.98 24.52 24.40 24.09 23.36 23.14 22.60 21.97
0.8 0.9 1.0 1.1 1.2 1.3 1.4 1.5 1.6 1.7
lower threshold - $p_T^{\pi^+}$ (GeV/c)
cos($\theta_{pointing}$)≥0.9998, $d0^{B^+}_{xy}$≤20.0 μm, $L^{D^0}_{decay}$ ≥500 μm, $d0^{\pi^+}\cdot d0^{\bar{D}^0}$ ≤ -2.5e-04 cm^2
FT2
Pb-Pb, $\sqrt{s_{NN}}$ = 5.5 TeV
Centrality 0-10 %

(n)

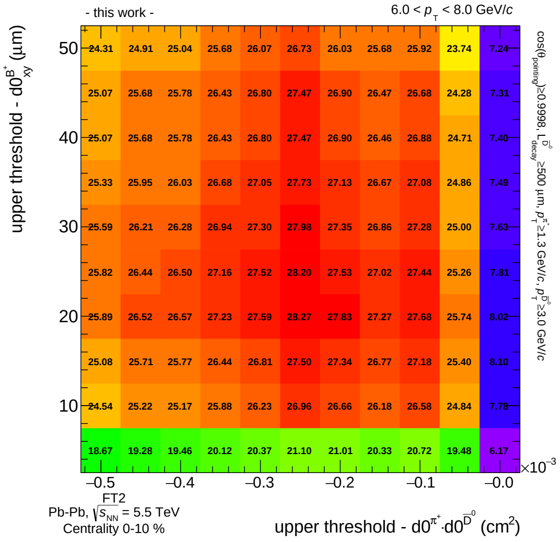
- this work -
6.0 < p_T < 8.0 GeV/c
upper threshold - $d0^{B^+}_{xy}$ (μm)
50 40 30 20 10
24.31 24.91 25.04 25.68 26.07 26.73 26.03 25.68 25.92 23.74 7.24
25.07 25.68 25.78 26.43 26.80 27.47 26.90 26.47 26.68 24.28 7.31
25.07 25.68 25.78 26.43 26.80 27.47 26.90 26.46 26.88 24.71 7.40
25.33 25.95 26.03 26.68 27.05 27.73 27.13 26.67 27.08 24.86 7.49
25.59 26.21 26.28 26.94 27.30 27.88 27.35 26.86 27.28 25.00 7.63
25.82 26.44 26.50 27.16 27.52 28.20 27.53 27.02 27.44 25.26 7.81
25.89 26.52 26.57 27.23 27.59 28.27 27.83 27.27 27.68 25.74 8.02
25.08 25.71 25.77 26.44 26.81 27.50 27.34 26.77 27.18 25.40 8.10
24.54 25.22 25.17 25.88 26.23 26.96 26.66 26.18 26.58 24.84 7.78
18.67 19.28 19.46 20.12 20.37 21.10 21.01 20.33 20.72 19.48 6.17
−0.5 −0.4 −0.3 −0.2 −0.1 −0.0 ×10^{-3}
upper threshold - $d0^{\pi^+}\cdot d0^{\bar{D}^0}$ (cm^2)
cos($\theta_{pointing}$)≥0.9998, $L^{D^0}_{decay}$ ≥500 μm, $p_T^{\pi^+}$≥1.3 GeV/c, $p_T^{\bar{D}^0}$≥3.0 GeV/c
FT2
Pb-Pb, $\sqrt{s_{NN}}$ = 5.5 TeV
Centrality 0-10 %

(o)

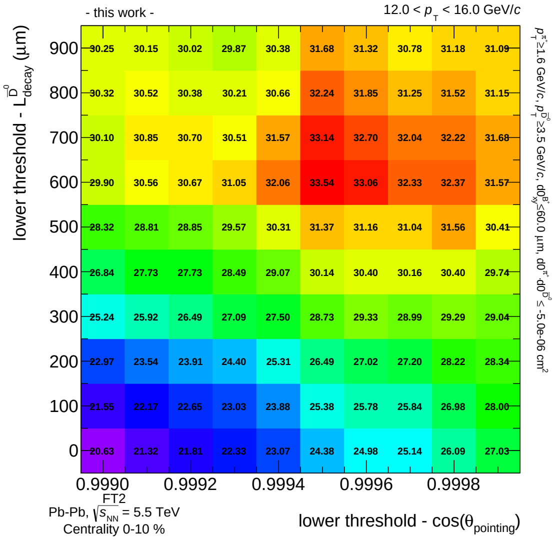
- this work -
12.0 < p_T < 16.0 GeV/c
lower threshold - $L_{decay}^{\overline{D}^0}$ (μm)
900: 30.25 30.15 30.02 29.87 30.38 31.68 31.32 30.78 31.18 31.09
800: 30.32 30.52 30.38 30.21 30.66 32.24 31.85 31.25 31.52 31.15
700: 30.10 30.85 30.70 30.51 31.57 33.14 32.70 32.04 32.22 31.68
600: 29.90 30.56 30.67 31.05 32.06 33.54 33.06 32.33 32.37 31.57
500: 28.32 28.81 28.85 29.57 30.31 31.37 31.16 31.04 31.56 30.41
400: 26.84 27.73 27.73 28.49 29.07 30.14 30.40 30.16 30.40 29.74
300: 25.24 25.92 26.49 27.09 27.50 28.73 29.33 28.99 29.29 29.04
200: 22.97 23.54 23.91 24.40 25.31 26.49 27.02 27.20 28.22 28.34
100: 21.55 22.17 22.65 23.03 23.88 25.38 25.78 25.84 26.98 28.00
0: 20.63 21.32 21.81 22.33 23.07 24.38 24.98 25.14 26.09 27.03
0.9990 0.9992 0.9994 0.9996 0.9998
FT2
Pb-Pb, $\sqrt{s_{NN}}$ = 5.5 TeV
Centrality 0-10 %
lower threshold - cos($\theta_{pointing}$)
$p_T^{\pi^+}$≥1.6 GeV/c, $p_T^{\overline{D}^0}$≥3.5 GeV/c, $d0_{xy}^{B^+}$≤60.0 μm, $d0^{\pi^+}$·$d0^{\overline{D}^0}$ ≤ -5.0e-06 cm²

(p)

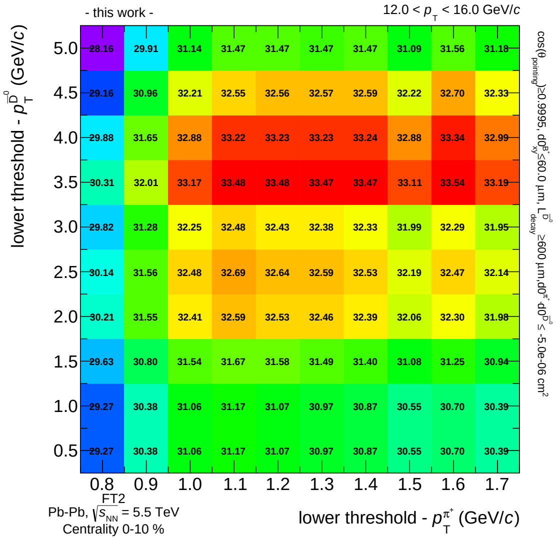
- this work -
12.0 < p_T < 16.0 GeV/c
lower threshold - $p_T^{\overline{D}^0}$ (GeV/c)
5.0: 28.16 29.91 31.14 31.47 31.47 31.47 31.47 31.09 31.56 31.18
4.5: 29.16 30.96 32.21 32.55 32.56 32.57 32.59 32.22 32.70 32.33
4.0: 29.88 31.65 32.88 33.22 33.23 33.23 33.24 32.88 33.34 32.99
3.5: 30.31 32.01 33.17 33.48 33.48 33.47 33.47 33.11 33.54 33.19
3.0: 29.82 31.28 32.25 32.48 32.43 32.38 32.33 31.99 32.29 31.95
2.5: 30.14 31.56 32.48 32.69 32.64 32.59 32.53 32.19 32.47 32.14
2.0: 30.21 31.55 32.41 32.59 32.53 32.46 32.39 32.06 32.30 31.98
1.5: 29.63 30.80 31.54 31.67 31.58 31.49 31.40 31.08 31.25 30.94
1.0: 29.27 30.38 31.06 31.17 31.07 30.97 30.87 30.55 30.70 30.39
0.5: 29.27 30.38 31.06 31.17 31.07 30.97 30.87 30.55 30.70 30.39
0.8 0.9 1.0 1.1 1.2 1.3 1.4 1.5 1.6 1.7
FT2
Pb-Pb, $\sqrt{s_{NN}}$ = 5.5 TeV
Centrality 0-10 %
lower threshold - $p_T^{\pi^+}$ (GeV/c)
cos($\theta_{pointing}$)≥0.9995, $d0_{xy}^{B^+}$≤60.0 μm, $L_{decay}^{\overline{D}^0}$ ≥600 μm,$d0^{\pi^+}$·$d0^{\overline{D}^0}$ ≤ -5.0e-06 cm²

(q)

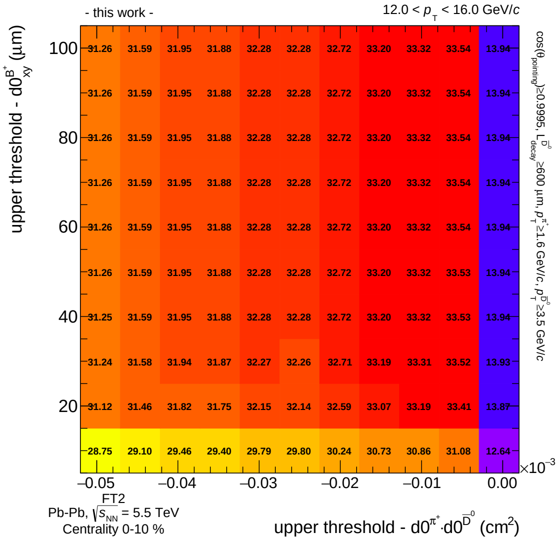
- this work -
12.0 < p_T < 16.0 GeV/c
upper threshold - $d0_{xy}^{B^+}$ (μm)
100: 31.26 31.59 31.95 31.88 32.28 32.28 32.72 33.20 33.32 33.54 13.94
31.26 31.59 31.95 31.88 32.28 32.28 32.72 33.20 33.32 33.54 13.94
80: 31.26 31.59 31.95 31.88 32.28 32.28 32.72 33.20 33.32 33.54 13.94
31.26 31.59 31.95 31.88 32.28 32.28 32.72 33.20 33.32 33.54 13.94
60: 31.26 31.59 31.95 31.88 32.28 32.28 32.72 33.20 33.32 33.54 13.94
31.26 31.59 31.95 31.88 32.28 32.28 32.72 33.20 33.32 33.53 13.94
40: 31.25 31.59 31.95 31.88 32.28 32.28 32.72 33.20 33.32 33.53 13.94
31.24 31.58 31.94 31.87 32.27 32.26 32.71 33.19 33.31 33.52 13.93
20: 31.12 31.46 31.82 31.75 32.15 32.14 32.59 33.07 33.19 33.41 13.87
28.75 29.10 29.46 29.40 29.79 29.80 30.24 30.73 30.86 31.08 12.64
×10⁻³
–0.05 –0.04 –0.03 –0.02 –0.01 0.00
FT2
Pb-Pb, $\sqrt{s_{NN}}$ = 5.5 TeV
Centrality 0-10 %
upper threshold - $d0^{\pi^+}$·$d0^{\overline{D}^0}$ (cm²)
cos($\theta_{pointing}$)≥0.9995, $L_{decay}^{\overline{D}^0}$ ≥600 μm, $p_T^{\pi^+}$≥1.6 GeV/c, $p_T^{\overline{D}^0}$≥3.5 GeV/c

(r)

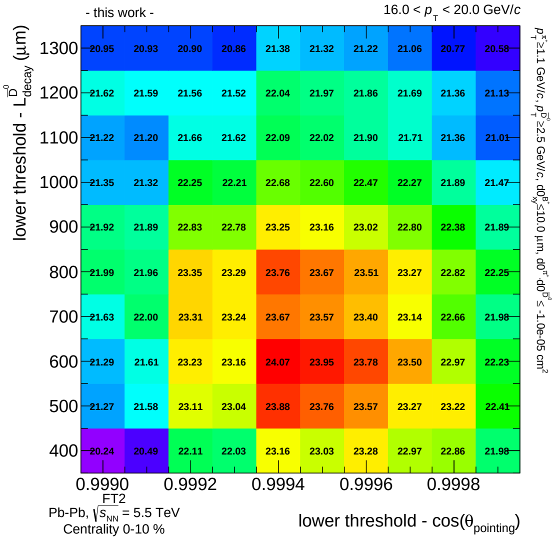
- this work -
16.0 < p_T < 20.0 GeV/c
lower threshold - $L_{decay}^{\overline{D}^0}$ (μm)
1300: 20.95 20.93 20.90 20.86 21.38 21.32 21.22 21.06 20.77 20.58
1200: 21.62 21.59 21.56 21.52 22.04 21.97 21.86 21.69 21.36 21.13
1100: 21.22 21.20 21.66 21.62 22.09 22.02 21.90 21.71 21.36 21.01
1000: 21.35 21.32 22.25 22.21 22.68 22.60 22.47 22.27 21.89 21.47
900: 21.92 21.89 22.83 22.78 23.25 23.16 23.02 22.80 22.38 21.89
800: 21.99 21.96 23.35 23.29 23.76 23.67 23.51 23.27 22.82 22.25
700: 21.63 22.00 23.31 23.24 23.67 23.57 23.40 23.14 22.66 21.98
600: 21.29 21.61 23.23 23.16 24.07 23.95 23.78 23.50 22.97 22.23
500: 21.27 21.58 23.11 23.04 23.88 23.76 23.57 23.27 23.22 22.41
400: 20.24 20.49 22.11 22.03 23.16 23.03 23.28 22.97 22.86 21.98
0.9990 0.9992 0.9994 0.9996 0.9998
FT2
Pb-Pb, $\sqrt{s_{NN}}$ = 5.5 TeV
Centrality 0-10 %
lower threshold - cos($\theta_{pointing}$)
$p_T^{\pi^+}$≥1.1 GeV/c, $p_T^{\overline{D}^0}$≥2.5 GeV/c, $d0_{xy}^{B^+}$≤10.0 μm, $d0^{\pi^+}$·$d0^{\overline{D}^0}$ ≤ -1.0e-05 cm²

(s)

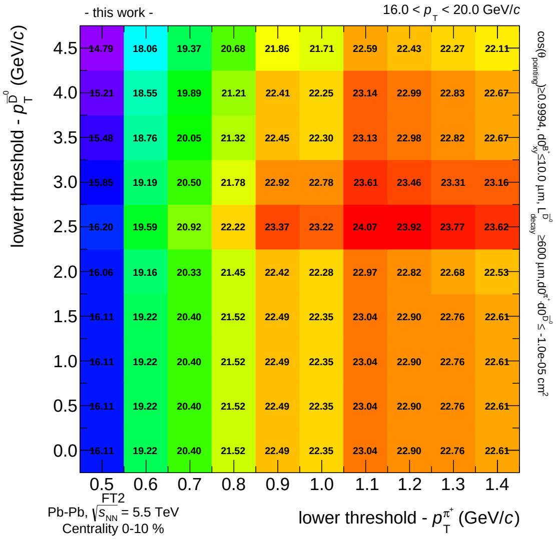
- this work -
16.0 < p_T < 20.0 GeV/c
lower threshold - $p_T^{\overline{D}^0}$ (GeV/c)
4.5: 14.79 18.06 19.37 20.68 21.86 21.71 22.59 22.43 22.27 22.11
4.0: 15.21 18.55 19.89 21.21 22.41 22.25 23.14 22.99 22.83 22.67
3.5: 15.48 18.76 20.05 21.32 22.45 22.30 23.13 22.98 22.82 22.67
3.0: 15.85 19.19 20.50 21.78 22.92 22.78 23.61 23.46 23.31 23.16
2.5: 16.20 19.59 20.92 22.22 23.37 23.22 24.07 23.92 23.77 23.62
2.0: 16.06 19.16 20.33 21.45 22.42 22.28 22.97 22.82 22.68 22.53
1.5: 16.11 19.22 20.40 21.52 22.49 22.35 23.04 22.90 22.76 22.61
1.0: 16.11 19.22 20.40 21.52 22.49 22.35 23.04 22.90 22.76 22.61
0.5: 16.11 19.22 20.40 21.52 22.49 22.35 23.04 22.90 22.76 22.61
0.0: 16.11 19.22 20.40 21.52 22.49 22.35 23.04 22.90 22.76 22.61
0.5 0.6 0.7 0.8 0.9 1.0 1.1 1.2 1.3 1.4
FT2
Pb-Pb, $\sqrt{s_{NN}}$ = 5.5 TeV
Centrality 0-10 %
lower threshold - $p_T^{\pi^+}$ (GeV/c)
cos($\theta_{pointing}$)≥0.9994, $d0_{xy}^{B^+}$≤10.0 μm, $L_{decay}^{\overline{D}^0}$ ≥600 μm,$d0^{\pi^+}$·$d0^{\overline{D}^0}$ ≤ -1.0e-05 cm²

(t)

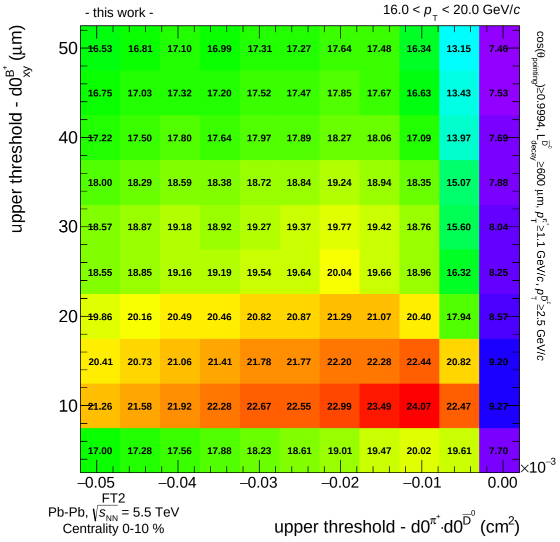
- this work -
16.0 < p_T < 20.0 GeV/c
upper threshold - $d0_{xy}^{B^+}$ (μm)
50: 16.53 16.81 17.10 16.99 17.31 17.27 17.64 17.48 16.34 13.15 7.46
16.75 17.03 17.32 17.20 17.52 17.47 17.85 17.67 16.63 13.43 7.53
40: 17.22 17.50 17.80 17.64 17.97 17.89 18.27 18.06 17.09 13.97 7.69
18.00 18.29 18.59 18.38 18.72 18.84 19.24 18.94 18.35 15.07 7.88
30: 18.57 18.87 19.18 18.92 19.27 19.37 19.77 19.42 18.76 15.60 8.04
18.55 18.85 19.16 19.19 19.54 19.64 20.04 19.66 18.96 16.32 8.25
20: 19.86 20.16 20.49 20.46 20.82 20.87 21.29 21.07 20.40 17.94 8.57
20.41 20.73 21.06 21.41 21.78 21.77 22.20 22.28 22.44 20.82 9.20
10: 21.26 21.58 21.92 22.28 22.67 22.55 22.99 23.49 24.07 22.47 9.27
17.00 17.28 17.56 17.88 18.23 18.61 19.01 19.47 20.02 19.61 7.70
×10⁻³
–0.05 –0.04 –0.03 –0.02 –0.01 0.00
FT2
Pb-Pb, $\sqrt{s_{NN}}$ = 5.5 TeV
Centrality 0-10 %
upper threshold - $d0^{\pi^+}$·$d0^{\overline{D}^0}$ (cm²)
cos($\theta_{pointing}$)≥0.9994, $L_{decay}^{\overline{D}^0}$ ≥600 μm, $p_T^{\pi^+}$≥1.1 GeV/c, $p_T^{\overline{D}^0}$≥2.5 GeV/c

(u)

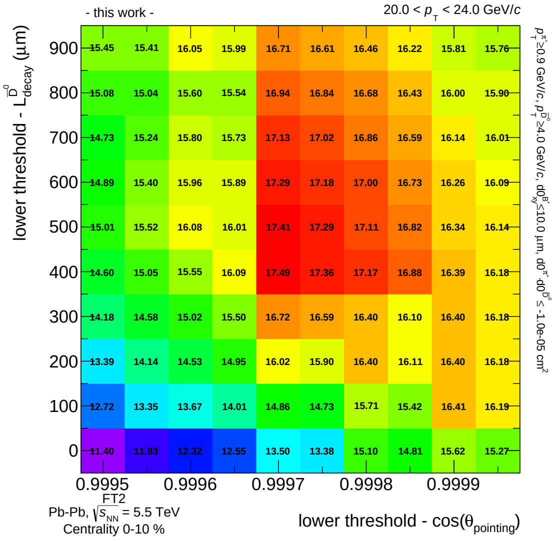

900	15.45	15.41	16.05	15.99	16.71	16.61	16.46	16.22	15.81	15.76
800	15.08	15.04	15.60	15.54	16.94	16.84	16.68	16.43	16.00	15.90
700	14.73	15.24	15.80	15.73	17.13	17.02	16.86	16.59	16.14	16.01
600	14.89	15.40	15.96	15.89	17.29	17.18	17.00	16.73	16.26	16.09
500	15.01	15.52	16.08	16.01	17.41	17.29	17.11	16.82	16.34	16.14
400	14.60	15.05	15.55	16.09	17.49	17.36	17.17	16.88	16.39	16.18
300	14.18	14.58	15.02	15.50	16.72	16.59	16.40	16.10	16.40	16.18
200	13.39	14.14	14.53	14.95	16.02	15.90	16.40	16.11	16.40	16.18
100	12.72	13.35	13.67	14.01	14.86	14.73	15.71	15.42	16.41	16.19
0	11.40	11.83	12.32	12.55	13.50	13.38	15.10	14.81	15.62	15.27

(v)

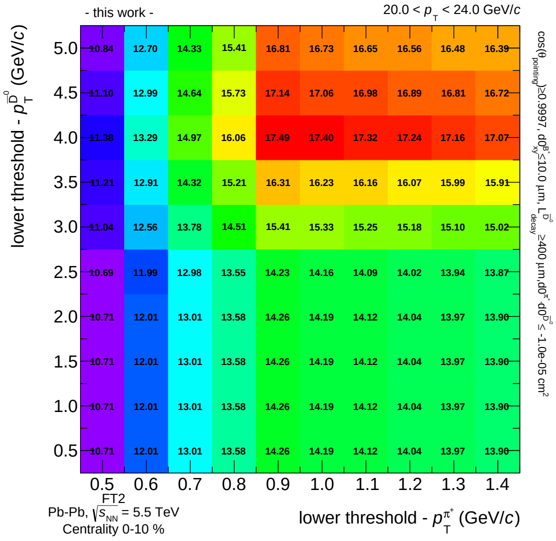

5.0	10.84	12.70	14.33	15.41	16.81	16.73	16.65	16.56	16.48	16.39
4.5	11.10	12.99	14.64	15.73	17.14	17.06	16.98	16.89	16.81	16.72
4.0	11.38	13.29	14.97	16.06	17.49	17.40	17.32	17.24	17.16	17.07
3.5	11.21	12.91	14.32	15.21	16.31	16.23	16.16	16.07	15.99	15.91
3.0	11.04	12.56	13.78	14.51	15.41	15.33	15.25	15.18	15.10	15.02
2.5	10.69	11.99	12.98	13.55	14.23	14.16	14.09	14.02	13.94	13.87
2.0	10.71	12.01	13.01	13.58	14.26	14.19	14.12	14.04	13.97	13.90
1.5	10.71	12.01	13.01	13.58	14.26	14.19	14.12	14.04	13.97	13.90
1.0	10.71	12.01	13.01	13.58	14.26	14.19	14.12	14.04	13.97	13.90
0.5	10.71	12.01	13.01	13.58	14.26	14.19	14.12	14.04	13.97	13.90

(w)

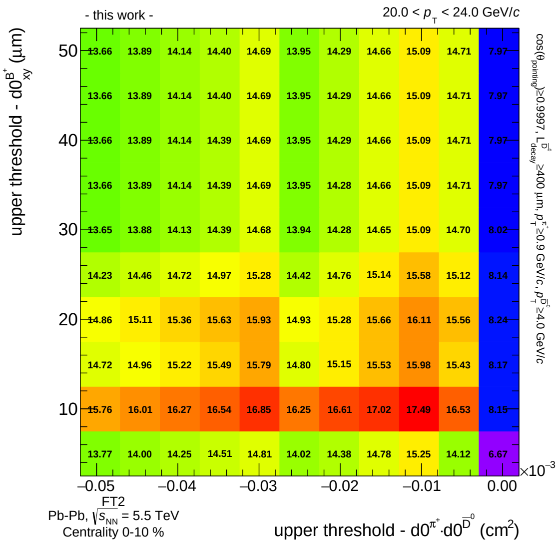

50	13.66	13.89	14.14	14.40	14.69	13.95	14.29	14.66	15.09	14.71	7.97
	13.66	13.89	14.14	14.40	14.69	13.95	14.29	14.66	15.09	14.71	7.97
40	13.66	13.89	14.14	14.39	14.69	13.95	14.29	14.66	15.09	14.71	7.97
	13.66	13.89	14.14	14.39	14.69	13.95	14.28	14.66	15.09	14.71	7.97
30	13.65	13.88	14.13	14.39	14.68	13.94	14.28	14.65	15.09	14.70	8.02
	14.23	14.46	14.72	14.97	15.28	14.42	14.76	15.14	15.58	15.12	8.14
20	14.86	15.11	15.36	15.63	15.93	14.93	15.28	15.66	16.11	15.56	8.24
	14.72	14.96	15.22	15.49	15.79	14.80	15.15	15.53	15.98	15.43	8.17
10	15.76	16.01	16.27	16.54	16.85	16.25	16.61	17.02	17.49	16.53	8.15
	13.77	14.00	14.25	14.51	14.81	14.02	14.38	14.78	15.25	14.12	6.67

(x)

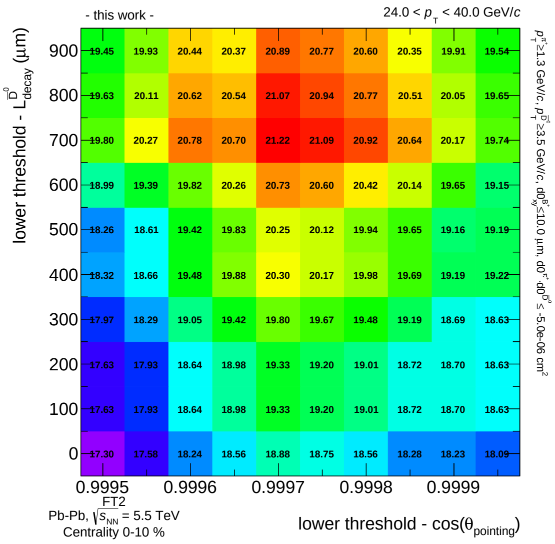

900	19.45	19.93	20.44	20.37	20.89	20.77	20.60	20.35	19.91	19.54
800	19.63	20.11	20.62	20.54	21.07	20.94	20.77	20.51	20.05	19.65
700	19.80	20.27	20.78	20.70	21.22	21.09	20.92	20.64	20.17	19.74
600	18.99	19.39	19.82	20.26	20.73	20.60	20.42	20.14	19.65	19.15
500	18.26	18.61	19.42	19.83	20.25	20.12	19.94	19.65	19.16	19.19
400	18.32	18.66	19.48	19.88	20.30	20.17	19.98	19.69	19.19	19.22
300	17.97	18.29	19.05	19.42	19.80	19.67	19.48	19.19	18.69	18.63
200	17.63	17.93	18.64	18.98	19.33	19.20	19.01	18.72	18.70	18.63
100	17.63	17.93	18.64	18.98	19.33	19.20	19.01	18.72	18.70	18.63
0	17.30	17.58	18.24	18.56	18.88	18.75	18.56	18.28	18.23	18.09

(y)

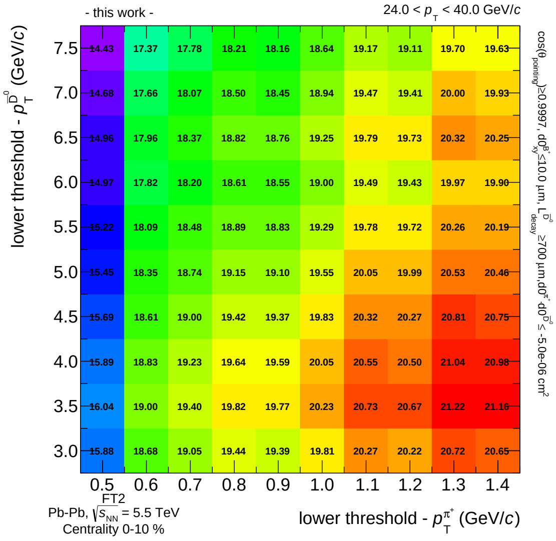

7.5	14.43	17.37	17.78	18.21	18.16	18.64	19.17	19.11	19.70	19.63
7.0	14.68	17.66	18.07	18.50	18.45	18.94	19.47	19.41	20.00	19.93
6.5	14.96	17.96	18.37	18.82	18.76	19.25	19.79	19.73	20.32	20.25
6.0	14.97	17.82	18.20	18.61	18.55	19.00	19.49	19.43	19.97	19.90
5.5	15.22	18.09	18.48	18.89	18.83	19.29	19.78	19.72	20.26	20.19
5.0	15.45	18.35	18.74	19.15	19.10	19.55	20.05	19.99	20.53	20.46
4.5	15.69	18.61	19.00	19.42	19.37	19.83	20.32	20.27	20.81	20.75
4.0	15.89	18.83	19.23	19.64	19.59	20.05	20.55	20.50	21.04	20.98
3.5	16.04	19.00	19.40	19.82	19.77	20.23	20.73	20.67	21.22	21.16
3.0	15.88	18.68	19.05	19.44	19.39	19.81	20.27	20.22	20.72	20.65

(z)

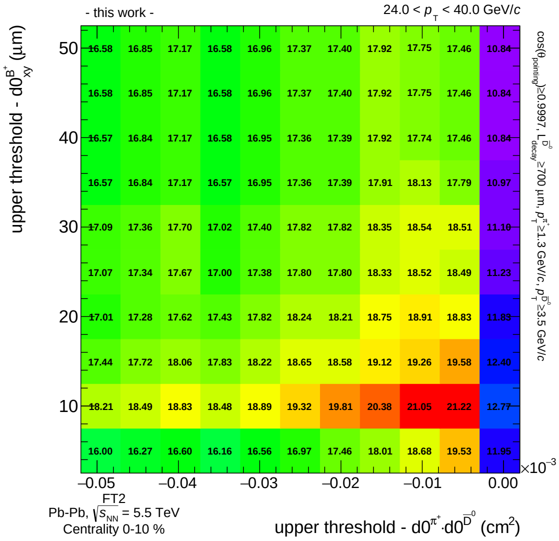

50	16.58	16.85	17.17	16.58	16.96	17.37	17.40	17.92	17.75	17.46	10.84
	16.58	16.85	17.17	16.58	16.96	17.37	17.40	17.92	17.75	17.46	10.84
40	16.57	16.84	17.17	16.58	16.95	17.36	17.39	17.92	17.74	17.46	10.84
	16.57	16.84	17.17	16.57	16.95	17.36	17.39	17.91	18.13	17.79	10.97
30	17.09	17.36	17.70	17.02	17.40	17.82	17.82	18.35	18.54	18.51	11.10
	17.07	17.34	17.67	17.00	17.38	17.80	17.80	18.33	18.52	18.49	11.23
20	17.01	17.28	17.62	17.43	17.82	18.24	18.21	18.75	18.91	18.83	11.83
	17.44	17.72	18.06	17.83	18.22	18.65	18.58	19.12	19.26	19.58	12.40
10	18.21	18.49	18.83	18.48	18.89	19.32	19.81	20.38	21.05	21.22	12.77
	16.00	16.27	16.60	16.16	16.56	16.97	17.46	18.01	18.68	19.53	11.95

(a)

G. Invariant mass spectra of fully reconstructed B^+ mesons

In this section, the sampled invariant mass spectra in the remaining kinematic bins are presented. These were obtained by generating the expected signal and background yields within templates obtained from the full kinematic reconstruction, as explained in section 5.4.3.

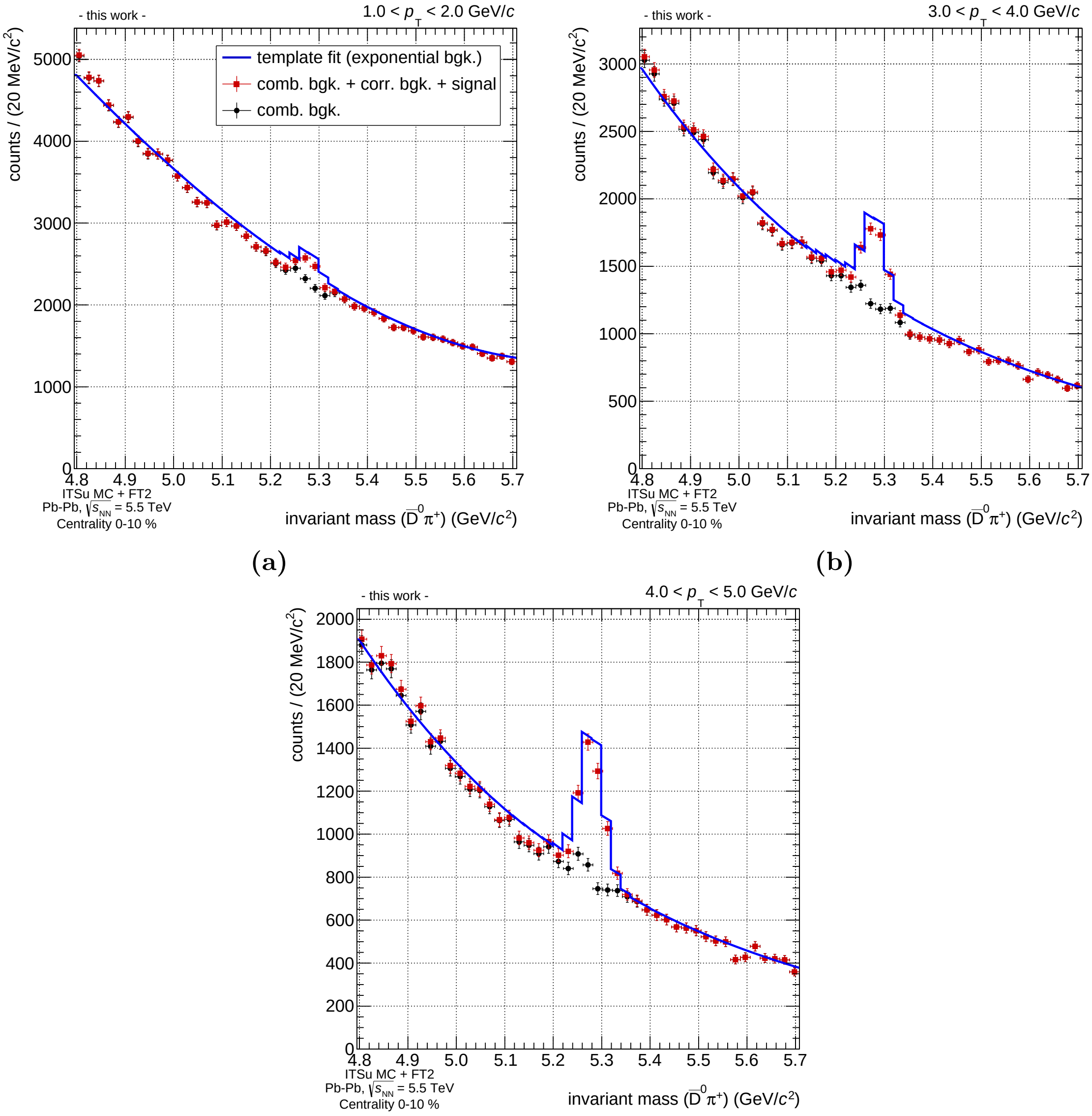

(a) **(b)**

(c)

Figure G.1.: Invariant mass spectra sampled to the expected statistics from signal, correlated and combinatorial background sources.

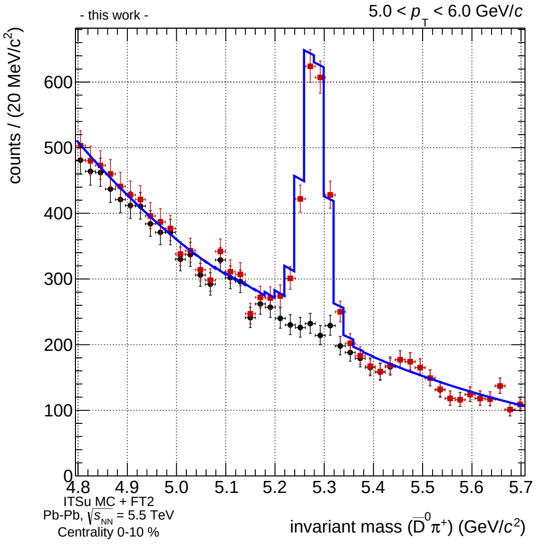
- this work -
5.0 < p_T < 6.0 GeV/c
counts / (20 MeV/c²)
0
100
200
300
400
500
600
4.8
4.9
5.0
5.1
5.2
5.3
5.4
5.5
5.6
5.7
ITSu MC + FT2
Pb-Pb, √s_NN = 5.5 TeV
Centrality 0-10 %
invariant mass (D̄⁰π⁺) (GeV/c²)

(d)

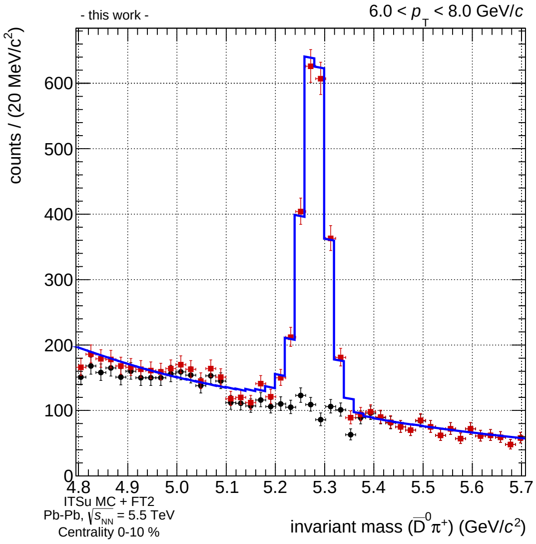
- this work -
6.0 < p_T < 8.0 GeV/c
counts / (20 MeV/c²)
0
100
200
300
400
500
600
4.8
4.9
5.0
5.1
5.2
5.3
5.4
5.5
5.6
5.7
ITSu MC + FT2
Pb-Pb, √s_NN = 5.5 TeV
Centrality 0-10 %
invariant mass (D̄⁰π⁺) (GeV/c²)

(e)

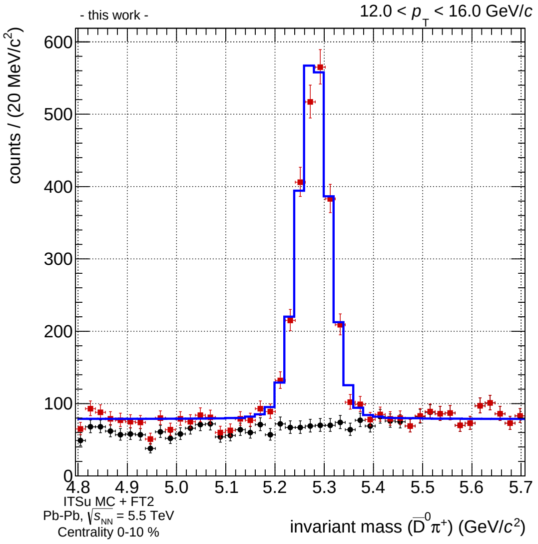
- this work -
12.0 < p_T < 16.0 GeV/c
counts / (20 MeV/c²)
0
100
200
300
400
500
600
4.8
4.9
5.0
5.1
5.2
5.3
5.4
5.5
5.6
5.7
ITSu MC + FT2
Pb-Pb, √s_NN = 5.5 TeV
Centrality 0-10 %
invariant mass (D̄⁰π⁺) (GeV/c²)

(f)

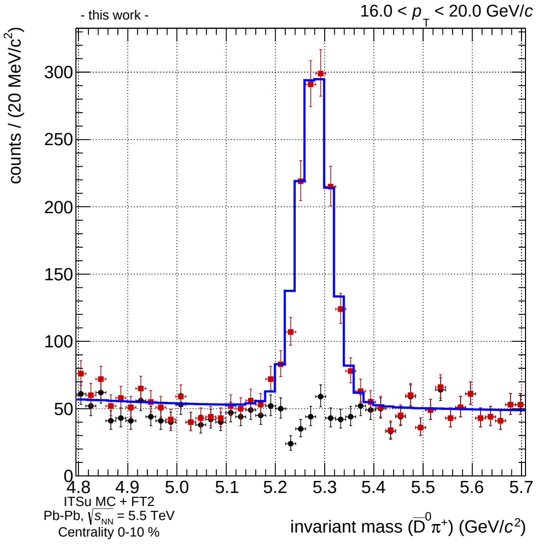
- this work -
16.0 < p_T < 20.0 GeV/c
counts / (20 MeV/c²)
0
50
100
150
200
250
300
4.8
4.9
5.0
5.1
5.2
5.3
5.4
5.5
5.6
5.7
ITSu MC + FT2
Pb-Pb, √s_NN = 5.5 TeV
Centrality 0-10 %
invariant mass (D̄⁰π⁺) (GeV/c²)

(g)

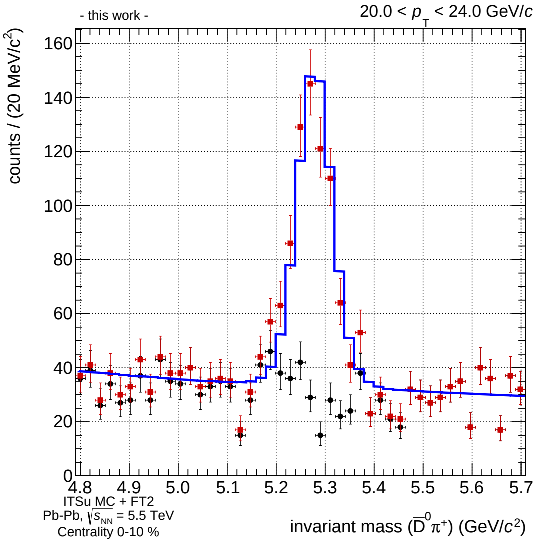
- this work -
20.0 < p_T < 24.0 GeV/c
counts / (20 MeV/c²)
0
20
40
60
80
100
120
140
160
4.8
4.9
5.0
5.1
5.2
5.3
5.4
5.5
5.6
5.7
ITSu MC + FT2
Pb-Pb, √s_NN = 5.5 TeV
Centrality 0-10 %
invariant mass (D̄⁰π⁺) (GeV/c²)

(h)

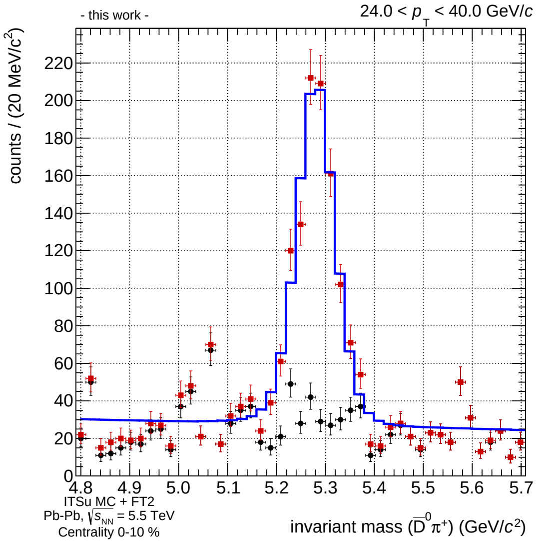
- this work -
24.0 < p_T < 40.0 GeV/c
counts / (20 MeV/c²)
0
20
40
60
80
100
120
140
160
180
200
220
4.8
4.9
5.0
5.1
5.2
5.3
5.4
5.5
5.6
5.7
ITSu MC + FT2
Pb-Pb, √s_NN = 5.5 TeV
Centrality 0-10 %
invariant mass (D̄⁰π⁺) (GeV/c²)

(i)

H. Expected significance and signal-to-background ratio in Pb–Pb collisions

In this section, the expected significance and signal-to-background ratio are presented with their total combined uncertainties. The values displayed in table H.1 correspond to those shown in figures 5.23a and 5.23b.

$p_{\mathrm{T}}^{\mathrm{B}^+}$ (GeV/c)	significance $\pm$ combined unc.	S/B $\pm$ combined unc.
0.0 – 0.5	-	-
0.5 – 1.0	-	-
1.0 – 2.0	$5.46^{+2.85}_{-2.70}$	$0.04^{+0.02}_{-0.02}$
2.0 – 3.0	$10.63^{+4.90}_{-4.64}$	$0.08^{+0.04}_{-0.04}$
3.0 – 4.0	$16.23^{+6.87}_{-6.22}$	$0.17^{+0.09}_{-0.08}$
4.0 – 5.0	$19.98^{+8.18}_{-6.93}$	$0.27^{+0.14}_{-0.13}$
5.0 – 6.0	$23.69^{+8.75}_{-6.98}$	$0.70^{+0.43}_{-0.38}$
6.0 – 8.0	$34.66^{+10.01}_{-6.97}$	$1.91^{+1.11}_{-0.91}$
8.0 – 12.0	$46.82^{+12.50}_{-8.36}$	$2.59^{+1.27}_{-0.94}$
12.0 – 16.0	$38.72^{+8.51}_{-5.86}$	$1.80^{+0.88}_{-0.69}$
16.0 – 20.0	$27.38^{+6.02}_{-4.50}$	$2.01^{+1.26}_{-1.03}$
20.0 – 24.0	$17.66^{+5.02}_{-3.80}$	$1.30^{+1.30}_{-0.97}$
24.0 – 40.0	$24.47^{+4.10}_{-3.24}$	$2.24\ ^{+1.44}_{-1.11}$

Table H.1.: In this table, the expected significance and signal-to-background ratio are presented including the PID scaling factors. In addition, the respective combined errors, which consist of the quadratic sum of all uncertainties based on input from table 5.5 (figures 5.22a and 5.22b) are quoted.

I. Calculation of required p+p reference statistics from $(\mathrm{S/B})^{\mathrm{Pb–Pb}}$

I.0.1. Monte Carlo simulations used in the calculation

- LHC10f6a: Full MC production of p+p events at $\sqrt{s} = 7\,\mathrm{TeV}$ using PYTHIA6 with the Perugia0 tune and LHC10d anchor runs

- LHC12c4: Full MC production of Pb–Pb events at $\sqrt{s_{\mathrm{NN}}} = 5.5\,\mathrm{TeV}$ using HIJING and LHC10h anchor runs. Additional signals were injected for the ITSu studies:
  - 20 % probability for a $\mathrm{c\bar{c}}$ pair, with at least one within $|\mathrm{y}| < 1.5$ and D mesons decaying only hadronically.
  - 20 % probability for a $\mathrm{b\bar{b}}$ pair, with at least one within $|\mathrm{y}| < 1.5$ and D mesons decaying only hadronically.
  - 20 % probability for a $\mathrm{c\bar{c}}$ pair and no decays forced, however at least one electron from charm is required in $|y| < 1.2$.
  - 20 % probability for a $\mathrm{b\bar{b}}$ pair and no decays forced, however at least one electron from charm or beauty is required in $|y| < 1.2$.
  - 10 % probability for a $\mathrm{J}/\psi \rightarrow \mathrm{e}^+\mathrm{e}^-$ decay and the J/ψ within $|y| < 1.0$.
  - 10 % probability for a $\mathrm{B} \rightarrow \mathrm{J}/\psi \rightarrow \mathrm{e}^+\mathrm{e}^-$ decay while the B meson and the J/ψ are required within $|y| < 2.0$.
  - Another set of 10 signal decays, equally distributed over particle and anti-particle, were injected per event for performance studies of the ITSu detector:
    - * $\mathrm{D}_s^+ \rightarrow \mathrm{K}^+\mathrm{K}^-\pi^+$
    - * $\mathrm{D}^+ \rightarrow \mathrm{K}^-\pi^+\pi^+$
    - * $\mathrm{B}^+ \rightarrow \overline{\mathrm{D}}^0\pi^+$
    - * $\mathrm{B}^0 \rightarrow \mathrm{D}^*(2010)^-\pi^+$
    - * $\Lambda_c^+ \rightarrow p^+\mathrm{K}^-\pi^+$
    - * $\Lambda_b^0 \rightarrow \Lambda_c^+\pi^-$
    - * χ_c

I.0.2. Full calculation of reference statistics in p+p

$$
\begin{aligned}
\mathcal{L}^{\mathrm{p+p}}_{\mathrm{B+}} &= \frac{(\mathcal{S}^{\mathrm{p+p}})^2}{\sigma^{\mathrm{p+p}}_{\mathrm{B+}}} \cdot \left(1+\mathcal{C}\cdot\left(\frac{B}{S}\right)^{\mathrm{Pb-Pb}}\right)\\
&= \frac{(\mathcal{S}^{\mathrm{p+p}})^2}{\sigma^{\mathrm{p+p}}_{\mathrm{B+}}} \cdot \left(1+\mathcal{E}^{B}_{7\,\mathrm{TeV}}\cdot\frac{f^{B}_{\mathrm{Pb-Pb\to p+p}}}{f^{S}_{\mathrm{Pb-Pb\to p+p}}}\cdot\left(\frac{B_{\mathrm{Pb-Pb}}}{S_{\mathrm{Pb-Pb}}}\right)\right)\\
\text{using } \mathcal{E}^{B}_{7\,\mathrm{TeV}} &= \frac{\int_{p_{\mathrm{T}}^{\max}}^{p_{\mathrm{T}}^{\min}}\left(\frac{\mathrm{d}\sigma}{\mathrm{d}p_{\mathrm{T}}}\right)^{\mathrm{FONLL}^{5.5\,\mathrm{TeV}}_{14\,\mathrm{TeV}}}_{\mathrm{B+}}\cdot(\mathrm{acc.}\cdot\mathrm{eff.})}{\int_{p_{\mathrm{T}}^{\max}}^{p_{\mathrm{T}}^{\min}}\left(\frac{\mathrm{d}\sigma}{\mathrm{d}p_{\mathrm{T}}}\right)^{\mathrm{FONLL}^{7.0\,\mathrm{TeV}}}_{\mathrm{B+}}\cdot(\mathrm{acc.}\cdot\mathrm{eff.})},\\
f^{B}_{\mathrm{Pb-Pb\to p+p}} &= \frac{B_{\mathrm{p+p}}}{B_{\mathrm{Pb-Pb}}},\\
\text{and } f^{S}_{\mathrm{Pb-Pb\to p+p}} &= \frac{S_{\mathrm{Pb-Pb}}\cdot\sigma_{\mathrm{VBAND}}}{2\cdot f_{b\to B}\cdot\mathrm{BR}\cdot\int_{p_{\mathrm{T}}^{\max}}^{p_{\mathrm{T}}^{\min}}\left(\frac{\mathrm{d}\sigma}{\mathrm{d}p_{\mathrm{T}}}\right)^{\mathrm{FONLL}^{5.5\,\mathrm{TeV}}_{14\,\mathrm{TeV}}}_{\mathrm{B+}}\cdot(\mathrm{acc.}\cdot\mathrm{eff.})}\\
\Rightarrow \mathcal{L}^{\mathrm{p+p}}_{\mathrm{B+}} &= \frac{(\mathcal{S}^{\mathrm{p+p}})^2}{\sigma^{\mathrm{p+p}}_{\mathrm{B+}}} \cdot \left(1+\frac{\sigma_{\mathrm{VBAND}}}{\int_{p_{\mathrm{T}}^{\max}}^{p_{\mathrm{T}}^{\min}}\left(\frac{\mathrm{d}\sigma}{\mathrm{d}p_{\mathrm{T}}}\right)^{\mathrm{FONLL}^{7.0\,\mathrm{TeV}}}_{\mathrm{B+}}\cdot(\mathrm{acc.}\cdot\mathrm{eff.})}\cdot\left(\frac{B_{\mathrm{p+p}}}{B_{\mathrm{Pb-Pb}}}\right)\cdot B^{Pb-Pb}\right)\\
&= \frac{(\mathcal{S}^{\mathrm{p+p}})^2}{\sigma^{\mathrm{p+p}}_{\mathrm{B+}}}\cdot\mathcal{C}_1\\
&= \frac{1}{\sigma^{\mathrm{p+p}}_{B+}}\cdot\left(\sqrt{2}\cdot\frac{\mathrm{S}_{\mathrm{Pb-Pb}}}{\sqrt{\mathrm{S}_{\mathrm{Pb-Pb}}+\mathrm{B}_{\mathrm{Pb-Pb}}}}\right)^2\cdot\mathcal{C}_1\\
&= \frac{2\mathrm{S}_{\mathrm{Pb-Pb}}}{\sigma^{\mathrm{p+p}}_{B+}}\cdot\left(\frac{1}{\frac{\mathrm{B}_{\mathrm{Pb-Pb}}}{\mathrm{S}_{\mathrm{PbPb}}}}\right)\cdot\mathcal{C}_1\\
&= \frac{2\cdot\mathrm{S}_{\mathrm{Pb-Pb}}}{\sigma^{\mathrm{p+p}}_{B+}}\cdot\mathcal{C}_2\cdot\mathcal{C}_1\\
&= 2\cdot\frac{2\cdot f_{b\to B}\cdot\mathrm{BR}\cdot\left(\frac{d\sigma}{dp_T}\right)^{\mathrm{FONLL}}\cdot R^{B^+}_{\mathrm{AA}}\cdot\langle T_{\mathrm{AA}}\rangle^{0-10\,\%}\cdot(\mathrm{acc.}\cdot\mathrm{eff.})}{2\cdot f_{b\to B}\cdot\mathrm{BR}\cdot\int_{p_{\mathrm{T}}^{\max}}^{p_{\mathrm{T}}^{\min}}\left(\frac{\mathrm{d}\sigma}{\mathrm{d}p_{\mathrm{T}}}\right)^{\mathrm{FONLL}^{5.5\,\mathrm{TeV}}_{14\,\mathrm{TeV}}}_{\mathrm{B+}}\cdot(\mathrm{acc.}\cdot\mathrm{eff.})}\cdot 8\cdot\mathcal{C}_2\cdot\mathcal{C}_1\\
&= 16\cdot R^{B^+}_{\mathrm{AA}}\cdot\langle T_{\mathrm{AA}}\rangle^{0-10\,\%}\cdot\frac{\int_{p_{\mathrm{T}}^{\max}}^{p_{\mathrm{T}}^{\min}}\left(\frac{\mathrm{d}\sigma}{\mathrm{d}p_{\mathrm{T}}}\right)^{\mathrm{FONLL}^{5.5\,\mathrm{TeV}}}_{\mathrm{B+}}}{\int_{p_{\mathrm{T}}^{\max}}^{p_{\mathrm{T}}^{\min}}\left(\frac{\mathrm{d}\sigma}{\mathrm{d}p_{\mathrm{T}}}\right)^{\mathrm{FONLL}^{5.5\,\mathrm{TeV}}_{14\,\mathrm{TeV}}}_{\mathrm{B+}}}\cdot\mathcal{C}_2\cdot\mathcal{C}_1\\
&= 16\cdot R^{B^+}_{\mathrm{AA}}\cdot\langle T_{\mathrm{AA}}\rangle^{0-10\,\%}\cdot\mathcal{C}_3\cdot\mathcal{C}_2\cdot\mathcal{C}_1
\end{aligned}
\tag{I.1}
$$

In this section, the calculation of the required p+p reference luminosity based on the expected signal-to-background ratio and significance found in central Pb–Pb collisions is presented in full detail. Some color coding is used to in order to outline relevant terms: Blue terms cancel in the ratios, green terms originate from FONLL and are varied within their uncertainties for a minimal/maximal estimate of the luminosity, while red terms are propagated and added in quadrature in the final uncertainty. The uncertainties of the terms $\mathcal{C}_1$, $\mathcal{C}_2$ and $\mathcal{C}_3$ correspond to the uncertainties labeled "$(\mathrm{S/B})^{\mathrm{p+p}}$", "S and B" and "FONLL ratio" in figures 6.4b and 6.5b respectively. Note that σ_{VBAND} is used as explained in equation 6.5.

J. Study on dedicated multiplicity trigger in p+p collisions

Within the scope of the heavy-flavor studies for the upgraded ITS detector development, it was found that some measurements of the charm and beauty sector, i.e. $\overline{\mathrm{D}}^0 \rightarrow \mathrm{K}^+\pi^-$ and $\Lambda_b^0 \rightarrow \Lambda_c^+\pi^-$, crucially depend on the particle identification capabilities of the TOF detector. The spectra of the decay daughters in these decays is softer than for the $\mathrm{B}^+ \rightarrow \overline{\mathrm{D}}^0\pi^+$ ($\mathrm{B}^+ \rightarrow \overline{\mathrm{D}}^0\pi^+$), which, as previously shown, is not as sensitive to the PID information (especially at higher momentum). In the upgrade scenario it is foreseen, that the upgraded ITS and TPC detectors will read out p+p collisions at a maximum rate of about 1 MHz, whereas the readout rate of the TOF detector could be limited to 260 kHz [162], even though improved readout schemes are already being developed.

In order to enhance the fraction of (high-multiplicity) events containing particle identification information from the TOF detector, the possibility of a multiplicity-driven TOF trigger was evaluated. Further, a possible correlation to the hit multiplicity in the ITSu detector was studied. The idea was motivated by previous studies based on the PYTHIA6 MC generator [204], which revealed that events containing charmed mesons had on average more signal hits in the central barrel detectors than minimum bias events. In a first, very simple approach to evaluate the possible benefit for the readout rate, detector efficiencies were neglected.

J.0.3. Analysis

For a first estimate the charged particle multiplicities were studied on kinematic level only, based on available full MC productions (appendix J.1). The charged particle multiplicity in the ITSu was estimated with selection criteria on $|\eta| < 1.5$, $p_{\mathrm{T}} > 30\,\mathrm{MeV}/c$ and point of origin within a radial distance of $\mathrm{R} < 3\,\mathrm{cm}$ inside the ALICE central barrel (z-axis). The latter criterion was introduced to reject particles produced in interactions with the material, i.e. delta or conversion electrons. For the TOF detector, charged particles with $|\eta| < 0.9$, $p_{\mathrm{T}} > 300\,\mathrm{MeV}/c$ were evaluated. Based on these assumptions the fraction of minimum bias events and of events containing charm and/or beauty mesons as a function of multiplicity threshold in ITSu and TOF were compared. The heavy-flavor meson was required to be generated within $|\mathrm{y}| < 0.9$, and further the effect of a lower threshold on the transverse momentum was evaluated.

J.0.4. Results

Figure J.1 displays the fraction of events above the multiplicity threshold as a function of the threshold in the TOF and ITS detector, respectively. In figures J.1c and J.1d an additional lower threshold on the transverse momentum of the meson of $p_{\mathrm{T}} > 3\,\mathrm{GeV}/c$ is applied. The effect of a lowered selection on the p_{T} threshold can be found in the appendix J.2, figure J.3. All distributions are normalized to the maximal detectable multiplicity, given the respective criteria described above. For comparison, the fraction of events above the corresponding threshold for minimum bias events is superimposed.

In both, TOF and ITS detector, the charged particle multiplicity is significantly larger for events containing a charmed and/or beauty meson when compared to minimum bias events. Given the large mean transverse momentum of the heavy-flavor mesons, an additional p_{T} requirement enhances this differences. In order to suppress the low-multiplicity minimum bias events by a factor of four, a multiplicity threshold of around 25 in the ITS or TOF detector would be required. As a consequence, the fraction of events above threshold containing charm or beauty meson would be reduced to about $60-70\,\%$ for $p_{\mathrm{T}}^{\mathrm{meson}} > 0\,\mathrm{GeV}/c$, and about $75\,\%$ for $p_{\mathrm{T}}^{\mathrm{meson}} > 3\,\mathrm{GeV}/c$. For events with charmed and beauty mesons, this fraction increases by about $20\,\%$.

In order to estimate the reduction of data volume in case the multiplicity trigger is applied with a given threshold, the mean fraction of reconstructed tracks in the ITS and TPC was evaluated as a function of the threshold. The results are presented in figure J.2. Without a multiplicity cut, the mean number of tracks per event is about eight. For a multiplicity selection larger than 25, the number of refitted tracks per event and thus the size of each event increases by a factor of about 2.5. Given the reduction of events by a factor four, the reduction of data volume is thus only about $37\,\%$.

So far, in this approach no detector effects where taken into account. As described in [247], pathologically noisy channels of the TOF detector, which spoil the multiplicity estimate, would have to be masked out on a run-by-run basis. Further, missing or inactive detector elements and additional problems, such as malfunctions in the conversion and forwarding of the information at the trigger level, introduce large inefficiencies for a multiplicity trigger on raw data level. Given these drawbacks and the rather small reduction of data volume, the approach of a multiplicity trigger was not further investigated for these purposes.

J.1. Run list

For the analysis of the multiplicity trigger in the ITS and TOF detector it was sufficient to analyze data on kinematic level. As statistics were sufficient, only small chunks of the complete datasets were analyzed.

LHC10d4 (ESD) p+p, Pythia6 Perugia-0, 7.0 TeV, LHC10c anchor runs - analyzed 10 chunks containing 5 000 events in run 120829.

LHC10f7a (ESD) p+p, Enhanced heavy-flavor signals, LHC10b+c+d anchor runs - analyzed 10 chunks containing 124 000 events in run 117222.

J.2. Additional results

Figure J.3 displays the remaining results, using a kinematic threshold cut at $p_{\mathrm{T}}^{\mathrm{meson}} > 1\,\mathrm{GeV}/c$ and $p_{\mathrm{T}}^{\mathrm{meson}} > 2\,\mathrm{GeV}/c$.

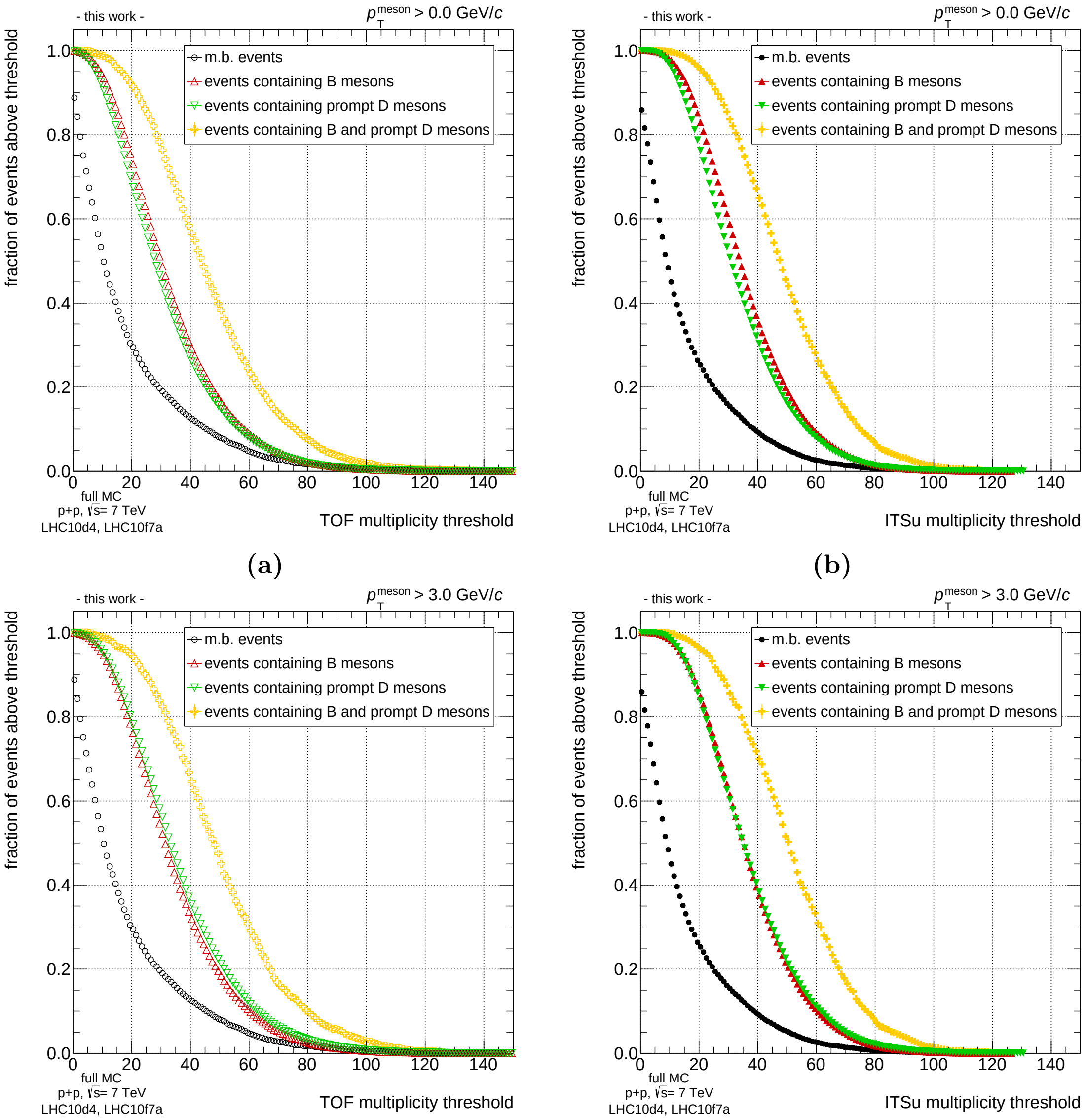

(a) (b) (c) (d)

Figure J.1.: Fraction of events passing the ITS or TOF multiplicity trigger threshold. For figures J.1c and J.1d and additional minimum threshold on the transverse momentum of the meson was applied. For comparison, the corresponding result for minimum bias events is superimposed.

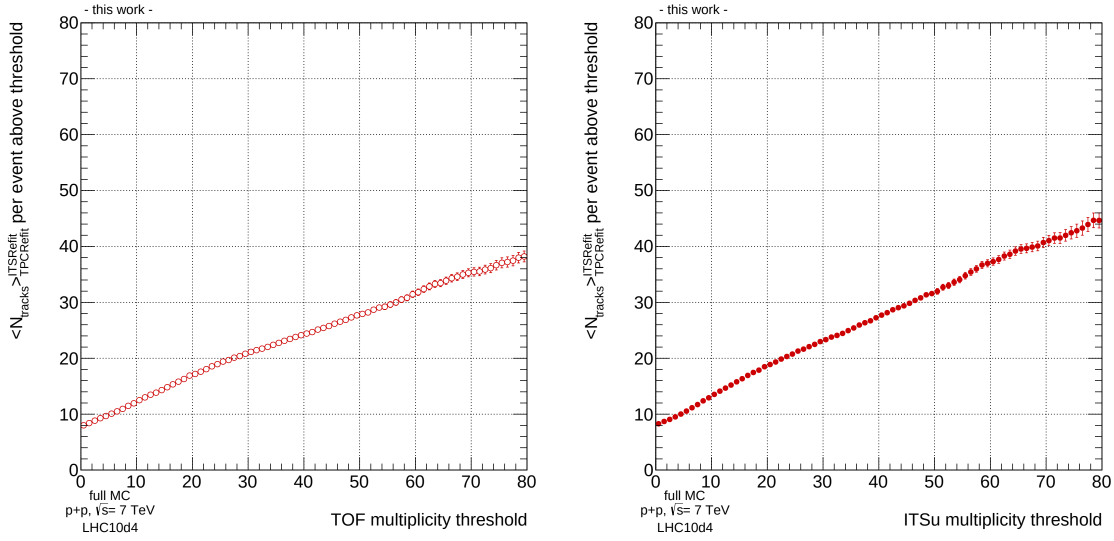

(a) (b)

Figure J.2.: Mean number of tracks refitted in ITS and TPC passing the ITS or TOF multiplicity trigger threshold as a function of the threshold. The mean number of tracks per event is about 8 if no threshold is applied. Only statistical uncertainty is displayed

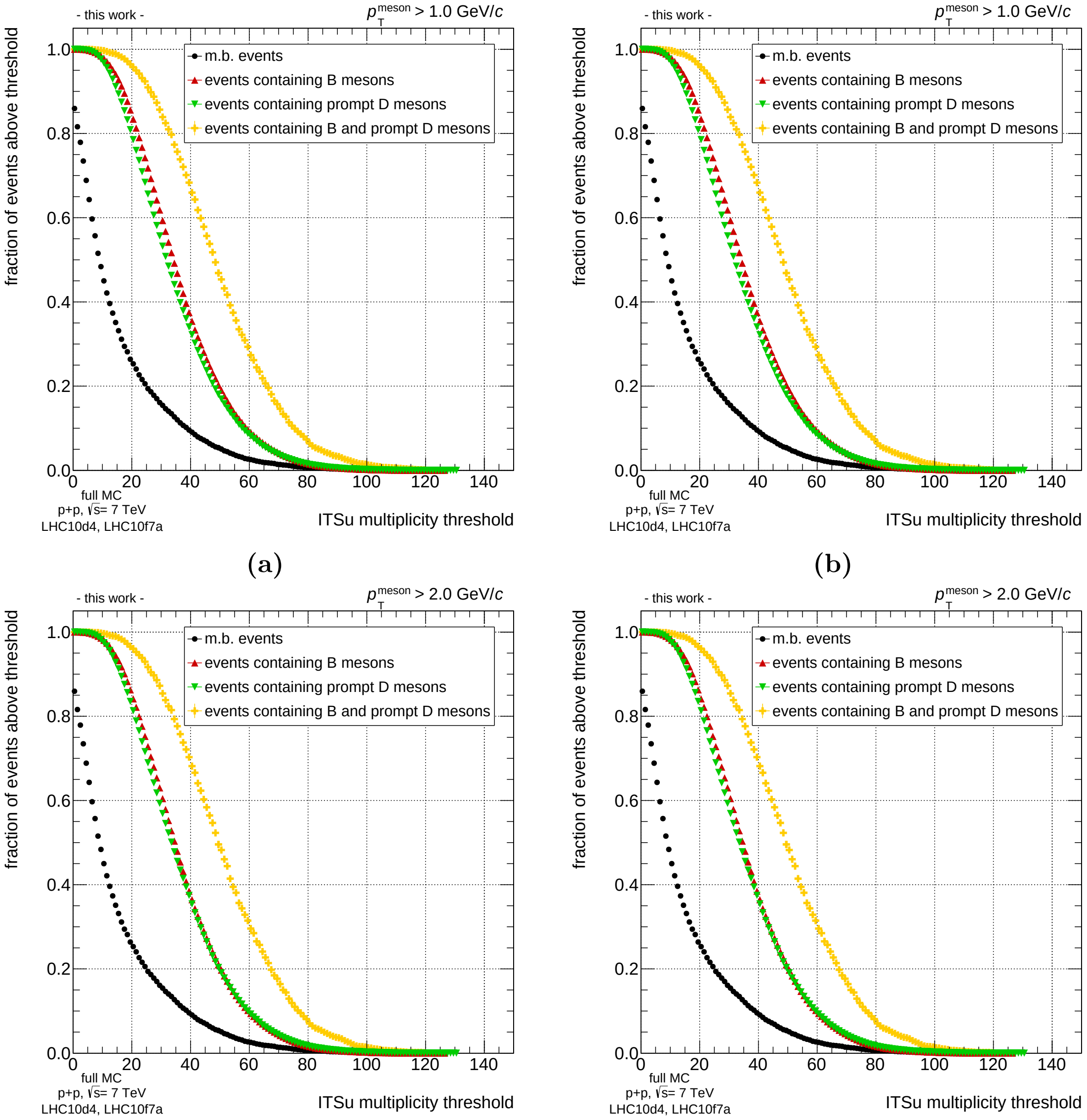

(a) **(b)**

(c) **(d)**

Figure J.3.: Fraction of events passing the ITS or TOF multiplicity trigger threshold. Additional minimum thresholds on the transverse momentum of the meson were applied. For comparison, the corresponding result for minimum bias events is superimposed.

K. Expected sensitivity on v_2

In this section, the expected sensitivity on v_2 is presented together with the predictions by BAMPS and TAMU at different centralities, as explained in section 7.

$p_{\mathrm{T}}^{\mathrm{B}^+}$ (GeV/c)	$\langle v_2^{\mathrm{BAMPS},0-10\,\%}\rangle$ $\langle v_2^{\mathrm{TAMU},20-40\,\%}\rangle$ $\langle v_2^{\mathrm{TAMU},30-50\,\%}\rangle$	Expected sensitivity
1.0 – 2.0	- 0.0145 ± 0.0005 0.0776 ± 0.0029	- 181 – 329 % 45 – 81 %
2.0 – 3.0	0.0113 0.0329 ± 0.0017 0.1262 ± 0.0033	145 – 249 % 58 – 99 % 20 – 33 %
3.0 – 4.0	0.0350 0.0540 ± 0.0008 0.1224 ± 0.0080	43 – 73 % 33 – 54 % 19 – 31 %
4.0 – 5.0	0.0325 0.0665 ± 0.0037 0.0950 ± 0.0074	45 – 76 % 25 – 44 % 23 – 40 %
5.0 – 6.0	0.0495 0.0689 ± 0.0045 0.0722 ± 0.0051	34 – 64 % 28 – 53 % 35 – 66 %
6.0 – 8.0	0.0373 0.0642 ± 0.0061 0.0470 ± 0.0026	39 – 68 % 26 – 46 % 47 – 83 %
8.0 – 12.0	0.0333 0.0481 ± 0.0066 0.0321 ± 0.0066	33 – 52 % 26 – 41 % 52 – 81 %
12.0 – 16.0	0.0273 0.0308 ± 0.0046 -	52 – 79 % 53 – 81 % -
16.0 – 20.0	- 0.0223 ± 0.0013 -	- 95 – 175 % -

Table K.1.: In this table, the theoretically predicted v_2 in Pb–Pb collisions at $\sqrt{s_{\mathrm{NN}}} = 2.76$ TeV by TAMU (He *et al.*,20–40 % (beauty), 30–50 % (charm)) [98] and BAMPS (Uphoff *et al.*, 0–10 %) [91] are compared to the expected sensitivity in the full kinematic reconstruction via $\mathrm{B}^+ \rightarrow \overline{\mathrm{D}}^0\pi^+$ ($\overline{\mathrm{D}}^0 \rightarrow \mathrm{K}^+\pi^-$).

Bibliography

[1] NA49 Collaboration, *Hadronic expansion dynamics in central Pb+Pb collisions at 158 GeV per nucleon*, Eur. Phys. J. C **2** 661, 1998

[2] NA50 Collaboration, *Evidence for deconfinement of quarks and gluons from the* J/ψ *suppression pattern measured in Pb–Pb collisions at the CERN-SPS*, CERN-EP-2000-013, Phys. Lett. **477B** 28, 2000

[3] WA97 Collaboration, *Strangeness enhancement at mid-rapidity in Pb–Pb collisions at 158 A GeV/c*, Phys. Lett. **449B** 401, 1999

[4] WA98 Collaboration, *Observation of Direct Photons in Central 158A GeV* $^{208}Pb+^{208}Pb$ *Collisions*, Phys. Lett. **85B** 3595, 2000

[5] U. Heinz *et al.*, *Evidence for a New State of Matter: An Assessment of the Results from the CERN Lead Beam Programme*, 2000, arXiv:nucl-th/0002042

[6] D. Boyanovsky *et a.l*, *Phase transitions in the early and the present Universe*, Ann.Rev.Nucl.Part.Sci. **56** 441, 2006, arXiv:hep-ph/0602002

[7] CMS Collaboration, *Study of high-*p_{T} *charged particle suppression in PbPb compared to pp collisions at* $\sqrt{s_{\mathrm{NN}}} = 2.76\,TeV$, CMS-HIN-10-005, CERN-PH-EP-2012-043, Eur. Phys. J. C **72** 1945, 2012, arXiv:1202.2554 [nucl-ex]

[8] C. Gale *et al.*, *Event-by-event anisotropic flow in heavy-ion collisions from combined Yang-Mills and viscous fluid dynamics*, Phys. Rev. Lett. **110**, 012302, 2013, arXiv:1209.6330 [nucl-th]

[9] A. Dainese, *Charm production and in-medium QCD energy loss in nucleus nucleus collisions with ALICE: A Performance study*, Ph.D. thesis, Padova University, 2003, arXiv:nucl-ex/0311004

[10] K.A. Olive *et al.* (Particle Data Group), Chin. Phys. C, **38**, 090001, 2014

[11] K. Schweda *et al.*, *DDbar Correlations probing Thermalization in High-Energy Nuclear Collisions*, proceedings of the ISMD06 conference, Paraty, Brazil, 2006, arXiv:nucl-ex/0610043

[12] ALICE Collaboration, *ALICE Heavy Ion Event Displays - 25 November 2015*, 01/31/2015, Retrieved from https://cds.cern.ch/record/2108293?ln=en

[13] ALICE Collaboration, *Measurement of* D_s^+ *production and nuclear modification factor in Pb-Pb collisions at* $\sqrt{s_{\mathrm{NN}}} = 2.76\,TeV$, CERN-PH-EP-2015-253, 2015, arXiv:1509.07287 [nucl-ex]

[14] ALICE Collaboration, *D meson elliptic flow in non-central Pb-Pb collisions at* $\sqrt{s_{\mathrm{NN}}} = 2.76\,TeV$, CERN-PH-EP-2013-085, Phys. Rev. Lett. **111** 102301, 2013, arXiv:1305.2707 [nucl-ex]

[15] ALICE Collaboration, *Measurement of electrons from heavy-flavour decays in pp and Pb-Pb collisions with ALICE at the LHC*, proceedings from Hard Probes 2012, arXiv:1208.5411 [nucl-ex]

[16] ALICE Collaboration, *Inclusive, prompt and non-prompt* J/ψ *production at mid-rapidity in Pb–Pb collisions at* $\sqrt{s_{\mathrm{NN}}} = 2.76\,TeV$, JHEP 07 **051**, CERN-PH-EP-2015-092, 2015, arXiv:1504.07151 [nucl-ex]

[17] CMS Collaboration, *Study of B meson production in pPb collisions at* $\sqrt{s_{\mathrm{NN}}} = 5.02\,TeV$, CMS-HIN-14-004, CERN-PH-EP-2015-209, 2015, arXiv:1508.06678 [nucl-ex]

[18] CMS Collaboration, *Open Heavy Flavor Measurement in heavy ion collisions with CMS*, CMS-CR-2015-170, 2015

[19] ALICE Collaboration, *Letter of Intent for the Upgrade of the ALICE Experiment*, CERN-LHCC-2012-012, LHCC-I-022, 2012

[20] ALICE Collaboration, *Technical Design Report for the Upgrade of the ALICE Inner Tracking System*, CERN-LHCC-2013-024, ALICE-TDR-017, 2011

[21] N. Armesto *et al.*, *Testing the color charge and mass dependence of parton energy loss with heavy-to-light ratios at RHIC and CERN LHC*, CERN-PH-TH-2005-008, Phys.Rev. D **71** 054027, 2005

[22] S.L. Glashow, *Partial-Symmetries of Weak Interactions*, Nucl. Phys. **22** 579, 1961

[23] S. Weinberg, *A Model of Leptons*, Phys. Rev. Lett. **19** 1264, 1967

[24] A. Salam, *Weak and Electromagnetic Interactions*, Conf.Proc. **C680519** 367, 1968

[25] G. 't Hooft, *Renormalization of massless Yang-Mills fields*, Nuclear Physics B **33** 173, 1971

[26] G. 't Hooft *et al.*, *Regularization and renormalization of gauge fields* Nuclear Physics B **44** 189, 1972

[27] F.J. Hasert *et al*, *Observation of neutrino-like interactions without muon or electron in the Gargamelle neutrino experiment*, Phys. Lett. **46B** 138, 1971

[28] ALEPH, DELPHI, L3, OPAL, and SLD Collaborations, and LEP Electroweak Working Group, and SLD Electroweak Group, and SLD Heavy Flavour Group, *Precision Electroweak Measurements on the Z Resonance*, CERN-PH-EP/2005-041, SLAC-R-774, Phys.Reports **427** 257, 2006, arXiv:hep-ex/0509008

[29] M. Thomson, *Modern particle physics*, Cambridge University Press, ISBN: 978-1-107-03426-6, 2013

[30] I. Brock *et al.*, *Physics at the Terascale* Wiley-VCH, ISBN: 978-3-527-41001-9, 2011

[31] The UA1 Collaboration, *Experimental observation of lepton pairs of invariant mass around 95 GeV/*c^2 *at the CERN SPS collider*, Phys. Lett. **126B** 398, 1983

[32] The UA2 Collaboration, *Evidence for* $Z^0 \rightarrow e^+e^-$ *at the CERN* $\overline{p}p$ *Collider*, Phys. Lett. **129B** 310, 1983

[33] The UA1 Collaboration, *Experimental observation of isolated large transverse energy electrons with associated missing energy at* $\sqrt{s}$*=540 GeV*, Phys. Lett. **122B** 103, 1983

[34] The UA2 Collaboration, *Observation of single isolated electrons of high transverse momentum in events with missing transverse energy at the CERN Full-size image* $\overline{p}p$ *collider*, Phys. Lett. **122B** 476, 1983

[35] MissMJ, *Standard Model of Elementary Particles*, input from *PBS NOVA*, *Fermilab, Office of Science, United States Department of Energy* and the *Particle Data Group*, 12/31/2015, Retrieved from https://commons.wikimedia.org/wiki/File:Standard_Model_of_Elementary_Particles.svg#/media/File:Standard_Model_of_Elementary_Particles.svg

[36] ATLAS Collaboration, *Observation of a new particle in the search for the Standard Model Higgs boson with the ATLAS detector at the LHC*, Phys. Lett. **B716** 1, CERN-PH-EP-2012-218, 2012, arXiv:1207.7214 [nucl-ex]

[37] CMS Collaboration, *Observation of a new boson at a mass of 125 GeV with the CMS experiment at the LHC*, Phys. Lett. **B716** 30, CERN-PH-EP-2012-220, 2012, arXiv:1207.7235 [nucl-ex]

[38] LIGO Scientific Collaboration and Virgo Collaboration, *Observation of Gravitational Waves from a Binary Black Hole Merger*, Phys. Rev. Lett. **116** 061102, 2016, arXiv:1602.03837 [gr-qc]

[39] LIGO Scientific Collaboration and Virgo Collaboration, *Tests of general relativity with GW150914*, LIGO-P1500213, 2016, arXiv:1602.03841 [gr-qc]

[40] D.H. Perkins, *Introduction to Higher Energy Physics*, Cambridge University Press, ISBN: 978-0-521-62196-0, 2000

[41] LHCb Collaboration, *Observation of* J/ψp *resonances consistent with pentaquark states in* $\Lambda_b^0 \rightarrow$J/$\psi K^- p$ *decays*, CERN-PH-EP-2015-153, LHCb-PAPER-2015-029, Phys. Rev. Lett. **115** 072001, 2015, arXiv:1507.03414 [hep-ex]

[42] G. Dissertori *et al.*, *Precise determination of the strong coupling constant at NNLO in QCD from the three-jet rate in electron-positron annihilation at LEP*, ZU-TH 15/09, IPPP/09/87, ETH-IPP-2009-11, Phys.Rev.Lett. **104** 072002, 2010, arXiv:0910.4283 [hep-ph]

[43] ATLAS Collaboration, *Measurement of multi-jet cross-section ratios and determination of the strong coupling constant in proton-proton collisions at* $\sqrt{s} =$ 7 *TeV with the ATLAS detector*, ATLAS-CONF-2013-041, 2013

[44] CMS Collaboration, *Measurement of the inclusive 3-jet production differential cross section in proton-proton collisions at 7 TeV and determination of the strong coupling constant in the TeV range* , CMS-SMP-12-027, CERN-PH-EP-2014-287, Eur. Phys. J. C **75** 186, 2015

[45] S. Hands, *The Phase Diagram of QCD*, SWAT/01/287, Contemp. Phys. **42** 209, 2001, arXiv:physics/0105022 [physics.ed-ph]

[46] Y. Aoki *et al.*, *The order of the quantum chromodynamics transition predicted by the standard model of particle physics*, Nature **443** 675, 2006, arXiv:hep-lat/0611014

[47] C. DeTar *et al.*, *QCD thermodynamics from the lattice*, Eur. Phys. J. A **41** 405, 2009, arXiv:0905.2949 [hep-lat]

[48] M. A. Stephanov, *QCD phase diagram: An overview*, PoS LAT2006, 024, 2006, arXiv:hep-lat/0701002

[49] HotQCD collaboration, *Chiral and deconfinement aspects of the QCD transition*, Phys. Rev. D **85**, 054503, 2012

[50] A. Ukawa, *Kenneth Wilson and lattice QCD*, Journal of Statistical Physics Vol. 160 Iss **5** 1081, 2015, arXiv:1501.04215 [hep-lat]

[51] S. Sarkar *et al.*, *The physics of the quark-gluon plasma*, Lect. Notes Phys. **785** 1, 2010

[52] J. Danzer *et al.*, *A study of the sign problem for lattice QCD with chemical potential*, Phys. Lett. B **682** 240, 2009, arXiv:0907.3084 [hep-lat]

[53] M. Alford *et al.*, *Color-Flavor Locking and Chiral Symmetry Breaking in High Density QCD*, IASSNS-HEP-98/29, MIT-CTP-2731, Nucl. Phys. B **537** 443, 1999, arXiv:hep-ph/9804403

[54] ALICE Collaboration, *Centrality determination of Pb-Pb collisions at* $\sqrt{s_{\rm NN}} = 2.76$ *TeV with ALICE*, Phys. Rev. C **88**, 044909, 2013

[55] M. L. Miller *et al.*, *Glauber Modeling in High Energy Nuclear Collisions*, Ann.Rev.Nucl.Part.Sci. **57** 205, 2007, arXiv:nucl-ex/0701025

[56] ALICE Collaboration, *Measurement of inelastic, single- and double-diffraction cross sections in proton-proton collisions at the LHC with ALICE*, CERN-PH-EP-2012-238, Eur. Phys. J. C **73** 2456, 2013, arXiv:1208.4968 [hep-ex]

[57] C. Loizides *et al.*, *Improved version of the PHOBOS Glauber Monte Carlo*, SoftwareX **1-2** 13, 2015, arXiv:1408.2549 [nucl-ex]

[58] K. Yagi *et al.*, *Quark-Gluon Plasma*, Cambridge University Press, ISBN: 978-052-108-924-1, 2005

[59] E. Iancu *et al.*, *The Color Glass Condensate and High Energy Scattering in QCD*, review for QGP3, ISBN: 978-981-238-077-7, Eds. R. C. Hwa and X.-N. Wang, World Scientific, 2003 arXiv:hep-ph/0303204

[60] STAR Collaboration, *Experimental and Theoretical Challenges in the Search for the Quark Gluon Plasma: The STAR Collaboration's Critical Assessment of the Evidence from RHIC Collisions*, Nucl. Phys. A **757** 102, 2005, arXiv:nucl-ex/0501009

[61] ALICE Collaboration, *Two-pion Bose-Einstein correlations in central PbPb collisions at* $\sqrt{s_{\mathrm{NN}}} = 2.76\,TeV$, CERN-PH-EP-ALICE-2010-006, Phys.Lett. **B696** 328, 2011, arXiv:1012.4035 [nucl-ex]

[62] ZEUS Collaboration, *Bose-Einstein Correlations of Charged and Neutral Kaons in Deep Inelastic Scattering at HERA*, DESY-07-069, Phys.Lett. **B652** 1, 2007, arXiv:0706.2538 [hep-ex]

[63] J. Stachel *et al.*, *Quark-Gluon Plasma Physics: from fixed target to LHC*, lecture, University of Heidelberg, 2011

[64] A.M. Poskanzer *et al.*, *Methods for analyzing anisotropic flow in relativistic nuclear collisions*, Phys. Rev. C **58** 1671, 1998, arXiv:nucl-ex/9805001

[65] M. Luzum, *Flow fluctuations and long-range correlations: elliptic flow and beyond*, J. Phys. G: Nucl. Part. Phys. **38** 124026, 2011, arXiv:1107.0592 [nucl-th]

[66] R. Grajcarek, *Anisotropic flow of the charmed* D^{*+} *meson in non-central Pb–Pb collisions at* $\sqrt{s_{\mathrm{NN}}} = 2.76\,TeV$, Ph.D. thesis, University of Heidelberg, 2013

[67] N. Borghini, *Flow analysis from multiparticle azimuthal correlations*, Phys. Rev. C **64** 054901, 2001, arXiv:nucl-th/0105040

[68] ALICE Collaboration, *Higher harmonic anisotropic flow measurements of charged particles in Pb-Pb collisions at 2.76 TeV*, CERN-PH-EP-2011-073, Phys. Rev. Lett. **107** 032301, 2011, arXiv:1105.3865 [nucl-ex]

[69] C. Gale, *Hydrodynamic Modeling of Heavy-Ion Collisions*, Int. J. of Mod. Phys. A Vol. **28** 1340011, 2013, arXiv:1301.5893 [nucl-th]

[70] P. Huovinen *et al.*, *Radial and elliptic flow at RHIC: further predictions*, Phys.Lett. **B503** 58, 2001, arXiv:hep-ph/0101136

[71] T. Hirano *et al.*, *Collective flow and two-pion correlations from a relativistic hydrodynamic model with early chemical freeze out*, Phys.Rev. **C66** 054905, 2002, arXiv:nucl-th/0205043

[72] K. Kajantie, *Physics of LHC (theory)*, Nucl. Phys. A **715**, 432c, 2003

[73] M. Cacciari *et al.*, *The* p_{T} *spectrum in heavy-flavour hadroproduction*, CERN-TH/98-77, LPTHE-Orsay/98-11, IFUM/613-FT, LNF-98/008(P), JHEP **9805** 007, 1998, arXiv:hep-ph/9803400

[74] M. Cacciari *et al.*, *Theoretical predictions for charm and bottom production at the LHC*, CERN-PH-TH/2011-227, JHEP **1210** 137, 2012, arXiv:1205.6344 [hep-ph]

[75] M. Cacciari *et al.*, *Gluon PDF constraints from the ratio of forward heavy quark production at the LHC at $\sqrt{s}$=7 and 13 TeV*, CERN-PH-TH/2015-171, 2015, arXiv:1507.06197 [hep-ph]

[76] C. Peterson *et al.*, *Scaling violations in inclusive e^+e^- annihilation spectra*, Phys. Rev. D **27** 105, 1983

[77] V. G. Kartvelishvili *et al.*, *On the Fragmentation Functions of Heavy Quarks Into Hadrons*, Phys. Lett. **B78** 615, 1978

[78] J. Pumplin *et al.*, *New Generation of Parton Distributions with Uncertainties from Global QCD Analysis*, JHEP **0207** 012, 2002, arXiv:hep-ph/0201195

[79] DELPHI Collaboration, *A measurement of the branching fractions of the b-quark into charged and neutral b-hadrons*, Physics Letters **B576**, 29, 2003

[80] R. Vogt, *The A Dependence of Open Charm and Bottom Production*, Int. J. Mod. Phys. **E12** 211, 2003, arXiv:hep-ph/0111271

[81] K.J. Eskola *et al.*, *Nuclear parton distributions in the DGLAP approach*, 2001, arXiv:hep-ph/0110348

[82] J.D. Bjorken, *Energy Loss of Energetic Partons in Quark-Gluon Plasma: Possible Extinction of High p_T Jets in Hadron-Hadron Collisions*, FERMILAB-PUB-82-59-THY, 1982

[83] M.H. Thoma, *Quark-Gluon Plasma 2*, ed. R.C. Hwa, p. 51, World Scientific, ISBN: 978-981-02-2399-1, 1995

[84] A.B. Migdal, *Bremsstrahlung and Pair Production in Condensed Media at High Energies*, Phys. Rev. **103** 1811, 1956

[85] K. Zapp *et al.*, *Local Monte Carlo Implementation of the Non-Abelian Landau-Pomeranchuk-Migdal Effect*, Phys. Rev. Lett. **103**, 152302, 2009, arXiv:0812.3888 [hep-ph]

[86] Yu.L. Dokshitzer *et al.*, *Heavy quark colorimetry of QCD matter*, LPT-Orsay-01/58, BNL-NT-01/9, Phys. Lett. B **519** 199, 2001, arXiv:hep-ph/0106202

[87] Z. Xu *et al.*, *Thermalization of gluons in ultrarelativistic heavy ion collisions by including three-body interactions in a parton cascade*, Phys.Rev. C **71** 064901, 2005, arXiv:hep-ph/0406278

[88] Z. Xu *et al.*, *Transport rates and momentum isotropization of gluon matter in ultrarelativistic heavy-ion collisions*, Phys. Rev. C **76** 024911, 2007, arXiv:hep-ph/0703233

[89] F. Senzel *et al.*, *Open heavy flavor in Pb+Pb collisions at $\sqrt{s} = 2.76$ TeV within a transport model*, Nucl. Phys. A **932** 158, 2013

[90] J. Uphoff *et al.*, *Elliptic flow and energy loss of heavy quarks in ultra-relativistic heavy ion collisions*, Phys. Rev. C **84** 024908, 2011, arXiv:1104.2295 [hep-ph]

[91] J. Uphoff *et al.*, *Open heavy flavor in Pb+Pb collisions at* $\sqrt{s} = 2.76$ *TeV within a transport model*, Phys. Lett. B **717** 430, 2012, arXiv:1205.4945 [hep-ph]

[92] T. Sjöstrand, *A Brief Introduction to PYTHIA 8.1*, CERN-LCGAPP-2007-04, LU TP 07-28, FERMILAB-PUB-07-512-CD-T, Comput. Phys. Commun. **178** 852, 2008, arXiv:0710.3820 [hep-ph]

[93] R. Rapp *et al.*, *Heavy Quarks in the Quark-Gluon Plasma*, *Quark-Gluon Plasma 4*, World Scientific, ISBN: 978-981-4293-28-0, 2010, arXiv:0903.1096 [hep-ph]

[94] F. Riek *et al.*, *Quarkonia and heavy-quark relaxation times in the quark-gluon plasma*, Phys. Rev. C **82** 035201, 2010, arXiv:1005.0769 [hep-ph]

[95] M. He *et al.*, *Non-perturbative Heavy-Flavor Transport at RHIC and LHC*, proceedins for Hard Probes 2012, arXiv:1208.0256 [nucl-th]

[96] M. He *et al.*, *Heavy-quark diffusion and hadronization in quark-gluon plasma*, Phys. Rev. C **86** 014903, 2012 arXiv:1106.6006 [nucl-th]

[97] M. He *et al.*, D_s*-Meson as Quantitative Probe of Diffusion and Hadronization in Nuclear Collisions*, Phys. Rev. Lett. **110** 112301, 2013, arXiv:1204.4442 [nucl-th]

[98] M. He *et al.*, *Heavy Flavor at the Large Hadron Collider in a Strong Coupling Approach*, 2014, arXiv:1401.3817 [nucl-th]

[99] P.F. Kolb *et al.*, *Hydrodynamic description of ultrarelativistic heavy-ion collisions*, invited review for *Quark Gluon Plasma 3*, ISBN: 978-981-238-077-7, Editors: R.C. Hwa and X.-N. Wang, World Scientific, 2003, Singapore, arXiv:nucl-th/0305084

[100] L. Ravagli *et al.*, *Quark coalescence based on a transport equation*, Phys. Lett. B **655** 126, 2007

[101] R. Averbeck, *Heavy-flavor production in heavy-ion collisions and implications for the properties of hot QCD matter*, Prog. Part. Nucl. Phys. 70 159, 2015, arXiv:1505.03828 [nucl-ex]

[102] K. Schweda, *Prompt production of D mesons with ALICE at the LHC*, 2013, arXiv:1402.1370 [nucl-ex]

[103] ALICE Collaboration, *Measurement of charm production at central rapidity in proton-proton collisions at* $\sqrt{s} = 2.76$ *TeV*, CERN-PH-EP-2012-133, JHEP **07** 191, 2012, arXiv:1205.4007 [hep-ex]

[104] ALICE Collaboration, *Measurement of charm production at central rapidity in proton-proton collisions at* $\sqrt{\mathrm{s}} = 7$ *TeV*, JHEP **1201** 128, 2012, arXiv:1111.1553 [hep-ex]

[105] R. Averbeck *et al.*, *Reference Heavy Flavour Cross Sections in pp Collisions at* $\sqrt{s_{\mathrm{NN}}} = 2.76$ *TeV, using a pQCD-Driven* $\sqrt{s_{\mathrm{NN}}}$*-Scaling of ALICE Measurements at* $\sqrt{s_{\mathrm{NN}}} = 7$ *TeV*, 2011, arXiv:1107.3243 [hep-ph]

[106] Fermilab E769 Collaboration, *Forward Cross Sections for Production of D^+, D^0, D_s, D^{*+}, and λ_c in 250 GeV $\pi^\pm$, $K^\pm$, and p Interactions with Nuclei*, Phys. Rev. Lett. **77** 2388, 1996

[107] LHCb Collaboration, *Measurement of $\sigma(pp \to b\bar{b}X)$ at $\sqrt{s} = 7$ TeV in the forward region*, LHCb-PAPER-2010-002, CERN-PH-EP-2010-029, Phys.Lett. **B694** 209, 2010, arXiv:1009.2731 [hep-ex]

[108] M. Mangano *et al.*, *Heavy-quark correlations in hadron collisions at next-to-leading order*, Nucl. Phys. B **373** 295, 1992

[109] ALICE Collaboration, *Beauty production in pp collisions at $\sqrt{s} = 2.76$ TeV measured via semi-electronic decays*, CERN-PH-EP-2014-089, Phys. Lett. B **738** 97, 2014, arXiv:1405.4144 [nucl-ex]

[110] CMS Collaboration, *Nuclear Modification Factor of prompt D^0 in PbPb Collisions at $\sqrt{s_{\mathrm{NN}}} = 2.76$ TeV*, CMS-PAS-HIN-15-005, 2015

[111] ALICE Collaboration, *Centrality dependence of high-p_{T} D meson suppression in Pb-Pb collisions at $\sqrt{s_{\mathrm{NN}}} = 2.76$ TeV*, CERN-PH-EP-2015-151, submitted to JHEP, 2015, arXiv:1506.06604 [nucl-ex]

[112] CERN LHC, *LHC Design Report*, CERN-2004-003-V-1, 2004

[113] L. Evans *et al.*, *LHC Machine*, JINST, 3:S08001, 2008

[114] CERN press office, *The LEP story*, 09/12/2015, Retrieved from http://press.web.cern.ch/press-releases/2000/10/lep-story

[115] J. Klein, *Jet Physics with A Large Ion Collider Experiment at the Large Hadron Collider*, CERN-THESIS-2014-186, 2014

[116] LHCb Collaboration, *Proposed measurement programme to test beam-gas imaging in LHCb enhanced with gas injection*, EDMS 1166432 v1, 2011

[117] *Ions for LHC (I-LHC) Project*, 15/11/2015, Retrieved from http://project-i-lhc.web.cern.ch/project-i-lhc/Overview.htm

[118] *The CERN accelerator complex*, 15/11/2015, Retrieved from http://cds.cern.ch/record/1260465?ln=en

[119] B. Mandelli, *Detector and System Developments for LHC Detector Upgrades*, CERN-THESIS-2015-044, 1623, ISSN1501-7710, 2015

[120] G. Apollinari, *et al.*, *High-Luminosity Large Hadron Collider (HL-LHC) : Preliminary Design Report*, CERN-2015-005, ISBN: 978-929-083-422-9, 2015

[121] J.M. Jowett *et al.*, *Heavy Ions in 2011 and beyond*, proceedings of Chamonix 2011 workshop on LHC Performance, 2011

[122] F. Bordry, *Presentation to Scientific Policy Committee and Finance Committe*, June 2015, Retrieved from https://lhc-commissioning.web.cern.ch/lhc-commissioning/schedule/LHC-long-term.htm

[123] J.M. Jowett *et al.*, *Heavy ion operation from Run 2 to HL-LHC*, RLIUP: Review of LHC and Injector Upgrade Plans, 167, 2013

[124] J.M. Jowett *et al.*, *Heavy Ions in 2012 and the Progamme up to 2022*, proceedings of Chamonix 2012 workshop on LHC Performance, 2012

[125] R. Bruce *et al.*, *Final Report : Milestone: MS53*, CERN-ACC-2015-0126, 2015

[126] ATLAS Collaboration, *The ATLAS Experiment at the CERN Large Hadron Collider*, JINST, 3:S08003, 2008

[127] CMS Collaboration, *The CMS experiment at the CERN LHC*, JINST, 3:S08004, 2008

[128] LHCb Collaboration, *The LHCb Detector at the LHC*, JINST, 3:S08005, 2008

[129] ALICE Collaboration, *The ALICE experiment at the CERN LHC*, JINST, 3:S08002, 2008

[130] TOTEM Collaboration, *The TOTEM experiment at the CERN Large Hadron Collider*, JINST, 3:S08007, 2008

[131] LHCf Collaboration, *The LHCf detector at the CERN Large Hadron Collider*, JINST, 3:S08006, 2008

[132] MoEDAL Collaboration, *Technical Design Report of the MoEDAL Experiment*, Technical Report CERN-LHCC-2009-006. MoEDAL-TDR-001, CERN, Geneva, 2009

[133] M. Nessi, *Detector Plan for LS1*, proceeding of Chamonix 2012 Workshop on LHC Performance, 2012

[134] ATLAS Collaboration, *ATLAS Insertable B-Layer Technical Design Report*, CERN-LHCC-2010-013, ATLAS-TDR-19, 2010

[135] ATLAS Collaboration, *ATLAS Insertable B-Layer Technical Design Report Addendum*, CERN-LHCC-2012-009, ATLAS-TDR-19-ADD-1, 2012

[136] A. Ball, *Chronicles of CMS: the saga of LS1*, CERN Courier, http://cerncourier.com/cws/article/cern/60877, April 27, 2015

[137] M. Albrow, *et al.*, *CMS-TOTEM Precision Proton Spectrometer*, CERN-LHCC-2014-02, TOTEM-TDR-003, CMS-TDR-13, 2014

[138] R. Lindner, *LS1: A special opportunity for LHCb*, CERN Newsletter of the PH Department, http://ph-news.web.cern.ch/content/ls1-special-opportunity-lhcb, December 13, 2013

[139] ATLAS Collaboration, *Letter of Intent for the Phase-I Upgrade of the ATLAS Experiment*, CERN-LHCC-2011-012, LHCC-I-020, 2011

[140] ATLAS Collaboration, *New Small Wheel Technical Design Report*, CERN-LHCC-2013-006, ATLAS-TDR-020, 2013

[141] ATLAS Collaboration, *ATLAS Liquid Argon Calorimeter Phase-I Upgrade Technical Design Report*, CERN-LHCC-2013-017, ATLAS-TDR-022, 2013

[142] ATLAS Collaboration, *Technical Design Report for the ATLAS Forward Proton Detector*, CERN-LHCC-2015-009, ATLAS-TDR-024, 2015

[143] ATLAS Collaboration, *Technical Design Report for the Phase-I Upgrade of the ATLAS TDAQ System*, CERN-LHCC-2013-018, ATLAS-TDR-023, 2013

[144] ATLAS Collaboration, *Letter of Intent for the Phase-II Upgrade of the ATLAS Experiment*, CERN-LHCC-2012-022, LHCC-I-023, 2012

[145] CMS Collaboration, *CMS Technical Design Report for the Pixel Detector Upgrade*, CERN-LHCC-2012-016, CMS-TDR-11, 2012

[146] CMS Collaboration, *CMS Technical Design Report for the Phase 1 Upgrade of the Hadron Calorimeter*, CERN-LHCC-2012-015, CMS-TDR-10, 2012

[147] CMS Collaboration, *CMS TECHNICAL DESIGN REPORT FOR THE MUON ENDCAP GEM UPGRADE*, CERN-LHCC-2015-012, CMS-TDR-013, 2015

[148] CMS Collaboration, *CMS Technical Design Report for the Level-1 Trigger Upgrade*, CERN-LHCC-2013-11, CMS-TDR-12, 2013

[149] LHCb Collaboration, *Letter of Intent for the LHCb Upgrade*, CERN-LHCC-2011-001, LHCC-I-018, 2011

[150] LHCb Collaboration, *Framework TDR for the LHCb Upgrade : Technical Design Report*, CERN-LHCC-2012-007, LHCb-TDR-12, 2012

[151] LHCb Collaboration, *LHCb VELO Upgrade Technical Design Report*, CERN-LHCC-2013-021, LHCb-TDR-013, 2013

[152] LHCb Collaboration, *LHCb PID Upgrade Technical Design Report*, CERN-LHCC-2013-022, LHCb-TDR-014, 2013

[153] LHCb Collaboration, *LHCb Tracker Upgrade Technical Design Report*, CERN-LHCC-2014-001, LHCb-TDR-015, 2014

[154] LHCb Collaboration, *LHCb Trigger and Online Upgrade Technical Design Report*, CERN-LHCC-2014-016, LHCb-TDR-016, 2014

[155] ALICE Collaboration, *ALICE physics performance: Technical Design Report*, ALICE-TDR-13, CERN-LHCC-2005-030, 2005

[156] ALICE Collaboration, *Performance of the ALICE Experiment at the CERN LHC*, Int. J. Mod. Phys. A 29 1430044, 2014, arXiv:1402.4476 [nucl-ex]

[157] ALICE Collaboration, *ALICE Inner Tracking System (ITS) : Technical Design Report*, ALICE-TDR-4, CERN-LHCC-99-012, 1999

[158] ALICE Collaboration, *ALICE time projection chamber : Technical Design Report*, CERN-OPEN-2000-183, ALICE-TDR-7, CERN-LHCC-2000-001, 2000

[159] ALICE Collaboration, *ALICE transition-radiation detector : Technical Design Report*, ALICE-TDR-9, CERN-LHCC-2001-021, LYCEN-2001-97, 2001

[160] ALICE Collaboration, *ALICE high-momentum particle identification : Technical Design Report*, ALICE-TDR-1, CERN-LHCC-98-019, 1998

[161] ALICE Collaboration, *ALICE Electromagnetic Calorimeter Technical Design Report*, CERN-LHCC-2008-014, ALICE-TDR-14, 2008

[162] ALICE Collaboration, *ALICE Time-Of-Flight system (TOF) : Technical Design Report*, ALICE-TDR-8, CERN-LHCC-2000-012, 2000

[163] ALICE Collaboration, *ALICE Time-Of Flight system (TOF) : addendum to the Technical Design Report*, ALICE-TDR-8-add-1, CERN-LHCC-2002-016, 2002

[164] ALICE Collaboration, *ALICE Photon Multiplicity Detector (PMD) : Technical Design Report*, CERN-OPEN-2000-184, ALICE-TDR-6, CERN-LHCC-99-032, 1999

[165] ALICE Collaboration, *ALICE Photon Multiplicity Detector (PMD) : addendum to the Technical Design Report*, ALICE-TDR-6-add-1, CERN-LHCC-2003-038, 2003

[166] ALICE Collaboration, *ALICE forward detectors: FMD, TO and VO : Technical Design Report*, ALICE-TDR-11, CERN-LHCC-2004-025, 2004

[167] ALICE Collaboration, *ALICE Photon Spectrometer (PHOS) : Technical Design Report*, ALICE-TDR-2, CERN-LHCC-99-004, 1999

[168] ALICE Collaboration, *ACORDE a Cosmic Ray Detector for ALICE*, Nucl. Instrum. Methods Phys. Res., **A 572**, 102, 2007

[169] ALICE Collaboration, *ALICE Zero-Degree Calorimeter (ZDC) : Technical Design Report*, ALICE-TDR-3, CERN-LHCC-99-005, 1999

[170] ALICE Collaboration, *ALICE dimuon forward spectrometer : Technical Design Report*, ALICE-TDR-5, CERN-LHCC-99-022

[171] ALICE Collaboration, *ALICE dimuon forward spectrometer : addendum to the Technical Design Report*, ALICE-TDR-5-add-1, CERN-LHCC-2000-046, 2000

[172] L. Rossi *et al.*, *Pixel Detectors: From Fundamental to Applications*, Springer, Berlin, Heidelberg, 2006

[173] ALICE Collaboration, *Centrality dependence of π, K, p production in Pb-Pb collisions at $\sqrt{s_{\rm NN}}$=2.76 TeV*, Phys. Rev. C **88**, 044910, 2013, arXiv:1303.0737 [hep-ex]

[174] F. Ronchetti, *ALICE: from LS1 to readiness for Run 2*, Retrieved from: http://alicematters.web.cern.ch/?q=ALICE_LS1_readiness, 05/27/2015

[175] J. Alme *et al.*, *The ALICE TPC, a large 3-dimensional tracking device with fast readout for ultra-high multiplicity events*, Nucl. Instrum. Meth. **A622**, 316, 2010, arXiv:1001.1950 [physics.ins-det]

[176] A. Kalweit, *Energy Loss Calibration of the ALICE Time Projection Chamber*, Diploma thesis, TU Darmstadt, 2008

[177] F. Barile for the ALICE Collaboration, *Light (Hyper-)Nuclei production at the LHC measured with ALICE*, proceedings of 3rd International Conference on New Frontiers in Physics conference, 2014, arXiv:1411.1941v1 [hep-ex]

[178] C. Grupen *et al.*, *Particle Detectors*, ISBN: 978-052-184-006-4, Cambridge University Press, 2008

[179] ALICE Collaboration, *ALICE trigger data-acquisition high-level trigger and control system : Technical Design Report*, ALICE-TDR-10, CERN-LHCC-2003-062, 2004

[180] ALICE Collaboration, *ALICE computing : Technical Design Report*, ALICE-TDR-12, CERN-LHCC-2005-018, 2005

[181] J. Klein for the ALICE Collaboration, *The ALICE Transition Radiation Detector: status and perspectives for Run II*, proceeding to LHCP 2015, arXiv:1601.00493 [physics.ins-det]

[182] ALICE Collaboration, *ALICE DCal: An Addendum to the EMCal Technical Design Report Di-Jet and Hadron-Jet correlation measurements in ALICE*, CERN-LHCC-2010-011, ALICE-TDR-14-add-1, 2010

[183] G. Herrera Corral, *Diffractive Physics with ALICe at the LHC: tre control of quantum collisions*, Journal of Physics: Conference Series **624** 012008, 2015

[184] The LHC Forward Physics Working Group, *LHC Forward Physics*, CERN-PH-LPCC-2015-001, SLAC-PUB-16364, DESY 15-167, 2015

[185] ALICE Collaboration, *Addendum of the Letter Of Intent for the Upgrade of the ALICE Experiment: The Muon Forward Tracker*, CERN-LHCC-2013-014, LHCC-I-022-ADD-1, 2013

[186] ALICE Collaboration, *Conceptual Design Report for the Upgrade of the ALICE ITS*, CERN-LHCC-2012-005, LHCC-G-159, 2012

[187] ALICE Collaboration, *Upgrade of the ALICE Time Projection Chamber*, CERN-LHCC-2013-020, ALICE-TDR-016, 2013

[188] ALICE Collaboration, *Upgrade of the Readout & Trigger System*, CERN-LHCC-2013-019, ALICE-TDR-015, 2014

[189] ALICE Collaboration, *Upgrade of the Online-Offline computing system*, CERN-LHCC-2015-006, ALICE-TDR-019, 2015

[190] M. Kofarago for the ALICE Collaboration, *Upgrade of the Inner Tracking System of ALICE*, proceeding of VERTEX2015, POS(VERTEX2015)009, 2015, arXiv:1511.08368 [physics.ins-det]

[191] P. Yang *et al.*, *MAPS development for the ALICE ITS upgrade*, JINST 10 C03030, 2015

[192] F. Reidt, *Studies on the ALICE Inner Tracking System Upgrade*, Ph.D. thesis, University of Heidelberg, 2016

[193] R. Brun *et al.*, *GEANT detector description and simulation tool*, CERN-W5013, CERN-W-5013, 1994

[194] I. Antcheva *et al*, *ROOT – A C++ framework for petabyte data storage, statistical analysis and visualization*, Comput. Phys. Commun., 180 **2499**, 2009

[195] R. Brun *et al.*, *ROOT*, http://root.cern.ch

[196] *AliRoot*, http://aliweb.cern.ch/Offline

[197] ALICE Collaboration, *The ALICE Offline Bible*, URL *http://aliweb.cern.ch/secure/Offline/sites/aliweb.cern.ch.Offline/files/uploads/OfflineBible.pdf*, (08/20/2015)

[198] ALICE Collaboration, *ALICE computing : Technical Design Report*, ALICE-TDR-12, CERN-LHCC-2005-018, 2005

[199] R. Shahoyan, *private communication*

[200] M. Ivanov, *private communication*

[201] A. Dainese, *private communication*

[202] J. Belikov, *private communication*

[203] X. N. Wang *et al.*, *HIJING: A Monte Carlo model for multiple jet production in pp, pA, and AA collisions*, Phys. Rev. D **44**(11) 3501, 1991

[204] T. Sjöstrand *et al.*, *PYTHIA 6.4 physics and manual*, JHEP **05** 026, 2006, arXiv:hep-ph/0603175

[205] R. Brun *et al.*, *ROOT - TTree class*, 19/10/2015, Retrieved from https://root.cern.ch/root/html518/TTree.html

[206] P. Farthouat *et al.*, *TTC-VMEbus Interface TTCvi MkII*, Rev 1.1, RD12 project, 2000

[207] GEANT4 Collaboration, *et al.*, *GEANT4 - a simulation toolkit*, Nucl. Instr. and Meth. **A 506**, 250-303, SLAC-PUB-9350, FERMILAB-PUB-03-339, 2003

[208] A. Ferrari *et al.*, *FLUKA: A multi-particle transport code (Program version 2005)*, CERN-2005-010, SLAC-R-773, INFN-TC-05-11, 2005

[209] R. Frühwirth, *Application of Kalman filtering to track and vertex fitting*, Nucl. Instr. and Meth. **A 262**, 444, 1987

[210] ALICE Collaboration, *Centrality Dependence of the Charged-Particle Multiplicity Density at Midrapidity in Pb-Pb Collisions at* $\sqrt{s_{\mathrm{NN}}} = 2.76\,TeV$, CERN-PH-EP-2010-071, Phys. Rev. Lett. **106** 032301, 2011, arXiv:1012.1657 [nucl-ex]

[211] G. Welch *et al.*, *An Introduction to the Kalman Filter: SIGGRAPH 2001 Course 8*, Computer Graphics, Annual Conference on Computer Graphics & Interactive Techniques 12-17, 2001

[212] K. Gade, *Introduction to Inertial Navigation and Kalman Filtering*, Tutorial for IAIN World Congress, Stockholm, October 2009

[213] Y. Belikov *et al.*, *TPC tracking and particle identification in high density environment*, eConf **C0303241**, TULT011, 2003, arXiv:physics/0306108 [physics.data-an]

[214] B. Batyunya *et al.*, *Kalman filtering application for track recognition and reconstruction in ALICE tracking system*, ALICE Internal Note /PAT ALICE/97-24, 1997

[215] M. Bondila, *Detection of charged kaons using the decay topology in ALICE TPC*, PhD thesis, Jyväskylä, 2006

[216] M. Ivanov *et al.*, *Track reconstruction in high density environment*, Nucl. Instr. and Meth. **A 566**, 70, 2006

[217] S. Gorbunov *et al.*, *Reconstruction of decayed particles based on the Kalman filter*, CBM-SOFT-note-2007-003, May 2007

[218] J.D. Jackson, *Classical Electrodynamics*, John Wiley & Sons Ltd., 1962

[219] P. Billoir, *Error propagation in the helix track model.*, DELPHI 87-4 PROG 63, 1986

[220] L. Layer, *Development of a fast simulation tool for vertexing studies in ALICE*, bachelor thesis, Heidelberg, 2015

[221] R.K. Bock *et. al.*, *Data analysis techniques for high-energy physics experiments*, Cambridge University Press, 1990

[222] B. Rossi *et al.*, *Cosmic-Ray Theory*, Rev. Mod. Phys. **13**, 240, 1941

[223] R.L. Glückstern, *Uncertainties in track momentum and direction, due to multiple scattering and measurement errors*, Nucl. Instr. and Meth. **24**, 381, 1963

[224] ATLAS Collaboration, *Fast Simulation for ATLAS: Atlfast-II and ISF*, Journal of Physics: Conference Series, **396**, 022031, 2012

[225] ATLAS Collaboration, *FATRAS - the ATLAS Fast Track Simulation project*, ATL-SOFT-PROC-2011-008, 2011

[226] A. Giammanco, *The Fast Simulation of the CMS Experiment*, Journal of Physics: Conference Series, **513**, 022012, 2014

[227] A. Mastroserio *et al.*, *Simulation tools for the ALICE ITS upgrade*, ALICE internal note, 2012

[228] STAR Collaboration, *A Heavy Flavor Tracker for STAR*, LBNL-PUB-5509-2008, 2008

[229] N. Nethercote *et al.*, *Valgrind: A Framework for Heavyweight Dynamic Binary Instrumentation*, proceedings of PLDI 2007, San Diego, California, USA, June 2007. See also: http://valgrind.org

[230] *massif visualizer*, 12/02/2016, Retrieved from https://projects.kde.org/projects/extragear/sdk/massif-visualizer

[231] *GSI Cluster Computing*, 27/12/2015, Retrieved from https://wiki.gsi.de/foswiki/bin/view/Linux/BatchFarm

[232] CMS Collaboration, *Suppression of non-prompt* J/ψ*, prompt* J/ψ*, and* Υ(1S) *in PbPb collisions at* $\sqrt{s_{\mathrm{NN}}} = 2.76$ *TeV*, JHEP **1205** 063, 2012, arXiv:arXiv:1201.5069 [nucl-ex]

[233] CMS Collaboration, *Measurements of b-jet Nuclear Modification Factors in pPb and PbPb Collisions with CMS*, proceedings from Quark Matter 2014, arXiv:1410.2576 [nucl-ex]

[234] ALICE Collaboration, *Centrality determination of Pb-Pb collisions at* $\sqrt{s_{\mathrm{NN}}} = 2.76$ *TeV with ALICE*, Phys. Rev. **C88** 044909, 2013, arXiv:1301.4361 [nucl-ex]

[235] M. Djordjevic *et al.*, *Heavy flavor suppression predictions at 5.1 TeV Pb+Pb collisions at LHC*, Phys. Rev. C **92** 024918, 2015, arXiv:1505.04316 [nucl-th]

[236] ALICE Collaboration, *Suppression of high transverse momentum D mesons in central Pb–Pb collisions at* $\sqrt{s_{\mathrm{NN}}} = 2.76$ *TeV*, JHEP 09 **112**, 2012, arXiv:1203.2160 [nucl-ex]

[237] ALICE Collaboration, *Reference cross section measurements with ALICE in pp and Pb–Pb collisions at LHC*, proceedings from LHC Lumi Days 2012, 2013, arXiv:1305.7044 [nucl-ex]

[238] CMS Collaboration, *Inelastic proton-proton cross section measurements in CMS at* $\sqrt{s} = 7$ *TeV*, CMS-FWD-11-001, CERN-PH-EP-2012-293, Phys. Lett. B **722** 5, 2013, arXiv:1210.6718 [hep-ex]

[239] ATLAS Collaboration, *Measurement of the Inelastic Proton-Proton Cross Section at* $\sqrt{s} = 13$ *TeV with the ATLAS Detector at the LHC*, ATLAS-CONF-2015-038, 2015

[240] R. Rapp, *private communication*

[241] J. Uphoff, *private communication*

[242] CMS Collaboration, *Measurement of the* B^{+} *Production Cross Section in pp Collisions at* $\sqrt{s} = 7$ *TeV*, Phys. Rev. Lett. **106** 112001, 2011

[243] P. Sorensen, *Elliptic Flow: A study of space-momentum correlations in relativistic nuclear collisions*, *Quark-Gluon Plasma 4*, World Scientific, ISBN: 978-981-4293-28-0, 2010, arXiv:0905.0174 [nucl-ex]

[244] C. Möhler, Master Thesis, *D-meson production at ultra-low transverse momentum in proton-proton collisions with ALICE at the LHC*, Ruprecht-Karls Universität Heidelberg, 2014

[245] ALICE Collaboration, K_s^0 *and* λ *production in Pb–Pb collisions with the ALICE experiment*, proceedings of Quark Matter 2011, arXiv:1109.4807 [hep-ex]

[246] A. Ryd *et al.*, *EvtGen A Monte Carlo Generator for B-Physics*, EVTGEN-V00-11-07

[247] B. Hess, Diploma Thesis, *Online Electron Identification for Triggering with the ALICE Transition Radiation Detector*, Ruprecht-Karls Universität Heidelberg, 2011